Data-driven simulation of magnetic fields in accelerator magnets

Datengetriebene Simulation von Magnetfeldern in Beschleunigermagneten
Zur Erlangung des akademischen Grades Doktor-Ingenieur (Dr.-Ing.)
genehmigte Dissertation von Luisa Fabiola Fleig aus Emmendingen, Deutschland
Fachbereich Elektrotechnik und Informationstechnik
Tag der Einreichung: 25.06.2024, Tag der Prüfung: 07.10.2024

1. Gutachten: Prof. Dr. Sebastian Schöps
2. Gutachten: Univ. Doz. Dr.-Ing. Stephan Russenschuck
3. Gutachten: Prof. Dr. techn. Dr. h.c. Manfred Kaltenbacher
Darmstadt, Technische Universität Darmstadt

TECHNISCHE UNIVERSITÄT DARMSTADT

Fachbereich 18
Computational Electromagnetics Group

Data-driven simulation of magnetic fields in accelerator magnets
Datengetriebene Simulation von Magnetfeldern in Beschleunigermagneten

genehmigte Dissertation von Luisa Fabiola Fleig aus Emmendingen, Deutschland
Fachbereich Elektrotechnik und Informationstechnik

Date of submission: 25.06.2024
Date of thesis defense: 07.10.2024

Darmstadt, Technische Universität Darmstadt

Bitte zitieren Sie dieses Dokument als:
URN: urn:nbn:de:tuda-tuprints-285618
URL: https://tuprints.ulb.tu-darmstadt.de/28561
Jahr der Veröffentlichung auf TUprints: 2024

Dieses Dokument wird bereitgestellt von tuprints,
E-Publishing-Service der TU Darmstadt
https://tuprints.ulb.tu-darmstadt.de
tuprints@ulb.tu-darmstadt.de

Erklärungen laut Promotionsordnung

§ 8 Abs. 1 lit. c PromO

Ich versichere hiermit, dass die elektronische Version meiner Dissertation mit der schriftlichen Version übereinstimmt.

§ 8 Abs. 1 lit. d PromO

Ich versichere hiermit, dass zu einem vorherigen Zeitpunkt noch keine Promotion versucht wurde. In diesem Fall sind nähere Angaben über Zeitpunkt, Hochschule, Dissertationsthema und Ergebnis dieses Versuchs mitzuteilen.

§ 9 Abs. 1 PromO

Ich versichere hiermit, dass die vorliegende Dissertation – abgesehen von den in ihr ausdrücklich genannten Hilfen – selbstständig verfasst wurde und dass die „Grundsätze zur Sicherung guter wissenschaftlicher Praxis an der Technischen Universität Darmstadt“ und die „Leitlinien zum Umgang mit digitalen Forschungsdaten an der TU Darmstadt“ in den jeweils aktuellen Versionen bei der Verfassung der Dissertation beachtet wurden.

§ 9 Abs. 2 PromO

Die Arbeit hat bisher noch nicht zu Prüfungszwecken gedient.

Darmstadt, 25.06.2024

Luisa Fabiola Fleig

Das Universum ist voll der wunderbaren Dinge,
die geduldig darauf warten, dass unsere Sinne schärfer werden.

Eden Phillpotts

Zusammenfassung

Der am Europäischen Kernforschungszentrum (CERN) betriebene Beschleunigerkomplex umfasst Tausende normal- und supraleitende Elektromagnete sowie Permanentmagnete, welche die Teilchenstrahlen leiten, fokussieren und defokussieren. In diesem Zusammenhang muss das Magnetfeld in der Regel strengen Qualitätsanforderungen genügen, wobei relative Fehler von nur wenigen Zehntausendstel toleriert werden. Für den Betrieb der Magnete werden Messungen und Simulationen der Magnetsysteme und der von ihnen erzeugten Felder verwendet. Trotz der Fortschritte in numerischen Methoden und Rechenleistung in den vergangenen Jahrzehnten sind simulierte Feldvorhersagen für den Betrieb von Beschleunigermagneten weiterhin unzureichend. Die Simulationen sind sowohl mit bekannten und unbekannten Fehlern als auch mit aleatorischen und epistemischen Unsicherheiten behaftet, beispielsweise ist das Wissen über die zugrunde liegenden physikalischen Prozesse oft begrenzt. Messungen wiederum sind mit zufälligen und systematischen Unsicherheiten behaftet. Um feldbezogene Größen vorherzusagen (Interpolation und Extrapolation) und um Einblicke in schwer messbare lokale Größen (Introspektion) zu erhalten, wurden Modelle von Beschleunigermagneten und den von ihnen erzeugten Feldern entwickelt, die Simulationen mit Messdaten kombinieren. Durch die Kombination beider Ansätze können einige der jeweiligen Einschränkungen überwunden werden. Diese Strategie wird auch als hybride Modellierung bezeichnet. Obwohl die Modelle von Beschleunigermagneten sehr verschieden sind, lassen sich einige gemeinsame Methoden zu ihrer Entwicklung und Anpassung erkennen. Dazu gehören deterministische und stochastische Modellaktualisierung sowie das Lösen inverser und nicht wohlgestellter Probleme.

Unter Anwendung dieser Methoden werden in dieser Arbeit drei magnetostatische Modelle von Beschleunigermagneten entwickelt, die sich auf unterschiedliche Aspekte konzentrieren. Zuerst wird ein datengetriebenes stochastisches $B(H)$-Kurvenmodell, das auf Permeameter-Messungen von Materialproben des Jochs und der Karhunen-Loève-Entwicklung basiert, verwendet, um die Aktualisierung der $B(H)$-Kurve des Jochs durch eine Approximation mit niedrigem Rang zu regularisieren. Im zweiten Projekt werden die Permanentmagnetisierungen in einem dreidimensionalen Modell des ersten kurzen Halbach-Dipols des FASER-Experiments mit Bayes'scher Inferenz aktualisiert. Dabei wird aufgezeigt, dass die Diskrepanz zwischen den gemessenen und den vorhergesagten Multipolkoeffizienten höherer Ordnung durch die Anpassung der Magnetisierungen im Bereich ihrer Fertigungstoleranzen erklärt werden kann. Die dritte Anwendung befasst sich mit der Feldbeschreibung in gekrümmten Magnetsystemen, bei denen die klassische Feldbeschreibung basierend auf Multipolen in zylindrischen Koordinaten nicht richtig ist. Die toroidale harmonische Entwicklung ist eine bekannte Alternative, jedoch sind Algorithmen zur Bestimmung ihrer Koeffizienten anhand von Feldbeobachtungen bisher kaum untersucht worden. Zu diesem Zweck werden ein Identifizierungsansatz mit Hilfe der Methode der kleinsten Quadrate und eine integralbasierte Identifizierungsmethode hergeleitet und beurteilt. Die drei entwickelten Modelle folgen dem Konzept hybrider Modellierung, indem sie physikbasierte Methoden mit datenbasierten Methoden kombinieren. Die Einbeziehung des aus Messungen gewonnenen Wissens verbessert in allen untersuchten Anwendungsfällen die Feldvorhersagen der Modelle, sogar über den Bereich der Trainingsdaten hinaus. Die Validierung dieser Methodik im Kontext von Beschleunigermagneten trägt dazu bei, eine engere Verbindung zwischen den Modellen, den Datensätzen und den physischen Objekten herzustellen, die in der TE-MSC-TM Abteilung am CERN betrieben werden.

Abstract

The accelerator complex operated at the European Organization for Nuclear Research (CERN) consists of thousands of normal- and superconducting electromagnets and permanent magnets, which are guiding, focusing, and defocusing the particle beams. In this context, the magnetic field usually has to meet high quality requirements allowing relative errors of only a few units in 10000. Simulations and measurements of magnet systems and their generated fields are used for operation. Despite the improvements in numerical methods and computing power in the last decades, simulated field predictions are insufficient for the operation of accelerator magnets, because the simulations are affected by aleatory and epistemic uncertainty as well as acknowledged and unacknowledged errors. For example, the knowledge of the underlying physical processes is often limited. Measurements on the other hand are affected by random and systematic uncertainties. To predict field-related quantities of interest (interpolation and extrapolation), and to gain insight into local quantities (introspection) that are not easily measurable, system models of accelerator magnets and their generated field have been developed that combine simulations with measurement data. By the combination of both approaches, some of their respective limitations can be overcome. This strategy is also known as hybrid modeling. Even though the system models of accelerator magnets found in the literature are heterogeneous, some common methods can be identified to build and adjust them. These include deterministic and stochastic model updating, solving inverse problems, and addressing their ill-posedness.

Applying these methods, three system models of accelerator magnets in the static operation mode are derived in this thesis, focusing on different aspects. First, we use a data-driven stochastic $B(H)$-curve model, based on permeameter measurements of yoke material specimens and the Karhunen-Loève expansion, to regularize by low-rank approximation the updating of the yoke's $B(H)$-curve. Second, the permanent magnetizations in a three-dimensional system model of the first short Halbach dipole of the FASER experiment are updated with Bayesian inference. We show that the mismatch between the measured and the predicted higher-order multipole coefficients can be explained by adjusting the magnetizations in the range of their manufacturing tolerances. The third application addresses the field description in curved magnet systems, where the classical field description based on the circular harmonic expansion fails. The toroidal harmonic expansion is a well-known alternative, but algorithms to determine its coefficients based on field observations have rarely been studied. For this purpose, we derive and evaluate an identification approach based on linear least squares fitting and an identification method based on integration.

The three derived system models follow the spirit of hybrid modeling by combining physics-based methods with data-based methods. Including knowledge obtained from measurements improves in all the studied use cases the field predictions of the system model, even outside the regime of the training data. The validation of this methodology in the context of accelerator magnets contributes to establishing more interconnections between the models, data sets, and physical objects operated at the TE-MSC-TM section at CERN.

Contents

List of figures

List of tables

1 Introduction

1.1 CERN

The European Organization for Nuclear Research (CERN) is one of the largest research facilities in particle physics in the world. Its mission is to uncover what the universe is made of [32]. For this purpose, collisions of charged particles at high energies are studied. To increase the particle energy and to steer the particles to the interaction points within the four large experiments ATLAS, ALICE, CMS, and LHCb, a particle accelerator complex, including the world's largest and most powerful particle accelerator, the Large Hadron Collider (LHC), is operated at CERN.

Charged particles are affected by electromagnetic fields, according to the Lorentz force $\mathbf{F} = q(\mathbf{E} + \mathbf{v} \times \mathbf{B})$, where $\mathbf{E}$ is the electric field, $\mathbf{B}$ is the magnetic flux density, q is the charge, and $\mathbf{v}$ is the velocity of the particle. The change of the particle's energy can be only influenced by the electric field, since $\mathbf{v} \cdot \mathbf{F} = q\mathbf{v} \cdot \mathbf{E}$. Therefore, the particles are accelerated using oscillating electric fields that are contained in radio frequency cavities. Charged particles can be steered in other directions than their trajectory using electric and magnetic fields. However, at high energy, an electric field having the same influence as a magnetic field of $1\,\mathrm{T}$ would require a field strength of $\mathrm{GV\,m^{-1}}$ magnitude. Therefore, solely magnetic fields are used for particle steering in high-energy circular accelerators [119].

The CERN accelerator complex consists of thousands of magnets. Thereof, 1232 main dipoles, each $15\,\mathrm{m}$ long and with a weight of around $35\,\mathrm{t}$, are installed in the LHC. The various magnets serve different purposes, e.g., dipole magnets bend the particle beam, quadrupole magnets focus and defocus the particle beam, separation dipoles bring together the two opposing particle beams before and separate them after they pass the interaction points, higher-order multipole magnets correct for imperfections, and spectrometer magnets within the experiments bend charged particles after the collision for characterization. Magnets are used not only in the accelerator complex and in the large experiments, but there are also various smaller experiments hosted by CERN. Besides the accelerators, two particle decelerators are operated. Different magnet technologies, such as normal- and superconducting electromagnets as well as permanent magnets are used at CERN. Moreover, magnet systems find use in other disciplines such as nuclear fusion [11] and medicine [22].
Each application of a magnet system specifies a set of field requirements such as field gradient, field homogeneity, field integrals, or multipoles. These requirements are associated with tolerable error budgets that specify the desired field quality. For the LHC main dipole, error limits for the dimensionless relative multipole coefficients at a $17\,\mathrm{mm}$ reference radius are derived in [27]. Their magnitude is a few units in 10000. Meeting the field requirements is essential for machine performance because a high field quality reduces the probability of particle losses that can cause quenches and a high field quality increases the particle circulation duration, leading to higher beam intensities and higher luminosity [27].

1.2 Motivation

1.2.1 Magnetic measurements and simulations

The TM section in the MSC group of the TE department (TE-MSC-TM) at CERN is in charge of testing and measuring CERN's accelerator magnets. One mission of the TE-MSC-TM section is to provide the latest technologies for magnetic measurements [31]. This includes developing, operating, and maintaining measurement systems, data acquisition software, and data processing software.

The magnetic field generated by a magnet system can be simulated using numerical models and measured using suitable field transducers. For this purpose, various field transducers such as rotating coil magnetometers, fluxmeters, stretched wires, and a 3D Hall probe mapper are operated by the TE-MSC-TM section. The numerical models are usually based on the finite element method (FEM), the boundary element method (BEM), or a combination of both. Software tools such as the Routine for the Optimization of magnet X - sections, Inverse field calculation and coil End design (ROXIE) [121], GetDP [60] Opera [42], or RAT [93] are used for implementation.

Purpose of magnetic measurements and simulations Magnetic measurements and simulations accompany the entire life cycle of a magnet system, consisting of the design, prototype, production, characterization, and operation phases. A discussion about the necessity of measurements and simulations in each phase can be found in [120]:

- In the design phase of a magnet system, numerical models are used to find a magnet configuration that generates the magnetic field that meets the requirements of a physical experiment.
  To validate the material laws, implemented in the model of the magnet, and to study the effects of manufacturing tolerances on the field requirements, measurements of material specimens for magnetic characterization are conducted. Examples are split-coil permeameter measurements to obtain the $B(H)$-curve of the iron yoke material and Helmholtz coil measurements for determining the magnetization vector of permanent magnet blocks.
- In the prototype phase of a magnet system, field measurements of the prototype are performed to validate the field prediction of the numerical model. If the field predictions and the field measurements differ significantly, the model assumptions and model parameters are reconsidered to find a reason for the deviation and to improve the model or prototype accordingly.
- During the production phase of a series of magnets, measurement campaigns are carried out to follow up production and for quality assurance of the magnet components.
- For magnet systems that went through a long Research and Development (R&D) phase and that are manufactured in series production such as the LHC main dipoles, field predictions of numerical models and field measurements usually coincide and achieve the required accuracy to confirm the specified field requirements. However, field predictions and field measurements can differ significantly for magnet systems that cannot benefit from long R&D phases to validate their numerical models and from series production that reduces variations in the manufacturing process. Therefore, field measurements are performed after the production phase, and solely the measurements are used to characterize the magnet as built.

- To provide field-related quantities of interest for magnet operation, the numerical model of the magnet system itself is often not required. Instead, less complex models based on solutions to the Laplace equation in vacuum such as multipole expansions are used to describe the characterized field. For some specific magnets, e.g., in the LHC injector chain, where dynamic effects, hysteresis, and the powering cycle of the magnet during operation have to be taken into account, the predictions of the common models are often not sufficiently accurate. In these cases, real-time field measurements of reference magnets are conducted that are excited with the same powering cycle as the magnet in operation.

Challenges of magnetic measurements According to the Guide to the Expression of Uncertainty in Measurement (GUM), the word "uncertainty" means doubt [16, Def. 2.2.1]. The *uncertainty of a measurement* is defined as a "parameter, associated with the result of a measurement that characterizes the dispersion of the values that could reasonably be attributed to the measurand", where the *result of a measurement* is the best estimate for the value of the measurand [16, Def. 2.2.3]. Uncertainty in measurements arises from random effects and the imperfect correction of systematic effects. These effects include for example variations in repeated measurements, inadequate knowledge of the effects of environmental conditions, approximations and wrong assumptions incorporated in the measurement method, and finite instrument resolution [16, Def. 3.3.2].
The *error of a measurement* is the "result of a measurement minus a true value of the measurement" [16, Def. B.2.19]. Because a true value is indeterminate by nature, measurement errors are an idealized concept and can not be known exactly [16, Def. 3.2.1, Def. B.2.3]. Therefore, the GUM suggests discussing measurement uncertainty rather than measurement errors.

Uncertainty in magnetic measurements arises for example due to random measurement noise, systematic errors such as stray fields and perturbations caused by the measurement device, and uncertainties and errors of the sensor model that maps raw signals to the result of the measurement, e.g., wrong calibration data, numerical approximations, or mathematical simplifications and assumptions such as the linearity of a sensor response or the orthogonality of the sensor alignment in a Hall probe.
Moreover, field measurements are limited by the availability of suitable measurement equipment, aperture constraints (not every position can be measured), and budget constraints (not every operation mode can be measured).

Challenges of magnetic simulations A general framework to identify uncertainties and errors in computational simulations that involve the solution of partial differential equations is developed in [101]. The terms "aleatory uncertainty" and "epistemic uncertainty" describe the uncertainty in modeling and simulation. *Aleatory uncertainty* describes the "inherent variation associated with the physical system or environment under consideration" [101], an example is the randomness of input parameters such as material laws or geometry parameters. Uncertainties that occur due to limited or inadequate knowledge of the involved physical processes are part of the *epistemic uncertainty* that is "a potential inaccuracy in any phase of the modeling process that is due to the lack of knowledge" [101].
In simulation and modeling, the term "error" refers to "a recognizable inaccuracy in any phase or activity of modeling and simulation that is not due to lack of knowledge" [101]. One distinguishes between acknowledged errors such as the ignorance of physical effects, simplifications in the mathematical representation or discretization errors, and unacknowledged errors such as implementation mistakes. Typical acknowledged errors in the simulation of accelerator magnets are the neglection of non-linear, anisotropic, hysteretic material properties, the neglection of the coupling of magnetic, thermal, and mechanical phenomena, or the neglection of dynamic effects such as eddy currents.

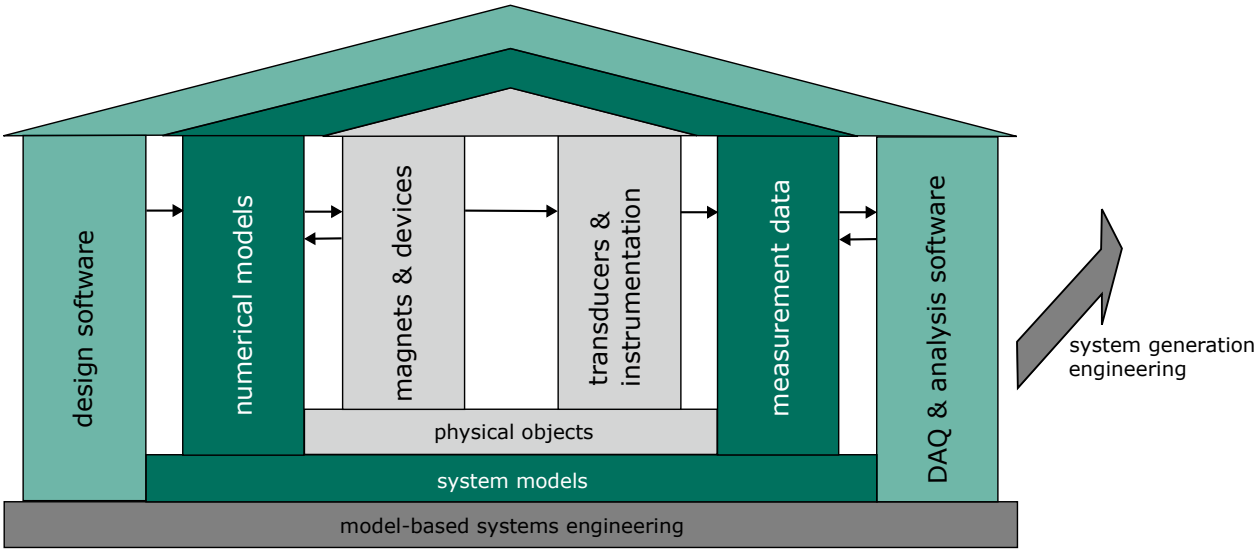

Figure 1.1: Organization of physical objects, system models, and software tools that are operated by the TE-MSC-TM section. Figure adapted from [120].

Framework for magnetic measurements and simulations The physical objects, system models, and software tools that are developed and used in the TE-MSC-TM section can be organized into six main categories which are (1) design software, (2) numerical models, (3) magnets and devices, (4) transducers and instrumentation, (5) measurement data, and (6) data acquisition (DAQ) and analysis software. The magnets and devices together with the transducers and instrumentation can be summarized as physical objects. The numerical models and measurement data both belong to the system models. Figure 1.1 (adapted from [120]) depicts these categories' organization, interrelations, and underlying management methodologies. Model-based systems engineering and system generation engineering are required for project management and traceability. In this overall picture, the project of this thesis is located within the system model category and its interactions with the physical objects category.

1.2.2 System models

In this work, the term *model* is understood as specified by the definition of Stachowiak [128] according to that a model can be characterized by the following three properties: (1) Mapping: a model is related to an original, (2) Reduction: a model does not capture all of the original's attributes, and (3) Pragmatism: a model serves a certain purpose, e.g., being a replacement of the original for a certain purpose and under certain circumstances.
A zoom-in into the physical objects and system models categories and their interrelations is shown in Figure 1.2 (adapted from [120]). Given an admissible operation mode, system models can predict quantities of interest, such as field maps, and derive quantities comparable to measured quantities by applying an observation function. System models should have the pragmatic property of also enabling interpolative and extrapolative predictions. For example, they should be able to make accurate predictions for parts of their admissible range, e.g. concerning the space or the excitation currents that were not used to build the models.

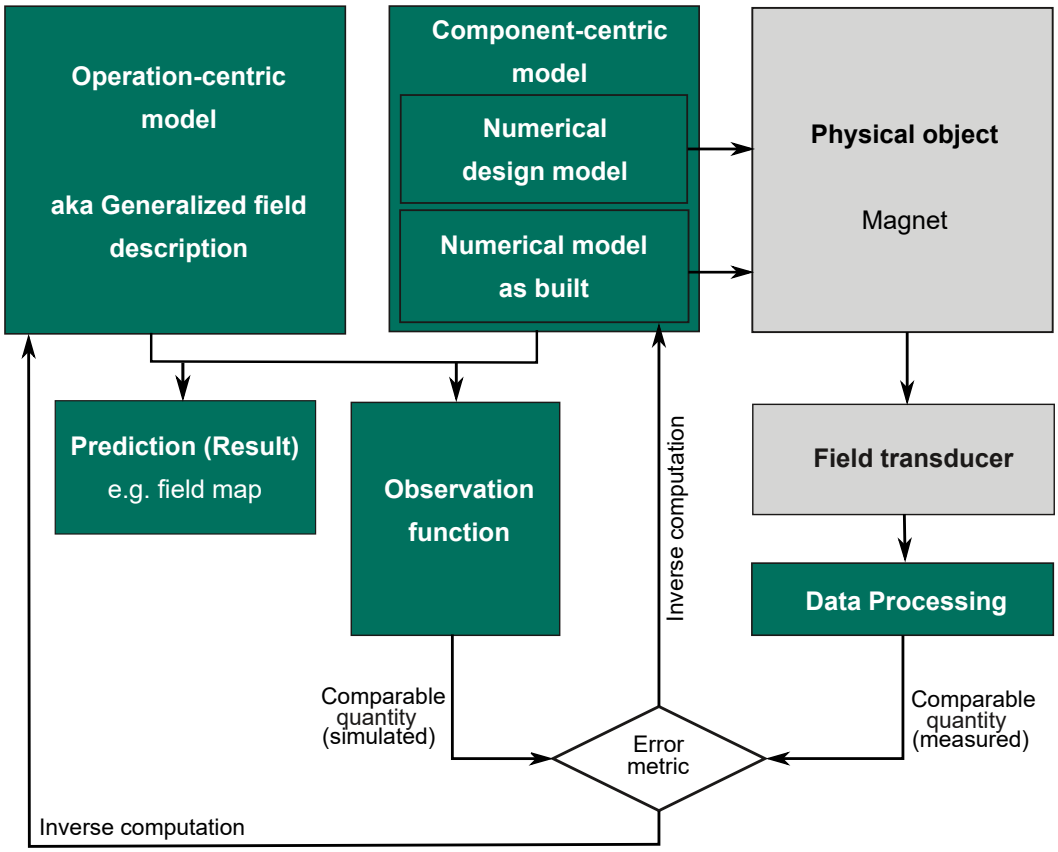

Figure 1.2: Interrelations between physical objects and system models. Figure adapted from [120].

We distinguish between operation-centric and component-centric models. The operation-centric models are also referred to as *generalized field descriptions* [120]. Component-centric models are divided into models used for design and models that are adapted to a magnet system as built. The difference between operation-centric and component-centric models is, that component-centric models include a model of the magnet system such as the yoke and the conductors while the operation-centric models only describe the field in free space. Therefore, component-centric models require additional knowledge about the magnet system such as material laws or geometry parameters. Consequently, operation-centric models can be retrieved from component-centric models, whereas the inverse is not possible without additional knowledge of the magnet system. The advantage of component-centric models is that they are also suitable for *magnet introspection*. This means that they can be used to gain insight into quantities related to the magnet system that are not (easily) measurable, such as material curves of the yoke. This capability is especially of interest during the prototype phase of a magnet to find explanations for observed deviations between predicted and measured quantities and to diagnose deficiencies of the prototype. For characterizing the field of a magnet as built, both operation-centric models and component-centric models can be used. However, operation-centric models are usually chosen, as they require less knowledge.

In this work, both operation-centric and component-centric models for field prediction and magnet introspection are investigated. The available sources of knowledge to build these models are the numerical design model, which is limited by the challenges of simulation, and measurement data, which is limited by the challenges of magnetic measurements. The approach is therefore to combine both sources of knowledge to overcome

some of the limitations. We restrict the investigation to the magnetostatic case and to describing the magnet system and its generated magnetic field at a given time in the magnet life cycle, e.g., the characterization after production, and neglect changes of the magnet system over time.

1.3 State of the art and related concepts

An abstract workflow to derive system models is given in [73]. It consists of (1) conceptual modeling, (2) mathematical modeling, (3) approximate analytical modeling, (4) numerical modeling, and (5) computational modeling. In case a simplification of the model is required, these steps can be followed by a model order reduction. Each step depends on the modeled device and the purpose of the system model and requires expert knowledge.
Applying this workflow results in an *initial system model* that has to be validated and most likely adapted to a specific magnet system as built and its measured observable quantities. Therefore, further expert knowledge on acknowledged errors and the aleatory uncertainty is required. The possibilities for improving the model are limited by the epistemic uncertainty, the availability of data, and the computational effort to avoid acknowledged errors. Typically not only information about governing physical laws but also measured observations from different sources are available that can be combined to improve the model.

Due to the problem and application dependence of system models, the models and methods for their creation found in the literature are heterogeneous. However, common concepts and approaches can be identified such as model updating and model refinement [145], inverse problems [80], and hybrid modeling [86]. The concept of digital twins [144] is also related to the idea of system models, however, in this work we limit the investigations to system models that do not reflect changes in the described physical object over time.

1.3.1 State of the art

Operation-centric system models A prominent operation-centric system model suitable for straight magnet systems and integral fields and already in use for decades is referred to as “field harmonics” or “multipoles” [119]. This model relies on the circular harmonic expansion of the radial magnetic flux density component on a reference radius, located in the free space of the magnet aperture. The model parameters, the multipole coefficients or field harmonics, can be determined using rotating coil magnetometers. From the circular harmonic expansion of the magnetic scalar potential, scaling laws can be derived to extrapolate the coefficients to other radii than the reference radius. Consequently, in space extrapolated predictions of the magnetic flux density are possible.
More recent examples of generalized field descriptions can be found, e.g., in [8, 74, 92, 122]. The system models in [74] and [122] are similar to the field harmonics. Instead of the two-dimensional circular harmonic expansion, a Fourier-Bessel expansion and a Lobatto spline Fourier expansion are used to describe three-dimensional solutions to the Laplace equation. In [92], the boundary element method is used to describe solutions to the Laplace equation. For an overview of further series expansions and closed-form expansions to describe three-dimensional magnetic fields, particularly including the fringe field region of an accelerator magnet, the reader is referred to [143, Section 1.3].
A fully data-driven system model used in the context of material characterization is derived in [8]. Instead of relying on Maxwell’s equations, a multi-layered neural network is trained to predict the maximal magnetic field in a quadrupole, given an excitation current and previous excitation currents.

Component-centric system models Numerical models of magnets as built are investigated, e.g., in [126, 127, 132]. In [127], the system model is a time-dependent reduced-order model of a normal-conducting coil-dominated magnet without iron magnetization. The model is based on coupled linear reduced-order models of the yoke and the coil. The matrix coefficients of the reduced-order model are the parameters of this system model. The method described in [126] extends the method of [127] by considering also non-linear materials. The model is based on FEM and the magnetization coefficients of the yoke domain are used as parameters. The system model in [132] is based on a FEM model of the two-dimensional transient eddy-current problem. In this work, high- and low-fidelity models of the same magnet system, which differ by the mesh choice, are compared. Moreover, a discrepancy function describing the difference between the two is learned using a recurrent neural network.

1.3.2 Digital twin

The concept of system models is closely related to digital twins. In literature, varying definitions of the term "digital twin" can be found, e.g., in [96, 113, 144]. In [113], *digital twins* are defined as a "virtual representation of a physical asset enabled through data and simulators for real-time prediction, optimization, monitoring, controlling, and improved decision making". The concept of getting a virtual representation of a physical asset agrees with the definition of system models, however, the use cases differ. While digital twins reflect the change of a physical asset over time using dynamic updates and adjustments [144], we restrict our definition of system models to describing a magnet system and predicting field-related quantities only at a given time in the magnet life cycle.

1.3.3 Deterministic and stochastic model updating and model refinement

Strategies for improving and adapting a system model to a specific magnet and its measured quantities can be divided into two categories: model refinement and model updating [145]. For model updating, one can further distinguish between deterministic and stochastic model updating.

- **Model refinement** is defined in [145, Section 1] as "changing the physical principles in modeling or using other means to build a more sophisticated model that better represents the physics of the problem". Consequently, model refinement reduces the acknowledged error of the simulation model.
- **Model updating** is defined in [145, Section 1] as utilizing "mathematical means to match model predictions with the physical observations", such as determining model parameters or bias correction, i.e. deriving a discrepancy function, which describes the difference between observations and model predictions. The observations used to derive a model update are referred to as *observation training data* in this work. Within model updating, one can further distinguish between deterministic and stochastic updating [137]. *Deterministic model updating* estimates a deterministic parameter, while *stochastic model updating* includes the uncertainty of the observation and estimates a parameter distribution. Consequently, deterministic model updating will answer the question *what is the value of this parameter?*, while stochastic model updating answers the question *what is our information about this parameter?* [78, Section 3]. Methods for statistical inversion that can be used for stochastic model updating are introduced in more detail in Chapter 3.

The state-of-the-art system models introduced in Section 1.3.1 use both deterministic and stochastic model updating methods with the following characteristics:

- *Deterministic model updating*. In [8], the hyperparameters and weights of a multi-layered neural network are learned, which predicts a field-related quantity of interest, given an excitation current and a set of previous excitation currents and responses. In [132], deterministic model updating of a low-fidelity model is realized using a neural network that determines a discrepancy function for bias correction. In [126], deterministic magnetization coefficients of an iron-dominated magnet are determined by solving a constraint optimization problem based on fitting integrated multipole coefficients.
- *Stochastic model updating*. In [122], the coefficients of the Fourier-Bessel expansion are determined either by least squares fitting using Hall-probe measurements leading to a deterministic model updating method or from rotating coil measurements using a Wiener-Kolmogorov filter leading to a stochastic model updating method. The model and the updating method in [74] are similar. The Fourier-Bessel expansion is replaced by a Lobatto spline Fourier expansion, and the values of the coefficients are derived by Kalman filtering based on rotating coil measurements. The method described in [92] is another extension to the two preceding methods, instead of an expansion, the solution to the Laplace equation is parameterized with the boundary element method. Using ensemble Kalman filtering, the boundary values are determined from magnetic flux density measurements with a Hall probe mapper system. In [127], the matrix coefficients of a reduced-order model of a linear dynamic system that predicts the transient field of an air-coil magnet are stochastically updated using Kalman filtering.

1.3.4 Inverse problems and ill-posedness

Determining model parameters to match model predictions and observations is a typical inverse problem. Following [80], two problems are called *inverse* to each other if the formulation of each involves all or part of the solution of the other. Often, the two problems have different properties regarding their well-posedness. A definition of well-posedness according to the three criteria defined by Hadamard is given in [50] and [83]: A problem is called *well-posed* if:

1. **Existence.** For all admissible data, a solution exists.
2. **Uniqueness.** For all admissible data, the solution is unique.
3. **Stability.** The solution depends continuously on the data.

Problems for which at least one of the properties does not hold are called *ill-posed*. In our case, the direct problem, predicting the field given the parameters, is well-posed, while determining parameters given field observations is rather ill-posed.
Ill-posedness can have various reasons [55, 62]. An over-determined problem and noisy data can lead to the non-existence of a solution. The solution is not unique if the operator that describes the forward problem has a non-trivial null space. If the inverse problem is ill-conditioned, the noise of the data is amplified, leading to an unstable solution.
Mathematical methods can neither compensate a lack of information [87] that leads to non-uniqueness nor make an inherently unstable problem stable [50]. However, the ill-posedness of inverse problems can be addressed with several methods, depending on the problem and the cause of the ill-posedness. An overview is given in [50, Section 2]. Existence can be enforced by relaxing the notion of a solution. In the case of non-unique solutions, prior and expert knowledge about the problem can be used to decide which solution is of interest [50].
In case of instability, regularization, that is approximating the ill-posed problem with a well-posed problem [28, 50], can be applied. Popular regularization methods are for example the Tikhonov regularization [50, 78, 83], Landweber iteration [50, 78, 83], finite-dimensional approximations, e.g., using Galerkin methods [83]

or low-rank approximations such as the truncated singular value decomposition [83]. It is important to notice that the listed methods to address ill-posedness are interconnected. For example, it is helpful to define the regularization functional within the Tikhonov regularization based on prior knowledge of reasonable parameter values, and it can be shown that determining the maximum a posteriori estimate resulting from statistical inversion can be equivalent to Tikhonov regularizations under some assumptions [28].
Besides mathematical concepts, the experimental setup can be adjusted to improve the conditioning of a parameter determination problem. In [91], for example, the geometry of an induction coil magnetometer is optimized such that zeros in the sensitivity function are avoided within a spatial frequency domain of interest, leading to a better-conditioned problem.

1.3.5 Hybrid modeling

Model updating and especially parameter determination are popular and successful approaches for good reason. This becomes clear when considering these methods in the context of hybrid modeling. Following [86], *hybrid models* combine first principle-based with data-based models into a joint architecture. Thereby, the first principle-based models refer to the domain knowledge that results from physics, in the context of system models of accelerator magnets, this includes Maxwell's equations and constitutive equations. The data can be obtained from any source, especially from field and material measurements or simulations.
To combine first principle-based models with data, different architectures are possible. In the above-discussed examples for model updating in [74, 92, 122, 126, 127, 132], the preliminary system model is based on first principles. Consequently, model updating, which involves the comparison of the prediction with data, leads to a hybrid model. Another possibility to combine data and first principles is addressing the ill-posedness of the inverse problem of parameter determination by using prior knowledge gained from data.
The advantages and disadvantages of purely data-based and purely first principle-based models are discussed, e.g., in [109, 113, 140]. Purely data-based models are flexible and do not require knowledge of the physical laws that govern a problem. However, their predictions often fail beyond the regime of the training data, their predictions might not be consistent with physics, and they can not observe causal relationships, thus the results lack interpretability and are therefore not suitable for magnet introspection. Purely first principle-based models are advantageous in terms of consistency, predictive capacities, and interpretability, but the required knowledge might not be available or simplifications have to be applied that lead to acknowledged errors. Hybrid models combine available data and available first-principle knowledge in one model that comprises the best of both worlds [109].

1.4 Structure of this thesis

This thesis studies methods to build and update hybrid system models for magnet introspection and field prediction. As the methods and the sources of knowledge for building system models are highly problem- and application-specific, the investigation is based on three specific examples, which are treated in detail in Chapters 4, 5 and 6. The most important methods and findings for each example are summarized in the following paragraphs of this section. Well-known methods that are used in more than one chapter such as the fundamentals of electromagnetism required for the first principle-based part of the hybrid models and methods for statistical inference required for stochastic model updating are introduced in Chapter 2 and Chapter 3.

Overall problem structure Figure 1.3 shows an overview of the sources of knowledge and the methods that we apply to build and update the system models. All system models treated in this thesis are hybrid models as they combine knowledge of the underlying electromagnetic laws with data derived from magnetic field measurements. The component-centric models also allow the inclusion of measured material data. The material data is mainly used to identify suitable parameters of the model and to obtain prior knowledge of the distribution of these parameters. The field observations are mainly used as a reference to update the initial model, such that the model predictions are improved and the system model is tailored to a specific physical object. The weighting between data-driven methods and first principle-based methods differs between the studied system models.

Update of the B(H)-curve in iron-dominated magnets (Chapter 4) For iron-dominated magnets, the $B(H)$-curve of the yoke material is a crucial input of their component-centric system model. In Chapter 4, we formulate, regularize, and solve in a test case an inverse problem to determine the $H(B)$-curve from observations of the magnetic flux density. For regularization, we propose a low-rank approximation of the search space with the data-driven stochastic model [117, 118], which is derived using truncated Karhunen-Loève expansion (KLE) and split-coil permeameter measurements of yoke material specimens. We show with a 4-fold cross-fold validation that this KLE-based $H(B)$-curve model is more suitable to describe the measured (B, H)-data of American Rolling Milling Company (ARMCO)® Pure Iron [5] specimens, than common closed-form expression for $B(H)$- and $H(B)$-curves that can be found in the literature.
With the sensitivity analysis derived in [117], we analyze the stability of the approximated inverse problem, showing that despite the regularization, there remain choices of training data on which the approximated inverse problem is unstable and thus ill-posed. We solve the approximated inverse problem with deterministic and stochastic model updating methods and evaluate field predictions of the updated model, finding that the updated models are suitable for interpolative field predictions for excitation currents that are not included in the training data.

Update of the magnetization of circular Halbach arrays (Chapter 5) The magnet system of the Forward Search Experiment (FASER) experiment [3] consists of three circular Halbach dipoles, each composed of a series of circularly arranged permanent magnet (PM) blocks. Former studies [49] have shown a mismatch between predicted and measured higher-order multipole coefficients that might be caused by manufacturing-related variations of the PM blocks' magnetizations [131].
In Chapter 5, we update the magnetization of the PM blocks in the system model of the first short FASER dipole. With Bayesian inference, measurement data of the magnetization of the PM blocks determined with a tri-axial Helmholtz coil system, measurement data of field-related quantities of interest observed with a Hall probe mapper system, and first principle-based knowledge on the magnetostatic problem are combined into a stochastically updated hybrid model. The updating method is first verified on simulated observation data and then applied to measured observations of multipole coefficients. It is shown that adjustments of the magnetization within the 3σ neighborhood of the Helmholtz coil system measurements can explain the mismatch between the observed and the measured multipole coefficients. Moreover, the magnetic flux density prediction with the updated model in the homogeneous field region is improved by around one order of magnitude.

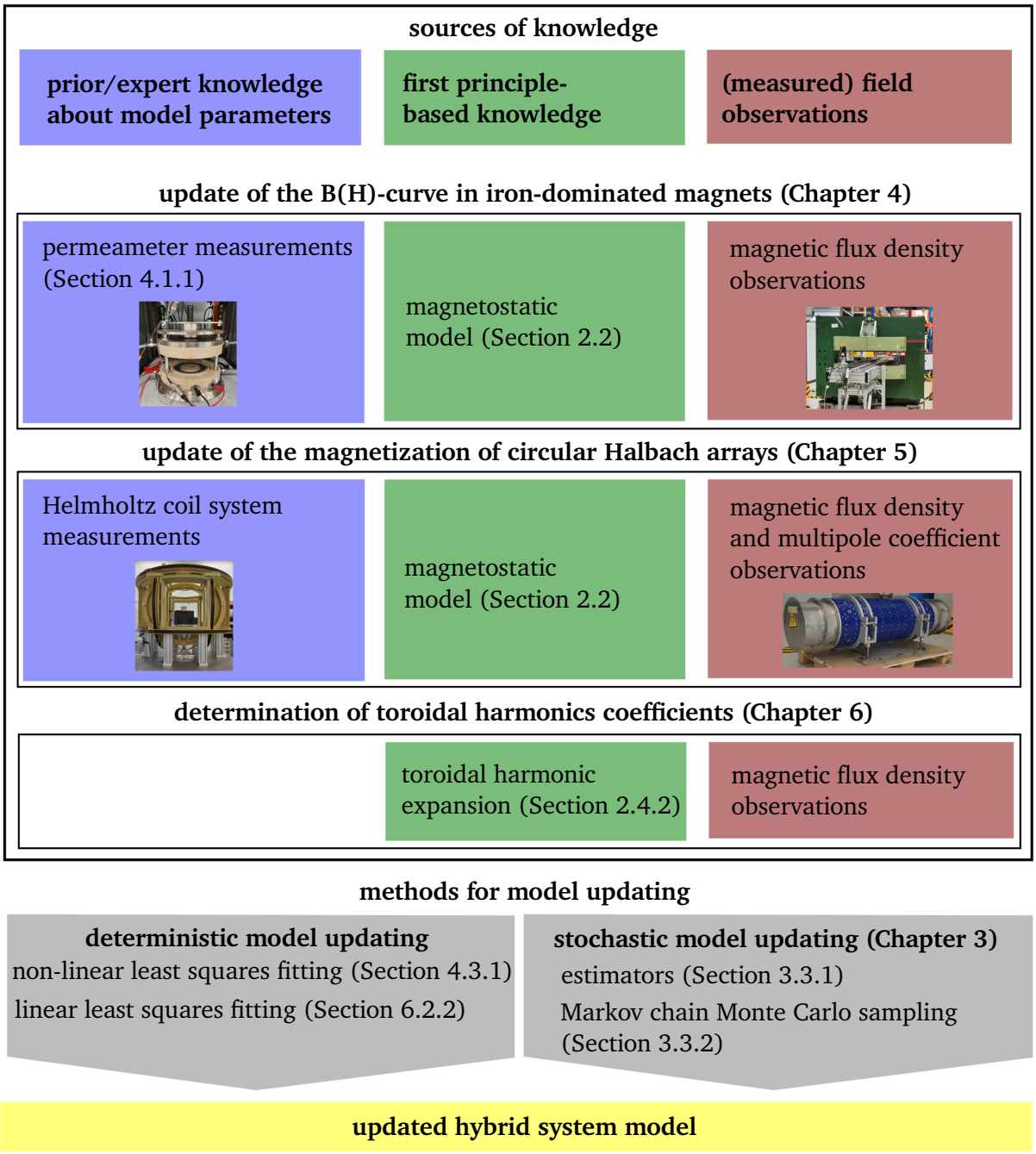

Figure 1.3: Sources of knowledge and methods to build and update system models of accelerator magnets.

Determination of toroidal harmonic coefficients from the magnetic flux density (Chapter 6) In the aperture's free space of strongly curved magnet systems, the toroidal harmonic expansion is more suitable to describe the magnetic field than the circular harmonic expansion [135]. In Chapter 6, two methods are derived to determine the toroidal harmonic coefficients from observations of the magnetic flux density. The first method is based on integrating the magnetic flux density and using the orthogonality of the trigonometric functions, which leads to recursive formulas for the toroidal harmonic coefficients. However, these formulas are not stable due to recursive error propagation. The second method approximates a finite number of toroidal harmonic coefficients by linear least squares fitting. The conditioning of the problem is improved by optimizing the observation positions of the magnetic flux density. Moreover, we prove that the functions spanning the skew part of the magnetic flux density in the toroidal harmonic expansion are linearly dependent, consequently, as for other methods based on scalar potential formulations, a gauging condition is required to uniquely determine the toroidal harmonic coefficients from the magnetic flux density.
The predictions of the operation-centric system models, whose coefficients are determined by least squares fitting are validated on the example of the magnetic fields generated by the coil arrangements of the International Thermonuclear Experimental Reactor (ITER) tokamak and a curved canted cosine theta (CCT) dipole simulated with the CERN field computation program ROXIE [121]. The derived system model can describe the magnetic field generated by the ITER coil arrangement with only a few coefficients. More coefficients are required in the curved CCT dipole example, and still, the relative error in the fringe field region is above the common accuracy threshold of 1 unit in 10000. Hence, other field descriptions, not based on the toroidal harmonic expansion might be more suitable for building an operation-centric system model for this application.

2 Electromagnetic fundamentals

The system models discussed in this work rely on solving the magnetostatic problem. This chapter summarizes the key concepts to derive and solve the magnetostatic problem starting from the full set of Maxwell's equations. These concepts can be identified with the steps of the workflow to derive an initial system model described in [73]:

1. **Conceptual modeling:** model assumptions (domain, material, boundary, sources), Maxwell's equations, constitutive equations,
2. **Mathematical modeling:** strong and weak formulation of the magnetostatic problem, expansions of solutions to the Laplace equation, gauging,
3. **Approximate analytical modeling:** discretization with finite elements, discrete Fourier transform, truncation of expansions,
4. **Numerical modeling:** Picard method, Newton-Raphson method, algorithms to solve linear equation systems, numerical integration,
5. **Computational model:** software such as GetDP [60] for implementation.

A more comprehensive treatment of Maxwell's equations, the derivation of the boundary value problem of magnetostatics, and more details on field harmonics are given, e.g., in [65, 76, 119]. For more details on the numerical approximation of the boundary value problem of magnetostatics in vector potential formulation, the reader is referred to [21, 23, 99, 119].

2.1 Maxwell's equations

Maxwell's equations in integral form and SI units are given by

$$\int_{\partial\mathscr{A}} \mathbf{H}\cdot\mathrm{d}\mathbf{r} = \int_{\mathscr{A}} \mathbf{J}\cdot\mathrm{d}\mathbf{a} + \frac{\mathrm{d}}{\mathrm{d}t}\int_{\mathscr{A}} \mathbf{D}\cdot\mathrm{d}\mathbf{a} \tag{2.1}$$

$$\int_{\partial\mathscr{A}} \mathbf{E}\cdot\mathrm{d}\mathbf{r} = -\frac{\mathrm{d}}{\mathrm{d}t}\int_{\mathscr{A}} \mathbf{B}\cdot\mathrm{d}\mathbf{a} \tag{2.2}$$

$$\int_{\partial\mathscr{V}} \mathbf{B}\cdot\mathrm{d}\mathbf{a} = 0 \tag{2.3}$$

$$\int_{\partial\mathscr{V}} \mathbf{D}\cdot\mathrm{d}\mathbf{a} = \int_{\mathscr{V}} \rho\,\mathrm{d}V, \tag{2.4}$$

where $\mathscr{A}\subset\mathbb{R}^3$ is a surface and $\mathscr{V}\subset\mathbb{R}^3$ is a volume. Thereby, $\mathbf{H}$ is the magnetic field ($[\mathbf{H}] = 1\,\mathrm{A\,m^{-1}}$) and $\mathbf{B}$ is the magnetic flux density ($[\mathbf{B}] = 1\,\mathrm{V\,s\,m^{-2}} = 1\,\mathrm{T}$), $\mathbf{E}$ is the electric field ($[\mathbf{E}] = 1\,\mathrm{V\,m^{-1}}$) and $\mathbf{D}$ is the

electric flux density ($[\mathbf{D}] = 1\,\mathrm{A\,s\,m^{-2}}$), ρ is the electric charge density ($[\rho] = 1\,\mathrm{A\,s\,m^{-3}}$), and $\mathbf{J}$ is the electric current density ($[\mathbf{J}] = 1\,\mathrm{A\,m^{-2}}$). The electric current density $\mathbf{J} = \mathbf{J}_\mathrm{s} + \sigma\mathbf{E}$ consists of the source current density $\mathbf{J}_\mathrm{s}$ and the ohmic part $\sigma\mathbf{E}$, where σ is the electric conductivity ($[\sigma] = 1\,\mathrm{A\,V^{-1}\,m^{-1}}$). All quantities are functions of space and time. These dependencies are omitted for readability. With $\mathrm{d}\mathbf{r}$, we denote the line element that is aligned with the tangent of the integration curve, and with $\mathrm{d}\mathbf{a}$ we denote the vectorial surface element that is aligned with the surface normal.

Assuming all necessary conditions on the regularity of the surface $\mathscr{A}$ and the volume $\mathscr{V}$ and on the differentiability of the involved functions to apply Stokes Theorem and Gauss Theorem yields the local form of Maxwell's equations

$$\operatorname{curl}\mathbf{H} = \mathbf{J} + \frac{\partial}{\partial t}\mathbf{D} \tag{2.5}$$

$$\operatorname{curl}\mathbf{E} = -\frac{\partial}{\partial t}\mathbf{B} \tag{2.6}$$

$$\operatorname{div}\mathbf{B} = 0 \tag{2.7}$$

$$\operatorname{div}\mathbf{D} = \rho. \tag{2.8}$$

In the magnetostatic case, Maxwell's equations can be simplified to

$$\operatorname{curl}\mathbf{H} = \mathbf{J}_\mathrm{s} \tag{2.9}$$

$$\operatorname{div}\mathbf{B} = 0. \tag{2.10}$$

Consequently, $\mathbf{J}_\mathrm{s}$ has to be divergence-free. The applications in this work are restricted to magnetostatics. Therefore, the eddy currents phenomenon is disregarded and it holds $\mathbf{J} = \mathbf{J}_\mathrm{s}$. Equation (2.9) is referred to as Ampère's law, and equation (2.10) is known as the magnetic flux conservation law. Having more unknowns than equations, Maxwell's equations are underdetermined. To find solutions to Maxwell's equations in the magnetostatic case, the magnetic field $\mathbf{H}$ and the magnetic flux density $\mathbf{B}$ are related by a material law that is given by the constitutive equation

$$\mathbf{B} = \mu\mathbf{H}, \tag{2.11}$$

where μ is the permeability ($[\mu] = 1\,\mathrm{V\,s\,A^{-1}\,m^{-1}}$). The permeability of air is close to the vacuum permeability $\mu_0 = 4\pi \cdot 10^{-7}\,\mathrm{V\,s\,A^{-1}\,m}$. The inverse of the permeability is the reluctivity ν ($[\nu] = 1\,\mathrm{A\,m\,V^{-1}\,s^{-1}}$) with the corresponding constitutive equation

$$\mathbf{H} = \nu\mathbf{B}. \tag{2.12}$$

If permanent magnetic material is involved, the constitutive equation is

$$\mathbf{B} = \mu(\mathbf{H} + \mathbf{M}). \tag{2.13}$$

where $\mathbf{M}$ ($[\mathbf{M}] = 1\,\mathrm{A\,m^{-1}}$) is the magnetization.

In the following section, we further specify conditions for the domain and the material for which we solve Maxwell's equations. Moreover, boundary conditions and interface conditions between different materials are formulated.

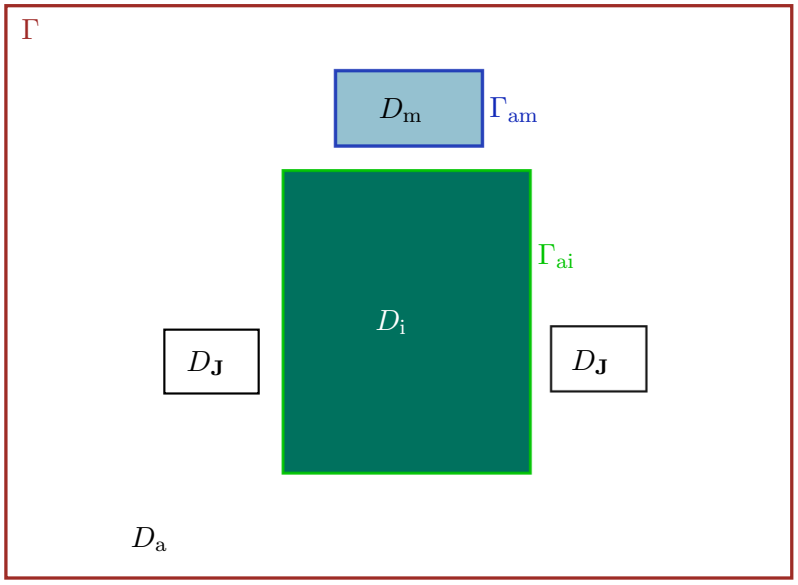

Figure 2.1: Elementary model problem on a domain D with its subdomains and interfaces.

2.2 Magnetostatic model

All system models that are considered in this thesis are based on solving the magnetostatic approximation of Maxwell's equations, neglecting time-dependent effects. To formulate suitable boundary value problems, we specify further assumptions on the domain and the material, impose conditions on the boundary and the interfaces, and define the magnetic scalar potential and the magnetic vector potential.

2.2.1 Model assumptions

Domain assumptions To study the solution of Maxwell's equations within and around a magnet system, it is sufficient to consider a two- or three-dimensional bounded domain D covering the magnetic sources and the fringe fields. Choosing the boundaries far enough from the magnet system allows the assumption that its boundary $\Gamma := \partial D$ is piecewise Lipschitz and connected. Moreover, it is assumed, if not stated otherwise, that the domain D is simply-connected.

The domain D consists usually of two disjoint sub-regions D_i and D_a with $\overline{D} = \overline{D_\mathrm{i}} \cup \overline{D_\mathrm{a}}$. The subregion D_a contains all material regions of D for which we can assume vacuum permeability, e.g., air and copper both have almost vacuum permeability. The source region is denoted by $D_\mathbf{J} := \mathrm{supp}(\mathbf{J}) \subset D_\mathrm{a}$. The subregion D_i contains materials with non-linear permeabilities such as the iron yoke. The interface between the two regions is denoted by $\Gamma_\mathrm{ai} = \overline{D_\mathrm{i}} \cap \overline{D_\mathrm{a}}$. If permanent magnetic material is involved, the domain is subdivided into three disjoint regions $\overline{D} = \overline{D_\mathrm{i}} \cup \overline{D_\mathrm{a}} \cup \overline{D_\mathrm{m}}$ where $D_\mathrm{m} := \mathrm{supp}(\mathbf{M})$ is the domain of the permanent magnetic material. The interface between the air region and the permanent magnetic material is denoted by $\Gamma_\mathrm{am} = \overline{D_\mathrm{a}} \cap \overline{D_\mathrm{m}}$. For all interfaces, we assume as for the boundary that they are piecewise Lipschitz. Notice that we specified interfaces only between regions with different permeabilities. Since we assume the same permeability for air and copper, no interface is defined at the boundary of $D_\mathbf{J}$. A sketch of a domain D and its subdomains and interfaces can be found in Figure 2.1.

Material assumptions The permeability and the reluctivity are material dependent. In this thesis, we assume that all materials are homogeneous, isotropic, stationary, and anhysteretic.

For linear material laws, the permeability is independent of the magnetic field strength and can be expressed by

$$\mu = \mu_0 \mu_\mathrm{r}, \tag{2.14}$$

where $\mu_0 = 4\pi \cdot 10^{-7}\,\mathrm{V\,s\,A^{-1}\,m}$ is the the vacuum permeability and $\mu_\mathrm{r} \in \mathbb{R}^+$ is a material dependent and dimensionless constant. For air, copper, and aluminum, we assume $\mu_\mathrm{r} = 1$.
In linear isotropic permanently magnetized material, the magnetic field, and the magnetization are in the proportional relation

$$\mathbf{M} = \chi_\mathrm{m}\mathbf{H}, \tag{2.15}$$

where χ_m is the dimensionless magnetic susceptibility. Inserting equation (2.15) into equation (2.13) yields $\mu_\mathrm{r} = 1 + \chi_\mathrm{m}$ due to

$$\mathbf{B} = \mu_0(\mathbf{H} + \chi_\mathrm{m}\mathbf{H}) = \mu_0(1 + \chi_\mathrm{m})\mathbf{H}. \tag{2.16}$$

In non-linear material such as iron, the permeability $\mu(H)$ also depends on the intensity $H \coloneqq \|\mathbf{H}\|$ of the magnetic field and the reluctivity $\nu(B)$ depends on the intensity of the magnetic flux density $B \coloneqq \|\mathbf{B}\|$. Here and throughout the thesis we refer with $\|\cdot\|$ to the Euclidean norm. The non-linear relations for $B, H \neq 0$ are given by

$$\mu(H) = \frac{f_\mathrm{BH}(H)}{H} \quad \text{and} \quad \nu(B) = \frac{f_\mathrm{HB}(B)}{B}, \tag{2.17}$$

where $f_\mathrm{HB}, f_\mathrm{BH} : \mathbb{R}_0^+ \to \mathbb{R}_0^+$ are the bijective functions defined by

$$f_\mathrm{BH} :\ H \mapsto B \quad \text{and} \quad f_\mathrm{HB} :\ B \mapsto H. \tag{2.18}$$

They are by definition inverse to each other and f_BH is referred to as $B(H)$-*curve* and f_BH is referred to as $H(B)$-*curve*.

Assumption 1. *Following [103], we assume four natural properties for the $H(B)$-curve:*

1. *The curve f_HB is continuously differentiable,*
2. *there is a constant $\alpha > 0$ such that $0 < \alpha \leq f'_\mathrm{HB}(B) \leq \frac{1}{\mu_0} < \infty$ for all $B \in \mathbb{R}_0^+$,*
3. *$f_\mathrm{HB}(0) = 0$, and*
4. *$\lim_{B\to\infty} f'_\mathrm{HB}(B) = \frac{1}{\mu_0}$.*

Corollary 1. *From the properties of f_HB, the following properties of the reluctivity function $\nu : \mathbb{R}_0^+ \to \mathbb{R}^+$ (according to [77], we set $\nu(0) \coloneqq \alpha$) can be deducted [103, Corollary 2.2]:*

1. *ν is continuous and $\alpha \leq \nu(B) \leq \frac{1}{\mu_0}$ for all $B \in \mathbb{R}_0^+$,*
2. *$B \mapsto \nu(B)B = f_\mathrm{HB}(B)$ is strongly monotone, and*
3. *$B \mapsto \nu(B)B = f_\mathrm{HB}(B)$ is Lipschitz continuous.*

We will later see that these conditions are required to prove the existence of unique solutions to the boundary value problem of magnetostatics with the Zaratonello Lemma [148]. An alternative set of assumptions on the reluctivity function, which is also sufficient to verify the conditions of the Zaratonello Lemma, can be found in [70].

To take into account different definitions of the reluctivity in different material regions of the domain D, the reluctivity function is also denoted as $\nu : D \times \mathbb{R}_0^+ \to \mathbb{R}^+$ with

$$\nu(\mathbf{x}, B) = \begin{cases} \nu_0 & \mathbf{x} \in D_\mathrm{a} \\ \nu_\mathrm{r}\nu_0 & \mathbf{x} \in D_\mathrm{m} \\ \nu_\mathrm{i}(B) & \mathbf{x} \in D_\mathrm{i} \end{cases} \tag{2.19}$$

where $\nu_0 = \mu_0^{-1}$ is the vacuum reluctivity, $\nu_\mathrm{r} = \mu_\mathrm{r}^{-1}$, and $\nu_\mathrm{i} : \mathbb{R}_0^+ \to \mathbb{R}^+$ is the non-linear reluctivity in the iron domain. To save on notation, we often omit the position dependence of ν.

Boundary and interface conditions On the boundary $\Gamma = \partial D$, the magnetic flux density $\mathbf{B}$ and the magnetic field $\mathbf{H}$ satisfy boundary conditions. These conditions are either related to magnetic surface charges or surface currents and imposed on disjoint domains $\Gamma_\mathrm{B}, \Gamma_\mathrm{H}$ with $\Gamma = \overline{\Gamma_\mathrm{B}} \cup \overline{\Gamma_\mathrm{H}}$.

On Γ_B, the normal component of the magnetic flux density is imposed by the condition

$$\mathbf{B} \cdot \mathbf{n} = \sigma_\mathrm{m} \qquad \text{on } \Gamma_\mathrm{B}, \tag{2.20}$$

where $\mathbf{n}$ is the outer unit normal of D and σ_m is a fictitious magnetic surface charge density. On boundaries far from the iron yoke and the sources, or boundaries parallel to the magnetic flux density, $\sigma_\mathrm{m} = 0$ can be assumed. This condition is also known as the perfect electric conductor condition.

On Γ_H, the tangential component of the magnetic field is imposed by

$$\mathbf{H} \times \mathbf{n} = \boldsymbol{\alpha} \qquad \text{on } \Gamma_\mathrm{H}, \tag{2.21}$$

where $\boldsymbol{\alpha}$ is a real or fictitious surface current density. On boundaries where the field enters the domain perpendicularly, the condition

$$\mathbf{n} \times (\mathbf{H} \times \mathbf{n}) = \mathbf{0} \qquad \text{on } \Gamma_\mathrm{H} \tag{2.22}$$

is imposed. This condition is met in particular, if $\mathbf{H} \times \mathbf{n} = \mathbf{0}$ on Γ_H, and also known as the perfect magnetic conductor condition.

On the interface Γ_ai, two regions with different permeabilities meet and the magnetic flux density and the magnetic field are discontinuous. To formulate boundary conditions, the jump of a vector field is introduced: For a vector field $\mathbf{F}$ on D and $\mathbf{x} \in \Gamma_\mathrm{ai}$ the *jump* $[\![\mathbf{F}]\!]_\mathrm{ai}$ is defined by

$$[\![\mathbf{F}]\!]_\mathrm{ai}(\mathbf{x}) \coloneqq \lim_{\mathbf{x}_1 \in D_\mathrm{a} \to \mathbf{x}} \mathbf{F}(\mathbf{x}_1) - \lim_{\mathbf{x}_2 \in D_\mathrm{i} \to \mathbf{x}} \mathbf{F}(\mathbf{x}_2). \tag{2.23}$$

With the flux conservation law, it can be shown that in the absence of magnetic surface charges at the interface, the normal component of the magnetic flux density is continuous at the interface

$$\mathbf{n} \cdot [\![\mathbf{B}]\!]_\mathrm{ai} = 0 \qquad \text{on } \Gamma_\mathrm{ai}, \tag{2.24}$$

where $\mathbf{n}$ is the outer unit normal of D_i. Similarly, with Ampère's law, it can be shown that if no surface currents are present at the interface, the tangential component of the magnetic field is continuous at the interface, i.e.

$$\mathbf{n} \times [\![\mathbf{H}]\!]_\mathrm{ai} = \mathbf{0} \qquad \text{on } \Gamma_\mathrm{ai}. \tag{2.25}$$

If permanent magnetized material is involved, surface currents occur at the interface Γ_am, leading to the interface condition

$$\mathbf{n} \times [\![\mathbf{H}]\!]_\mathrm{am} - \mathbf{n} \times [\![\mathbf{M}]\!]_\mathrm{am} = \mathbf{0} \qquad \text{on } \Gamma_\mathrm{am}, \tag{2.26}$$

where $\mathbf{n}$ is the outer unit normal of D_m.

2.2.2 Magnetostatic boundary value problem formulations

In the magnetostatic case, Maxwell's equations reduce to (2.9) and (2.10). A solution to Maxwell's equations can be found using a constitutive equation that relates $\mathbf{B}$ and $\mathbf{H}$ and imposing boundary conditions on ∂D and interface conditions at the interfaces of different materials. This problem is referred to as the boundary value problem of magnetostatics.
In the literature, e.g., in [17], different formulations of the boundary value problem of magnetostatics can be found based on the definition of further scalar or vector potentials. The idea is to combine the two remaining equations of Maxwell's equations. In this work, the scalar potential formulation is only applied if the considered domain has vacuum permeability and is free of sources ($\mathbf{J} = 0$ and $\mathbf{M} = 0$), otherwise, the vector potential formulation is used. Hence, we use the scalar potential formulation for operation-centric models, and the vector potential formulation for component-centric models.

Vector potential formulation Given Maxwell's equations in the magnetostatic case,

$$\operatorname{curl} \mathbf{H} = \mathbf{J} \quad \text{and} \quad \operatorname{div} \mathbf{B} = 0 \quad \text{in } D \tag{2.27}$$

a divergence-free magnetic flux density is obtained by introducing a vector potential $\mathbf{A}$ ($[\mathbf{A}] = 1\,\mathrm{V\,s\,m^{-1}}$) that satisfies

$$\operatorname{curl} \mathbf{A} = \mathbf{B} \tag{2.28}$$

because $\operatorname{div} \mathbf{B} = \operatorname{div} \operatorname{curl} \mathbf{A} = 0$. Inserting equations (2.28) and (2.11) into Ampère's law yields

$$\operatorname{curl} \nu(\|\operatorname{curl} \mathbf{A}\|) \operatorname{curl} \mathbf{A} = \mathbf{J} \qquad \text{in } D \tag{2.29}$$

which is also known as the curl-curl equation or the magnetostatic vector potential equation. Using the magnetic vector potential, the boundary and interface conditions can be written as

$$\begin{aligned} \mathbf{n} \times \nu(\|\operatorname{curl} \mathbf{A}\|) \operatorname{curl} \mathbf{A} &= \mathbf{0} && \text{on } \Gamma_\mathrm{H} \\ \mathbf{n} \cdot \operatorname{curl} \mathbf{A} &= 0 && \text{on } \Gamma_\mathrm{B} \\ \mathbf{n} \times [\![\nu(\|\operatorname{curl} \mathbf{A}\|) \operatorname{curl} \mathbf{A}]\!]_\mathrm{ai} &= \mathbf{0} && \text{on } \Gamma_\mathrm{ai} \\ \mathbf{n} \cdot [\![\operatorname{curl} \mathbf{A}]\!]_\mathrm{ai} &= 0 && \text{on } \Gamma_\mathrm{ai}. \end{aligned} \tag{2.30}$$

Notice that the first equation in (2.30) yields a Neumann boundary condition on Γ_H and the second a Dirichlet boundary condition on Γ_B. Equation (2.29) together with the conditions (2.30) is referred to as the *boundary value problem of magnetostatics in vector potential formulation*.

If $\mathbf{A}$ satisfies the boundary value problem of magnetostatics in vector potential formulation, the problem is also satisfied by $\mathbf{A} + \operatorname{grad}\psi$ for any sufficiently smooth scalar field ψ. To avoid non-uniqueness, the following conditions of the Coulomb gauge

$$\begin{aligned} \operatorname{div}\nu\mathbf{A} &= 0 && \text{in } D \\ \mathbf{n}\cdot\mathbf{A} &= 0 && \text{on } \Gamma_{\mathrm{H}} \\ \mathbf{n}\cdot[\![\mathbf{A}]\!]_{\mathrm{ai}} &= 0 && \text{on } \Gamma_{\mathrm{ai}} \\ \mathbf{n}\times\mathbf{A} &= \mathbf{0} && \text{on } \Gamma_{\mathrm{B}} \\ [\![\mathbf{A}]\!]_{\mathrm{ai}} &= \mathbf{0} && \text{on } \Gamma_{\mathrm{ai}} \end{aligned} \tag{2.31}$$

can be imposed [39, 119]. Notice that due to $\mathbf{n}\cdot\operatorname{curl}\mathbf{A} = \operatorname{div}(\mathbf{n}\times\mathbf{A})$ the two last conditions in (2.31) imply the boundary condition $\mathbf{n}\cdot\operatorname{curl}\mathbf{A} = 0$ on Γ_{B} and interface condition $\mathbf{n}\cdot[\![\operatorname{curl}\mathbf{A}]\!]_{\mathrm{ai}} = 0$ on Γ_{ai} in (2.30). To avoid a mixed formulation [119, equation 4.151] we apply Coulomb gauging only for two-dimensional problems. Otherwise, the tree-cotree gauging method introduced in Section 2.3.3 is applied.

If permanent magnetic material is involved, the constitutive equation (2.13) is inserted into the equations (2.27) instead, which yields

$$\operatorname{curl}\nu(\|\operatorname{curl}\mathbf{A}\|)\operatorname{curl}\mathbf{A} = \mathbf{J} + \operatorname{curl}\mathbf{M} \qquad \text{in } D. \tag{2.32}$$

The interface condition on Γ_{am} rewritten for the vector potential is

$$\mathbf{n}\times[\![\nu(\|\operatorname{curl}\mathbf{A}\|)\operatorname{curl}\mathbf{A}]\!]_{\mathrm{am}} - \mathbf{n}\times[\![\mathbf{M}]\!]_{\mathrm{am}} = \mathbf{0} \qquad \text{on } \Gamma_{\mathrm{am}}. \tag{2.33}$$

Scalar potential formulation Since the scalar potential formulation is in this work only applied on source-free ($\mathbf{J} = \mathbf{0}$ and $\mathbf{M} = \mathbf{0}$) domains D with vacuum permeability, the scalar potential formulation is derived under these assumptions. In a source-free domain, the magnetostatic approximation of Maxwell's equations simplifies to

$$\operatorname{curl}\mathbf{H} = \mathbf{0} \quad \text{and} \quad \operatorname{div}\mathbf{B} = 0 \quad \text{in } D. \tag{2.34}$$

By introducing a total magnetic scalar potential ϕ_{m} ($[\phi_{\mathrm{m}}] = 1\,\mathrm{A}$) with

$$-\operatorname{grad}\phi_{\mathrm{m}} = \mathbf{H}, \tag{2.35}$$

a curl-free magnetic field is obtained because $\operatorname{curl}\mathbf{H} = \operatorname{curl}\operatorname{grad}\phi_{\mathrm{m}} = \mathbf{0}$. Inserting equations (2.35) and (2.11) into the flux conservation law yields

$$\operatorname{div}(\mu_0\ \operatorname{grad}\phi_{\mathrm{m}}) = 0 \qquad \text{in } D. \tag{2.36}$$

Due to the linearity of the permeability, this equation further simplifies to the Laplace equation

$$\Delta\phi_{\mathrm{m}} = 0 \qquad \text{in } D. \tag{2.37}$$

Inserting the magnetic scalar potential into the boundary yields

$$\begin{aligned} \mathbf{n}\times(\operatorname{grad}\phi_{\mathrm{m}}\times\mathbf{n}) &= \mathbf{0} && \text{on } \Gamma_{\mathrm{H}} \\ \mathbf{n}\cdot\mu_0\ \operatorname{grad}\phi_{\mathrm{m}} &= 0 && \text{on } \Gamma_{\mathrm{B}} \end{aligned} \tag{2.38}$$

Notice that the first equation (2.38) yields a Dirichlet boundary condition on Γ_{H}, and the second equation is a Neumann boundary condition on Γ_{B}. Equation (2.36) together with the conditions (2.38) is referred to as the *boundary value problem of magnetostatics in scalar potential formulation*.

If ϕ_m solves the boundary value problem of magnetostatics in scalar potential formulation with Neumann boundary conditions, the problem is also solved by $\phi_\mathrm{m} + c$ for any constant $c \in \mathbb{R}$. To avoid non-uniqueness, the magnetic scalar potential can be gauged by imposing $\phi_\mathrm{m}(\mathbf{x}_0) = \phi_0$ at an arbitrary point $\mathbf{x}_0 \in D$ and with an arbitrary constant $\phi_0 \in \mathbb{R}$. Hence, a Dirichlet boundary condition can be used for gauging.

In the following sections, a numerical approach based on the approximation with finite elements to finding solutions to the boundary value problem of magnetostatics in vector potential formulation and a theoretical approach to finding solutions to the scalar potential formulation based on the separation of variables in various coordinate systems [100] are introduced.

2.3 Numerical approximation of the vector potential formulation

The boundary value problem of magnetostatics in vector potential formulation can be formulated in weak form by weighting the curl-curl equation with suitable test functions and integrating over the domain D. Based on this weak formulation, the problem can be discretized and solved using the FEM [21, 23, 99, 111].
Recall that in Section 2.2.1 it was assumed that the boundary Γ of the studied domain D is piecewise Lipschitz. This condition is used in this section for the definition of the function spaces [99, Theorem 3.33].

2.3.1 Weak formulation

For the weak formulation of the magnetostatic problem in the vector potential formulation, the following Sobolev spaces [99] are required

$$H^1(D) \coloneqq \left\{v \in L^2(D) \mid \operatorname{grad} v \in L^2(D, \mathbb{R}^3)\right\} \tag{2.39}$$
$$H(\operatorname{curl}; D) \coloneqq \left\{\mathbf{v} \in L^2(D, \mathbb{R}^3) \mid \operatorname{curl} \mathbf{v} \in L^2(D, \mathbb{R}^3)\right\} \tag{2.40}$$
$$H(\operatorname{div}; D) \coloneqq \left\{\mathbf{v} \in L^2(D, \mathbb{R}^3) \mid \operatorname{div} \mathbf{v} \in L^2(D, \mathbb{R})\right\}. \tag{2.41}$$

If the functions additionally meet zero Dirichlet boundary conditions on Γ_B we write

$$H_0^1(D) \coloneqq \left\{v \in H^1(D) \mid v = 0 \text{ on } \Gamma_\mathrm{B}\right\} \tag{2.42}$$
$$H_0(\operatorname{curl}; D) \coloneqq \left\{\mathbf{v} \in H(\operatorname{curl}; D) \mid \mathbf{v} \times \mathbf{n} = \mathbf{0} \text{ on } \Gamma_\mathrm{B}\right\} \tag{2.43}$$
$$H_0(\operatorname{div}; D) \coloneqq \left\{\mathbf{v} \in H(\operatorname{div}; D) \mid \mathbf{v} \cdot \mathbf{n} = 0 \text{ on } \Gamma_\mathrm{B}\right\}, \tag{2.44}$$

where $\mathbf{n}$ is the outward pointing unit normal vector of D. Following [99, Section 3.7] the image of each operator of the sequence

$$H_0^1(D) \overset{\operatorname{grad}}{\to} H_0(\operatorname{curl}; D) \overset{\operatorname{curl}}{\to} H_0(\operatorname{div}; D) \overset{\operatorname{div}}{\to} L^2(D) \tag{2.45}$$

equals the kernel of the following operator in the sequence, if the domain D is simply-connected. This property also holds for the analog sequence without zero Dirichlet boundary conditions on Γ_B [33, Section 2.9]. This justifies the existence of suitable functions $\phi_\mathrm{m} \in H^1(D)$ to define the magnetic scalar potential via equation (2.35) and $\mathbf{A} \in H_0(\operatorname{curl}; D)$ to define the magnetic vector potential via equation (2.28).

A weak version of Coulomb gauging is included in $H_0(\operatorname{curl}, D)$ by defining

$$\mathcal{V} \coloneqq \left\{\mathbf{v} \in H_0(\operatorname{curl}; D) \;\middle|\; \int_D \mathbf{v} \cdot \operatorname{grad} \varphi \, \mathrm{d}V = 0 \quad \forall \varphi \in H_0^1(D)\right\}, \tag{2.46}$$

because all $\mathbf{v} \in \mathcal{V}$ satisfy

$$\int_D \varphi \cdot \operatorname{div} \mathbf{v} \, \mathrm{d}V = -\int_D \mathbf{v} \cdot \operatorname{grad} \varphi \, \mathrm{d}V + \int_{\partial D} \varphi(\mathbf{v} \cdot \mathbf{n}) \, \mathrm{d}a = 0 \quad \forall \varphi \in H_0^1(D). \tag{2.47}$$

Multiplying the curl-curl equation (2.29) with a test function $\mathbf{v} \in \mathcal{V}$ and applying the boundary and interface conditions of the magnetostatic problem and the boundary condition of $\mathbf{v} \in \mathcal{V}$ yields the following *weak formulation of the magnetostatic problem in vector potential formulation*: Find $\mathbf{A} \in \mathcal{V}$ such that

$$\int_D \operatorname{curl} \mathbf{v} \cdot \nu(\|\operatorname{curl} \mathbf{A}\|) \operatorname{curl} \mathbf{A} \, \mathrm{d}V = \int_D \mathbf{v} \cdot \mathbf{J} \, \mathrm{d}V \tag{2.48}$$

for all $\mathbf{v} \in \mathcal{V}$.

Analogously, the weak formulation of the magnetostatic problem in vector potential formulation involving permanent magnetic material can be obtained: Find $\mathbf{A} \in \mathcal{V}$ such that

$$\int_D \operatorname{curl} \mathbf{v} \cdot \nu(\|\operatorname{curl} \mathbf{A}\|) \operatorname{curl} \mathbf{A} \, \mathrm{d}V = \int_D \mathbf{v} \cdot \mathbf{J} \, \mathrm{d}V + \int_D \operatorname{curl} \mathbf{v} \cdot \mathbf{M} \, \mathrm{d}V \quad \forall \mathbf{v} \in \mathcal{V}. \tag{2.49}$$

Notice that in the derivation of the last equation, the interface condition (2.33) and the assumption that the interface Γ_{am} does neither intersect with the boundary of the iron domain nor the boundary Γ of the computational domain, are used.

According to [39], the weak magnetostatic problem remains well-posed if $\mathcal{V}$ is replaced by $H_0(\operatorname{curl}, D)$, but uniqueness can not be guaranteed. For linear reluctivities ν, the solution's existence, and uniqueness can be proven with the Lax-Milgram Theorem [129]. For non-linear reluctivities, the existence and the uniqueness can be proven with the Zaratonello Lemma [148, Theorem 25.B]. To verify the conditions of the Zaratonello Lemma, the existence of the lower bound $0 < \alpha < \nu$, i.e. the strong monotonicity of the $H(B)-$curve f_{HB}, the weak divergence-freeness of $\mathcal{V}$, and the stronger boundary and interface conditions discussed in Section 2.2.2 are crucial [39, 147].

2.3.2 Simplifications in 2D

Although all accelerator magnet systems are three-dimensional objects, working with two-dimensional system models is justified in some cases. Solving a 2D instead of a 3D problem is advantageous because it reduces the degrees of freedom and with that the model complexity and the computation time. Typical scenarios for which we choose 2D models are the simulation of magnet systems having a homogeneous field region, unaffected by fringe effects, along one axis in their center (e.g., $B_z = 0$, $\partial/\partial z$=0). Homogeneity along one axis can also be achieved by integration along that axis, and the integrated quantities of interest can be simulated using two-dimensional system models. A proof that solving the Laplace equation and integrating the solution along a straight axis perpendicular to a plane of symmetry of the magnet system, can be interchanged is given in [119, Section 6.1.2].
Working with a two-dimensional domain D and with isotropic material, several simplifications can be made. We generally assume that D is a subset of the xy-plane (i.e. $\partial/\partial z = 0$) and we assume that the source current $\mathbf{J} = (0, 0, J_z)^\top$ flows parallel to the z-axis, several simplifications can be made. The curl operator simplifies to $\operatorname{curl}(0, 0, A_z) = \operatorname{grad} A_z \times \mathbf{e}_z$ and the Euclidean vector norms are equal

$$\|\operatorname{curl}(0, 0, A_z)\| = \|\operatorname{grad} A_z\| \, . \tag{2.50}$$

The boundary conditions on Γ_{B} and the interface condition on Γ_{ai} included for Coulomb gauging can be simplified to

$$A_z = 0 \quad \text{on } \Gamma_{\mathrm{B}}, \tag{2.51}$$

$$[\![A_z]\!]_{\mathrm{ai}} = 0 \quad \text{on } \Gamma_{\mathrm{ai}} \tag{2.52}$$

since $\mathbf{n}$ is perpendicular to $\mathbf{A} = (0, 0, A_z)^\top$. The Coulomb gauge condition $\operatorname{div} \nu \mathbf{A} = 0$ is automatically satisfied since $\partial/\partial z = 0$. Thus, the weak formulation of the magnetostatic problem in 2D is: Find $A_z \in H_0^1(D)$ such that

$$\int_D \operatorname{grad} v \cdot \nu(\|\operatorname{grad} A_z\|) \operatorname{grad} A_z \, \mathrm{d}V = \int_D v \, J_z \, \mathrm{d}V \tag{2.53}$$

for all $v \in H_0^1(D)$.

2D conductor model In the two-dimensional setting, the source region $D_{\mathbf{J}} \subset D$ is subdivided into two disjoint subdomains $D_{\mathbf{J}} = D_{\mathbf{J}}^{(+)} \cup D_{\mathbf{J}}^{(-)}$. In $D_{\mathbf{J}}^{(+)}$ the imposed current flows in the direction of the z-axis, in $D_{\mathbf{J}}^{(-)}$ it flows in the opposite direction. To avoid the resolution of single wires in the FEM, the stranded conductor model [15] is used to model $D_{\mathbf{J}} \subset D$. Thereby, we assume that the source current density J_z is constant within the subdomains and set

$$J_z = \begin{cases} \frac{N_{\mathbf{J}} I_{\mathbf{J}}}{\operatorname{area}(D_{\mathbf{J}}^{(+)})} & \text{on } D_{\mathbf{J}}^{(+)} \\ \frac{-N_{\mathbf{J}} I_{\mathbf{J}}}{\operatorname{area}(D_{\mathbf{J}}^{(-)})} & \text{on } D_{\mathbf{J}}^{(-)}, \end{cases} \tag{2.54}$$

where $N_{\mathbf{J}}$ is the number of turns and $I_{\mathbf{J}}$ is the electric current.

2.3.3 Finite element method

For linear $B(H)$-curves, the discretization using the finite element method (FEM) transforms the weak formulation of the magnetostatic problem in vector potential formulation into a system of linear equations. The drawback of the FEM compared to other methods such as the boundary element method (BEM) [119, Section 15.1] or the combination of both [119, Chapter 15] is that finer meshes with a high number of degrees of freedom are necessary for magnet systems with detailed geometry because FEM requires the meshing of each subdomain of D. However, the resulting matrices of the linear equation system are sparse which simplifies their solution.
For non-linear $B(H)$-curves that lead to non-linear reluctivities, the discretization with the FEM yields a non-linear equation system which we solve iteratively using the Picard method [59] or the Newton-Raphson method [43]. For implementation, the open-source FEM solver GetDP [60] is chosen. We summarize in this section only the key concepts of the FEM. For a more detailed description, the reader is referred, e.g., to [13, 21, 23, 99].

Discretization The weak formulation of the magnetostatic problem in vector potential formulation (2.48) is discretized by choosing a family of finite-dimensional subspaces $V_h \subset H_0(\mathrm{curl}; D)$ to approximate the solution space and the space of test functions. This approach is known as the Ritz-Galerkin method (see, e.g., [23,

Chapter 4]). Let N_{dof} be the dimension of the subspace V_h, and let $\{\mathbf{v}_1, \dots, \mathbf{v}_{N_{\mathrm{dof}}}\}$ be a set of basis functions. Thus, every element $\mathbf{A}_h \in V_h$ can be expressed in this basis by

$$\mathbf{A}_h = \sum_{n=1}^{N_{\mathrm{dof}}} a_n \mathbf{v}_n \tag{2.55}$$

where $\mathbf{a} = (a_1, \dots, a_{N_{\mathrm{dof}}})^\top$ is a (possibly after gauging) uniquely defined coefficient vector. Substituting $\mathcal{V}$ with the space V_h in the weak form formulation of the magnetostatic problem (2.48) yields the problem: Find $\mathbf{a} \in \mathbb{R}^{N_{\mathrm{dof}}}$ such that

$$\sum_{n=1}^{N_{\mathrm{dof}}} a_n \int_D \nu \left(\left\| \sum_{n=1}^{N_{\mathrm{dof}}} a_n \operatorname{curl} \mathbf{v}_n \right\| \right) \operatorname{curl} \mathbf{v}_n \cdot \operatorname{curl} \mathbf{v}_m \, \mathrm{d}V = \int_D \mathbf{v}_m \cdot \mathbf{J} \, \mathrm{d}V \tag{2.56}$$

for all basis functions $\mathbf{v}_m \in \{\mathbf{v}_1, \dots, \mathbf{v}_{N_{\mathrm{dof}}}\}$. Under the assumption that the reluctivity ν is linear (the Picard method and the Newton-Raphson method to treat the non-linearity are discussed below), equation (2.56) can be written in matrix form

$$\mathbf{K}\mathbf{a} = \mathbf{f} \tag{2.57}$$

where the *stiffness matrix* $\mathbf{K}$ is given by

$$(\mathbf{K})_{mn} = \int_D \nu \, \operatorname{curl} \mathbf{v}_m \cdot \operatorname{curl} \mathbf{v}_n \, \mathrm{d}V \tag{2.58}$$

and the right hand side $\mathbf{f}$ is given by

$$(\mathbf{f})_m = \int_D \mathbf{v}_m \cdot \mathbf{J} \, \mathrm{d}V. \tag{2.59}$$

Consequently, an approximation $\mathbf{A}_h \in V_h$ of the weak solution to the magnetostatic problem can be found by solving the linear equation system (2.57). The choice of V_h influences the convergence of the solution. Notice that the definitions of $\mathbf{K}$ and $\mathbf{f}$ require the evaluation of an integral. We use an approximation of these integrals via Gaussian quadrature [107, Section 6.8].

Meshing To construct the finite-dimensional subspace V_h, an approximation of the domain D and its subdomains D_{i}, D_{a}, $D_{\mathbf{J}}$ and D_{m} with a triangular mesh for two-dimensional domains and a tetrahedral mesh for three-dimensional domains is used. Both meshes are referred to with $\mathcal{T}_h$, where the index h describes the maximal diameter of an element $T \in \mathcal{T}_h$. The meshes have to satisfy the geometric constraints specified in [99, Section 5.3] such that the edges and faces of the mesh respect the boundaries of the subdomains. The domains D and their subdomains studied in this thesis have polyhedral boundaries, such that they can be discretized with a suitable triangular or tetrahedral mesh $\mathcal{T}_h$ without approximation error. To generate the mesh, we use the software Gmsh [61].
The definition of the finite-dimensional subspace V_h for the FEM is based on the definition of piecewise polynomial functions on $\mathcal{T}_h$. Moreover, the basis functions of V_h are chosen such that each basis function has only local support. Consequently, the stiffness matrix $\mathbf{K}$ defined in equation (2.58) is sparse, which simplifies the solution of the problem (2.57).

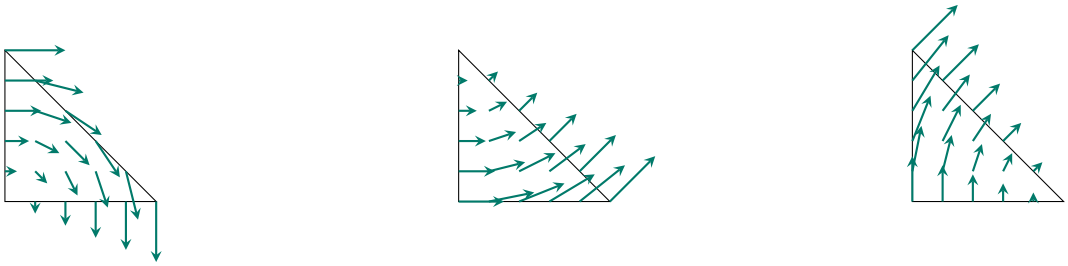

Figure 2.2: 2D basis vector fields of first-order edge elements visualized on the reference triangle.

Lagrange elements In the two-dimensional setting, we use first-order Lagrange elements [111, page 85] on a triangular mesh $\mathcal{T}_h$ that are defined by the finite-dimensional subspace $V_h \subset H_0(D)$ with

$$V_h \coloneqq \left\{ v_h \in C^0(D) \mid v_h|_T \in P_1(T) \ \forall T \in \mathcal{T}_h,\ v_h|_{\Gamma_\mathrm{B}} = 0 \right\} \tag{2.60}$$

where $P_1(T)$ denotes the space of polynomials on T of degree 1. Since the functions in V_h are by definition elementwise affine, they are uniquely determined by the function values at the nodes of the mesh. Consequently, the dimension N_dof of V_h is given by the number of nodes of the mesh $\mathcal{T}_h$ without the nodes on Γ_B because in these nodes the functions are set to zero to meet the boundary condition (2.51). A basis on V_h is given by the nodal basis $\{\varphi_1, \ldots, \varphi_{N_\mathrm{dof}}\}$ that satisfies

$$\varphi_i(k_j) = \delta_{ij} \quad \forall 1 \leq j \leq N_\mathrm{dof} \tag{2.61}$$

where k_j are the nodes of $\mathcal{T}_h$ that are not on Γ_B. Due to the continuity of the basis functions in V_h across edges and the assumption that material interfaces align with the edges, the interface condition (2.52) is satisfied. An a priori estimate of the convergence depending on h can be found in [111, Theorem 3.1].

Edge elements In three dimensions we use first-order edge elements [99, 139] on a tetrahedral mesh $\mathcal{T}_h$ that are defined by the finite-dimensional subspace $V_h \subset H_0(\mathrm{curl}; D)$ [99, Theorem 5.37] with

$$V_h \coloneqq \{ \mathbf{v}_h \in H(\mathrm{curl}; D) \mid \mathbf{v}_h|_T \in R_1(T) \ \forall T \in \mathcal{T}_h,\ \mathbf{v}_h|_{\Gamma_\mathrm{B}} \times \mathbf{n} = \mathbf{0} \} \tag{2.62}$$

where $R_1(T)$ is defined by

$$R_1(T) \coloneqq (P_0(T))^3 \oplus \left\{ \mathbf{r} \in (\widetilde{P}_1)^3 \,\middle|\, \mathbf{x} \cdot \mathbf{r}(\mathbf{x}) = 0, \quad \forall\, \mathbf{x} \in T \right\}. \tag{2.63}$$

Thereby, P_n is the space of polynomials of order n, and $\widetilde{P}_n$ is the space of homogeneous polynomials of order n. An a priori estimate of the convergence can be found in [99, Theorem 5.41]. Following [139], a six-dimensional basis of $R_1(T)$ can be defined such that each coefficient of the basis representation of a vector field $\mathbf{v} \in R_1(T)$ is related to the average of $\mathbf{v} \cdot \mathbf{t}$ on one of the edges of T, where $\mathbf{t}$ is the unit tangent vector. A two-dimensional plot of the three basis vector fields of the first-order edge elements on the reference triangle can be found in Figure 2.2. The basis vectors $\mathbf{v}_h \in V_h$ are tangentially continuous across edges and faces and the dimension N_dof of V_h is given by the number of edges in $\mathcal{T}_h$ without the edges on Γ_B. On Γ_B, the tangential component of $\mathbf{v}_h$ is set to zero to satisfy the boundary condition. However, the elements of V_h in the three-dimensional setting do not automatically satisfy conditions (2.31) for Coulomb gauging. Thus, additional gauging conditions are imposed to obtain a unique solution.

Tree-cotree gauging We apply tree-cotree gauging (see, e.g., [6, 39, 112]) to obtain a unique solution $\mathbf{A}_h \in V_h$ to the weak formulation of the magnetostatic problem in vector potential formulation when edge elements are used for discretization. A *tree* τ of the mesh $\mathcal{T}_h$ is defined as a loop-free subset of edges of $\mathcal{T}_h$ that connects all nodes. The complement $\tau' = \mathcal{T}_h \backslash \tau$ is called the *cotree*. We assume in this section that $\Gamma_\mathrm{B} = \partial D$ and that the tree is chosen such that it defines also a tree on Γ_B. A subspace of V_h spanned by the first-order edge element basis functions ψ_e, that correspond to edges in the cotree τ', is defined by

$$V_{h,\tau'} = \operatorname{span}\left\{\psi_e \mid e \in \tau' \setminus \Gamma_\mathrm{B}\right\}. \tag{2.64}$$

Following [39, Theorem 2.2], for all $\mathbf{A}_h \in V_h$, there is a decomposition

$$\mathbf{A}_h = \mathbf{A}_{h,\tau'} + \operatorname{grad} w \tag{2.65}$$

with $w \in H_0^1(D)$ and $\mathbf{A}_{h,\tau'} \in V_{h,\tau'}$. The basis representation (2.55) of $\mathbf{A}_h \in V_h$ with the coefficient vector $\mathbf{a} \in \mathbb{R}^{N_\mathrm{dof}}$ can be rearranged such that $\mathbf{a} = (\mathbf{a}_\tau, \mathbf{a}_{\tau'})$, where the coefficients in $\mathbf{a}_\tau$ correspond to edges in the tree and $\mathbf{a}_{\tau'}$ corresponds to edges in the cotree respectively. Likewise, the linear equation system (2.57) can be rewritten as

$$\begin{pmatrix} \mathbf{K}_{\tau'\tau'} & \mathbf{K}_{\tau'\tau} \\ \mathbf{K}_{\tau\tau'} & \mathbf{K}_{\tau\tau} \end{pmatrix} \begin{pmatrix} \mathbf{a}_{\tau'} \\ \mathbf{a}_\tau \end{pmatrix} = \begin{pmatrix} \mathbf{f}_{\tau'} \\ \mathbf{f}_\tau \end{pmatrix}. \tag{2.66}$$

The classical tree-cotree gauging method consists of choosing $\mathbf{a}_\tau = \mathbf{0}$ and solving the subsystem $\mathbf{K}_{\tau'\tau'}\mathbf{a}_{\tau'} = \mathbf{f}_{\tau'}$ on the cotree that admits a unique solution [112, Theorem 1]. It can be shown that the resulting magnetic flux density $\operatorname{curl} \mathbf{A}_{h,\tau}$ is independent of the choice of the tree τ [39, Corollary 2.1].

Picard method and Newton-Raphson method Due to non-linear $H(B)$-curves, non-linear reluctivities can occur such that instead of the linear problem (2.57) the equation

$$\mathbf{K}(\mathbf{a})\mathbf{a} = \mathbf{f} \tag{2.67}$$

has to be solved with a non-linear dependence of $\mathbf{K}$ on $\mathbf{a}$. Using the Picard method (also known as fixed point method, see e.g., [59, Section 5.2.2]), equation (2.67) is solved iteratively, inserting in the i-th iteration step the solution to the preceding iteration step into the reluctivity function. Given an initial guess $\mathbf{a}_0$ close enough to the solution, the linear problems

$$\mathbf{K}(\mathbf{a}_{i-1})\mathbf{a}_i = \mathbf{f} \tag{2.68}$$

can be solved subsequently, yielding the formal iteration $\mathbf{a}_i = \mathbf{K}(\mathbf{a}_{i-1})^{-1}\mathbf{f}$. However, the Picard method features only linear convergence, while with the Newton-Raphson method locally quadratic convergence can be achieved in some cases, however, not in the limit $h \to 0$. A discussion on the convergence of both methods in the context of the non-linear magnetostatic problem can be found in [117, Section 3.4] and [103, Section 4.1.3]. In the Newton-Raphson method [43, Section 1.2], the iteration

$$\mathbf{a}_i = \mathbf{a}_{i-1} + \left(D\mathbf{r}(\mathbf{a}_{i-1})\right)^{-1} \left(\mathbf{f} - \mathbf{K}(\mathbf{a}_{i-1})\mathbf{a}_{i-1}\right) \tag{2.69}$$

is used, where the matrix $D\mathbf{r}(\mathbf{a}_{i-1})$ is the Jacobian matrix of the residual function $\mathbf{r}(\mathbf{a}) \coloneqq \mathbf{K}(\mathbf{a})\mathbf{a} - \mathbf{f}$ evaluated at $\mathbf{a}_{i-1}$. The definition of this iteration step is based on equating the first-order Taylor approximation of the residual function $\mathbf{r}$ with zero [43, Section 1.2].

Writing out the weak formulation of the m-th line of the Picard method reads: Find $\mathbf{A}_i \in V_h$ such that

$$\int_D \nu\left(\|\operatorname{curl} \mathbf{A}_{i-1}\|\right) \operatorname{curl} \mathbf{A}_i \cdot \operatorname{curl} \mathbf{v}_m \,\mathrm{d}V = \int_D \mathbf{v}_m \cdot \mathbf{J} \,\mathrm{d}V, \tag{2.70}$$

where $\mathbf{v}_m \in V_h$ is the m-th basis function. The m-th line of the Newton-Raphson method reads respectively [117, equation 3.53]: Find $\mathbf{A}_i \in V_h$ such that

$$\begin{aligned} \int_D \mathbf{v}_m \cdot \mathbf{J} \, \mathrm{d}V = \quad & \int_D \nu \left(\|\operatorname{curl} \mathbf{A}_{i-1}\| \right) \operatorname{curl} \mathbf{A}_{i-1} \cdot \operatorname{curl} \mathbf{v}_m \, \mathrm{d}V \\ & + \int_D \boldsymbol{\nu}_\mathrm{d} \left(\operatorname{curl} \mathbf{A}_{i-1} \right) \operatorname{curl} \mathbf{A}_i \cdot \operatorname{curl} \mathbf{v}_m \, \mathrm{d}V \\ & - \int_D \boldsymbol{\nu}_\mathrm{d} \left(\operatorname{curl} \mathbf{A}_{i-1} \right) \operatorname{curl} \mathbf{A}_{i-1} \cdot \operatorname{curl} \mathbf{v}_m \, \mathrm{d}V \end{aligned} \tag{2.71}$$

is satisfied for the basis function $\mathbf{v}_m \in V_h$. Thereby, $\boldsymbol{\nu}_\mathrm{d}$ is the differential reluctivity tensor [117, definition 5] which is for $\mathbf{t} \in \mathbb{R}^3$ defined by

$$\boldsymbol{\nu}_\mathrm{d}(\mathbf{t}) \coloneqq \nu(\|\mathbf{t}\|)\mathbb{I} + \frac{\nu'(\|\mathbf{t}\|)}{\|\mathbf{t}\|} \mathbf{t} \otimes \mathbf{t}. \tag{2.72}$$

A proof that deriving the Jacobian matrix $D\mathbf{r}$ yields the differential reluctivity is given in [117, Lemma 3].

2.4 Field harmonics

Unlike the numerical approximation introduced in the last section, the field harmonic approach seeks closed-form expressions of solutions to the boundary value problem of magnetostatics. The field harmonic approach can be applied in the vacuum domain to the scalar potential formulation and the two-dimensional vector potential formulation. In both cases, the formulation yields a Laplace equation that can be solved using variable separation [100]. The coefficients of these solutions are also referred to as *field harmonics* or *multipoles*. For instance, in the two-dimensional polar coordinates, this approach yields the normal and skew dipoles, quadrupoles, etc. which are well-known coefficients in the magnet design community.

An overview of field harmonic expansions in different coordinate systems is given in [120]. In this work, we are using polar coordinates and toroidal coordinates. Methods to determine the coefficients of the toroidal harmonic expansion will be derived and discussed in Chapter 6. The coefficients of the circular harmonic expansion can be determined, e.g., by equating the coefficients of the general solution with the Fourier coefficients of Neumann boundary data, and by measurements with rotating coil magnetometers [119]. This establishes a valuable link between system models based on circular harmonics and magnetic measurements. In particular, this link yields a set of comparable quantities (see Figure 1.2) that can be used for inverse computations and model updating.

2.4.1 Circular harmonics

Circular cylindrical coordinates (r, θ, y) [100, p. 12] are defined by the mapping

$$(r, \theta, y) \mapsto \big(r\cos(\theta), \quad y, \quad r\sin(\theta) \big) \tag{2.73}$$

where (r, θ) are the polar coordinates in the xz-plane and y describes the longitudinal position. Thereby, the longitudinal position along the y-axis is chosen for consistency with the toroidal coordinate system defined in (2.82). A formula for the Laplace operator $\Delta = \operatorname{div} \operatorname{grad}$ in curvilinear coordinates depending on scaling factors (here $h_r = 1, h_\theta = r, h_y = 1$) is given in [119, equation 3.224]. Thus, in circular cylindrical coordinates, Laplace's equation for the magnetic scalar potential ϕ_m is given by

$$\frac{1}{r} \frac{\partial}{\partial r} \left(r \frac{\partial \phi_\mathrm{m}}{\partial r} \right) + \frac{1}{r^2} \frac{\partial^2 \phi_\mathrm{m}}{\partial \theta^2} + \frac{\partial^2 \phi_\mathrm{m}}{\partial y^2} = 0. \tag{2.74}$$

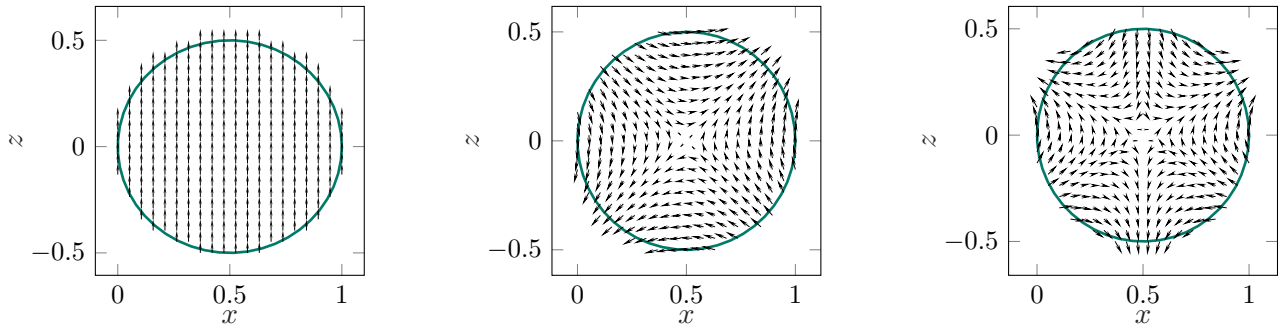

Figure 2.3: Magnetic flux density in a normal circular dipole, quadrupole, and sextupole (from left to right). The arrow length is scaled with the absolute value.

In long and straight magnet systems that generate homogeneous magnetic flux densities $\mathbf{B}$ with respect to the longitudinal position y, we can assume

$$0 = \frac{\partial B_y}{\partial y} = \frac{\partial^2 \phi_\mathrm{m}}{\partial y^2}. \tag{2.75}$$

Consequently, the last summand in the Laplace equation (2.74) vanishes. The remaining differential equation can be solved using variable separation. All possible solutions can be found in [100, p. 14]. Omitting solutions that are infinite for $r \to 0$ and solutions that are aperiodic in θ yields

$$\phi_\mathrm{m}(r,\theta) = \sum_{n=0}^{\infty} r^n (\mathcal{A}_n^\mathrm{c} \cos(n\theta) + \mathcal{B}_n^\mathrm{c} \sin(n\theta)). \tag{2.76}$$

The coefficients $\mathcal{A}_n^\mathrm{c}, \mathcal{B}_n^\mathrm{c} \in \mathbb{R}$ are referred to as *circular harmonic coefficients* or *multipole coefficients*. Notice that they are independent of the coordinates r and θ. The magnetic scalar potential is related to the magnetic flux density via $\mathbf{B} = -\mu_0 \operatorname{grad} \phi_\mathrm{m}$, hence the radial component B_r of the magnetic flux density is given by

$$B_r(r,\theta) = -\mu_0 \sum_{n=1}^{\infty} n r^{n-1} (\mathcal{A}_n^\mathrm{c} \cos(n\theta) + \mathcal{B}_n^\mathrm{c} \sin(n\theta)). \tag{2.77}$$

Using the orthogonality of the trigonometric functions, we obtain on a reference circle with radius r_0

$$\mathcal{A}_n^\mathrm{c} = -\frac{1}{n\pi\mu_0 r_0^{n-1}} \int_0^{2\pi} B_r(r_0,\theta) \cos(n\theta)\, \mathrm{d}\theta \tag{2.78}$$

$$\mathcal{B}_n^\mathrm{c} = -\frac{1}{n\pi\mu_0 r_0^{n-1}} \int_0^{2\pi} B_r(r_0,\theta) \sin(n\theta)\, \mathrm{d}\theta \tag{2.79}$$

for $n \geq 1$. However, the circular harmonic coefficient $\mathcal{A}_0^\mathrm{c}$ can not be obtained from the magnetic flux density but is given by a gauge condition, i.e. $\mathcal{A}_0^\mathrm{c} = \phi_\mathrm{m}(0,0)$. For $\mathcal{B}_0^\mathrm{c}$ we can assume that $\mathcal{B}_0^\mathrm{c} = 0$ because $\sin(0\theta) = 0$. From the circular harmonic coefficients $\mathcal{A}_n^\mathrm{c}, \mathcal{B}_n^\mathrm{c}$, the circular *skew* and *normal multipole coefficients* $A_n(r_0), B_n(r_0)$ in units of tesla [119, Section 6.1.1.1] can be derived by

$$A_n(r_0) = -n r_0^{n-1} \mu_0 \mathcal{A}_n^\mathrm{c}, \qquad B_n(r_0) = -n r_0^{n-1} \mu_0 \mathcal{B}_n^\mathrm{c}. \tag{2.80}$$

The scaling laws of these coefficients regarding different radii r are

$$A_n(r) = \frac{r^{n-1}}{r_0^{n-1}} A_n(r_0), \qquad B_n(r) = \frac{r^{n-1}}{r_0^{n-1}} B_n(r_0). \tag{2.81}$$

The magnetic flux density in a normal dipole, quadrupole, and sextupole is illustrated in Figure 2.3.

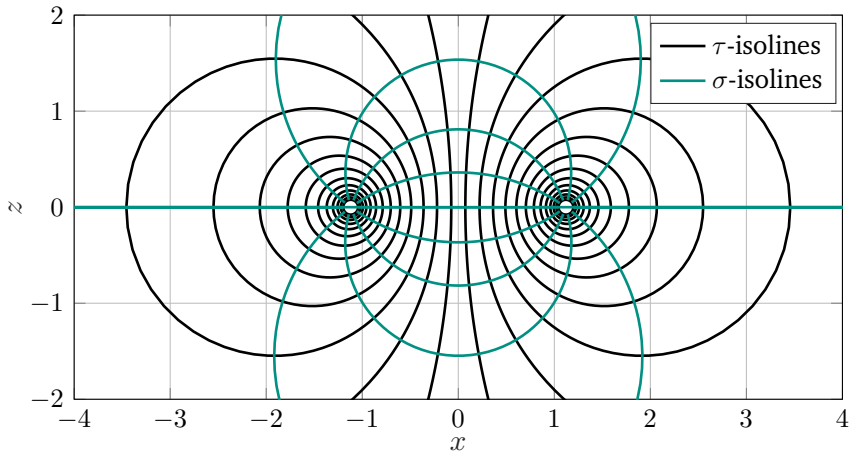

Figure 2.4: Apollonian circles, the isolines of the bipolar coordinates with focal points $F_1 = (-1.11, 0)$ and $F_2 = (1.11, 0)$.

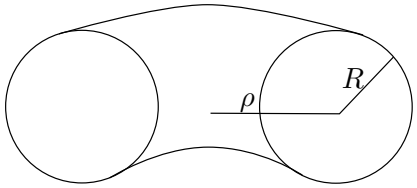

Figure 2.5: Sketch of a toridal wedge with toroidal radius ρ and poloidal radius R.

2.4.2 Toroidal harmonics

Toroidal coordinates Toroidal coordinates (τ, σ, φ) [100, p. 112] are defined by the mapping

$$(\tau, \sigma, \varphi) \mapsto \left(\frac{a \sinh(\tau) \cos(\varphi)}{\cosh(\tau) - \cos(\sigma)}, \quad \frac{a \sinh(\tau) \sin(\varphi)}{\cosh(\tau) - \cos(\sigma)}, \quad \frac{a \sin(\sigma)}{\cosh(\tau) - \cos(\sigma)} \right), \tag{2.82}$$

where (τ, σ) are the bipolar coordinates [100, p. 64]. In the xz-plane, the τ- and σ-isolines are the set of Apollonian circles with focal points $F_1 = (-a, 0)$ and $F_2 = (a, 0)$, see Figure 2.4. The τ-isosurfaces are tori. Let D be a solid torus with major, toroidal radius ρ and minor, poloidal radius R (Figure 2.5). This domain can be defined as the product $D = U^2 \times S^1$ of the disk U^2 with radius R and the circle S^1 with radius ρ. The radius a of the focal ring, such that a τ-isosurface of the corresponding toroidal coordinates (2.82) describes the boundary of D, is given by

$$a = R\sqrt{(\rho/R)^2 - 1}. \tag{2.83}$$

The boundary $\Gamma = \partial D$ is then described by the τ-isosurface with

$$\cosh(\tau) = \rho/R. \tag{2.84}$$

These formulas are given, e.g., in [135] and can be easily verified using the definition (2.82) of the toroidal coordinates. The *eccentricity* is the ratio $\epsilon := \rho/R$ of major to minor radius which determines the shape of the torus. An American donut has the eccentricity $\epsilon \approx 2$, a toroidal domain with the eccentricity $\epsilon = 19$ resembles a bicycle tube. The scaling factors of the toroidal coordinates system are given by

$$h_\tau = h_\sigma = \frac{a}{\cosh(\tau) - \cos(\sigma)} \qquad \text{and} \qquad h_\varphi = \frac{a \sinh(\tau)}{\cosh(\tau) - \cos(\sigma)}. \tag{2.85}$$

Scalar potential formulation in multiply-connected domains The toroidal domain $D = U^2 \times S^1$ is multiply-connected. On simply-connected domains we have, according to [33, Theorem 8],

$$\operatorname{im}\left(\operatorname{grad}\left(H^1(D)\right)\right) = \ker\left(\operatorname{curl}\left(H(\operatorname{curl}; D)\right)\right). \tag{2.86}$$

The image of the gradient is always a subset of the kernel of the curl operator, whereas the inverse is not true in multiply-connected domains D. Consequently, finding solutions $\phi_\mathrm{m} \in H^1(D)$ to the Laplace equation in D is not sufficient to obtain via $\mathbf{H} = -\operatorname{grad}\phi_\mathrm{m}$ all $\mathbf{H} \in H(\operatorname{curl}; D)$ with $\operatorname{curl}\mathbf{H} = \mathbf{0}$. Instead, again following [33, Theorem 8], each $\mathbf{H} \in H(\operatorname{curl}; D)$ with $\operatorname{curl}\mathbf{H} = \mathbf{0}$ admins a decomposition

$$\mathbf{H} = \operatorname{grad}\psi + \mathbf{h}, \tag{2.87}$$

where $\psi \in H^1(D)$ and $\mathbf{h}$ is an element of the cohomology space $H_1(D)$. This cohomology space is characterized in [33, Proposition 8]. Let D be a multiply-connected domain with boundary $\Gamma = \partial D$ and let Σ_i be cuttings of D such that $\dot{D} := D \setminus \bigcup_i \Sigma_i$ is simply-connected. Then, the cohomology space $H_1(D)$ is given by

$$H_1(D) = \left\{ \mathbf{h} \in L^2(D, \mathbb{R}^3) \,\middle|\, \begin{array}{l} \exists\, f \in H^1(\dot{D}) \text{ such that } \mathbf{h} = \operatorname{grad} f \text{ in } \dot{D}, \text{ with} \\ \Delta f = 0 \text{ in } \dot{D},\ \partial_\mathbf{n} f|_\Gamma = \mathbf{0},\ [\![f]\!]_{\Sigma_i} = c_i \text{ const.},\ [\![\partial_\mathbf{n} f]\!]_{\Sigma_i} = \mathbf{0} \end{array} \right\} \tag{2.88}$$

where $\mathbf{n}$ is the outward unit normal vector on Γ or respectively the unit normal vector on the cut Σ_i. Moreover, the dimension of $H_1(D)$ equals the number of required cuts Σ_i. For the toroidal domain D, the cut $\Sigma = U^2 \times \{0\}$ is sufficient such that $\dot{D} = D \setminus \Sigma$ is simply-connected, thus $H_1(D)$ is one-dimensional. Let $f : \dot{D} = U^2 \times [0, 2\pi] \to \mathbb{R}$ be the mapping defined by

$$f : (\tau, \sigma, \varphi) \mapsto \mathcal{E}^\mathrm{t}\varphi \tag{2.89}$$

for a constant $\mathcal{E}^\mathrm{t} \in \mathbb{R}$. It can be easily verified that f satisfies the conditions in (2.88) and that the resulting cohomology space

$$H_1(D) = \left\{ \operatorname{grad}\mathcal{E}^\mathrm{t}\varphi \,\middle|\, \mathcal{E}^\mathrm{t} \in \mathbb{R} \right\} \tag{2.90}$$

is one-dimensional. Therefore, we found all functions $\mathbf{h}$ relevant for the decomposition in equation (2.87). As a result, we seek on toroidal domains magnetic scalar potentials ϕ_m of the form

$$\phi_\mathrm{m}(\tau, \sigma, \varphi) = \mathcal{E}^\mathrm{t}\varphi + \psi(\tau, \sigma, \varphi), \tag{2.91}$$

where $\psi \in H^1(D)$ is a solution to the Laplace equation on D. Notice that ϕ_m also solves the Laplace equation on $\dot{D}$. However, for $\mathcal{E}^\mathrm{t} \neq 0$ the potential is not an element of $H^1(D)$ because it has a jump at the cut Σ. According to [40, Section 6.5.2], the term $\mathcal{E}^\mathrm{t}\varphi$ considers currents through the hole of the current-free toroidal domain D.

In the next paragraph, we derive a general formula using R-separation that describes all possible solutions $\psi \in H^1(D)$ to the Laplace equation.

Toroidal harmonic expansion Inserting the scaling factors (2.85) into the Laplace equation in curvilinear coordinates [119, equation 3.224] yields the Laplace equation in toroidal coordinates

$$\begin{aligned} 0 = \tfrac{(\cosh(\tau)-\cos(\sigma))^3}{a^3\sinh(\tau)} \Big[&\tfrac{\partial}{\partial\tau}\left(\tfrac{a\sinh(\tau)}{\cosh(\tau)-\cos(\sigma)}\tfrac{\partial\psi}{\partial\tau}\right) + \tfrac{\partial}{\partial\sigma}\left(\tfrac{a\sinh(\tau)}{\cosh(\tau)-\cos(\sigma)}\tfrac{\partial\psi}{\partial\sigma}\right) \\ &+ \tfrac{\partial}{\partial\varphi}\left(\tfrac{a}{(\cosh(\tau)-\cos(\sigma))\sinh(\tau)}\tfrac{\partial\psi}{\partial\varphi}\right)\Big]. \end{aligned} \tag{2.92}$$

Unlike the cylindrical coordinates, which admit a simple separation [100, Definition I, p. 96] of the Laplace equation, the Laplace equation is not simply separable in toroidal coordinates. However, it is *R-separable* [100, Definition II, p. 96], meaning that using the assumption

$$\psi(\tau,\sigma,\varphi) = R(\tau,\sigma,\varphi)X_1(\tau)\,X_2(\sigma)\,X_3(\varphi) \tag{2.93}$$

for $R \neq$ const. permits a separation of the Laplace equation into three ordinary differential equations. Those are according to [100, p. 114] given by

$$\begin{cases} \frac{d^2X_1}{d\tau^2}(\tau) + \coth(\tau)\frac{dX_1(\tau)}{d\tau} + (\frac{1}{4} - \alpha_1 - \frac{\alpha_2}{\sinh^2(\tau)})X_1(\tau) = 0, \\ \frac{d^2X_2}{d\sigma^2}(\sigma) + \alpha_1 X_2(\sigma) = 0, \\ \frac{d^2X_3}{d\phi^2}(\varphi) + \alpha_2 X_3(\varphi) = 0, \end{cases} \tag{2.94}$$

with parameters $\alpha_1, \alpha_2 \geq 0$. The corresponding term R is given by

$$R(\tau,\sigma,\varphi) \coloneqq \sqrt{\kappa(\tau,\sigma)} := \sqrt{\cosh(\tau) - \cos(\sigma)}. \tag{2.95}$$

Solutions to the ordinary differential equations (2.94) depending on α_1, α_2 can be found in [100, p. 114]. The solution to the differential equation concerning X_1 involves the *associated Legendre functions of the first and second kind of half-integer degree* $P^m_{n-1/2}$ and $Q^m_{n-1/2}$ [2, 64, 124]. More details on these functions are given in Appendix 8.1.
Omitting solutions that are aperiodic in σ or φ or that are infinite on the focal ring yields the following solution $\psi \in H^1(D)$ of the Laplace equation

$$\begin{aligned} \psi(\tau,\sigma,\varphi) = \sqrt{\kappa(\tau,\sigma)}\sum_{m,n=0}^{\infty} Q^m_{n-\frac{1}{2}}(\cosh(\tau)) \quad & \big(\mathcal{A}^{\mathrm{t}}_{n,m}\cos(n\sigma)\cos(m\varphi) + \mathcal{B}^{\mathrm{t}}_{n,m}\sin(n\sigma)\cos(m\varphi) \\ & + \mathcal{C}^{\mathrm{t}}_{n,m}\cos(n\sigma)\sin(m\varphi) + \mathcal{D}^{\mathrm{t}}_{n,m}\sin(n\sigma)\sin(m\varphi)\big) \end{aligned} \tag{2.96}$$

with constants $\mathcal{A}^{\mathrm{t}}_{n,m}, \mathcal{B}^{\mathrm{t}}_{n,m}, \mathcal{C}^{\mathrm{t}}_{n,m}, \mathcal{D}^{\mathrm{t}}_{n,m} \in \mathbb{R}$ that are independent of the coordinates (τ,σ,φ). Notice that we can assume by definition that $\mathcal{B}^{\mathrm{t}}_{0,m} = 0$ for all $m \geq 0$, $\mathcal{C}^{\mathrm{t}}_{n,0} = 0$ for all $n \geq 0$, $\mathcal{D}^{\mathrm{t}}_{0,m} = 0$ for all $m \geq 0$, and $\mathcal{D}^{\mathrm{t}}_{n,0} = 0$ for all $n \geq 0$.
Inserting the solution $\psi \in H^1(D)$ of the Laplace equation on D given in equation (2.96) into the magnetic scalar potential (2.91) yields

$$\begin{aligned} \phi_{\mathrm{m}}(\tau,\sigma,\varphi) = \mathcal{E}^{\mathrm{t}}\varphi + \sqrt{\kappa(\tau,\sigma)}\sum_{m,n=0}^{\infty} Q^m_{n-\frac{1}{2}}(\cosh(\tau)) \quad & \big(\mathcal{A}^{\mathrm{t}}_{n,m}\cos(n\sigma)\cos(m\varphi) + \mathcal{B}^{\mathrm{t}}_{n,m}\sin(n\sigma)\cos(m\varphi) \\ & + \mathcal{C}^{\mathrm{t}}_{n,m}\cos(n\sigma)\sin(m\varphi) + \mathcal{D}^{\mathrm{t}}_{n,m}\sin(n\sigma)\sin(m\varphi)\big)\,. \end{aligned} \tag{2.97}$$

We refer to this equation as the *toroidal harmonic expansion*. The coefficients are called *toroidal harmonics*. For numerical stability, it is suggested in [133] to normalize the toroidal harmonics by multiplication with the factor $Q^0_{n-1/2}(\cosh(\tau_0))$, where the parameter τ_0 is chosen such that the τ_0-isosurface is in the center of the region of interest. To save on notation, we introduce the symbol

$$\widetilde{Q}^m_{n-\frac{1}{2}}(\tau) := \frac{Q^m_{n-1/2}(\cosh(\tau))}{Q^m_{n-1/2}(\cosh(\tau_0))}, \tag{2.98}$$

and rewrite the toroidal harmonic expansion (abusing the notation of the toroidal harmonic coefficients) as

$$\begin{aligned} \phi_{\mathrm{m}}(\tau,\sigma,\varphi) = \mathcal{E}^{\mathrm{t}}\varphi + \sqrt{\kappa(\tau,\sigma)}\sum_{m,n=0}^{\infty} \widetilde{Q}^m_{n-\frac{1}{2}}(\tau) \quad & \big(\mathcal{A}^{\mathrm{t}}_{n,m}\cos(n\sigma)\cos(m\varphi) + \mathcal{B}^{\mathrm{t}}_{n,m}\sin(n\sigma)\cos(m\varphi) \\ & + \mathcal{C}^{\mathrm{t}}_{n,m}\cos(n\sigma)\sin(m\varphi) + \mathcal{D}^{\mathrm{t}}_{n,m}\sin(n\sigma)\sin(m\varphi)\big)\,. \end{aligned} \tag{2.99}$$

Having the normalized toroidal harmonic expansion (2.99), the components of magnetic flux density in toroidal coordinates can be derived using $\mathbf{B} = -\mu_0 \operatorname{grad} \phi_\mathrm{m}$. The formulas are reported in Appendix 8.2.

As described in Section 2.2.2, if a scalar potential ϕ_m solves Laplace's equation, then $\phi_\mathrm{m} + c$ is for any constant $c \in \mathbb{R}$ also a solution. Uniqueness can be achieved by gauging, e.g., by imposing that the scalar potential attains a certain value at a specific point in the computational domain D. For the circular harmonic expansion, this gauging condition uniquely determines the value of $\mathcal{A}_0^\mathrm{c}$. In Section 6.1.2 we prove that gauging the magnetic scalar potential in the toroidal harmonic expansion is equivalent to imposing an additional condition on the skew toroidal harmonic coefficients $\mathcal{A}_{n,m}^\mathrm{t}$. Moreover, methods to determine the toroidal harmonic coefficients from the magnetic flux density are derived in Chapter 6.

Rotationally symmetric case We are particularly interested in the toroidal harmonic expansion in configurations such that the magnetic flux density is independent of the coordinate φ, e.g., for local expansions inside homogeneous field regions. If the differentiable solution $\psi \in H^1(D)$ of the Laplace equation on D is independent of φ, the Laplace equation (2.92) simplifies to

$$0 = \frac{(\cosh(\tau) - \cos(\sigma))^3}{a^3 \sinh(\tau)} \left[\frac{\partial}{\partial \tau} \left(\frac{a \sinh(\tau)}{\cosh(\tau) - \cos(\sigma)} \frac{\partial \psi}{\partial \tau} \right) + \frac{\partial}{\partial \sigma} \left(\frac{a \sinh(\tau)}{\cosh(\tau) - \cos(\sigma)} \frac{\partial \psi}{\partial \sigma} \right) \right]. \tag{2.100}$$

Notice that this equation differs from the Laplace equation in bipolar coordinates. To find solutions, R-separation is applied with the ansatz

$$\psi(\tau, \sigma) = \sqrt{\kappa(\tau, \sigma)} X_1(\tau)\, X_2(\sigma) \tag{2.101}$$

yielding the two ordinary differential equations [100, p. 115]

$$\begin{cases} \frac{d^2 X_1(\tau)}{d\tau^2} + \coth(\tau) \frac{dX_1(\tau)}{d\tau} + (\frac{1}{4} - \alpha_1) X_1(\tau) = 0, \\ \frac{d^2 X_2(\sigma)}{d\sigma^2} + \alpha_1 X_2(\sigma) = 0. \end{cases} \tag{2.102}$$

Solutions to these ordinary differential equations can be found in [100, p. 115]. Again, we omit solutions that are aperiodic in σ and that are infinite on the focal ring. As a result, we obtain

$$\psi(\tau, \sigma) = \sqrt{\kappa(\tau, \sigma)} \sum_{n=0}^{\infty} Q_{n-\frac{1}{2}}^0(\cosh(\tau)) \left(\mathcal{A}_n^\mathrm{t} \cos(n\sigma) + \mathcal{B}_n^\mathrm{t} \sin(n\sigma) \right). \tag{2.103}$$

Including the normalization (2.98) and inserting $\psi \in H^1(D)$ into (2.91) yields the *normalized toroidal harmonic expansion in the rotationally symmetric case* of the magnetic scalar potential

$$\phi_\mathrm{m}(\tau, \sigma, \varphi) = \mathcal{E}^\mathrm{t} \varphi + \sqrt{\kappa(\tau, \sigma)} \sum_{n=0}^{\infty} \widetilde{Q}_{n-\frac{1}{2}}^0(\cosh(\tau)) \left(\mathcal{A}_n^\mathrm{t} \cos(n\sigma) + \mathcal{B}_n^\mathrm{t} \sin(n\sigma) \right). \tag{2.104}$$

In analogy to the circular harmonic coefficients, we call the coefficients $\mathcal{A}_n^\mathrm{t}$ *skew* coefficients and the coefficients $\mathcal{B}_n^\mathrm{t}$ *normal* coefficients. Notice that the magnetic scalar potential is not rotationally symmetric due to the linear term $\mathcal{E}^\mathrm{t}\varphi$. However, the corresponding magnetic flux density is rotationally symmetric. Its formulas are reported in Appendix 8.2. The rotationally symmetric magnetic flux density on the cross-section of a toroidal domain with $\rho/R = 3$ for a normal dipole ($\mathcal{B}_1^\mathrm{t} \neq 0$), a normal quadrupole ($\mathcal{B}_2^\mathrm{t} \neq 0$), and a normal sextupole ($\mathcal{B}_3^\mathrm{t} \neq 0$) is shown in Figure 2.6.

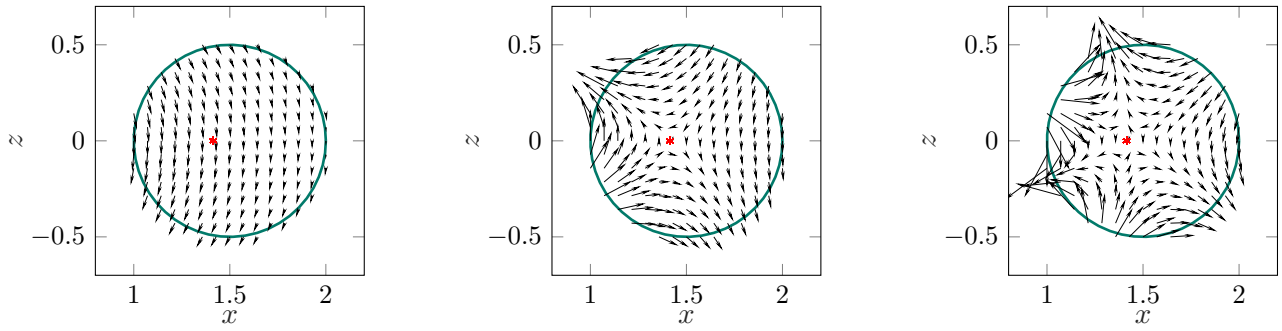

Figure 2.6: Magnetic flux density in a rotationally symmetric toroidal ($\mathcal{B}_1^{\mathrm{t}} \neq 0$), normal quadrupole ($\mathcal{B}_2^{\mathrm{t}} \neq 0$), and normal sextupole ($\mathcal{B}_3^{\mathrm{t}} \neq 0$) with $\rho/R = 3$ (from left to right). The focal point $F_1 = (a, 0)$ is marked in red. The arrow length is scaled with the absolute value. The magnetic flux density is computed using the formulas given in equation (8.15).

2.5 Summary

We introduced Maxwell's equations that describe electromagnetic fields in general. Neglecting time-dependent effects, we reduced the full set of Maxwell's equations to the magnetostatic case. To build system models of accelerator magnets, we introduced domain and material assumptions as well as boundary and interface conditions, yielding the scalar and vector potential formulation of the boundary value problem of magnetostatics. Subsequently, we discussed the numerical approximation of the vector potential formulation with the FEM. To find solutions to the scalar potential formulation, we introduced the field harmonics in polar and toroidal coordinates. In Chapters 4 and 5, we will apply the FEM to simulate a normal conducting iron-dominated magnet and a Halbach magnet that is composed of permanently magnetized blocks. The properties of the toroidal harmonic expansion and particularly the determination of its coefficients from magnetic flux density observations will be investigated in Chapter 6.

3 Methods for statistical inversion

In this chapter, methods of statistical inversion are introduced which will be applied for stochastic model updating in Chapter 4 and Chapter 5.
Deterministic and stochastic model updating was introduced in Section 1.3.3. Both methods aim to adjust a model such that the model's predictions match corresponding observations of comparable quantities [145]. A widely used approach for model updating is the update of model parameters. While deterministic model updating returns a parameter value, stochastic model updating returns a probability distribution of the parameter. Following [78, Section 3], stochastic model updating therefore rather answers the question "What is our information about this parameter?", than the question "What is the value of this parameter?", which is answered by deterministic model updating. Consequently, stochastic model updating is a suitable approach for updating system models of accelerator magnets where different sources of information about the magnet system that are affected by uncertainty are available such as measurement data of its components (e.g., material curves or magnetizations), and measurements of field-related quantities of interest (e.g., the magnetic flux density in the air gap or multipole coefficients). The Bayes formula is the key to combining these sources of information and inferring information about the parameters, see e.g., [12, 28, 78].
There are several advantages of stochastic model updating compared to deterministic model updating. First, the resulting probability distribution of the parameters can be used for uncertainty quantification. Propagating this uncertainty through the system model enables the quantification of uncertainties of the model's predictions. Second, although the aim of parameter updating is not to find the true parameters, but parameters such that predictions and observations match (pragmatic model property), the results of model updating can be used for magnet introspection, i.e. to gain insight into possible reasons that explain the observed differences between a numerical design model and a magnet system as built. For this application, as well as to ensure that the predictions of the updated model are also valid outside the regime of the training data, it is necessary that the updated model parameters are within physically reasonable ranges. In stochastic model updating with Bayesian inference, this consideration is automatically included via the prior distribution of the parameters. Third, according to [78, Section 3], stochastic model updating can help addressing the ill-posedness of an inverse problem by restating the problem in the space of probability distributions.

To apply stochastic model updating, the model parameters $\mathbf{p}$ and the model predictions $\mathbf{q}$ and the measured observations $\mathbf{q}^{\mathrm{obs}}$ are understood as realizations of random vectors $\mathbf{P}, \mathbf{Q}$ and $\mathbf{Q}^{\mathrm{obs}}$. With Bayesian inference, the conditional probability density of the random parameter vector $\mathbf{P}|\mathbf{Q}^{\mathrm{obs}}$ given observation data $\mathbf{q}^{\mathrm{obs}}$ is determined. Subsequently, properties of the corresponding distribution (e.g., expected value or covariance) can be explored, for example, with estimators or sampling methods such as the Metropolis-Hastings algorithm [28].

3.1 Stochastic setting

Basic definitions Let $(\Omega, \mathcal{F}, \mathbb{P})$ be a *probability space*, consisting of a sample space Ω, an event space $\mathcal{F}$ that is a σ-algebra on Ω and a probability measure $\mathbb{P} : \mathcal{F} \to \mathbb{R}$. For a more comprehensive introduction to the mathematical objects defined in this paragraph, the reader is referred to [18, 28, 78, 94]. An N-dimensional *random vector* is a measurable function $\mathbf{X} : \Omega \to \mathbb{R}^N$, vectors $\mathbf{X}(\omega) \in \mathbb{R}^N$ are called *realizations of* $\mathbf{X}$, and one-dimensional random vectors are called *random variables*. Notice that all concepts are more generally introduced for random vectors instead of random variables, since in the later applications, in Chapter 4 and Chapter 5, multi-dimensional parameter spaces are considered. The *expected value* $\mathbb{E}[\mathbf{X}]$, the *variance* $\mathrm{Var}[\mathbf{X}]$, and the *covariance* $\mathrm{Cov}(\mathbf{X})$ of a random vector $\mathbf{X}$ are defined by

$$\begin{aligned} \mathbb{E}[\mathbf{X}] &:= \int_\Omega \mathbf{X}(\omega)\, \mathrm{d}\mathbb{P} && (3.1)\\ \mathrm{Var}[\mathbf{X}] &:= \mathbb{E}[(\mathbf{X} - \mathbb{E}[\mathbf{X}])^2] && (3.2)\\ \mathrm{Cov}(\mathbf{X})_{n,m} &:= \mathbb{E}[(X_n - \mathbb{E}[X_n])(X_m - \mathbb{E}[X_m])]. && (3.3) \end{aligned}$$

Given a set of realizations $\{\mathbf{x}_1, \dots, \mathbf{x}_K\}$ of $\mathbf{X}$ the expected value and the covariance matrix can be estimated due to the Law of Large Numbers [28, Section 4.1] by the sample mean and the unbiased sample covariance

$$\begin{aligned} \widehat{\mathbf{m}} &:= \frac{1}{K}\sum_{k=1}^{K} \mathbf{x}_k && (3.4)\\ \widehat{\mathbf{C}} &:= \frac{1}{K-1}\sum_{k=1}^{K} (\mathbf{x}_k - \widehat{\mathbf{m}})(\mathbf{x}_k - \widehat{\mathbf{m}})^\top. && (3.5) \end{aligned}$$

The *probability distribution function* $\lambda_{\mathbf{X}}$ *of a random vector* $\mathbf{X}$ is a probability measure on the Borel σ-algebra $\mathfrak{B}$ such that

$$\lambda_{\mathbf{X}}(A) = \mathbb{P}(\mathbf{X}^{-1}(A)) \qquad \forall A \in \mathfrak{B}. \tag{3.6}$$

A function $\pi : \mathbb{R}^N \to \mathbb{R}$ that satisfies $\pi(\mathbf{x}) \geq 0$ and $\int_{\mathbb{R}^N} \pi(\mathbf{x})\, \mathrm{d}\mathbf{x} = 1$ is called a *probability density function*. If moreover a probability density function $\pi_{\mathbf{X}}$ satisfies

$$\lambda_{\mathbf{X}}(A) = \int_A \pi_{\mathbf{X}}(\mathbf{x})\, \mathrm{d}\mathbf{x} \qquad \forall A \in \mathfrak{B}, \tag{3.7}$$

then $\pi_{\mathbf{X}}$ is called a *probability density function of* $\mathbf{X}$. The *cumulative distribution function* $\phi_X : \mathbb{R} \to \mathbb{R}$ of a real-valued random variable X is defined by

$$\phi_X(x) := \int_{-\infty}^{x} \pi_X(x')\, \mathrm{d}x'. \tag{3.8}$$

Let $\mathbf{X} : \Omega \to \mathbb{R}^{N_1}, \mathbf{Z} : \Omega \to \mathbb{R}^{N_2}$ be two random vectors on the same sample space Ω. The *joint probability distribution* $\lambda_{\mathbf{XZ}}$ is defined by

$$\lambda_{\mathbf{XZ}}(A_1, A_2) = \mathbb{P}(\mathbf{X}^{-1}(A_1) \cap \mathbf{Z}^{-1}(A_2)) \qquad \forall A_1 \in \mathfrak{B}_1, A_2 \in \mathfrak{B}_2. \tag{3.9}$$

A non-negative function $\pi_{\mathbf{XZ}} : \mathbb{R}^{N_1} \times \mathbb{R}^{N_2} \to \mathbb{R}$ satisfying for all Borel sets $A_1 \in \mathfrak{B}_1, A_2 \in \mathfrak{B}_2$ that

$$\lambda_{\mathbf{XZ}}(A_1, A_2) = \int_{A_1 \times A_2} \pi_{\mathbf{XZ}}(\mathbf{x}, \mathbf{z})\, \mathrm{d}V(\mathbf{x}, \mathbf{z}) \tag{3.10}$$

is called *joint probability density of* $\mathbf{X}$ *and* $\mathbf{Z}$. The random vectors $\mathbf{X}$ and $\mathbf{Z}$ are called *independent* if

$$\pi_{\mathbf{XZ}}(\mathbf{x}, \mathbf{z}) = \pi_{\mathbf{X}}(\mathbf{x})\pi_{\mathbf{Z}}(\mathbf{z}). \tag{3.11}$$

For the two not necessarily independent random vectors $\mathbf{X}, \mathbf{Z}$ with joint probability density $\pi_{\mathbf{XZ}}$ the *marginal density of* $\mathbf{Z}$ is given by

$$\pi_{\mathbf{Z}}(\mathbf{z}) = \int_{\mathbb{R}^{N_1}} \pi_{\mathbf{XZ}}(\mathbf{x}, \mathbf{z}) \, \mathrm{d}V(\mathbf{x}) \tag{3.12}$$

and describes the probability of $\mathbf{Z}$ while $\mathbf{X}$ may take any value. Under the assumption $\pi_{\mathbf{Z}}(\mathbf{z}) \neq 0$, equation (3.12) can be rewritten as

$$\int_{\mathbb{R}^{N_1}} \frac{\pi_{\mathbf{XZ}}(\mathbf{x}, \mathbf{z})}{\pi_{\mathbf{Z}}(\mathbf{z})} \, \mathrm{d}V(\mathbf{x}) = 1. \tag{3.13}$$

Consequently, the integrand defines a probability density function $\pi_{\mathbf{X}|\mathbf{Z}}$ that is called *conditional probability density of* $\mathbf{X}$ *given* $\mathbf{Z}$

$$\pi_{\mathbf{X}|\mathbf{Z}}(\mathbf{x}|\mathbf{z}) = \frac{\pi_{\mathbf{XZ}}(\mathbf{x}, \mathbf{z})}{\pi_{\mathbf{Z}}(\mathbf{z})}. \tag{3.14}$$

Normal distribution An important example of a probability distribution that is used throughout this thesis is the multivariate Gaussian or normal distribution $\mathcal{N}(\mathbf{m}, \mathbf{\Sigma})$ with mean $\mathbf{m} \in \mathbb{R}^N$ and a covariance matrix $\mathbf{\Sigma} \in \mathbb{R}^{N \times N}$, which is is symmetric and positive definite [28, Section 3.2]. The corresponding probability density function of a random vector $\mathbf{X} \sim \mathcal{N}(\mathbf{m}, \mathbf{\Sigma})$ is given by

$$\pi_{\mathbf{X}}(\mathbf{x}) = \left(\frac{1}{(2\pi)^N \det(\mathbf{\Sigma})} \right)^{1/2} \exp\left(-\frac{1}{2} (\mathbf{x} - \mathbf{m})^\top \mathbf{\Sigma}^{-1} (\mathbf{x} - \mathbf{m}) \right). \tag{3.15}$$

By integration it can be verified that $\mathbb{E}[\mathbf{X}] = \mathbf{m}$ and $\mathrm{Cov}(\mathbf{X}) = \mathbf{\Sigma}$.

Given N mutually independent normal distributed random variables $X_1, \ldots, X_N$, it can be shown [28, Section 3.2] that the random vector $\mathbf{X} = (X_1, \ldots, X_N)$ is normal distributed.
To verify that a random variable is normal distributed, we conduct in Chapter 4 and Chapter 5 the Kolmogorov-Smirnov test [44] available in MATLAB® [130]. An overview of normality tests can be found in [41]. Given samples $x_1, \ldots, x_K$ of a real-valued random variable X and a cumulative distribution function ϕ, the two-sided Kolmogorov-Smirnov test compares ϕ to the empirical distribution function [44] defined by

$$h(x) \coloneqq \frac{1}{K} \#\left(\{ x_k \mid x_k \leq x \} \right), \tag{3.16}$$

where the operator $\#(\cdot)$ returns the cardinality of a set. The null hypothesis of the test is that $h = \phi$. The statistical test is defined by

$$T \coloneqq \sup_x |\phi(x) - h(x)|. \tag{3.17}$$

For a significance level $\alpha \in (0, 1)$ and dependent on the number of samples K, a value t can be looked up in Kolmogorov-Smirnov tables [116]. The null hypothesis is rejected if $T > t$. By inserting for ϕ the cumulative distribution function of the normal distribution

$$\phi(x) = \frac{1}{\sqrt{2\pi\sigma^2}} \int_{-\infty}^{x} \exp\left(-\frac{1}{2\sigma^2} (x - m)^2 \right) \, \mathrm{d}x, \tag{3.18}$$

the Kolmogorov-Smirnov test can be used to study if a set of samples $\{x_1, \ldots, x_K\}$ is normal distributed with $\mathcal{N}(m, \sigma^2)$.

Table 3.1: Overview of symbols and definitions to describe parameters, operation modes, and predictions and observations of quantities of interest.

symbol	meaning
$\mathcal{P} \subset \mathbb{R}^{N_1}$	parameter space
$\mathbf{P} : \Omega \to \mathcal{P}$	random parameter vector
$\mathbf{p} \in \mathcal{P}$	parameter vector, realization of $\mathbf{P}$
$\mathbf{Q} : \Omega \to \mathcal{Q}$	prediction of quantities of interest, $\mathbf{Q} = \mathcal{H}(\mathbf{P})$
$\mathbf{Q}^{\mathrm{obs}} : \Omega \to \mathcal{Q}$	observation of quantities of interest, $\mathbf{Q}^{\mathrm{obs}} = \mathcal{H}(\mathbf{P}) + \mathbf{U}$
$\mathbf{q} \in \mathcal{Q}$	realization of $\mathbf{Q}$
$\mathbf{q}^{\mathrm{obs}} \in \mathcal{Q}$	realization of $\mathbf{Q}^{\mathrm{obs}}$
$\mathbf{U} : \Omega \to \mathbb{R}^{N_2}$	random measurement uncertainty, $\mathbf{U} \sim \mathcal{N}(\mathbf{0}, \mathbf{\Sigma})$
$\mathbf{s}, \mathbf{s}_0 \in \mathcal{S} \subset \mathbb{R}^{N_3}$	operation modes
$\mathcal{M} : (\mathbf{p}, \mathbf{s}) \mapsto \mathbf{q}$ $\mathcal{M} : (\mathbf{P}, \mathbf{s}) \mapsto \mathbf{Q}$	system model
$\mathcal{H} : \mathbf{p} \mapsto \mathbf{q}$ $\mathcal{H} : \mathbf{P} \mapsto \mathbf{Q}$	forward model $\mathcal{M}(\cdot, \mathbf{s}_0) = \mathcal{H}(\cdot)$

Forward model A system model can be understood as a mapping

$$\begin{aligned} \mathcal{M} : \mathcal{P} \times \mathcal{S} &\to \mathcal{Q} \\ (\mathbf{p}, \mathbf{s}) &\mapsto \mathbf{q}, \end{aligned} \tag{3.19}$$

where $\mathcal{P}$ is a parameter space (e.g., parameters of a material curve, harmonic coefficients, boundary data), $\mathcal{S}$ is a space of operation modes (e.g., current excitations), and $\mathcal{Q}$ is the codomain of the system model (e.g., field maps, harmonics, field integrals). Generally, we can assume that the values that are taken by the parameters $\mathbf{p} \in \mathcal{P}$, the operation modes $\mathbf{s} \in \mathcal{S}$, and the predictions $\mathbf{q} \in \mathcal{Q}$ of the quantity of interest are real-valued vectors. A summary of the meaning of the symbols defined in this and the next paragraph is given in Table 3.1. In the stochastic setting, those vectors are modeled as random vectors that are affected by uncertainties according to the modeler's belief [28, Section 5]. In this work, we assume that the operation modes $\mathbf{s} \in \mathbb{R}^{N_3}$ are not affected by uncertainties while the predictions $\mathbf{q}$ and the parameters $\mathbf{p}$ are modeled as random vectors $\mathbf{P} : \Omega \to \mathcal{P} \subset \mathbb{R}^{N_1}$, $\mathbf{Q} : \Omega \to \mathcal{Q} \subset \mathbb{R}^{N_2}$ over a common sample space Ω. Fixing an operation mode $\mathbf{s}_0$ in the system model yields the forward model

$$\mathcal{H}(\mathbf{P}) \coloneqq \mathcal{M}(\mathbf{P}, \mathbf{s}_0) = \mathbf{Q} \tag{3.20}$$

that maps each random parameter vector $\mathbf{P}$ to a prediction $\mathbf{Q}$ of a quantity of interest. Notice that by abuse of notation, we use the same symbols $\mathcal{H}, \mathcal{M}$ to the random vectors $\mathbf{P}, \mathbf{Q}$ and their realizations $\mathbf{p}, \mathbf{q}$.

Noise model The random vector $\mathbf{Q} = \mathcal{H}(\mathbf{P})$ describes the prediction of a quantity of interest via the forward model given the random parameter vector $\mathbf{P}$. Using this model is based on the assumption that any randomness of $\mathbf{Q}$ is inherited from the randomness of $\mathbf{P}$ while other uncertainties of the model, e.g., due to inadequate knowledge of all relevant physical effects, are omitted.
If the quantity of interest can be measured with field transducers, there is along with the (simulated) prediction $\mathbf{Q} : \Omega \to \mathcal{Q}$ another random vector $\mathbf{Q}^{\text{obs}} : \Omega \to \mathcal{Q}$ that describes the (measured) observations of the same quantity of interest, i.e. measurement results $\mathbf{q}^{\text{obs}}$ are realizations of $\mathbf{Q}^{\text{obs}}$ [78, Section 3.1]. The two random vectors $\mathbf{Q}$ and $\mathbf{Q}^{\text{obs}}$ are referred to as comparable quantities in Figure 1.2. The randomness of $\mathbf{Q}^{\text{obs}}$ reflects the measurement uncertainty.
Different noise models to describe the conditional distribution of $\mathbf{Q}^{\text{obs}}$ given $\mathbf{P}$ can be found in the literature, e.g., [28, Section 5.2], [78, Section 3.2]. A popular noise model is the additive noise model

$$\mathbf{Q}^{\text{obs}} = \mathcal{H}(\mathbf{P}) + \mathbf{U} \tag{3.21}$$

where $\mathbf{U} : \Omega \to \mathbb{R}^{N_2}$ is a random vector that is independent of $\mathbf{P}$ and that describes the measurement uncertainty. Notice that the additive noise model omits errors and uncertainties of the forward model. Discussions on the determination of the distribution $\pi_{\mathbf{U}}$ of the measurement uncertainty $\mathbf{U}$ for rotating coil measurements of multipoles and for Hall probe mapper measurements of field maps can be found in [90]. In this work, we assume $\mathbf{U} \sim \mathcal{N}(\mathbf{0}, \mathbf{\Sigma})$.

Having a forward model, a noise model, and the measurement result $\mathbf{q}^{\text{obs}}$, the most likely model parameters $\mathbf{p} \in \mathbf{P}$ can be determined. This approach is known as maximum likelihood estimation [67, Section 2.3]. Bayesian inference exceeds this approach by deriving the distribution of $\mathbf{P}$ given $\mathbf{Q}^{\text{obs}} = \mathbf{q}^{\text{obs}}$ using the Bayes formula.

3.2 Bayesian inference

The conditional probability density of the random vector $\mathbf{Q}^{\text{obs}}|\mathbf{P}$ is given by

$$\pi_{\mathbf{Q}^{\text{obs}}|\mathbf{P}}(\mathbf{q}^{\text{obs}}|\mathbf{p}) = \frac{\pi_{\mathbf{Q}^{\text{obs}}\mathbf{P}}(\mathbf{q}^{\text{obs}}, \mathbf{p})}{\pi_{\mathbf{P}}(\mathbf{p})}. \tag{3.22}$$

Interchanging the roles of $\mathbf{Q}^{\text{obs}}$ and $\mathbf{P}$ and equating the two resulting expressions for $\pi_{\mathbf{Q}^{\text{obs}}\mathbf{P}}(\mathbf{q}^{\text{obs}}, \mathbf{p})$ yields

$$\pi_{\mathbf{Q}^{\text{obs}}\mathbf{P}}(\mathbf{q}^{\text{obs}}, \mathbf{p}) = \pi_{\mathbf{Q}^{\text{obs}}|\mathbf{P}}(\mathbf{q}^{\text{obs}}|\mathbf{p})\pi_{\mathbf{P}}(\mathbf{p}) = \pi_{\mathbf{P}|\mathbf{Q}^{\text{obs}}}(\mathbf{p}|\mathbf{q}^{\text{obs}})\pi_{\mathbf{Q}^{\text{obs}}}(\mathbf{q}^{\text{obs}}) \tag{3.23}$$

and thus the *Bayes formula*

$$\pi_{\mathbf{P}|\mathbf{Q}^{\text{obs}}}(\mathbf{p}|\mathbf{q}^{\text{obs}}) = \frac{\pi_{\mathbf{Q}^{\text{obs}}|\mathbf{P}}(\mathbf{q}^{\text{obs}}|\mathbf{p})\pi_{\mathbf{P}}(\mathbf{p})}{\pi_{\mathbf{Q}^{\text{obs}}}(\mathbf{q}^{\text{obs}})} \tag{3.24}$$

if $\pi_{\mathbf{Q}^{\text{obs}}}(\mathbf{q}^{\text{obs}}) \neq 0$. The marginal probability density $\pi_{\mathbf{Q}^{\text{obs}}}$ is independent of the realizations $\mathbf{p}$ and can be therefore interpreted as a normalizing constant that can be neglected. Thus, the Bayes formula can be rewritten as

$$\pi_{\mathbf{P}|\mathbf{Q}^{\text{obs}}}(\mathbf{p}|\mathbf{q}^{\text{obs}}) \propto \pi_{\mathbf{Q}^{\text{obs}}|\mathbf{P}}(\mathbf{q}^{\text{obs}}|\mathbf{p})\pi_{\mathbf{P}}(\mathbf{p}) \tag{3.25}$$

where the symbol $\propto$ indicates proportionality. The left-hand side is called the *posterior density function of* $\mathbf{P}$ and expresses the knowledge about $\mathbf{P}$ after observing $\mathbf{Q}^{\text{obs}} = \mathbf{q}^{\text{obs}}$. The conditional probability density of $\mathbf{Q}^{\text{obs}}$ given parameter realizations $\mathbf{p}$ of $\mathbf{P}$ can be viewed as a function $\mathbf{p} \mapsto \pi_{\mathbf{Q}^{\text{obs}}|\mathbf{P}}(\mathbf{q}^{\text{obs}}|\mathbf{p})$ called *likelihood*

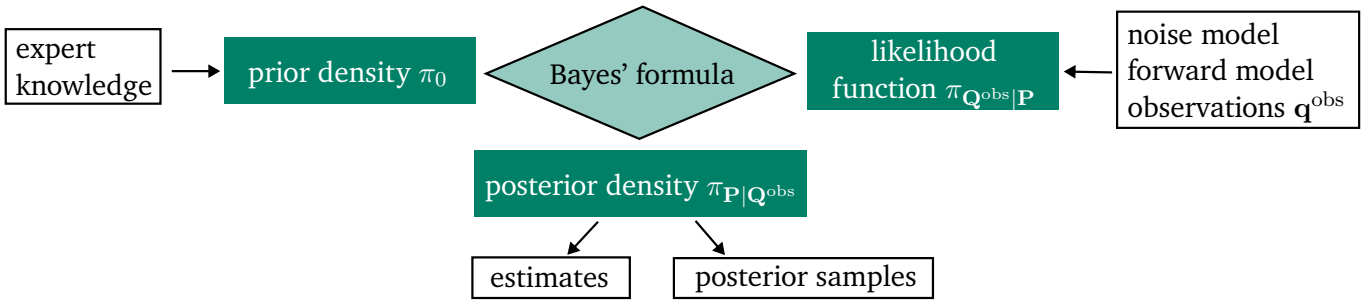

Figure 3.1: Overview of the Bayesian approach to inverse problems. Figure adapted from [29].

function [18, Section 1.2.3]. It describes the likelihood of the measurement result $\mathbf{Q}^{\text{obs}} = \mathbf{q}^{\text{obs}}$ given the realization $\mathbf{P} = \mathbf{p}$. The probability density function $\pi_{\mathbf{P}}$ is called *prior density* and expresses the expert knowledge on the unknown parameter $\mathbf{P}$ before the measurement. In this work, we also use the symbol π_0 to refer to prior densities.

Bayesian approach to inverse problems The Bayesian approach to inverse problems seeks the distribution of the random parameter vector $\mathbf{P}$ given observations $\mathbf{q}^{\text{obs}}$ of $\mathbf{Q}^{\text{obs}}$. This distribution is the posterior density function $\pi_{\mathbf{P}|\mathbf{Q}^{\text{obs}}}$ on the left-hand side of the Bayes formula (3.25). Figure 3.1 shows an overview of the approach. Following [78, Section 3.1], solving an inverse problem using Bayesian inference can be divided into three subtasks:

1. **Construction of a prior model.** Find a probability density function π_0 that reflects all prior information about $\mathbf{P}$. In this work, we gain this information from measurements of material specimens. For all of the studied applications, we verify with Kolmogorov-Smirnov tests the assumption that the prior distribution is given by $\mathcal{N}(\mathbf{m}_0, \mathbf{C}_0)$ for some $\mathbf{m}_0 \in \mathbb{R}^{N_1}$ and $\mathbf{C}_0 \in \mathbb{R}^{N_1 \times N_1}$.

2. **Construction of a likelihood model.** Find a likelihood function $\mathbf{p} \mapsto \pi_{\mathbf{Q}^{\text{obs}}|\mathbf{P}}(\mathbf{q}^{\text{obs}}|\mathbf{p})$. It can be constructed based on the forward model and the noise model. More details about the likelihood model used in this work are given in the following paragraph.

3. **Exploration of the posterior probability density.** If closed-form expressions of the posterior are available, estimators or statistical parameters such as the expected value and the variance can be computed. If no closed-form expression is available, we use Markov chain Monte Carlo sampling to draw samples of the posterior distribution and evaluate the sample mean and covariance.

Although the result of the Bayesian approach to an inverse problem is the posterior probability density $\pi_{\mathbf{P}|\mathbf{Q}^{\text{obs}}}$, a deterministic value $\mathbf{p}^{\text{up}}$ of the parameter vector can be derived subsequently for model updating, e.g., with estimators. Like the posterior distribution, the deterministic value $\mathbf{p}^{\text{up}}$ depends on both, the prior model and the likelihood model (including the noise model) and their assumed uncertainties, which weights their influence on $\pi_{\mathbf{P}|\mathbf{Q}^{\text{obs}}}$ and $\mathbf{p}^{\text{up}}$. The prior model ensures that samples of the posterior distribution are within a physically reasonable range, which is important for using the updated model for magnet introspection and predictions outside the regime of training data. The likelihood model ensures that the derived parameter vector $\mathbf{p}^{\text{up}}$ actually leads to a model update, in the sense of the definition in [145], by ensuring that there is an improvement of the predictions with the updated model on the regime of the training data.

Likelihood model Consider the forward model $\mathcal{H} : \mathbf{P} \to \mathbf{Q}$ and the additive noise model $\mathbf{Q}^{\text{obs}} = \mathcal{H}(\mathbf{P}) + \mathbf{U}$ with $\mathbf{U} \sim \mathcal{N}(\mathbf{0}, \boldsymbol{\Sigma})$ and let $\mathbf{U}$ be independent of $\mathbf{P}$. Due to the independence, we have $\pi_{\mathbf{U}|\mathbf{P}} = \pi_{\mathbf{U}}$. If $\mathbf{P} = \mathbf{p}$ is fixed, the randomness of $\mathbf{Q}^{\text{obs}}$ is only inherited from $\mathbf{U}$ according to the additive noise model. This yields the equation

$$\pi_{\mathbf{Q}^{\text{obs}}|\mathbf{P}}(\mathbf{q}^{\text{obs}}|\mathbf{p}) = \pi_{\mathbf{U}}(\mathbf{q}^{\text{obs}} - \mathcal{H}(\mathbf{p})). \tag{3.26}$$

Consequently, $\mathbf{Q}^{\text{obs}}|\mathbf{P} \sim \mathcal{N}(\mathcal{H}(\mathbf{p}), \boldsymbol{\Sigma})$ with likelihood function

$$\pi_{\mathbf{Q}^{\text{obs}}|\mathbf{P}}(\mathbf{q}^{\text{obs}}|\mathbf{p}) = \left(\frac{1}{(2\pi)^{N_2}\det(\boldsymbol{\Sigma})}\right)^{1/2} \exp\left(-\frac{1}{2}(\mathbf{q}^{\text{obs}} - \mathcal{H}(\mathbf{p}))^\top \boldsymbol{\Sigma}^{-1}(\mathbf{q}^{\text{obs}} - \mathcal{H}(\mathbf{p}))\right). \tag{3.27}$$

Posterior density for linear forward models In case of a linear forward model $\mathcal{H}\mathbf{p} = \mathbf{q}$, a Gaussian likelihood function (3.27) and a Gaussian prior distribution $\mathcal{N}(\mathbf{m}_0, \mathbf{C}_0)$, the posterior density function $\pi_{\mathbf{P}|\mathbf{Q}^{\text{obs}}}$ is also Gaussian distributed [18, Section 2.3.3]. Rearranging the terms on the right-hand side of equation (3.25) yields $\pi_{\mathbf{P}|\mathbf{Q}^{\text{obs}}} \sim \mathcal{N}(\mathbf{m}_1, \mathbf{C}_1)$ [28, Section 8.4], [78, Theorem 3.7] with

$$\mathbf{m}_1 = \mathbf{C}_1\left(\mathcal{H}^\top\boldsymbol{\Sigma}^{-1}\mathbf{q}^{\text{obs}} + \mathbf{C}_0^{-1}\mathbf{m}_0\right), \tag{3.28}$$

$$\mathbf{C}_1 = \left(\mathcal{H}^\top\boldsymbol{\Sigma}^{-1}\mathcal{H} + \mathbf{C}_0^{-1}\right)^{-1}. \tag{3.29}$$

The closed-form expression of the posterior density function is

$$\begin{aligned}\pi_{\mathbf{P}|\mathbf{Q}^{\text{obs}}}(\mathbf{p}|\mathbf{q}^{\text{obs}}) = \; & \left(\tfrac{1}{(2\pi)^{N_1}\det(\mathbf{C_1})}\right)^{1/2} \\ & \exp\left(-\tfrac{1}{2}\left(\mathbf{p} - \mathbf{C}_1\left(\mathcal{H}^\top\boldsymbol{\Sigma}^{-1}\mathbf{q}^{\text{obs}} + \mathbf{C}_0^{-1}\mathbf{m}_0\right)\right)^\top \mathbf{C}_1^{-1}\left(\mathbf{p} - \mathbf{C}_1\left(\mathcal{H}^\top\boldsymbol{\Sigma}^{-1}\mathbf{q}^{\text{obs}} + \mathbf{C}_0^{-1}\mathbf{m}_0\right)\right)\right).\end{aligned} \tag{3.30}$$

The next section focuses on the exploration of the posterior density by computing estimators and by drawing samples of the distribution. These techniques are particularly relevant to gain information about the posterior distribution if no closed-form expression such as in the linear case (3.30) is available.

3.3 Exploring the posterior distribution

Having the posterior density, we are interested in exploring its stochastical properties such as the expected value and covariance, or we want to retrieve a deterministic value $\mathbf{p}^{\text{up}}$ for insertion into the forward model for predictions. In the literature, many methods to explore the posterior distribution can be found:

- **Sampling methods.** An overview of sampling methods such as Markov chain Monte Carlo sampling or rejection sampling is given in [18, Section 11].
- **Estimators,** such as the maximum a posteriori estimate. A collection of useful estimators can be found in [78, Section 3.1.1].
- **Bayesian filtering**, e.g., using the ensemble Kalman filter [67, Section 3].
- **Approximate inference** [18, Section 10] that is based on analytical approximations of the posterior distribution, such as variational inference [18, Section 10.1], which minimizes the Kullback-Leibler divergence between the posterior distribution and its approximation.

In this work, we use the maximum a posteriori estimate for linear forward models to explore the posterior distribution. In the case of non-linear forward models, we use Markov chain Monte Carlo sampling based on the Metropolis-Hastings algorithm with the preconditioned Crank-Nicolson proposal, because it admits an easily implementable algorithm that requires only one evaluation of the forward model per step [28].

3.3.1 Estimators

The application of point estimators is particularly interesting for stochastic model updating when a deterministic value $\mathbf{p}^{\mathrm{up}}$ has to be retrieved from the posterior distribution for insertion into a deterministic numerical model. A popular point estimator is the *maximum a posteriori estimate* $\mathbf{p}_{\mathrm{MAP}}$ defined by

$$\mathbf{p}_{\mathrm{MAP}} \coloneqq \arg\max_{\mathbf{p}\in\mathcal{P}} \pi_{\mathbf{P}|\mathbf{Q}^{\mathrm{obs}}}(\mathbf{p}|\mathbf{q}^{\mathrm{obs}}), \tag{3.31}$$

provided that a maximizer exists. Notice that this estimate might not be unique. The maximum a posteriori estimate answers the question "*Given the data* $\mathbf{q}^{\mathrm{obs}}$ *and the prior, what is the most probable value of* $\mathbf{P}$*?*" [78, Section 3.1.1]. The *maximum likelihood estimate* $\mathbf{p}_{\mathrm{ML}}$ maximizes the likelihood function instead of the posterior density function

$$\mathbf{p}_{\mathrm{ML}} \coloneqq \arg\max_{\mathbf{p}\in\mathcal{P}} \pi_{\mathbf{Q}^{\mathrm{obs}}|\mathbf{P}}(\mathbf{q}^{\mathrm{obs}}|\mathbf{p}). \tag{3.32}$$

Although the definitions of the maximum a posteriori estimate and the maximum likelihood estimate read similar, the underlying ideas differ. While the maximum a posteriori estimate considers the parameters as a random vector and seeks the most probable realization given the data $\mathbf{q}^{\mathrm{obs}}$, the maximum likelihood estimate is a non-Bayesian estimator that seeks the (not necessarily random) parameters that are the most likely to produce the data $\mathbf{q}^{\mathrm{obs}}$ [67, Section 2.3], [78, Section 3.1.1].

Inserting the likelihood function (3.27) into the definition of the maximum likelihood estimate yields

$$\mathbf{p}_{\mathrm{ML}} = \arg\min_{\mathbf{p}\in\mathcal{P}} \left\| \mathbf{q}^{\mathrm{obs}} - \mathcal{H}(\mathbf{p}) \right\|^2_{\boldsymbol{\Sigma}^{-1}}. \tag{3.33}$$

Analogously, inserting the posterior density (3.25) with the Gaussian likelihood function (3.27) and the Gaussian prior distribution $\mathcal{N}(\mathbf{m}_0, \mathbf{C}_0)$ into the maximum a posteriori estimate yields

$$\mathbf{p}_{\mathrm{MAP}} = \arg\min_{\mathbf{p}\in\mathcal{P}} \left(\left\| \mathbf{q}^{\mathrm{obs}} - \mathcal{H}(\mathbf{p}) \right\|^2_{\boldsymbol{\Sigma}^{-1}} + \|\mathbf{p} - \mathbf{m}_0\|^2_{\mathbf{C}_0^{-1}} \right). \tag{3.34}$$

Consequently, the prior translates to a regularization functional, and using the maximum a posteriori estimate instead of the maximum likelihood estimate is equivalent to performing a Tikhonov regularization [28, Section 7.2]. In the case of the linear forward model with the posterior density function (3.30) the maximum a posteriori estimate is given by

$$\mathbf{p}_{\mathrm{MAP}} = \arg\min_{\mathbf{p}\in\mathcal{P}} \left\| \mathbf{p} - \mathbf{C}_1 \left(\mathcal{H}^{\top}\boldsymbol{\Sigma}^{-1}\mathbf{q}^{\mathrm{obs}} + \mathbf{C}_0^{-1}\mathbf{m}_0 \right) \right\|^2_{\mathbf{C}_1^{-1}} \tag{3.35}$$

and thus the maximum a posteriori estimate in the linear case is given by the expected value of the posterior distribution [78, Section 3.4].

Besides point estimators, spread estimators such as the conditional covariance or the Bayesian credibility set can be used to gain insight into the posterior distribution [28, Section 3.1.1].

3.3.2 Markov chain Monte Carlo sampling

Given the posterior probability density $\pi_{\mathbf{P}|\mathbf{Q}^{\text{obs}}}$ and its corresponding posterior distribution $\lambda_{\mathbf{P}|\mathbf{Q}^{\text{obs}}}$, the goal of Markov chain Monte Carlo sampling is the definition of a Markov chain whose states are samples of $\pi_{\mathbf{P}|\mathbf{Q}^{\text{obs}}}$. Based on these samples, statistical quantities such as the sample mean and the sample covariance can be determined using equations (3.4) and (3.5).
First, we briefly give an overview of useful definitions and technical details regarding Markov chains. For a more comprehensive introduction, the reader is referred to [18, 67, 78]. Subsequently, the Metropolis-Hastings algorithm [12, 28, 67, 78] in combination with the preconditioned Crank-Nicolson proposal [28, 37] are explained as one example of defining and implementing a suitable Markov chain.

Markov chain fundamentals A *time-discrete stochastic process* $\{\mathbf{X}_0, \mathbf{X}_1, \mathbf{X}_2, \dots\}$ is an ordered set of random vectors $\mathbf{X}_i : \Omega \to \mathbb{R}^N$, $i \geq 0$. The process is called *Markov chain* if

$$\mathbb{P}(\mathbf{X}_{i+1} \in A \mid \mathbf{X}_i = \mathbf{x}_i, \dots, \mathbf{X}_0 = \mathbf{x}_0) = \mathbb{P}(\mathbf{X}_{i+1} \in A \mid \mathbf{X}_i = \mathbf{x}_i) \tag{3.36}$$

for all Borel sets $A \in \mathfrak{B}$. Thus, the probability of the future state of a Markov chain only depends on the current state. A *probability transition kernel* is a mapping $K : \mathbb{R}^N \times \mathfrak{B} \to [0, 1]$ such that for all $A \in \mathfrak{B}$ the mapping $\mathbf{x} \mapsto K(\mathbf{x}, A)$ is a measurable function, and for all $\mathbf{x} \in \mathbb{R}^N$ the mapping $A \mapsto K(\mathbf{x}, A)$ is a probability distribution. A Markov chain is called *time homogeneous with transition kernel K* if there is a probability transition kernel K such that

$$\mathbb{P}(\mathbf{X}_{i+1} \in A \mid \mathbf{X}_i = \mathbf{x}_i) = K(\mathbf{x}_i, A) \tag{3.37}$$

for all $i \geq 0$. Thus, the transition probability is the same for all time steps i. The i-th iterate of the chain starting at $\mathbf{x}_0$ is defined as $K^i(\mathbf{x}_0, A) = \mathbb{P}(\mathbf{X}_n \in A \mid \mathbf{X}_0 = \mathbf{x}_0)$. The transition kernel K is called *λ-irreducible* for a probability distribution λ on $\mathfrak{B}$, if for all $\mathbf{x} \in \mathbb{R}^N$ and all sets $A \in \mathfrak{B}$ with $\lambda(A) > 0$, there is an integer $i \geq 1$ such that $K^i(\mathbf{x}_0, A) > 0$. Thus, the Markov chain generated by the transition kernel K will visit any set of non-zero measure with a positive probability, regardless of the starting point $\mathbf{x}_0$. A λ-irreducible transition kernel K is called *periodic* if there is an integer $I \geq 2$ and disjoint sets $A_1, \dots, A_I \in \mathfrak{B}$ with non-zero measure such that for all $\mathbf{x} \in A_i$ with $i \leq I - 1$ we have $K(\mathbf{x}, A_{i+1}) = 1$ and $K(\mathbf{x}, A_1) = 1$ for all $\mathbf{x} \in \mathbf{A}_I$. Thus, the Markov chain remains in a loop. Otherwise, the kernel K is called *aperiodic*. A probability distribution λ is called *invariant* or *stationary* distribution of a Markov chain with kernel K if

$$\lambda(A) = \int_{\mathbb{R}^N} K(\mathbf{x}, A)\lambda(\mathbf{x}) \, \mathrm{d}\mathbf{x} \tag{3.38}$$

for all $A \in \mathfrak{B}$. It can be shown [67, Lemma 2.1] that a distribution λ whose density function π satisfies the *detailed balance equation*

$$\pi(\mathbf{x})k(\mathbf{x}, \mathbf{y}) = \pi(\mathbf{y})k(\mathbf{y}, \mathbf{x}) \tag{3.39}$$

is a stationary distribution of a Markov chain with kernel K. In this case, the density function π is called *invariant density*. Thereby, $k : \mathbb{R}^N \times \mathbb{R}^N \to \mathbb{R}$ is a density function, called *transition kernel density* that satisfies for all $A \in \mathfrak{B}$

$$K(\mathbf{x}, A) = \int_A k(\mathbf{x}, \mathbf{y}) \, \mathrm{d}\mathbf{y}. \tag{3.40}$$

To draw samples of the posterior distribution $\lambda_{\mathbf{P}|\mathbf{Q}^{\text{obs}}}$ using a Markov chain, we are particularly interested in $\lambda_{\mathbf{P}|\mathbf{Q}^{\text{obs}}}$-irreducible and aperiodic Markov chains with a transition kernel K for which $\lambda_{\mathbf{P}|\mathbf{Q}^{\text{obs}}}$ is invariant

because it can be shown that under these conditions, the distribution of the Markov chain converges to $\lambda_{\mathbf{P}|\mathbf{Q}^{\text{obs}}}$ [78, Proposition 3.11], i.e.

$$\lim_{i\to\infty} K^i(\mathbf{x}_0, A) = \lambda_{\mathbf{P}|\mathbf{Q}^{\text{obs}}}(A) \tag{3.41}$$

for all $\mathbf{x}_0 \in \mathbb{R}^N$ and all Borel sets $A \in \mathfrak{B}$. Thus, the samples $\mathbf{X}_i$ generated by the iterations of the Markov chain with transition kernel K are samples of the posterior distribution $\lambda_{\mathbf{P}|\mathbf{Q}^{\text{obs}}}$ for i sufficiently large.

There are different possibilities to define a transition kernel K for which the posterior distribution $\lambda_{\mathbf{P}|\mathbf{Q}^{\text{obs}}}$ is invariant. Each choice leads to a different Markov chain Monte Carlo sampling method, such as the Gibbs sampler [12, 78] or the Metropolis-Hastings algorithm [12, 28, 67, 78], which is based on the definition of a kernel density function k that satisfies the detailed balance equation (3.39).

Metropolis-Hastings algorithm Let $l : \mathbb{R}^N \times \mathbb{R}^N \to \mathbb{R}^+$ be a transition kernel density, called *proposal density*, with $\int_{\mathbb{R}^N} l(\mathbf{x}, \mathbf{y})\, \mathrm{d}\mathbf{y} = 1$ for all $\mathbf{x} \in \mathbb{R}^N$. For now, we assume that l is given, common choices to define l are discussed below. If the proposal density l satisfies the detailed balance equation (3.39), we are done by setting $k = l$. Otherwise, we define

$$\alpha(\mathbf{x}, \mathbf{y}) \coloneqq \min\left\{1, \frac{\pi(\mathbf{y})l(\mathbf{y}, \mathbf{x})}{\pi(\mathbf{x})l(\mathbf{x}, \mathbf{y})}\right\} \tag{3.42}$$

and obtain by setting $k(\mathbf{x}, \mathbf{y}) = \alpha(\mathbf{x}, \mathbf{y})l(\mathbf{x}, \mathbf{y})$ a transition kernel density that satisfies the detailed balance equation (3.39) [28, Section 11.2.2]. To draw samples $\mathbf{x}_i$ using the Metropolis-Hastings algorithm, the following steps are to be conducted [12, 28, 78]:

1. Initialize with a point $\mathbf{x}_0 \in \mathbb{R}^N$. Since the Markov chain is supposed to be irreducible, the choice of the initialization point is arbitrary. However, if available, prior knowledge can be included, e.g., by choosing the expected value of the prior density as the initialization point. Set $i = 1$.
2. Draw a sample $\tilde{\mathbf{x}}$ of the proposal density $l(\mathbf{x}_{i-1}, \tilde{\mathbf{x}})$. Accept $\tilde{\mathbf{x}}$ by setting $\mathbf{x}_i \coloneqq \tilde{\mathbf{x}}$ with probability $\alpha(\mathbf{x}_{i-1}, \tilde{\mathbf{x}})$. Else, set $\mathbf{x}_i \coloneqq \mathbf{x}_{i-1}$.
3. Set $i = i + 1$. Return to step 2.

Due to the possibility of rejecting proposed samples, the resulting set of samples $\{\mathbf{x}_i\}_i$ can contain repetitions. These repetitions reflect the importance of the sample [28]. To only consider the samples that are drawn when the Markov chain already reached the stationary distribution, the first bunch of samples, referred to as *burn-in* is usually neglected. Further criteria to assess the quality of a Metropolis-Hastings sample set are discussed in [28, Section 11.2.3]. It can be shown [78, Proposition 3.12] that the transition kernel that corresponds to l has to satisfy the same conditions of aperiodicity and π-irreducibility as K to guarantee that the samples generated with the Metropolis-Hastings are samples of π.
Depending on the choice of the proposal density l, different versions of the Metropolis-Hastings algorithm can be defined: If l is chosen symmetric with $l(\mathbf{x}, \mathbf{y}) = l(\mathbf{y}, \mathbf{x})$ the Metropolis algorithm is obtained that immediately accepts the drawn sample $\tilde{\mathbf{x}}$ if it has a higher probability than the current sample $\mathbf{x}_{i-1}$ and sometimes moves to samples with lower probability depending on the probability ratio. Independence Metropolis-Hastings algorithms such as the randomize-then-optimize Metropolis-Hastings algorithm [12, Section 6.3.3] use proposal densities that are independent of the current state $l(\mathbf{x}, \mathbf{y}) = l(\mathbf{x})$. Adaptive Metropolis-Hastings algorithms update the proposal density based on the history of the Markov chain [12]. In this work, we use the preconditioned Crank-Nicolson proposal [28, 37] because it admits an easy and illustrative simplification of the acceptance probability α. Compared to the independence proposal that is used in the randomize-then-optimize Metropolis-Hastings algorithm [12, Section 6.3.3], the Crank-Nicolson proposal requires solely one

evaluation of the forward model $\mathcal{H}$ per iteration i. We apply the Metropolis-Hastings algorithm in Chapter 4 and Chapter 5.

Preconditioned Crank-Nicolson proposal In this work, we assume that the prior distribution is Gaussian with $\mathcal{N}(\mathbf{m}_0, \mathbf{C}_0)$ for some $\mathbf{m}_0 \in \mathbb{R}^{N_1}$ and $\mathbf{C}_0 \in \mathbb{R}^{N_1 \times N_1}$. The preconditioned Crank-Nicolson proposal [28, 37] is defined by

$$l(\mathbf{x}, \mathbf{y}) \sim \mathcal{N}(\sqrt{1-s^2}\mathbf{x}, s\mathbf{C}_0) \tag{3.43}$$

where $s \in (0,1)$ is a real parameter, called *step size*. Inserting into the acceptance probability (3.42) for π the posterior density function $\pi_{\mathbf{P}|\mathbf{Q}^{\text{obs}}}$ and for l the Crank-Nicolson proposal yields

$$\alpha(\mathbf{p}_{i-1}, \tilde{\mathbf{p}}) = \min\left\{1, \frac{\exp\left(-\frac{1}{2}\left\|\mathcal{H}(\tilde{\mathbf{p}}) - \mathbf{q}^{\text{obs}}\right\|^2_{\mathbf{\Sigma}^{-1}}\right)\exp(\langle\tilde{\mathbf{p}}, \mathbf{m}_0\rangle_{\mathbf{C}_0^{-1}})}{\exp\left(-\frac{1}{2}\left\|\mathcal{H}(\mathbf{p}_{i-1}) - \mathbf{q}^{\text{obs}}\right\|^2_{\mathbf{\Sigma}^{-1}}\right)\exp(\langle\mathbf{p}_{i-1}, \mathbf{m}_0\rangle_{\mathbf{C}_0^{-1}})}\right\}. \tag{3.44}$$

If we can further assume that the prior density has zero mean, i.e. by applying the translation $\mathbf{p} - \mathbf{m}_0$, the acceptance probability further simplifies to

$$\alpha(\mathbf{p}_{i-1}, \tilde{\mathbf{p}}) = \min\left\{1, \frac{\exp\left(\frac{1}{2}\left\|\mathcal{H}(\mathbf{p}_{i-1}) - \mathbf{q}^{\text{obs}}\right\|^2_{\mathbf{\Sigma}^{-1}}\right)}{\exp\left(\frac{1}{2}\left\|\mathcal{H}(\tilde{\mathbf{p}}) - \mathbf{q}^{\text{obs}}\right\|^2_{\mathbf{\Sigma}^{-1}}\right)}\right\}. \tag{3.45}$$

Notice that in the last equation, we also flipped the numerator and the denominator by omitting the signs within the exponential function. The proposal $\tilde{\mathbf{p}}$ is immediately accepted if the likelihood is higher than the likelihood of the current state $\mathbf{p}_{i-1}$. Moreover, it can be also accepted if the likelihood is lower. In this case, the acceptance probability depends on the ratio of the two likelihoods.
The only remaining choice to implement the Metropolis-Hastings algorithm, is the choice of the step size s. This parameter influences the acceptance rate of the Metropolis-Hastings algorithm that should be according to [28, Section 11.4] below or around 50%, and optimally between 20% and 30% [28, Section 11.2.3]. For high dimensions N_1 of the parameter space $\mathcal{P} \subset \mathbb{R}^{N_1}$ this acceptance rate typically results in a small step size s such that many samples are required. Consequently, the method may become computationally expensive as for each sample $\mathbf{p}_i$ the forward model $\mathcal{H}$ has to be evaluated on the proposal $\tilde{\mathbf{p}}$ to determine the acceptance probability with equation (3.44) or equation (3.45).

3.4 Summary

In this chapter, we introduced statistical fundamentals and methods for stochastic model updating. Thereby, parameters and observations were modeled as random vectors and related via a forward model and an additive noise model. For stochastic model updating, we were interested in determining the posterior distribution of the parameters given an observation. Thus, not only deterministic solution parameters can be estimated but also their uncertainty can be quantified. The key to finding the posterior distribution was Bayes' formula. It combines prior knowledge about the parameters with a likelihood model, that is based on the forward model, the additive noise model, and observations. Different strategies, e.g., the maximum a posteriori estimator and the Metropolis-Hastings algorithm, which is a Markov chain Monte Carlo sampler, were introduced to explore the posterior distribution. These methods will be applied in the following chapters to find stochastic updates of the parameters of a $B(H)$-curve model of an iron-dominated magnet and the magnetization parameters of the permanent magnet blocks in a Halbach magnet.

4 Update of the B(H)-curve of iron-dominated magnets

Component-centric system models of iron-dominated magnets depend on the yoke material's $B(H)$-curve. In this chapter, we combine a first principle-based FEM model of an accelerator magnet with data of material measurements of the yoke material, and data of measurable field-related quantities of interest to update the $B(H)$-curve of the system model. The goal is to obtain an updated model that correctly predicts the field-related quantities of interest on which it is trained, and that allows reliable field predictions for operation modes not considered in the training data. Parts of the results discussed in this chapter are published in the author's paper [53]. For simplification, we neglect hysteresis, anisotropy, and non-homogeneity and restrict our analysis to magnetostatic fields in this thesis.

System model In Chapter 3, a system model is abstractly described with the mapping (3.19)

$$\mathcal{M} : (\mathbf{p}, \mathbf{s}) \mapsto \mathbf{q}, \tag{4.1}$$

where $\mathbf{p}$ describes parameters, $\mathbf{s}$ describes operation modes and $\mathbf{q}$ is a prediction of a quantity of interest. Parameters and operation modes are both inputs of the system model. We distinguish between parameters that are the variables of the design and the prototype phase, and operation modes are the variables of the operation phase. In the case of normal conducting iron-dominated accelerator magnets, typical parameters are the yoke material and the magnet geometry (e.g., yoke shape, source position, number of turns). A typical operation mode is the excitation current. Only constant current excitations are considered since we restrict the study to magnetostatic fields. Typical quantities of interest in magnetostatics are for example evaluations of the magnetic flux density at certain points, integrated fields, or the multipole coefficients defined in equation (2.80). The prediction $\mathbf{q}$ of these quantities of interest can be derived from the parameters $\mathbf{p}$ and operation modes $\mathbf{s}$ by applying the methods introduced in Chapter 2.

In this chapter, we consider an example inspired by the magnet system "PXMBHGGHWC-OR000113" depicted in Figure 4.1, which was built in 1963 and used at the Proton Synchrotron at CERN. In 2015, it was refurbished to be re-used. It is an H-shaped dipole with a gap height of $170\,\mathrm{mm}$ and $N_{\mathbf{J}} = 180$ turns per coil. For current excitations of $600\,\mathrm{A}$, it provides a magnetic flux density of $1.5\,\mathrm{T}$ in the center of the air gap. A 2D sketch of the domain D including the source domain $D_{\mathbf{J}}$, the air domain D_{a} and the iron domain D_{i} is shown in Figure 4.1. Notice that the boundary ∂D is chosen far enough from the iron and the source domain such that $\partial D = \Gamma_{\mathrm{B}}$ and $\mathbf{B} \cdot \mathbf{n} = 0$ on Γ_{B} can be assumed. We further assume that the geometry is well enough known from drawings, such that the parameters reduce to the $B(H)$-curve or respectively its inverse, the $H(B)$-curve of the yoke material.

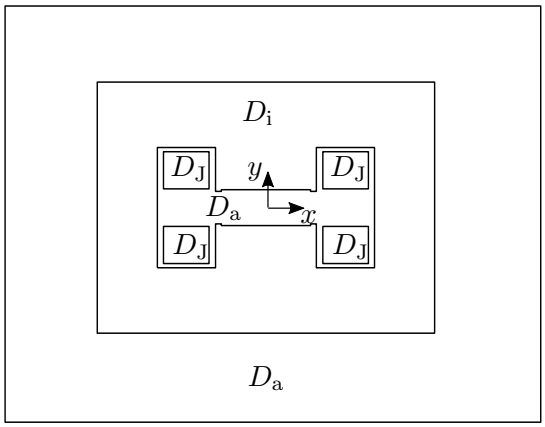

Figure 4.1: Left: "PXMBHGGHWC-OR000113" dipole magnet. Right: Sketch of the corresponding two-dimensional domain D with source domain D_J, air domain D_a and iron domain D_i. Figure adapted from [53]

The central field in the example magnet system is simulated by solving the weak formulation of the two-dimensional boundary value problem of magnetostatics in vector potential formulation on D introduced in Section 2.2.2: Given a source current density $\mathbf{J}$ and a reluctivity function $\nu : D \times \mathbb{R}_0^+ \to \mathbb{R}^+$

$$\nu(\mathbf{x}, t) = \begin{cases} \nu_0 & \mathbf{x} \in D_\mathrm{a} \\ \nu_\mathrm{i}(t) = f_\mathrm{HB}(t)/t & \mathbf{x} \in D_\mathrm{i}, \end{cases} \tag{4.2}$$

find $\mathbf{A} \in \mathcal{V}$ such that

$$\int_D \operatorname{curl} \mathbf{v} \cdot \nu(\|\operatorname{curl} \mathbf{A}\|) \operatorname{curl} \mathbf{A} \, \mathrm{d}V = \int_D \mathbf{v} \cdot \mathbf{J} \, \mathrm{d}V \tag{4.3}$$

for all $\mathbf{v} \in \mathcal{V}$. This problem is numerically solved using the FEM software GetDP [60]. Thereby, the 2D conductor model described in Section 2.3.2 is used to define $\mathbf{J}$. If the non-linear $H(B)$-curve defining the reluctivity function ν_i satisfies the properties given in Assumption 1, a unique solution to (4.3) exists, and thus there is a well-defined mapping

$$\nu_\mathrm{i} \mapsto \mathbf{A}[\nu_\mathrm{i}]. \tag{4.4}$$

Quantities of interest Quantities of interest such as evaluations of the magnetic flux density at certain points and multipole coefficients can be mathematically described as linear functionals $Q : \mathcal{V} \to \mathbb{R}$ of the form

$$Q(\mathbf{A}) \coloneqq \int_{D_\mathrm{obs}} q_1(\mathbf{A}) + q_2(\operatorname{curl} \mathbf{A}) \, \mathrm{d}V \tag{4.5}$$

with linear functionals $q_1, q_2 : \mathcal{V} \to \mathbb{R}$ and an observation domain $D_\mathrm{obs} \subset D$ [117, Section 4.1]. Since the mapping (4.4) is well-defined, we can similarly introduce a well-defined mapping

$$\widehat{Q} : \nu_\mathrm{i} \mapsto Q[\mathbf{A}[\nu_\mathrm{i}]]. \tag{4.6}$$

The quantities of interest that are studied in the following are the $B_y(\mathbf{x})$ component of the magnetic flux density evaluated at a position $\mathbf{x} \in D_\mathrm{a}$ and the normal multipole coefficients $B_n(r_0)$, defined in equation (2.80), on a reference radius r_0. The functional Q_B of the *field map quantity of interest* is given by

$$Q_\mathrm{B}(\mathbf{A}) \coloneqq Q_\mathrm{B}(\mathbf{A})(\mathbf{x}) \coloneqq B_y(\mathbf{x}) = \int_{\{\mathbf{x}\}} \mathrm{pr}_y(\operatorname{curl} \mathbf{A}) \, \mathrm{d}V \tag{4.7}$$

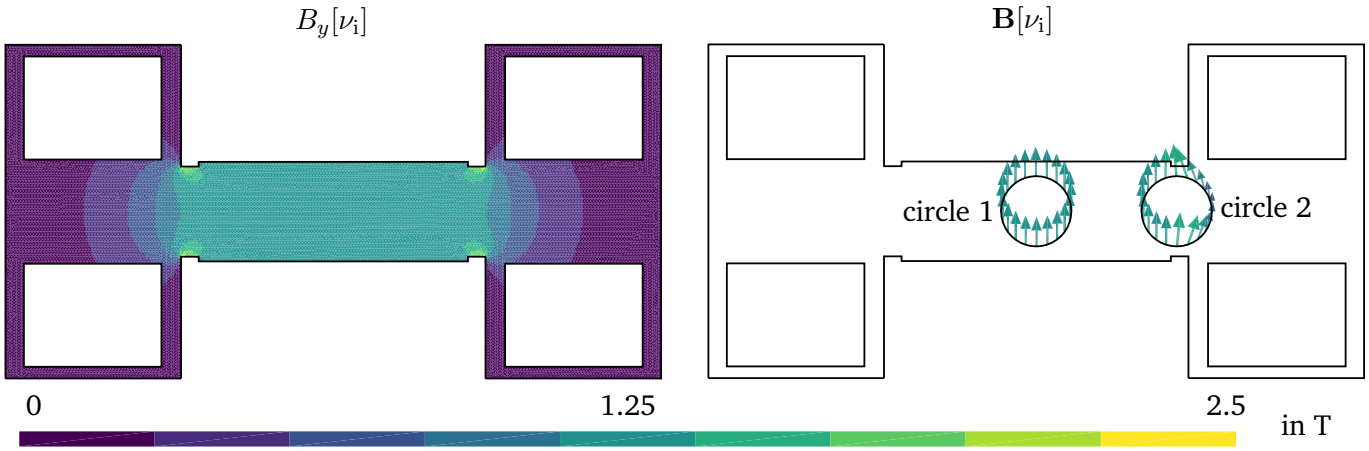

Figure 4.2: Magnetic flux density $\mathbf{B}[\nu_\mathrm{i}]$ for the excitation current $I = 500\,\mathrm{A}$. Left: B_y evaluated on the inner air domain. Right: $\mathbf{B}$ evaluated on circles with radius $r_0 = 6\,\mathrm{cm}$.

where $\mathrm{pr}_y : \mathbb{R}^3 \to \mathbb{R}$ is the projection on the y-component. The functional $Q_{\mathrm{M},n}$ of the *multipole coefficient quantity of interest* is given by

$$Q_{\mathrm{M},n}(\mathbf{A}) \coloneqq B_n(r_0) = \int_0^{2\pi} \frac{1}{\pi} \mathrm{pr}_r(\operatorname{curl} \mathbf{A}(r_0, \theta)) \sin(n\theta)\, \mathrm{d}\theta \tag{4.8}$$

where $\mathrm{pr}_r : \mathbb{R}^3 \to \mathbb{R}$ is the projection on the radial component and $\theta \in [0, 2\pi]$ is the parametrization of the observation domain D_obs that is given by a reference circle with radius r_0 in D_a. Notice that both functionals Q_B and $Q_{\mathrm{M},n}$ are linear because the projections pr_y and pr_r are linear.

The concatenation of the boundary value problem of magnetostatics with a quantity of interest Q yields the system model (4.1). For a given $H(B)$-curve (its determination will be explained later), and the operation mode of the excitation current $I = 500\,\mathrm{A}$, the predicted field map quantity of interest Q_B and the magnetic flux density along two reference circles, that are in the following used to analyze the multipole coefficient quantity of interest $Q_{\mathrm{M},n}$, are shown in Figure 4.2. The corresponding normal multipole coefficients $B_n(r_0)$ are shown in Figure 4.11.

Forward and inverse problem Assume that a set of J operation modes $\{\mathbf{s}_1, \ldots, \mathbf{s}_J\}$ is given by the set of excitation currents $\{I_1, \ldots, I_J\}$ corresponding to the source current densities $\{\mathbf{J}_1, \ldots, \mathbf{J}_J\}$. The following forward problem and the inverse problem have to be solved to compute predictions of quantities of interest given parameters and operation modes, or to update the parameters given operation modes and observations of quantities of interest.

Problem 1. ***(Forward problem)*** *Given a (non-linear) $H(B)$-curve $f_\mathrm{HB} : \mathbb{R}_0^+ \to \mathbb{R}_0^+$ that meets the properties of Assumption 1. Let $\nu_\mathrm{i} : \mathbb{R}_0^+ \to \mathbb{R}^+$ be the corresponding reluctivity function on the iron domain D_i defined by $\nu_\mathrm{i}(t) = f_\mathrm{HB}(t)/t$. Find for each $j = 1, \ldots, J$ the magnetic vector potential $\mathbf{A}_j[\nu_\mathrm{i}] \in \mathcal{V}$ that solves the weak formulation of the boundary value problem of magnetostatics* (4.3) *and evaluate the quantity of interest $Q(\mathbf{A}_j[\nu_\mathrm{i}])$.*

Problem 2. ***(Inverse problem)*** *Given observations Q_j^obs of a quantity of interest Q observed at the excitation currents $\{I_1, \ldots, I_J\}$. Find a $H(B)$-curve $f_\mathrm{HB} : \mathbb{R}_0^+ \to \mathbb{R}_0^+$ meeting the properties in Assumption 1, such that the solutions $\mathbf{A}_j[\nu_\mathrm{i}] \in \mathcal{V}$ of* (4.3) *satisfy $Q_j^\mathrm{obs} = Q(\mathbf{A}_j[\nu_\mathrm{i}])$ for all $j = 1, \ldots, J$, where the reluctivity ν_i on the iron domain D_i is defined by $\nu_\mathrm{i}(t) = f_\mathrm{HB}(t)/t$.*

B(H)- and H(B)-curves To solve the forward problem, a continuous $H(B)$-curve of the yoke material satisfying the properties of Assumption 1 is required. Hence, in the design phase of the magnet, toroidal material specimens (Figure 4.4) of the yoke material are often ordered, and a discrete (B, H)-data table of each specimen is measured, e.g., with a split-coil permeameter [10, 71]. More details on the measurement technology are given later in Section 4.1.1. Based on the discrete (B, H)-data tables, continuous $H(B)$-curves can be determined using different methods; most common are

1. **Closed-form expressions.** The parameters of a closed-form expression, that is based on expert knowledge of underlying physical laws, can be fitted to the measured (B, H)-data table, e.g., [1, 24, 72, 98, 110, 141]. Section 4.1.2 gives an overview of common closed-form expressions.
2. **Spline methods.** The values in the measured (B, H)-data table can be interpolated or approximated with monotone spline curves, e.g., [70, 104, 108, 114]. Section 4.1.3 gives an overview of suitable spline approaches.

Curve models with a few parameters and that have the flexibility to be adjusted to many different materials are favored. Spline methods typically have more parameters than the closed-form expressions found in the literature. However, closed-form expressions have limited flexibility to be adjusted to measured data [106, Section 5.1].

Split-coil permeameter measurements of a set of 26 ARMCO® Pure Iron Grade 4 [5] specimens revealed variations of the (B, H)-data tables between the specimens that exceed the measurement uncertainty significantly [106, Section 3.6]. The observed variation can be caused by material impurities and stresses during the manufacturing process [106, Section 3.6]. Also, material aging can affect the $H(B)$-curve [106, Section 3.5]. We assume that the yoke's (B, H)-data table is within the range of the measured (B, H)-data tables of the specimens. To include the measured variations of the (B, H)-data tables into the curve model of the yoke, the data-driven stochastic $H(B)$-curve model introduced by [117, 118] is used. The idea of this approach is based on describing the $H(B)$-curve of the yoke with a random field (an introduction to random fields is given in Section 4.1.4) rather than a single curve to reflect the uncertainty related to the measured variations. The continuous $H(B)$-curves derived from the (B, H)-data tables of material specimen measurements are interpreted as realizations of the random field in this setting. The random field is discretized in [117, 118] using the truncated KLE [88]. We refer to this model as the *KLE-based $H(B)$-curve model* and analyze its applicability in the context of model updating in this chapter. It combines the advantages of closed-form expressions and spline curves: Being adjustable to any $H(B)$-curve within the measured variations of the (B, H)-data tables of the material specimens while only having a minimal number of parameters. The latter is reduced to the number of the most important variations, observed in the measurements of the yoke material specimens because it can be shown that the truncated KLE satisfies an optimality condition [123, Theorem 2.7] regarding the best approximation of an underlying random field.

Model updating Having a continuous $H(B)$-curve obtained from spline interpolations or closed-form expressions, an initial system model of the magnet system can be obtained by solving the forward problem 1. In the prototype phase of the magnet, predictions of the initial system model and measurements of comparable quantities of interest (Figure 1.2) are compared for validation. If a non-negligible mismatch between the two quantities is detected, the initial system model needs to be adapted to improve the predictions and to find explanations for the observed deviations. Model updating by determining suitable model parameters given measured observations is a common strategy (see Section 1.3.3). Since the (B, H)-data table of the yoke is not measurable and the (B, H)-data tables of yoke material specimens show large variations due to the manufacturing process, the $H(B)$-curve of the yoke in the system model is a reasonable parameter to adjust.

Determining an $H(B)$- or $B(H)$-curve from observations of field-related quantities of interest requires the solution of the inverse problem 2. Several approaches to updating spline curves or the parameters of closed-form expression can be found in the literature [1, 38, 79, 98, 126]. Fitting the parameters of splines or closed-form expressions regularizes the inverse problem with a finite-dimensional approximation of the search space. Reducing the number of parameters of the search space of the inverse problem 2 by applying the truncated KLE yields a regularization by low-rank approximation. The idea of this regularization method is similar to the truncated singular value decomposition [83].

Structure of this chapter The different sources of knowledge and the updating methods used in this chapter are summarized in Figure 4.3. The updated model $\mathcal{M}(\mathbf{p}^{\mathrm{up}}, \cdot)$ is a hybrid model because it combines first principle-based domain knowledge with data from material and field measurements.
The remainder of this chapter is organized as follows: In Section 4.1 we derive and analyze the KLE-based $H(B)$-curve model. First, the measurement principle of a split-coil permeameter is introduced and we give an overview of popular closed-form expressions for $B(H)$- and $H(B)$-curves. Subsequently, the KLE-based $H(B)$-curve model is derived following the ideas of [117, 118] for the split-coil permeameter measurements of ARMCO® Pure Iron specimens given in [106, Section 3.6]. We show that a two-dimensional parameter space is sufficient to approximate the measured variations. Using 4-fold cross-validation, we assess the ability of the KLE-based $H(B)$-curve model and the closed-form expressions to describe the ARMCO® measurements and find that the KLE-based model is the most suitable $H(B)$-curve model and the Wlodarski model [141] is the most suitable $B(H)$-curve model in the comparison.
In Section 4.2, we address the ill-posedness of the inverse problem 2 by using the KLE-based $H(B)$-curve model to approximate the problem. Moreover, the inverse problem is relaxed such that the observations affection by random measurement uncertainty is also considered. Subsequently, the sensitivity analysis derived in [117] is applied to quantify changes in the prediction of the quantities of interest Q_{B} and $Q_{\mathrm{M},n}$ that are related to changes in the reluctivity in the direction of the most important modes of the truncated KLE. The sensitivity analysis results are used to assess the stability of the approximated and relaxed inverse problem. It is shown that there are observation positions $\mathbf{x} \in D$ and multipole orders n for which the inverse problem is unstable. Conversely, we use sensitivity analysis as a tool to improve the formulation of the inverse problem regarding stability by choosing suitable training data.
For the quantity of interest Q_{B}, the approximated and relaxed inverse problem is solved in Section 4.3. Since no magnet system is currently available in the laboratory for which both material data and magnetic flux density data are available, we first simulate observation training data that is disturbed with uncertainties of the same order of magnitude as the random measurement uncertainty that is to be expected. We conduct deterministic model updating by optimization and stochastic model updating using Bayesian inference and explore the resulting posterior distributing with Markov chain Monte Carlo sampling using the Metropolis-Hastings algorithm with the preconditioned Crank-Nicolson proposal. Evaluating the relative error between the ground truth prediction of Q_{B} and the prediction with the updated models shows that the accuracy of the updated model is better than the common threshold of 1 unit in 10000 for operation modes that interpolate the operation modes of the training data. For operation modes extrapolating the operation modes of the training data, the relative errors are less than 3 units in 10000.

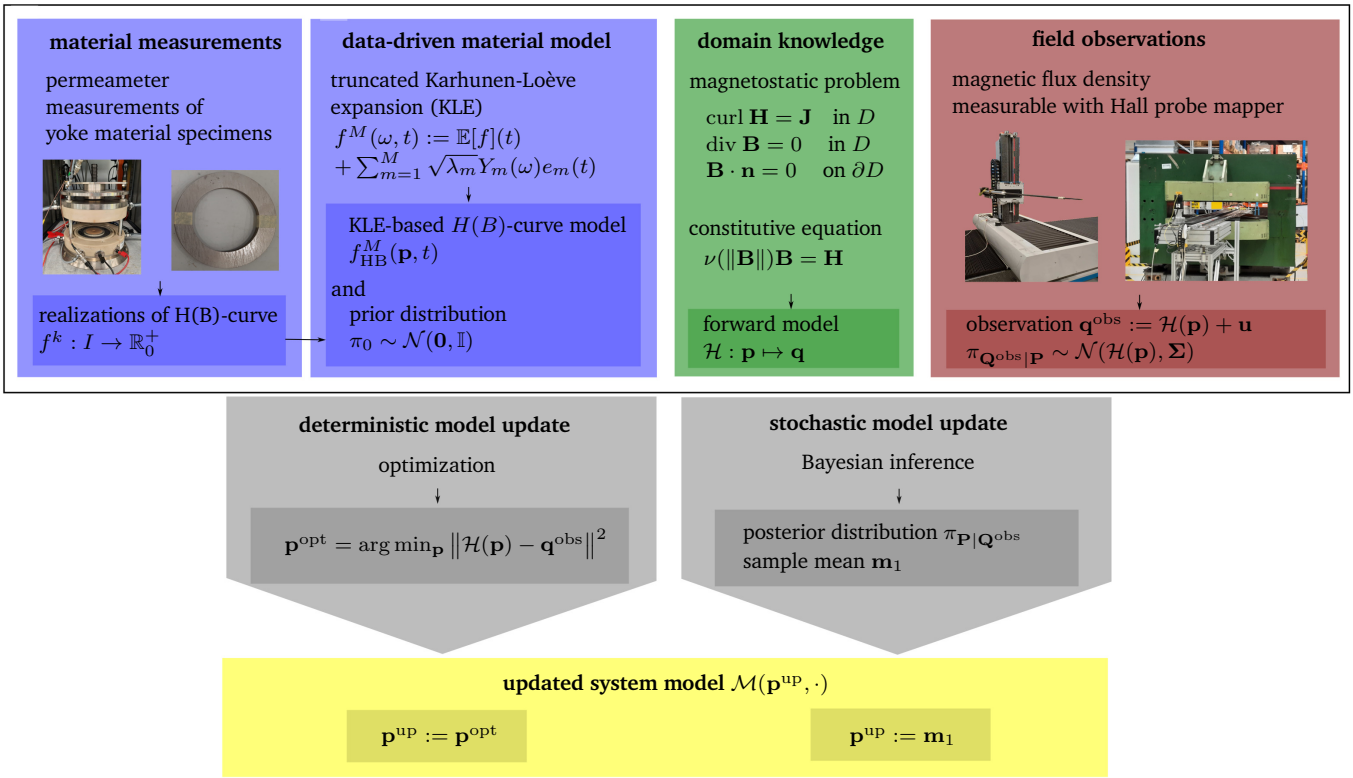

Figure 4.3: Overview of sources of knowledge and methods for data-driven updates of $H(B)$-curves. From split-coil permeameter measurements of yoke material specimens a data-driven material model called KLE-based $H(B)$-curve model is derived. The parameters $\mathbf{p}$ of this model are deterministically and stochastically updated using optimization and Bayesian inference. Thereby, the first principle-based magnetostatic problem is combined with observed data $\mathbf{q}^{\mathrm{obs}}$. Given an operation mode $\mathbf{s}$, the mapping $\mathbf{s} \mapsto \mathcal{M}(\mathbf{p}^{\mathrm{up}}, \mathbf{s})$ can be used to predict quantities of interest with the resulting updated hybrid system model.

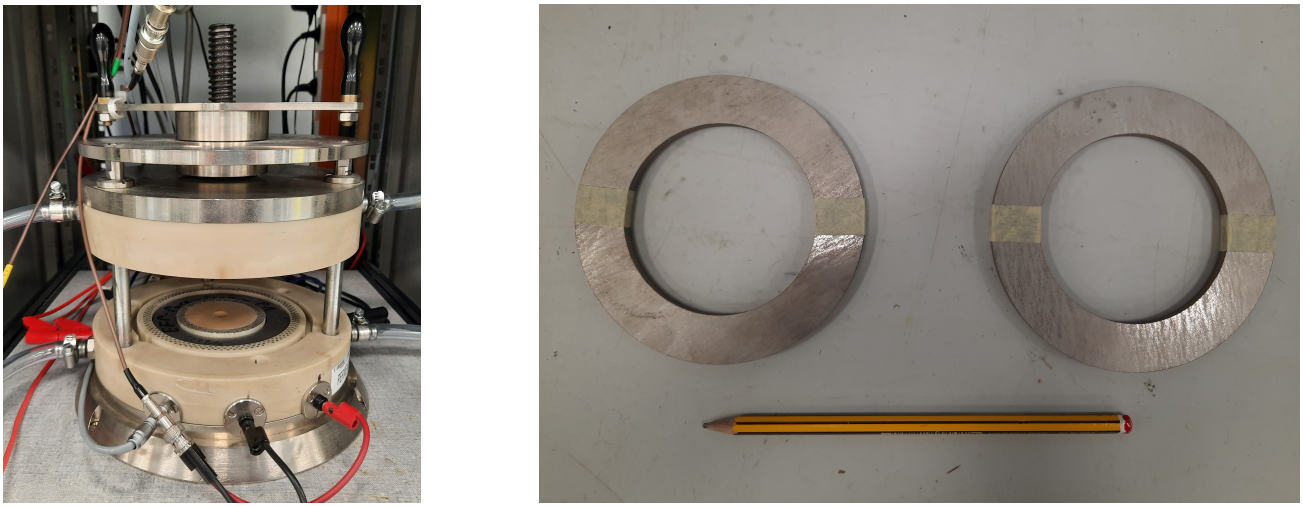

Figure 4.4: Left: Split-coil permeameter. Right: Toroidal ARMCO® Pure Iron Grade 4 material specimens.

4.1 Models of B(H)- and H(B)-curves

In this section, an introduction to the measurement principle of split-coil permeameters is given, and common closed-form expressions and spline-based methods to model continuous $B(H)$- and $H(B)$-curves are summarized. Subsequently, the stochastic data-driven $H(B)$-curve model [117, 118] which also includes the observed variations of the measured (B, H)-data tables corresponding to different material specimens is derived and analyzed. This model is based on the low-rank approximation of a random field with the truncated KLE [88] and is referred to in this work as *KLE-based $H(B)$-curve model*.

4.1.1 Split-coil permeameter measurements

A split-coil permeameter [10, 71] (see Figure 4.4 left) is a measurement device to sample the average magnetic induction $\bar{B}$ in a toroidal material specimen with rectangular cross-section shape (see Figure 4.4 right), given an average magnetizing field $\bar{H}$. The split-coil permeameter consists of two toroidal windings (a 180-turn winding for excitation and a 90-turn winding for measurement) that can be opened to place the specimen. The specimen is first demagnetized using an excitation cycle of several decreasing current plateaus [10, Section 3]. Subsequently, its virgin state that satisfies $\bar{B} = 0$ for $\bar{H} = 0$ can be measured. For the measurement, the excitation windings are powered with L increasing current plateaus. For the plateau current I_l with $1 \leq l \leq L$, the average magnetizing field is given by

$$\bar{H}_l = \frac{1}{r_1 - r_2} \int_{r_1}^{r_2} \frac{N_\mathrm{e} I_l}{2\pi r} \,\mathrm{d}r = \frac{N_\mathrm{e} I_l}{2\pi R}, \tag{4.9}$$

where N_e is the number of excitation windings, r_1 is the inner and r_2 is the outer radius of the toroidal specimen and $R = (r_2 - r_1)/\ln(r_2/r_1)$. The corresponding average magnetic induction $\bar{B}_l$ can be determined from the flux Φ_l that is measured with the search coil by using the formula

$$\bar{B}_l = \frac{1}{2N_\mathrm{c}A_\mathrm{c}}\Phi_l + \left(\frac{1}{2N_\mathrm{c}A_\mathrm{c}} - \frac{1}{2N_\mathrm{c}A_\mathrm{s}}\right)\Phi^0, \tag{4.10}$$

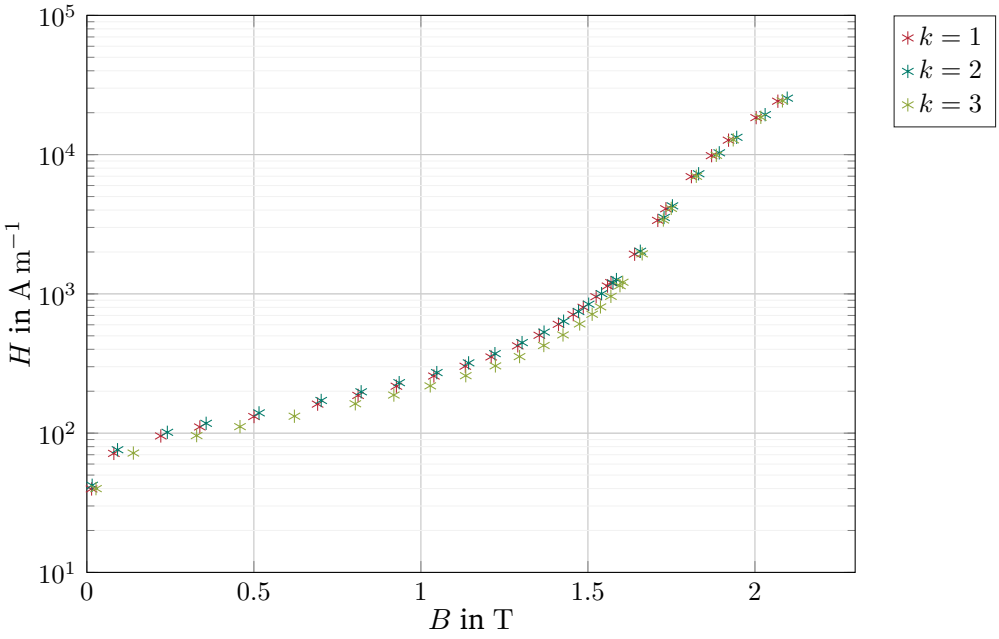

Figure 4.5: (B, H)-data tables of ARMCO® specimens, measured with a split-coil permeameter. For better visibility, only the datasets $k \leq 3$, corresponding to three specimens, are visualized.

where N_c is the number of turns of the search coil, A_c is the cross-section area of the search coil and A_s is the specimens cross-section area. Since the search coil windings are not tight on the specimen, the correction by the measured flux Φ^0 without the specimen is applied.

Assuming that the material is homogeneous, the (B_l, H_l) data points of the sample are identified with the average values $(\bar{B}_l, \bar{H}_l)$. Collecting data points for L current plateaus and repeating the measurement for K specimens, we obtain discrete sets $0 = B_1^k < \cdots < B_L^k$ and corresponding evaluations

$$0 = H_1^k = f_\mathrm{HB}^k(B_1^k) < \cdots < H_L^k = f_\mathrm{HB}^k(B_L^k) \tag{4.11}$$

of the $H(B)$-curve f_HB^k of each sample with $1 \leq k \leq K$. This data is referred to as (B, H)-*data tables*. The relations between the values at the evaluated points in (4.11) are a consequence of the required strict monotonicity of $H(B)$-curves. In this work, we use measured (B, H)-data of $K = 26$ specimens of ARMCO® Pure Iron Grade 4 [5] from AK Steel. In Figure 4.5, the measured (B, H)-data tables of the specimens with $1 \leq k \leq 3$ are visualized. It can be seen that there is a variation between the (B, H)-data tables corresponding to different specimens even though they are made of the same material. The variations can be caused by material impurities or stresses during the manufacturing process [106, Section 3.6].

Most solvers use continuous models of the $B(H)$-curve or the $H(B)$-curve. In the following sections, different methods to derive a continuous curve, given a (B, H)-data table are discussed.

4.1.2 Closed-form expressions

Closed-form expressions for anhysteretic $B(H)$-curves $f_{\mathrm{BH}} : H \mapsto B$ and $H(B)$-curves $f_{\mathrm{HB}} : B \mapsto H$ can be found, e.g., in [1, 24, 72, 98, 110, 141]

$$f_{\mathrm{BH}}(H) := \frac{H}{a+bH} \qquad \text{(Froelich equation)} \tag{4.12}$$

$$f_{\mathrm{BH}}(H) := a\tan^{-1}(bH) \tag{4.13}$$

$$f_{\mathrm{BH}}(H) := b\tan^{-1}\left(\frac{H}{c}\right) + a\mu_0 H \tag{4.14}$$

$$f_{\mathrm{HB}}(B) := c\left[\left(\frac{B}{b}\right) + \left(\frac{B}{b}\right)^a\right] \tag{4.15}$$

$$f_{\mathrm{HB}}(B) := (a\exp(bB^2) + c)B \qquad \text{(Brauer model)} \tag{4.16}$$

where $a, b, c \in \mathbb{R}$ are parameters. Moreover, formulas for $B(H)$-curves can be obtained by inserting a $M(H)$-curve (where $M := \|\mathbf{M}\|$) into

$$f_{\mathrm{BH}}(H) = \mu_0(H + M(H)). \tag{4.17}$$

This approach is based on the constitutive equation (2.13). Popular closed-form expressions for $M(H)$-curves are given, e.g., in [110, 141]

$$M(H) := aH + bH^2 \qquad \text{(Rayleigh model)} \tag{4.18}$$

$$M(H) := M_{\mathrm{sat}}\left[\frac{2J+1}{2J}\coth\left(\frac{2J+1}{2J}\frac{H}{a}\right) - \frac{1}{2J}\coth\left(\frac{1}{2J}\frac{H}{a}\right)\right] \qquad \text{(Brillouin equation)} \tag{4.19}$$

$$M(H) := M_a L\left(\frac{H}{a}\right) + M_b\tanh\left(\frac{H}{b}\right) L\left(\frac{H}{b}\right) \qquad \text{(Wlodarski model)} \tag{4.20}$$

with parameters $a, b, M_{\mathrm{sat}}, J, M_a, M_b \in \mathbb{R}$ and a function L that is defined by

$$L\left(\frac{H}{a}\right) := \coth\left(\frac{H}{a}\right) - \frac{a}{H}. \tag{4.21}$$

Moreover, these models can be combined by using piecewise different models [72]. Some parameters are related to physical meanings, M_{sat} for instance is the saturation magnetization, and M_a and M_b are the reversible and irreversible components of the saturation magnetization. The parameters of these models can be identified by fitting the models to measured discrete (B, H)-data. Repeating the parameter fitting for multiple (B, H)-data tables of different specimens of the same material allows the derivation of a probability distribution of the parameters [110].
The drawback of closed-form expressions is that a measured (B, H)-data table might not be in their span [106, Section 5.1]. Spline-based models, in contrast, are more flexible.

4.1.3 Spline-based models

Given the measured (B, H)-data table (4.11)

$$(B_l, f_{\mathrm{HB}}(B_l)) \qquad 1 \le l \le L \tag{4.22}$$

evaluated in L positions $0 = B_1 < \cdots < B_L$. Different spline-based approaches can be found in the literature [70, 104, 108, 114] to interpolate and approximate the (B, H)-data table:

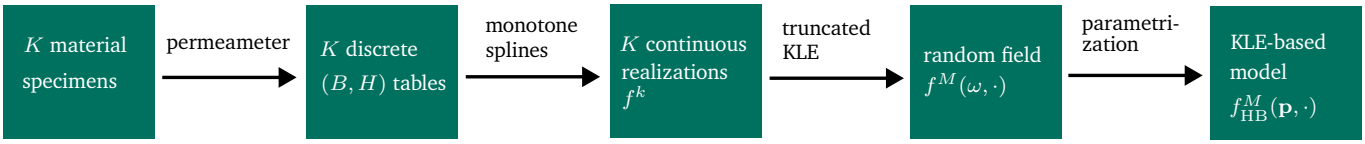

Figure 4.6: Workflow to derive the KLE-based $H(B)$-curve model from material measurements. Figure adapted from [53].

- Monotone cubic Fritsch-Carlson splines [57] can be used to interpolate the (B, H)-data table [70]. The resulting spline curve has $4(L-1)$ parameters.
- The method described in [114] and its further development described in [104] do not only interpolate the (B, H)-data table but take into account the measurement uncertainty of the split-coil permeameter measurements and approximate the measurement results of multiply (B, H)-data tables corresponding to the same specimen. The resulting spline has $2L-4$ or respectively at least more than L parameters.
- In [108], the $B(H)$-curve is subdivided into 5 segments, and to each segment a polynomial of order 3 is fitted, leading to a curve description with 20 parameters.

Since the variation between the measured (B, H)-data tables corresponding to different specimens of the same material exceeds the measurement uncertainty of the split-coil permeameter [106, Section 3.6], the uncertainty of the split-coil permeameter measurements is neglected in this work. To obtain for each of the K material specimens a continuous interpolating function

$$f^k : I \coloneqq [0, \min_k B_L^k] \to \mathbb{R}_0^+ \quad k = 1, \ldots, K, \tag{4.23}$$

we interpolate the measured (B, H)-data table with the monotone cubic Fritsch-Carlson spline [57]. Later, when a finite-dimensional basis representation of these functions is needed, the functions f^k are approximated with radial basis functions [68, Section 6.7].

4.1.4 Data-driven stochastic H(B)-curve model

Notice that the $B(H)$- and $H(B)$-curve models discussed so far are deterministic and do not include the observed variations between the (B, H)-data tables corresponding to different specimens. As suggested in [110], the spread of the parameters of fitted closed-form expressions or spline curves corresponding to different specimens could be analyzed. As an alternative, the data-driven stochastic $H(B)$-curve model derived in [117, 118] is introduced. The steps of its derivation are visualized with a flow chart in Figure 4.6 and each step of the derivation is explained in more detail in the remainder of this section. This model is based on interpreting the continuous spline functions f^k in equation (4.23) as realizations of a random field. This random field is approximated with the truncated KLE [88], yielding a $H(B)$-curve model, whose parametrization reflects the most important measured variations in the (B, H)-data tables of the material specimens.

The advantages of this model, besides the inclusion of the observed variations, are its flexibility to be adapted to any measured material, and its low number of parameters due to the low-rank approximation with the truncated KLE [88].

Stochastic setting Let I be the closed interval that reflects the dependence of the $H(B)$-curve on B and let $(\Omega, \mathcal{F}, \mathbb{P})$ be the probability space (see Section 3.1 for a definition) that reflects the random variation of the $H(B)$-curves. A more comprehensive introduction to the fundamentals of random fields, summarized in this paragraph, is given, e.g., in [4, 94, 146].
A *random field* f is a mapping $f : \Omega \times I \to \mathbb{R}$ such that for all $t \in I$ the function $f(\cdot, t) : \Omega \to \mathbb{R}$ is a random variable. The mean $\mathbb{E}[f]$ of f is defined by

$$\mathbb{E}[f](t) \coloneqq \int_\Omega f(\omega, t) \, \mathrm{d}\mathbb{P}. \tag{4.24}$$

The Hilbert space $L^2(\Omega, \mathcal{F}, \mathbb{P})$ [146, Chapter 2] of square-integrable random variables is defined by

$$L^2(\Omega, \mathcal{F}, \mathbb{P}) \coloneqq \left\{ Y \mid \mathbb{E}[Y^2] < \infty \right\} \tag{4.25}$$

endowed with the scalar product $\langle X, Y \rangle \coloneqq \mathbb{E}[XY]$. A random field f is called square-integrable if $f \in L^2(\Omega, \mathcal{F}, \mathbb{P}) \times L^2(I)$, i.e., $f(\cdot, t)$ is square-integrable for all $t \in I$. The covariance function $\mathrm{Cov}[f] : I \times I \to \mathbb{R}$ of a square-integrable random field f is defined by

$$\mathrm{Cov}[f](s, t) \coloneqq \int_\Omega \left(f(\omega, s) - \mathbb{E}[f](s) \right) \left(f(\omega, t) - \mathbb{E}[f](t) \right) \, \mathrm{d}\mathbb{P}. \tag{4.26}$$

The continuous monotone curves f^k that interpolate the measured (B, H)-data tables of the K material specimen can be interpreted as realizations of the random field f that describes reasonable $H(B)$-curves of the yoke. Consequently, the expected value and the covariance function of the random field f can be estimated from the sample mean $\hat{f} : I \to \mathbb{R}$ and the unbiased sample covariance $\hat{C} : I \times I \to \mathbb{R}$ defined by

$$\hat{f}(t) \coloneqq \frac{1}{K} \sum_{k=1}^{K} f^k(t) \tag{4.27}$$

$$\hat{C}(t, s) \coloneqq \frac{1}{K - 1} \sum_{k=1}^{K} \left(f^k(t) - \hat{f}(t) \right) \left(f^k(s) - \hat{f}(s) \right). \tag{4.28}$$

Karhunen-Loève expansion The KLE can be interpreted as a generalization of Fourier analysis from deterministic functions to random fields [138]. Analogously to Fourier analysis, the KLE yields a decomposition into orthonormal functions. The coefficients of the KLE are random variables. Applications of the KLE include dimensionality reduction and feature extraction [18].
Let $f \in L^2(\Omega, \mathcal{F}, \mathbb{P}) \times L^2(I)$ be a square-integrable random field with continuous covariance function $\mathrm{Cov}[f]$. Following the Karhunen-Loève Theorem [88] (a proof is given in [63, Theorem 4.6]), there are orthonormal functions $e_m \in L^2(I)$, real coefficients $\lambda_m \in \mathbb{R}$ and orthonormal random variables $Y_m \in L^2(\Omega, \mathcal{F}, \mathbb{P})$ with zero mean such that f can be expanded as

$$f(\omega, t) = \mathbb{E}[f](t) + \sum_{m=1}^{\infty} \sqrt{\lambda_m} Y_m(\omega) e_m(t). \tag{4.29}$$

Equation (4.29) is referred to as the *Karhunen-Loève expansion (KLE)*. We refer to the term $\sqrt{\lambda_m} e_m(t)$ as *m-th mode* of the KLE. An important property of the KLE is that it separates the dependence of the random field f on the random space Ω and on the interval I into the functions e_m, that only depend on I,

and the random variables Y_m, that only depend on Ω. The orthonormality of the functions $e_m \in L^2(I)$ is defined by

$$\int_I e_i(t)e_j(t)\,\mathrm{d}t = \delta_{ij} \tag{4.30}$$

and the random variables $Y_m \in L^2(\Omega, \mathcal{F}, \mathbb{P})$ are orthonormal in the sense that

$$\mathbb{E}[Y_i Y_j] = \int_\Omega Y_i(\omega)Y_j(\omega)\,\mathrm{d}\mathbb{P} = \delta_{ij}, \tag{4.31}$$

where δ_{ij} is the Kronecker delta. Consequently, the random variables Y_m are centered, uncorrelated, and with unit variance. For simplicity, it is assumed, such as in [117] that they are mutually independent.

Inserting the expansion (4.29) into the covariance function (4.26) and applying the orthonormality of the functions e_m and the random variables Y_m yields

$$\int_I \mathrm{Cov}[f](s,t)e_m(s)\,\mathrm{d}s = \lambda_m e_m(t). \tag{4.32}$$

Thus, the functions e_m are eigenfunctions of the operator

$$T_f : L^2(I) \to L^2(I), \quad T_f(u)(t) \coloneqq \int_I \mathrm{Cov}[f](s,t)u(s)\,\mathrm{d}s \tag{4.33}$$

and the real values λ_m are the corresponding eigenvalues. We assume that the eigenvalues are enumerated in decreasing order $\lambda_1 \geq \lambda_2 \geq \cdots \geq 0$. The eigenvalues are non-negative because the covariance function defines a positive semidefinite integration kernel [63, remark 4.1]. Moreover, the orthonormality of the functions e_m yields for non-zero eigenvalues that the random variables Y_m are given by

$$Y_m(\omega) = \frac{1}{\sqrt{\lambda_m}} \int_I \left(f(\omega,t) - \mathbb{E}[f](t)\right) e_m(t)\,\mathrm{d}t. \tag{4.34}$$

Consequently, the expansion (4.29) can be obtained by computing first the eigenpairs of T_f. Then, realizations of the random field can be inserted into equation (4.34) to obtain the corresponding realizations of the random variables Y_m.

The eigenvalue problem can be solved numerically using the Galerkin method [14]. To apply the method, we need the eigenvalue problem in its variational form: Find $0 \neq \lambda \in \mathbb{R}$ and $0 \neq u \in L^2(I)$ such that

$$\int_I \int_I \mathrm{Cov}[f](s,t)u(s)v(t)\,\mathrm{d}s\,\mathrm{d}t = \lambda \int_I v(t)u(t)\,\mathrm{d}t \tag{4.35}$$

for all $v \in L^2(I)$. Let $V_h \subset L^2(I)$ be a n-dimensional subspace of $L^2(I)$ spanned by the basis functions $\{\varphi_1, \ldots \varphi_n\}$. The coefficients $\mathbf{w} = (w_1, \ldots, w_n) \in \mathbb{R}^n$ of an eigenfunction $u_h = \sum_{i=1}^n w_i\varphi_i \in V_h$ and its corresponding eigenvalue λ_h that satisfy

$$\int_I \int_I \mathrm{Cov}[f](s,t)u_h(s)v_h(t)\,\mathrm{d}s\,\mathrm{d}t = \lambda_h \int_I v_h(t)u_h(t)\,\mathrm{d}t \tag{4.36}$$

for all $v_h \in V_h$, can be determined by solving the following matrix eigenvalue problem

$$\mathbf{K}\mathbf{w} = \lambda_h \mathbf{M}\mathbf{w} \tag{4.37}$$

with matrices $\mathbf{M}, \mathbf{K} \in \mathbb{R}^{n \times n}$ defined by

$$\mathbf{K}_{ij} = \int_I \int_I \mathrm{Cov}[f](s,t)\varphi_i(s)\varphi_j(t)\,\mathrm{d}s\,\mathrm{d}t \tag{4.38}$$

$$\mathbf{M}_{ij} = \int_I \varphi_i(t)\varphi_j(t)\,\mathrm{d}t. \tag{4.39}$$

According to [85, Theorem 18.1 and 18.2], the eigenpairs, found by solving the eigenvalue problem (4.37), converge to eigenpairs of the eigenvalue problem $T_f u = \lambda u$ as V_h approximates $L^2(I)$. In [117, 118], V_h is chosen as a B-spline space. In this work, we use a function space V_h spanned by radial basis functions [68, Section 6.7].

Truncated Karhunen-Loève expansion The KLE defined in equation (4.29) has infinitely many terms and is therefore unfeasible for implementations. We therefore use the approximation with the *truncated Karhunen-Loève expansion (KLE)* defined by

$$f^M(\omega,t) \coloneqq \mathbb{E}[f](t) + \sum_{m=1}^{M} \sqrt{\lambda_m} Y_m(\omega) e_m(t). \tag{4.40}$$

Using the orthonormality of e_m and Y_m, it can be shown that the $L^2(\Omega,\mathcal{F},\mathbb{P}) \times L^2(I)$-error between f and f^M is given by

$$\left\| f - f^M \right\|^2_{L^2(\Omega,\mathcal{F},\mathbb{P})\times L^2(I)} = \sum_{m=M+1}^{\infty} \lambda_m. \tag{4.41}$$

Following [56, Proposition 2.5], there is a constant $C > 0$ such that the eigenvalues λ_m satisfy

$$0 \le \lambda_m \le C m^{-l} \tag{4.42}$$

if $\mathrm{Cov}[f] \in C^l(I \times I)$. We therefore assume as in [118] that $l \ge 2$ such that we can deduct

$$\left\| f - f^M \right\|^2_{L^2(\Omega,\mathcal{F},\mathbb{P})\times L^2(I)} \le C \sum_{m=M+1}^{\infty} m^{-2} < \infty \tag{4.43}$$

and thus the truncated KLE f^M converges in $L^2(\Omega,\mathcal{F},\mathbb{P}) \times L^2(I)$ to the random field f as $M \to \infty$. Consequently, for M sufficiently large, the truncated KLE can approximate a random field f with arbitrarily high accuracy. A heuristic on how to choose a reasonable truncation threshold M is given in [117]. Moreover, it can be shown that the truncated KLE is optimal concerning the $L^2(\Omega,\mathcal{F},\mathbb{P}) \times L^2(I)$-error among all expansions that approximate f with a series of M terms [123, Theorem 2.7].

KLE-based H(B)-curve model The truncated KLE f^M is used as an approximation of the random field f, that describes possible $H(B)$-curves of the iron yoke, given K realizations of $H(B)$-curves f^k (equation (4.23)) derived from split-coil permeameter measurements of yoke material specimens. The dependence of truncated KLE f^M on the sample space Ω is only via the random variables Y_m. By inserting the realizations f^k of f and the sample mean $\hat{f}$ into equation (4.34), the corresponding realizations Y_m^k of Y_m can be determined

$$Y_m^k = \frac{1}{\sqrt{\lambda_m}} \int_I \left(f^k(t) - \hat{f}(t) \right) e_m(t)\,\mathrm{d}t. \tag{4.44}$$

Substituting the random variables Y_m in the truncated KLE (4.40) with real parameters $\mathbf{p} = (p_1, \ldots, p_m) \in \mathbb{R}^M$ and estimating the expected value of f with the sample mean $\hat{f}$ yields

$$f_{\mathrm{HB}}^M(\mathbf{p}, t) \coloneqq \hat{f}(t) + \sum_{m=1}^{M} \sqrt{\lambda_m} p_m e_m(t). \tag{4.45}$$

We refer to the function $f_{\mathrm{HB}}^M : \mathbb{R}^M \times I \to \mathbb{R}$ as the *KLE-based $H(B)$-curve model*. Due to the truncation and the property of the truncated KLE of being the optimal M-term expansion regarding the L^2-error, the number M of parameters of the KLE-based $H(B)$-curve model can be restricted to a small number of most important observed variations in the $H(B)$-curves f^k of the measured specimens.
The existence of a unique solution to the weak formulation of the boundary value problem of magnetostatics in vector potential formulation requires the properties of the $H(B)$-curve given in Assumption 1, e.g., the strict monotonicity. For a random field-based $H(B)$-curve $f(\omega, \cdot)$ it is sufficient to assume that the conditions in Assumption 1 are satisfied for almost all $\omega \in \Omega$ and that the parameter α is ω-independent [118, Section 3]. To guarantee the existence of a unique solution if the KLE-based $H(B)$-curve model (4.45) is used, a subset $\mathcal{P} \subset \mathbb{R}^M$ is defined such that for all $\mathbf{p} \in \mathcal{P}$ the KLE-based $H(B)$-curve model $f_{\mathrm{HB}}^M(\mathbf{p}, \cdot)$ is strictly monotone. Due to the monotonicity of the realizations f^k, the sample mean $\hat{f}$ is monotone. Let

$$p_m^{\min} \coloneqq \min_{1 \le k \le K} Y_m^k \qquad \text{and} \qquad p_m^{\max} \coloneqq \max_{1 \le k \le K} Y_m^k \qquad \forall 1 \le m \le M \tag{4.46}$$

be the minimal and the maximal realization of Y_m. We verify the strict monotonicity of the KLE-based $H(B)$-curve model f_{HB}^M for each combination of minimal and maximal realization, otherwise the bounds are subsequently tightened, starting with the parameter p_1 of the first mode with the highest weight $\sqrt{\lambda_1}$. Consequently, the KLE-based $H(B)$-curve model is a strictly monotone $H(B)$-curve that admits a unique solution to the weak formulation of the boundary value problem of magnetostatics in vector potential formulation for all

$$\mathbf{p} \in \mathcal{P} \coloneqq [p_1^{\min}, p_1^{\max}] \times \cdots \times [p_M^{\min}, p_M^{\max}]. \tag{4.47}$$

In the following, we compute the KLE-based $H(B)$-curve model for the ARMCO® Pure Iron Grade 4 measurements [106] and compare the resulting model to the closed-from expressions in Section 4.1.2.

4.1.5 B(H)- and H(B)-curve of ARMCO® Pure Iron

The iron yokes of the High Luminosity Large Hadron Collider (HL-LHC) magnets are made of ARMCO® Pure Iron Grade 4 from AK Steel [5]. For the follow-up of the magnet production, the anhysteretic $H(B)$-curves of $K = 26$ material specimens were measured [106] in $L = 28$ points with a split coil permeameter [71]. The specimen with $k = 5$ is selected as a test specimen to evaluate the ability of the KLE-based $H(B)$-curve model (4.45) and the closed-form expressions defined in Section 4.1.2 to describe a model that matches the measured (B, H)-data. The specimens with $k \neq 5$ are referred to as remaining specimens.

KLE-based H(B)-curve model The KLE-based $H(B)$-curve model is derived based on the measured (B, H)-data tables of the remaining specimens without the data of the test specimen. To determine a suitable truncation threshold M for the truncated KLE (4.40), [118] suggests to choose M such that the relative information content

$$\Psi_M \coloneqq \left(\sum_{m=1}^{M} \lambda_m \right) \left(\sum_{m=1}^{M'} \lambda_m \right)^{-1} \tag{4.48}$$

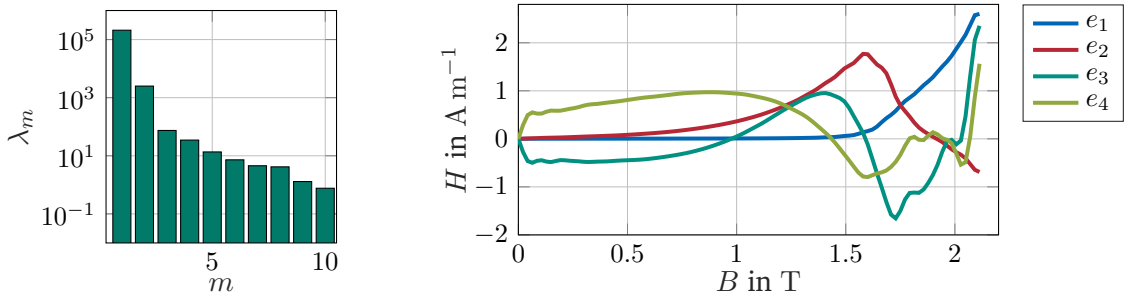

Figure 4.7: Ten largest eigenvalues λ_m and eigenfunctions e_m of the operator T_f defined in equation (4.33) evaluated for the ARMCO® Pure Iron Grade 4 specimens without the test specimen. Figure adapted from [53].

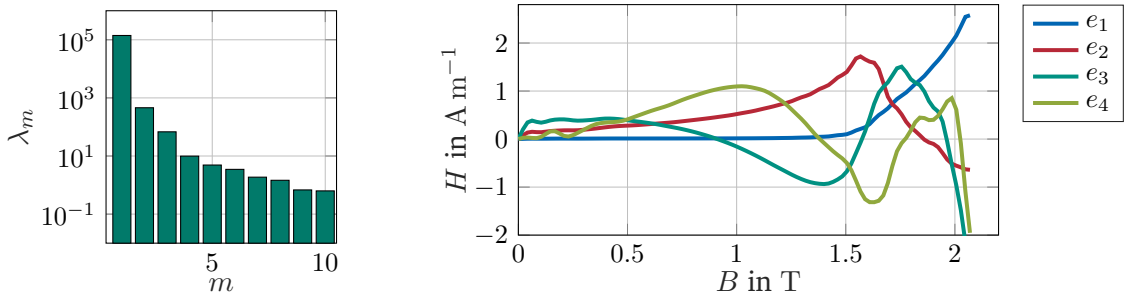

Figure 4.8: Ten largest eigenvalues λ_m and eigenfunctions e_m of the operator T_f defined in equation (4.33) evaluated for the FeSi M270-50A specimens.

satisfies $\Psi_M > 0.95$ where $M' \gg M$. The eigenpairs (λ_m, e_m) obtained for the ARMCO® specimens without the test specimen are depicted in Figure 4.7. For this dataset, the eigenvalues decay fast such that the relative information content for $M = 1$ already satisfies $\Psi_1 > 98.76\%$. For $M = 2$, we obtain $\Psi_2 > 99.93\%$ and thus select $M = 2$ for this study. Inserting the realizations f^k into equation (4.44) yields the realizations Y_m^k of the random variables Y_m of the KLE. Assuring that for all combinations of the upper and lower bounds of the random variable realizations the KLE-based $H(B)$-curve model is strictly monotone, we obtain the following parameter space

$$\mathcal{P} = [p_1^{\min}, p_1^{\max}] \times [p_2^{\min}, p_2^{\max}] = [-2.06, 2.50] \times [-2.55, 1.38]. \tag{4.49}$$

Additionally to the ARMCO® specimens, $L = 18$ ferrosilicon M270-50A (according to DIN EN 10106) specimens, the yoke material of the dipoles of the Synchrotron-Light for Experimental Science and Applications in the Middle East (SESAME) [125], were measured with a split-coil permeameter. The corresponding eigenpairs of the KLE are shown in Figure 4.8. It can be observed that the two eigenfunctions e_1 and e_2 that are weighted the most in the KLE, are similar to the corresponding eigenfunctions of the ARMCO® specimens. Analyzing more material groups might allow the relation of the shape of eigenfunctions to properties of the manufacturing process. However, this conjecture was not further investigated in this thesis.

X-fold cross-validation The prediction error of the KLE-based $H(B)$-curve model (4.45) and the closed-form expressions defined in Section 4.1.2 on the measured ARMCO® (B, H)-data is estimated using X-fold cross-validation [68]. For this purpose, the $L = 28$ data points of the test specimen ($k = 5$) are divided into $X = 4$ disjoint subsets $T_1, \ldots, T_4$ (see Figure 4.9). Each $B(H)$-curve model f_{BH} is trained four times by fitting

Table 4.1: 4-fold cross-validation estimates $CV(f_{\mathrm{BH}})$ and $CV(f_{\mathrm{HB}})$ of the prediction error of the $B(H)$-curves and $H(B)$-curves introduced in Section 4.1.2 and the KLE-based $H(B)$-curve model on measured ARMCO® (B, H)-data tables.

model	$CV(f_{\mathrm{BH}})$	$CV(f_{\mathrm{HB}})$
Froehlich equation (4.12)	0.0952	
equation (4.13)	0.0899	
equation (4.14)	0.0680	
equation (4.15)		0.0855
Brauer model (4.16)		0.2158
Rayleigh model (4.18)	0.5863	
Brillouin equation (4.19)	0.0901	
Wlodarski model (4.20)	**0.0324**	
KLE-based $H(B)$-curve model (4.45)		**0.0087**

the model parameters such that the residual

$$E_{\mathrm{BH}} \coloneqq \sum_{l=2}^{L-1} \frac{E_l + E_{l+1}}{2} \frac{H_{l+1} - H_l}{H_L - H_2} \qquad \text{with} \qquad E_l \coloneqq E(f_{\mathrm{BH}}(H_l), B_l) \coloneqq \sqrt{\left(\frac{f_{\mathrm{BH}}(H_l) - B_l}{f_{\mathrm{BH}}(H_l) + B_l}\right)^2} \tag{4.50}$$

defined in [141] is minimized. For $H(B)$-curve models f_{HB}, we minimize analogously the residual

$$E_{\mathrm{HB}} = \sum_{l=2}^{L-1} \frac{E'_l + E'_{l+1}}{2} \frac{B_{l+1} - B_l}{B_L - B_2} \qquad \text{with} \qquad E'_l \coloneqq E'(f_{\mathrm{HB}}(B_l), H_l) \coloneqq \sqrt{\left(\frac{f_{\mathrm{HB}}(B_l) - H_l}{f_{\mathrm{HB}}(B_l) + H_l}\right)^2}. \tag{4.51}$$

In the x-th training step, the data subset T_x is left out from the training data set. The fitted model in the x-th step is referred to as f^x_{BH} (or f^x_{HB}). Let $\kappa : l \mapsto \{1, 2, 3, 4\}$ be the mapping with $\kappa(l) = x$ if $l \notin T_x$. The cross-validation estimate [68] of the prediction error of a fitted $B(H)$-curve model is given by

$$CV(f_{\mathrm{BH}}) = \frac{1}{L} \sum_{l=1}^{L} E(f^{\kappa(l)}_{\mathrm{BH}}(H_l), B_l) \tag{4.52}$$

for the residual function E defined in equation (4.50). To compute the cross-validation estimate of the prediction error of a fitted $H(B)$-curve model, the residual function E is substituted by E' in equation (4.52). The smaller the cross-validation estimate of the prediction error, the more suitable the material model to describe the measured ARMCO® (B, H)-data.

Figure 4.9 shows the $B(H)$- and $H(B)$-curves that are fitted to the training set $T_2 \cup T_3 \cup T_4$. Besides the Rayleigh model, all of the investigated models can be roughly fitted to the data. The cross-validation estimates of the prediction error are given in Table 4.1. Among the $H(B)$-curves, the estimated prediction error of the KLE-based $H(B)$-curve model is the smallest. Among the $B(H)$-curves, the Wlodarski curve has the smallest cross-validation estimate. Due to the different relative error functions used in the definition of the cross-validation estimate for $B(H)$-curves and $H(B)$-curves, the values are not directly comparable. However, Figure 4.9 reveals that the Wlodarski model is less suitable than the KLE-based $H(B)$-curve model to describe the data in the low field region. The same observation was made by [106].

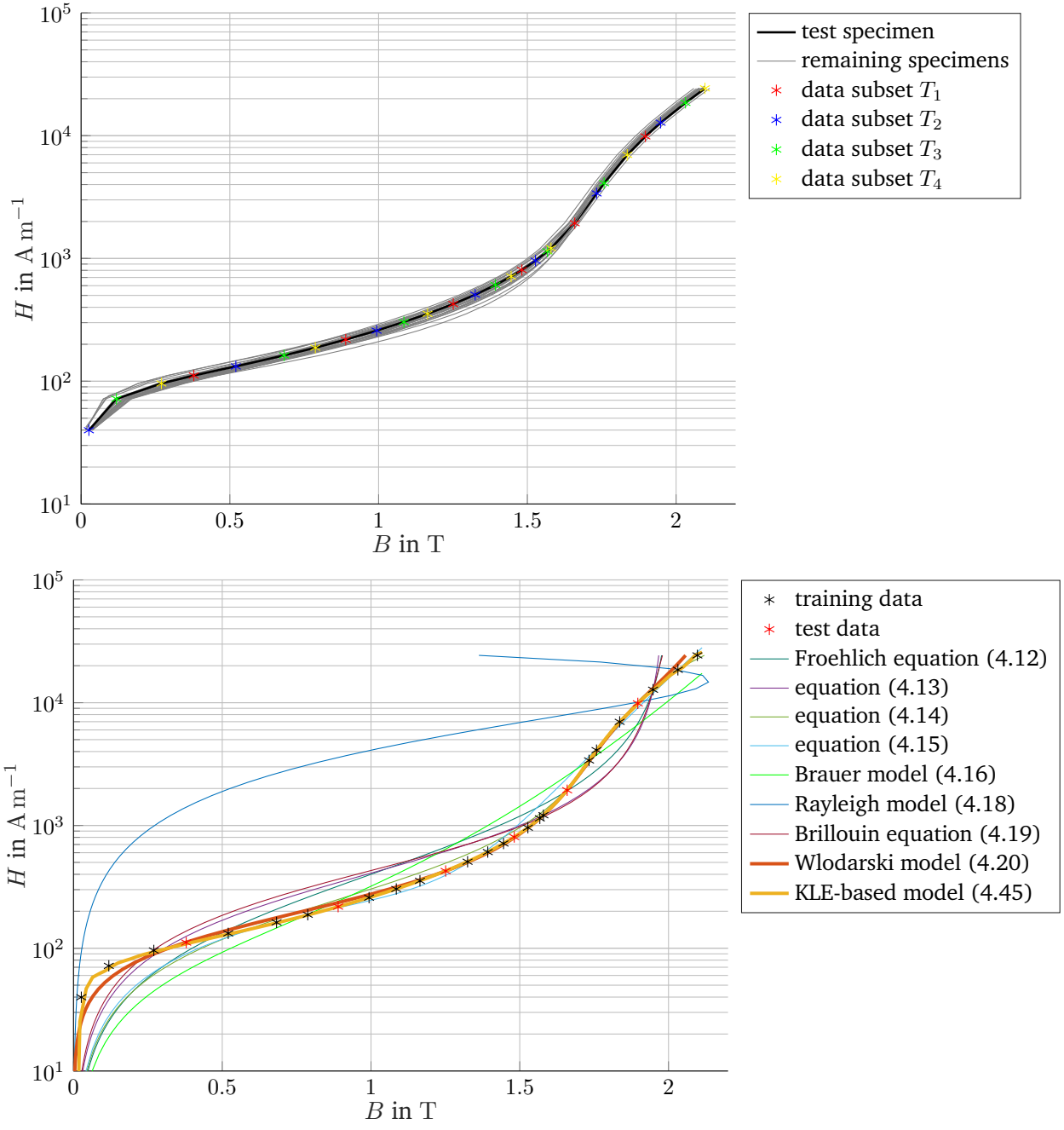

Figure 4.9: Top: Measured (B, H)-data of 26 ARMCO® Pure Iron Grade 4 specimens. Red line: linear interpolation of (B, H)-data of test specimen, grey lines: linear interpolation of (B, H)-data of remaining specimens, scattered: (B, H)-data of test specimen organized in four disjoint subsets $T_1, \ldots, T_4$ for cross-validation. Bottom: Best fitting $B(H)$- and $H(B)$-curves to the data $T_2 \cup T_3 \cup T_4$ according to the residual defined in equation (4.50) and (4.51).

4.2 Addressing the ill-posedness of the inverse problem

The magnet system "PXMBHGGHWC-OR000113" that is used as an example in this chapter, was built in 1963. Due to its age, no material specimens of the yoke material are available. Thus, a KLE-based $H(B)$-curve model (4.45) that matches the magnet as built can not be derived. However, in the prototype phase of new magnet systems, it can be assumed that the required material specimens are available. To study the methodology of updating the $H(B)$-curve using the KLE-based $H(B)$-curve model, we assume in the following that the yoke material of the studied example magnet system is ARMCO® Pure Iron Grade 4 [5]. Consequently, the KLE-based $H(B)$-curve model derived in Section 4.1.5 can be used.

In this section, we approximate the forward problem 1 and the inverse problem 2 using the KLE-based $H(B)$-curve model and the two-dimensional parameter space $\mathcal{P}$ determined in equation (4.49). This low-rank approximation leads to a regularization of the inverse problem. The sensitivity analysis derived in [117] is used to analyze the stability of the approximated problem. We show that there are observation positions $\mathbf{x} \in D$ and multipole orders n for which the inverse problem for the quantities of interest Q_{B} and $Q_{\mathrm{M},n}$ is still ill-posed due to instability.

4.2.1 Approximation of the forward and the inverse problem

Inserting the KLE-based $H(B)$-curve model $f_{\mathrm{HB}}^{M}(\mathbf{p},\cdot)$ defined in equation (4.45) into the definition of the reluctivity ν_{i} in the iron domain D_{i} in equation (4.2) yields

$$\nu_{\mathrm{i}}(t) = \nu_{\mathbf{p}}(t) \coloneqq \frac{f_{\mathrm{HB}}^{M}(\mathbf{p},t)}{t}. \tag{4.53}$$

To indicate the dependence of the reluctivity in D_{i} on the parameter $\mathbf{p}$, we use the notation $\nu_{\mathbf{p}}$.

Approximated forward problem Restricting the forward problem 1 to reluctivities that are induced by the KLE-based $H(B)$-curve model, we obtain the following problem: Given $\mathbf{p} \in \mathcal{P}$ and the set of source current densities $\{\mathbf{J}_1,\dots,\mathbf{J}_J\}$, find the magnetic vector potentials $\mathbf{A}_j[\nu_{\mathbf{p}}] \in \mathcal{V}$, for $j = 1,\dots,J$, that solve the weak formulation of the boundary value problem of magnetostatics (4.3) and evaluate the quantity of interest $Q(\mathbf{A}_j[\nu_{\mathbf{p}}])$.

Due to the choice of the parameter domain $\mathcal{P}$, that admits for all $\mathbf{p} \in \mathcal{P}$ unique solutions $\mathbf{A}_j[\nu_{\mathbf{p}}]$, the forward model

$$\begin{aligned} \mathcal{H} : \mathcal{P} &\to \mathcal{Q} \\ \mathbf{p} &\mapsto Q(\mathbf{A}_j[\nu_{\mathbf{p}}]), \end{aligned} \tag{4.54}$$

that maps the parameters $\mathbf{p}$ to evaluations of the quantities of interest, is well-defined. The forward model is related to the system model (4.1) via

$$\mathcal{M}(\mathbf{p}, I_j) = \mathcal{H}(\mathbf{p}) = Q(\mathbf{A}_j[\nu_{\mathbf{p}}]), \tag{4.55}$$

where the operation modes $\{\mathbf{s}_1,\dots,\mathbf{s}_J\}$ are given by the excitation currents $\{I_1,\dots,I_J\}$ which correspond to the source current densities $\{\mathbf{J}_1,\dots,\mathbf{J}_J\}$.

Approximated inverse problem Approximating the inverse problem 2 with the KLE-based $H(B)$-curve model yields the following problem: Given observations Q_j^{obs} of a quantity of interest Q observed at the excitation currents $\{I_1, \dots, I_J\}$, find $\mathbf{p} \in \mathcal{P}$ such that for all $j = 1, \dots, J$ the weak solution $\mathbf{A}_j[\nu_{\mathbf{p}}] \in \mathcal{V}$ of (4.3) satisfies $Q_j^{\mathrm{obs}} = Q(\mathbf{A}_j[\nu_{\mathrm{i}}])$.

Using the KLE-based $H(B)$-curve model $f_{\mathrm{HB}}^M(\mathbf{p}, \cdot)$ in equation (4.53) yields a finite-dimensional approximation of the search space. Additionally, prior knowledge is incorporated about which variations of the $H(B)$-curve are the most important according to the KLE of the random field, whose realizations are the $H(B)$-curves of the material specimens. Thus, we obtain not only a finite-dimensional but in particular a low-rank approximation of the inverse problem.
Due to the approximation and the fact that the observations are affected by uncertainty, a solution to the approximated inverse problem stated above might not exist. Typical standard deviations that have to be considered due to random measurement uncertainty with modern-day measurement equipment are $\sigma = 10^{-4}$ for relative observations of the magnetic flux density and the dipole coefficient, and $\sigma = 10^{-6}$ for relative observations of higher-order multipole coefficients. We therefore relax the notion of a solution by considering the following inverse problem.

Problem 3. ***(Approximated and relaxed inverse problem)*** *Given for $r = 1, \dots, R$ and $n = 1, \dots, N$ observations $B_{y,j}^{\mathrm{obs}}(\mathbf{x}_r)$ or $(B_n(r_0))_j^{\mathrm{obs}}$ of the respective quantity of interest observed at the excitation currents I_j. Find $\mathbf{p} \in \mathcal{P}$ such that the weak solution $\mathbf{A}_j[\nu_{\mathbf{p}}] \in \mathcal{V}$ of* (4.3) *satisfies*

$$\frac{1}{JR} \sum_{j,r} \frac{|B_{y,j}^{\mathrm{obs}}(\mathbf{x}_r) - Q_{\mathrm{B}}(\mathbf{A}_j[\nu_{\mathbf{p}}])(\mathbf{x}_r)|}{|B_{y,j}^{\max}|} < \epsilon_{\mathrm{tol,B}} \tag{4.56}$$

or respectively, depending on the quantity of interest,

$$\frac{1}{J} \sum_{j} \frac{|(B_n(r_0))_j^{\mathrm{obs}} - Q_{\mathrm{M},n}(\mathbf{A}_j[\nu_{\mathbf{p}}])|}{|(B_1(r_0))_j|} < \epsilon_{\mathrm{tol,M,n}} \quad \forall n = 1, \dots, N. \tag{4.57}$$

Thereby, the maximal central field $|B_{y,j}^{\max}|$ and the first normal multipole coefficient $|(B_1(r_0))_j|$ are used for normalization. We choose the tolerances $\epsilon_{\mathrm{tol,B}} \coloneqq \epsilon_{\mathrm{tol,M,1}} \coloneqq 10^{-4}$ and $\epsilon_{\mathrm{tol,M,n}} \coloneqq 10^{-6}$ for $n > 1$.

4.2.2 Sensitivity analysis

A framework to study the sensitivity of solutions to the boundary value problem of magnetostatics in vector potential formulation to perturbations of the reluctivity function ν_{i} in the iron domain is derived in [117, Section 4.4]. We apply this framework to assess the stability of the approximated and relaxed inverse problem 3 and to identify suitable positions $\{\mathbf{x}_1, \dots, \mathbf{x}_R\}$ and multipole orders n for the observation training data, which is used to solve the approximated and relaxed inverse problem for model updating. A similar method is used in Section 5.1 to study the sensitivity of solutions to the boundary value problem of magnetostatics in vector potential formulation to perturbations of the magnetization.

Sensitivity of linear quantities of interest to perturbations of the reluctivity In this section, we consider perturbations of the nominal reluctivity $\bar{\nu}_\mathrm{i}$ in the iron domain of the following form: For a function $\widetilde{\nu} : \mathbb{R}_0^+ \to \mathbb{R}^+$ we define

$$\nu_s(\mathbf{x}, t) = \begin{cases} \nu_0 & \mathbf{x} \in D_\mathrm{a} \\ \nu_\mathrm{i}(t) = \bar{\nu}_\mathrm{i}(t) + s\widetilde{\nu}(t) & \mathbf{x} \in D_\mathrm{i}. \end{cases} \tag{4.58}$$

According to [117, Section 4.3, Proposition 1], there is a constant s_0 such that for all $0 < s < s_0$ there is a weak solution $\mathbf{A}[\nu_s] \in \mathcal{V}$ of

$$\int_D \operatorname{curl} \mathbf{v} \cdot \nu_s(\|\operatorname{curl} \mathbf{A}[\nu_s]\|) \operatorname{curl} \mathbf{A}[\nu_s] \,\mathrm{d}V = \int_D \mathbf{v} \cdot \mathbf{J} \,\mathrm{d}V \tag{4.59}$$

for all $\mathbf{v} \in \mathcal{V}$. Moreover, $\mathbf{A}[\nu_s]$ converges to $\mathbf{A} \coloneqq \mathbf{A}[\bar{\nu}_\mathrm{i}]$ as $s \to 0$.

Let X, Y be normed spaces and $U \subset X$ an open subset. The function $f : U \to Y$ is called *Gâteaux differentiable* [105, definition 2.23] at $u_0 \in U$, if there is a linear and continuous map $f' : X \to Y$ such that for all $v \in U$

$$f'(v) = \lim_{s \searrow 0} \frac{f(u_0 + sv) - f(u_0)}{s}. \tag{4.60}$$

Gâteaux differentiability is weaker than the Fréchet differentiability [105, definition 2.43] in $u_0 \in U$, which requires the existence of a continuous linear map $\delta f : X \to Y$ and a remainder o [105, definition 2.39] such that for v close to 0

$$f(u_0 + v) = f(u_0) + \delta f(v) + o(v). \tag{4.61}$$

For the mapping $\nu_\mathrm{i} \to \mathbf{A}[\nu_\mathrm{i}]$, the Gâteaux derivative at $\bar{\nu}_\mathrm{i}$ in direction of the perturbation $\widetilde{\nu}$ is defined by

$$\mathbf{A}'[\widetilde{\nu}] = \lim_{s \searrow 0} \frac{\mathbf{A}[\bar{\nu}_\mathrm{i} + s\widetilde{\nu}] - \mathbf{A}[\bar{\nu}_\mathrm{i}]}{s}. \tag{4.62}$$

Following [117, Proposition 2], the Gâteaux derivative satisfies $\mathbf{A}' \in \mathcal{V}$ and can be found as the weak solution to the problem

$$\begin{aligned} \operatorname{curl}(\boldsymbol{\nu}_\mathrm{d}(\operatorname{curl} \mathbf{A}) \operatorname{curl} \mathbf{A}') &= -\operatorname{curl}(\widetilde{\nu}(\|\operatorname{curl} \mathbf{A}\|) \operatorname{curl} \mathbf{A}) && \text{on } D_\mathrm{i} \\ \operatorname{curl}(\nu_0 \operatorname{curl} \mathbf{A}') &= 0 && \text{on } D_\mathrm{a} \\ \mathbf{A}' \times \mathbf{n} &= \mathbf{0} && \text{on } \Gamma_\mathrm{B}, \\ [\![\boldsymbol{\nu}_\mathrm{d}(\operatorname{curl} \mathbf{A}) \operatorname{curl} \mathbf{A}']\!]_\mathrm{ai} &= -\widetilde{\nu}(\|\operatorname{curl} \mathbf{A}\|) \operatorname{curl} \mathbf{A} \times \mathbf{n} && \text{on } \Gamma_\mathrm{ai}, \\ [\![\mathbf{A}]\!]_\mathrm{ai} &= 0 && \text{on } \Gamma_\mathrm{ai} \end{aligned} \tag{4.63}$$

where $\boldsymbol{\nu}_\mathrm{d}$ is the differential reluctivity tensor [117, definition 5] that is for $\mathbf{t} \in \mathbb{R}^3$ defined by

$$\boldsymbol{\nu}_\mathrm{d}(\mathbf{t}) \coloneqq \bar{\nu}_\mathrm{i}(\|\mathbf{t}\|)\mathbb{I} + \frac{\bar{\nu}_\mathrm{i}'(\|\mathbf{t}\|)}{\|\mathbf{t}\|} \mathbf{t} \otimes \mathbf{t}. \tag{4.64}$$

The corresponding weak formulation is: Find $\mathbf{A}' \in \mathcal{V}$ such that

$$\int_{D_\mathrm{i}} \boldsymbol{\nu}_\mathrm{d}(\operatorname{curl} \mathbf{A}) \operatorname{curl} \mathbf{A}' \cdot \operatorname{curl} \mathbf{v} \,\mathrm{d}V + \int_{D_\mathrm{a}} \mu_0 \operatorname{curl} \mathbf{A}' \cdot \operatorname{curl} \mathbf{v} \,\mathrm{d}V = -\int_{D_\mathrm{i}} \widetilde{\nu}(\|\operatorname{curl} \mathbf{A}\|) \operatorname{curl} \mathbf{A} \cdot \operatorname{curl} \mathbf{v} \,\mathrm{d}V \tag{4.65}$$

for all $\mathbf{v} \in \mathcal{V}$.

For the sensitivity analysis of the forward problem, we are interested in the Gâteaux derivative

$$\widehat{Q}'[\widetilde{\nu}] = \lim_{s \searrow 0} \frac{\widehat{Q}[\bar{\nu}_\mathrm{i} + s\widetilde{\nu}] - \widehat{Q}[\bar{\nu}_\mathrm{i}]}{s} \tag{4.66}$$

of the mapping defined in equation (4.6) by a quantity of interest Q. According to [117, Section 4.4], this derivative can be computed by inserting $\mathbf{A}'$ into the (linear) quantity of interest

$$\widehat{Q}'[\widetilde{\nu}] = \int_{D_{\mathrm{obs}}} q_1(\mathbf{A}'[\widetilde{\nu}]) + q_2(\operatorname{curl} \mathbf{A}'[\widetilde{\nu}]) \,\mathrm{d}V. \tag{4.67}$$

Sensitivity analysis concerning perturbations related to the KLE-based H(B)-curve model The KLE-based $H(B)$-curve model (4.45) for the ARMCO® specimens is given by

$$f_{\mathrm{HB}}^2(\mathbf{p}, t) = \hat{f}(t) + p_1 \sqrt{\lambda_1} e_1(t) + p_2 \sqrt{\lambda_2} e_2(t) \tag{4.68}$$

where $\hat{f}$ is the sample mean, (λ_m, e_m) are the eigenpairs of the KLE and $\mathbf{p} = (p_1, p_2)$ is the parameter vector. This paragraph aims to study the sensitivity of the quantities of interest Q_{B} and $Q_{\mathrm{M},n}$ defined in equation (4.7) and (4.8), to perturbations of the KLE-based $H(B)$-curve model in the direction of the KLE's modes $\sqrt{\lambda_m} e_m$ at the sample mean $\hat{f}$. Thus, the sample mean reluctivity

$$\bar{\nu}_{\mathrm{i}}(t) = \hat{f}(t)/t \tag{4.69}$$

is used in equation (4.58) as nominal reluctivity in the iron domain D_{i} and for $m = 1, 2$ the reluctivity perturbations are defined by

$$\widetilde{\nu}_m(t) \coloneqq \frac{\sqrt{\lambda_m} e_m(t)}{t}. \tag{4.70}$$

We use the scaling of the reluctivity perturbations with $p_m = 1$ because the standard deviation of the random variables Y_m in the KLE (4.29), from which the parameters p_m are derived, is one. Due to the linearity of the Gâteaux derivative, the resulting values of the Gâteaux derivative can be scaled, e.g., with the upper bounds of $\mathcal{P}$ to estimate the maximal change of a quantity of interest caused by the corresponding perturbation.

The Gâteaux derivatives $\mathbf{A}'[\widetilde{\nu}_m]$ at $\bar{\nu}_{\mathrm{i}}$ are computed by solving for $m = 1, 2$ the problem (4.63) at a current excitation of $500\,\mathrm{A}$. Insertion of $\mathbf{A}'$ into the quantities of interest Q_{B} and $Q_{\mathrm{M},n}$ yields the Gâteaux derivatives

$$\widehat{Q}'_{\mathrm{B}}[\widetilde{\nu}_m] = B'_y[\widetilde{\nu}_m](\mathbf{x}) \tag{4.71}$$

$$\widehat{Q}'_{\mathrm{M},n}[\widetilde{\nu}_m] = B_n(r_0)'[\widetilde{\nu}_m]. \tag{4.72}$$

In Figure 4.10, the resulting absolute values $|B'_y[\widetilde{\nu}_m]|$ of the Gâteaux derivatives of Q_{B} at $\bar{\nu}_{\mathrm{i}}$ in the direction of $\widetilde{\nu}_m$ are plotted in logarithmic scale. Moreover, the Gâteaux derivatives $\mathbf{B}'[\widetilde{\nu}_m]$ are visualized on the two circles defined in Figure 4.2, and the corresponding Gâteaux derivatives $|B_n(r_0)'[\widetilde{\nu}_m]|$ of $Q_{\mathrm{M},n}$ are shown in Figure 4.11. For comparison, the simulated predictions of $\widehat{Q}_{\mathrm{B}}[\bar{\nu}_{\mathrm{i}}]$ and $\widehat{Q}_{\mathrm{M},n}[\bar{\nu}_{\mathrm{i}}]$ at $I = 500\,\mathrm{A}$ are shown in Figure 4.2 and Figure 4.11.
In the next paragraphs, these results are used to analyze the stability of the approximated and relaxed inverse problem 3.

Stability of the approximated and relaxed inverse problem for the field map quantity of interest The absolute values $|B'_y[\widetilde{\nu}_m]|$ of the Gâteaux derivatives of Q_{B} at $500\,\mathrm{A}$ shown in Figure 4.2 do not exceed the order of magnitude of $10^{-3}\,\mathrm{T}$ in the inner air gap. For the reluctivity perturbation $\widetilde{\nu}_1$, the maximum is attained towards the shims, for the perturbation $\widetilde{\nu}_2$ the maximum is attained towards the center of the air gap

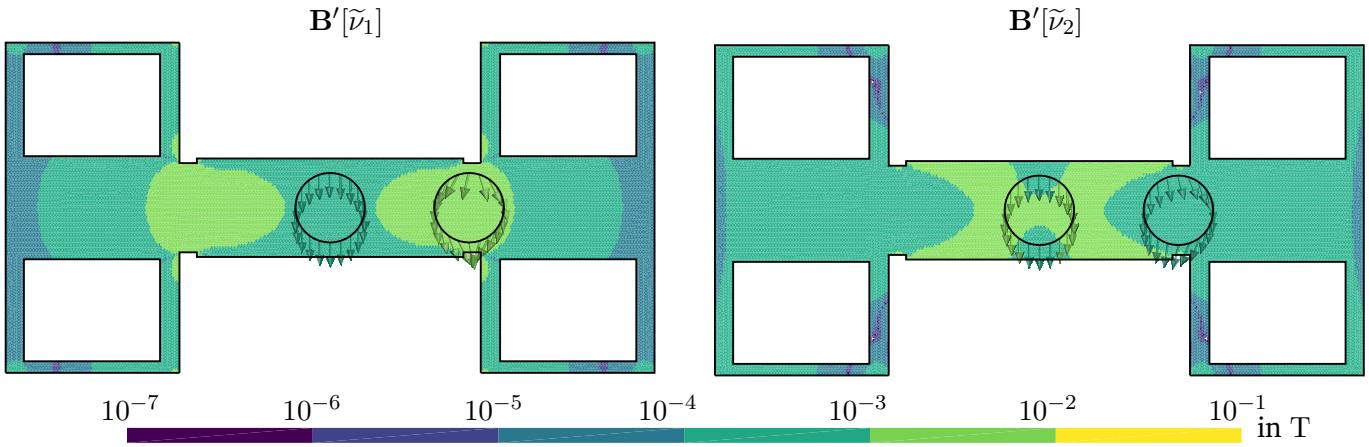

Figure 4.10: Gâteaux derivatives $\mathbf{B}'[\widetilde{\nu}_m]$ of the magnetic flux density in direction of the reluctivity perturbations corresponding to the scaled eigenfunctions of the KLE-based $H(B)$-curve model. On the inner air domain $|B'_y[\widetilde{\nu}_m]|$ is visualized, on the circles defined in Figure 4.2 $\mathbf{B}'[\widetilde{\nu}_m]$ is visualized. Figure adapted from [53].

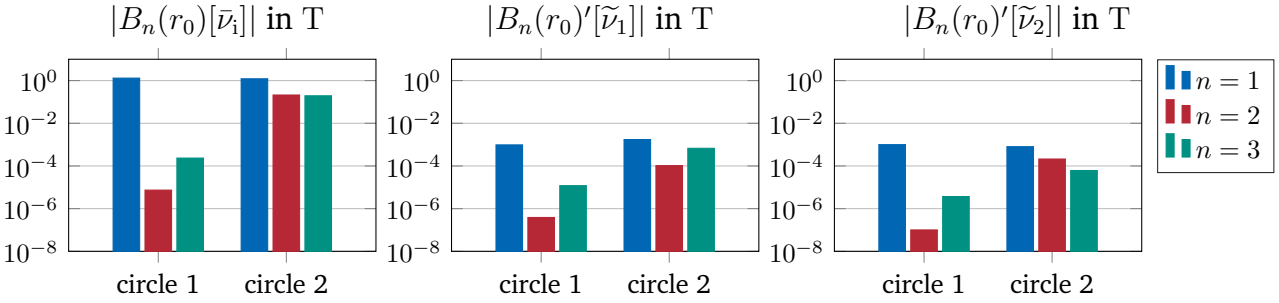

Figure 4.11: Absolute values of the normal multipoles at circle 1 and circle 2 (Figure 4.2) and their Gâteaux derivatives $|B_n(r_0)'[\widetilde{\nu}_2]|$ and $|B_n(r_0)'[\widetilde{\nu}_2]|$ in direction of the reluctivity perturbations corresponding to the scaled eigenfunctions of the KLE-based $H(B)$-curve model.

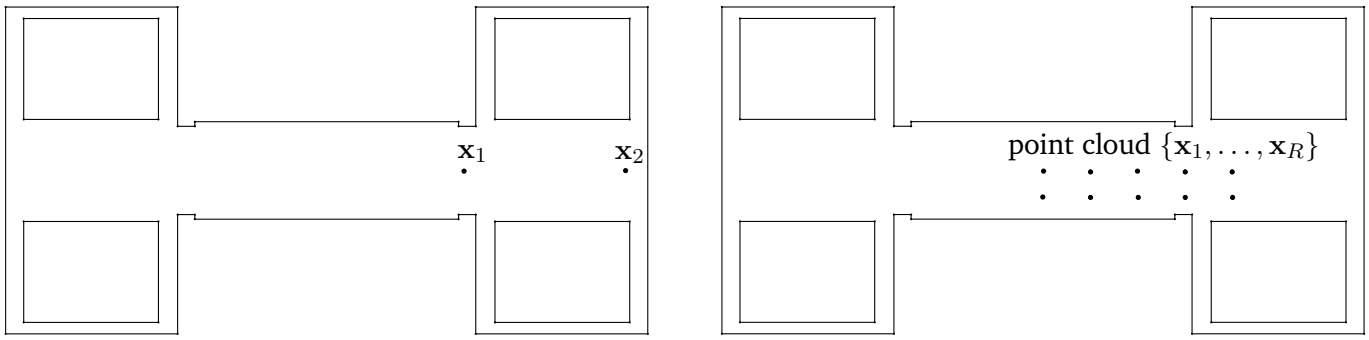

Figure 4.12: Left: Exaggerated positions $\mathbf{x}_1$ and $\mathbf{x}_2$ to demonstrate the stability and instability of the approximated and relaxed inverse problem 3. Right: Selected positions $\{\mathbf{x}_1, \ldots, \mathbf{x}_R\}$ to observe the quantity of interest $B_y(\mathbf{x}_r)$ for improved stability of the inverse problem. Figure adapted from [53].

(Figure 4.10). In both regions, the magnetic flux density $B_y[\bar{\nu}_\mathrm{i}]$ attains values around $1.25\,\mathrm{T}$. Consequently, a perturbation of $\mathbf{p}$ with $p_1 \geq 1$ or $p_2 \geq 1$ yields a relative change of the order of magnitude of 10^{-3} in the prediction of the quantity of interest Q_B in this region. We assumed that the standard deviation of the random measurement uncertainty of observations of Q_B relative to the maximal field is of the order of magnitude of 10^{-4}. Thus, the effects of the perturbation are distinguishable from the random measurement uncertainty. This is not necessarily the case in lower field regions between the source regions $D_\mathbf{J}$. To justify this claim, we compute the relative change

$$E^j_{\mathrm{rel,B}}(\mathbf{x}_r) \coloneqq \frac{|Q_\mathrm{B}(\mathbf{A}_j[\bar{\nu}_\mathrm{i}])(\mathbf{x_r}) - Q_\mathrm{B}(\mathbf{A}_j[\nu_\mathbf{p}])(\mathbf{x}_r)|}{|B^{\max}_{y,j}|} \tag{4.73}$$

between the prediction of Q_B for the unperturbed reluctivity $\bar{\nu}_\mathrm{i}$ and the perturbed reluctivity $\nu_\mathbf{p} = \bar{\nu}_\mathrm{i} + \widetilde{\nu}_1$ in two exaggerated positions $\mathbf{x}_1$ and $\mathbf{x}_2$ (Figure 4.12 left) in the inner air domain. Thereby, the position $\mathbf{x}_1$ is located centrally between the shims, where a high relative change of the quantity of interest is expected, and the position $\mathbf{x}_2$ is located far outside the center of the aperture, where a low relative change of the quantity of interest is expected according to the absolute values $|B'_y[\widetilde{\nu}_1]|$ of the Gâteaux derivative shown in Figure 4.11. For the excitation $I = 500\,\mathrm{A}$, we obtain in the two points $\mathbf{x}_1$ and $\mathbf{x}_2$ the relative changes

$$E^j_{\mathrm{rel,B}}(\mathbf{x}_1) = 1.31 \cdot 10^{-3} \tag{4.74}$$

$$E^j_{\mathrm{rel,B}}(\mathbf{x}_2) = 5.87 \cdot 10^{-5}. \tag{4.75}$$

Consequently, the inverse problem is unstable in $\mathbf{x}_2$ (in the sense of the definition given in Section 1.3.4) because small perturbations of the magnetic flux density observations in the order of magnitude below the standard deviation $\sigma = 10^{-4}$ of the relative random measurement uncertainty can lead to non-negligible differences in the solution ($\mathbf{p} = (0,0)$ versus $\mathbf{p} = (1,0)$ for $\mathcal{P} = [-2.06, 2.50] \times [-2.55, 1.38]$).
The choice of the position $\mathbf{x}_2$ is exaggerated on purpose to demonstrate the possibility of ill-posedness of the approximated and relaxed inverse problem 3. In contrast, in more reasonable and centered positions such as $\mathbf{x}_1$, the problem 3 is more stable. Consequently, the results of the sensitivity analysis can be used to identify suitable measurement positions. In the following, we use the point cloud $\{\mathbf{x}_1, \ldots, \mathbf{x}_R\}$ shown in Figure 4.12 (right) to solve the approximated and relaxed inverse problem 3 for observations of the quantity of interest Q_B.

Stability of the approximated and relaxed inverse problem for the multipole coefficient quantity of interest
A similar analysis of the stability of the approximated and relaxed inverse problem 3 formulated for the quantity of interest $Q_{\mathrm{M},n}$ can be conducted. According to the magnitude of the absolute values of the normal multipole coefficients shown in Figure 4.11, there is an almost perfect dipole field on circle 1. In contrast, on circle 2 for all $n = 1, 2, 3$ the absolute values $|B_n(r_0)[\bar{\nu}_\mathrm{i}]|$ of the normal multipole coefficients are around the same order of magnitude. The absolute values $|B_n(r_0)'[\widetilde{\nu}_m]|$ of the Gâteaux derivatives of the normal multipole coefficients in the direction of the reluctivity perturbations $\widetilde{\nu}_m$ are all above the standard deviation of the random measurement uncertainty except for the second coefficient $B_2(r_0)'[\widetilde{\nu}_m]$ on circle 1. To show that there are multipole coefficients for which the approximated and relaxed inverse problem is unstable, we compute the relative changes

$$E^j_{\mathrm{rel,M}}(n) \coloneqq \frac{|Q_{\mathrm{M},n}(\mathbf{A}_j[\bar{\nu}_\mathrm{i}]) - Q_{\mathrm{M},n}(\mathbf{A}_j[\nu_\mathbf{p}])|}{|(B_1(r_0))_j|} \tag{4.76}$$

between the prediction of $Q_{\mathrm{M},n}$ on circle 1 for the unperturbed reluctivity $\bar{\nu}_{\mathrm{i}}$ and the perturbed reluctivity $\nu_{\mathbf{p}} = \bar{\nu}_{\mathrm{i}} + \widetilde{\nu}_1$ at the excitation current $I = 500\,\mathrm{A}$. We obtain

$$E^j_{\mathrm{rel,M}}(1) = 7.35 \cdot 10^{-4} > \epsilon_{\mathrm{tol,M},1} \tag{4.77}$$

$$E^j_{\mathrm{rel,M}}(2) = 2.89 \cdot 10^{-7} < \epsilon_{\mathrm{tol,M},2} \tag{4.78}$$

$$E^j_{\mathrm{rel,M}}(3) = 9.01 \cdot 10^{-6} > \epsilon_{\mathrm{tol,M},3}. \tag{4.79}$$

With the same reasoning as above, we conclude that the approximated and relaxed inverse problem is unstable for $Q_{\mathrm{M},2}$ at circle 1 because variations in the observation caused by random measurement uncertainty can lead to large differences in solutions to the approximated and relaxed inverse problem 3. Again, the sensitivity analysis results can be used to determine appropriate multipole orders n and circle positions to improve the stability of the inverse problem.

4.3 Solution of the inverse problem

The goal of this section is to determine the parameters $\mathbf{p} \in \mathcal{P}$ of the KLE-based $H(B)$-curve model $f^M_{\mathrm{HB}}(\mathbf{p}, \cdot)$ from observations of a quantity of interest, i.e., solving the approximated and relaxed inverse problem 3. Having a solution $\mathbf{p}^{\mathrm{up}}$, we can update the system model (3.19) by predicting quantities of interest for given operation modes $\mathbf{s}$ with the mapping

$$\mathbf{s} \mapsto \mathcal{M}(\mathbf{p}^{\mathrm{up}}, \mathbf{s}). \tag{4.80}$$

The inverse problem 3 can be solved deterministically by solving an optimization problem or the statistical inversion methods introduced in Chapter 3 can be applied to estimate a solution. We restrict the analysis to observations of the field map quantity of interest Q_{B} defined in equation (4.7). For this quantity of interest, the forward model (4.54) is given by

$$\mathcal{H}(\mathbf{p}) = Q_{\mathrm{B}}(\mathbf{A}_j[\nu_{\mathbf{p}}])(\mathbf{x}_r) = B_{y,j}(\mathbf{x}_r) \tag{4.81}$$

depending on a current level I_j and an observation position $\mathbf{x}_r$. Notice that also the last term of this equation depends (implicitly) on $\mathbf{p}$. If we consider J current levels and R observation positions, we can summarize the single observations of the forward models (4.81) into the multi-observation forward model

$$\begin{aligned} \mathcal{H} : \mathcal{P} \subset \mathbb{R}^M &\rightarrow \mathcal{Q} \subset \mathbb{R}^{JR} \\ \mathbf{p} &\mapsto \mathbf{q} := (B_{y,1}(\mathbf{x}_1), \ldots, B_{y,J}(\mathbf{x}_1), \ldots, B_{y,1}(\mathbf{x}_1), \ldots, B_{y,J}(\mathbf{x}_R)) \end{aligned} \tag{4.82}$$

for which we use the same letter $\mathcal{H}$ by abuse of notation. The right-hand side $\mathbf{q}$ is also referred to as model prediction. Data that results from measurements or other simulations, and that is comparable to the prediction $\mathbf{q}$ is referred to as observation $\mathbf{q}^{\mathrm{obs}}$.

Observation training data Since the material of the magnet system "PXMBHGGHWC-OR000113" does not coincide with the available ARMCO® or ferrosilicon specimens whose measured (B, H)-data was used to build the KLE-based $H(B)$-curve model f^M_{HB}, we can not use measured magnetic flux density observations $\mathbf{q}^{\mathrm{obs}}$ in this section. Instead, simulated observation data $\mathbf{q}^{\mathrm{obs}}$ is used. To generate this observation data, a parameter vector $\mathbf{p}^{\mathrm{true}} \in \mathcal{P}$ is selected that represents the ground truth. We set $\mathbf{p}^{\mathrm{true}} = (1.5, -2)$ and obtain by insertion into equation (4.53) the ground truth reluctivity function

$$\nu_{\mathbf{p}^{\mathrm{true}}}(t) = \frac{f^2_{\mathrm{HB}}(\mathbf{p}^{\mathrm{true}}, t)}{t}. \tag{4.83}$$

Moreover, random measurement uncertainty is included in the simulated observation data using the additive noise model introduced in equation (3.21). Therefore, the random vector $\mathbf{U} : \Omega \to \mathbb{R}^{JR}$ is defined with $\mathbf{U} \sim \mathcal{N}(\mathbf{0}, \mathbf{\Sigma})$, where the covariance matrix is chosen by $\mathbf{\Sigma} = \sigma^2 \mathbb{I}$ with $\sigma \coloneqq 10^{-4}\,\mathrm{T}$, according to the standard deviation of modern day measurement equipment.
Let $\mathbf{u} = (u_{1,1}, \dots, u_{J,1}, \dots, u_{1,R}, \dots, u_{J,R}) \in \mathbb{R}^{JR}$ be a realization of $\mathbf{U}$. The observations $\mathbf{q}^{\mathrm{obs}}$ are then defined by

$$\mathbf{q}^{\mathrm{obs}} \coloneqq \mathcal{H}(\mathbf{p}^{\mathrm{true}}) + \mathbf{u}. \tag{4.84}$$

The $(r-1)J + j$-th component of $\mathbf{q}^{\mathrm{obs}}$ is given by

$$B_{y,j}^{\mathrm{obs}}(\mathbf{x}_r) \coloneqq q_{(r-1)J+j}^{\mathrm{obs}} = Q_{\mathrm{B}}(\mathbf{A}_j[\nu_{\mathbf{p}^{\mathrm{true}}}])(\mathbf{x}_r) + u_{(r-1)J+j} = B_{y,j}(\mathbf{x}_r) + u_{(r-1)J+j}. \tag{4.85}$$

In the following, we refer to $\mathbf{q}^{\mathrm{obs}}$ also as observation training data. We use $J = 8$ equally distributed current excitations $I_j \in [20\,\mathrm{A}, 450\,\mathrm{A}]$ and the $R = 10$ observation points in the air gap, which are visualized in Figure 4.12.
The ground truth prediction $Q_{\mathrm{B}}(\mathbf{A}_j[\nu_{\mathbf{p}^{\mathrm{true}}}])(\mathbf{x}_r)$ is computed by solving the forward problem. For each evaluation of the forward model $\mathcal{H}$ defined in equation (4.82), the boundary value problem of magnetostatics has to be solved J times for the different source current densities $\mathbf{J}_j$ with $1 \le j \le J$. Since the magnetostatic problems for different currents are independent of each other, they are solved in parallel.

4.3.1 Deterministic model updating

Given the observation training data $\mathbf{q}^{\mathrm{obs}} \in \mathbb{R}^{JR}$ defined in equation (4.85) with components $B_{y,j}^{\mathrm{obs}}(\mathbf{x}_r)$, a deterministic update of the parameter vector $\mathbf{p} = (p_1, p_2) \in \mathcal{P}$ can be determined by solving the following optimization problem

$$\begin{aligned}
&\min_{\mathbf{p}\in\mathcal{P}} \quad g(\mathbf{p}) \coloneqq \sum_{r,j} \left\| B_{y,j}^{\mathrm{obs}}(\mathbf{x}_r) - Q_{\mathrm{B}}(\mathbf{A}_j[\nu_{\mathbf{p}}])(\mathbf{x}_r) \right\|^2 \\
&\text{s.t.: } \forall 1 \le j \le J \text{ and } \forall \mathbf{v} \in \mathcal{V} \\
&\int_D \nu(\|\operatorname{curl} \mathbf{A}_j[\nu_{\mathbf{p}}]\|) \operatorname{curl} \mathbf{A}_j[\nu_{\mathbf{p}}] \cdot \operatorname{curl} \mathbf{v} \,\mathrm{d}V = \int_D \mathbf{v} \cdot \mathbf{J}_j \,\mathrm{d}V \\
&\nu(t) = \begin{cases} 1/t \left(\hat{f}(t) + \sum_{m=1}^{2} \sqrt{\lambda_m}\, p_m\, e_m(t) \right) & \text{in } D_{\mathrm{i}} \\ \nu_0 & \text{in } D_{\mathrm{a}}. \end{cases}
\end{aligned} \tag{4.86}$$

Notice that using the forward model (4.81), the objective function can be rewritten as $g(\mathbf{p}) = \left\| \mathbf{q}^{\mathrm{obs}} - \mathcal{H}(\mathbf{p}) \right\|^2$.

We solve the optimization problem using particle swarm optimization [81]. The advantage of the particle swarm optimizer is that it does not require gradients of the objective function g, there is an implementation available in MATLAB® [95, 130], and it is globally convergent. Particle swarm optimization is based on iteratively evaluating the objective function on a set of particles located in the search space $\mathcal{P}$ whose position is updated in each iteration. Initially, the particle positions are chosen randomly and each particle is related to an initially also randomly chosen velocity vector $\mathbf{w} \in \mathcal{P}$, which determines its position in the next iteration. Let $\mathbf{p}(i)$ and $\mathbf{w}(i)$ the position and the velocity of a particle in the swarm at the beginning of the i-th iteration of the particle swarm algorithm. First, the objective function $g(\mathbf{p}(i))$ is evaluated. The algorithm keeps track of the individual best position $\mathbf{p}_{\mathrm{best}}^{\mathrm{ind}}$ of each particle and the global best position $\mathbf{p}^{\mathrm{opt}}$ discovered by any particle.

Then, the subsequent position $\mathbf{p}(i+1)$ of the particle is determined by $\mathbf{p}(i+1) = \mathbf{p}(i) + \mathbf{w}(i+1)$, where the updated velocity vector is given by

$$\mathbf{w}(i+1) = a_1\mathbf{w}(i) + a_2u_1(\mathbf{p}_{\text{best}}^{\text{ind}} - \mathbf{p}(i)) + a_3u_2(\mathbf{p}_{\text{best}}^{\text{sub}} - \mathbf{p}(i)). \tag{4.87}$$

Thereby, $\mathbf{p}_{\text{best}}^{\text{sub}}$ is the best position of a particle within a randomly chosen subgroup of the swarm at the beginning of the i-th iteration, the coefficients $a_1, a_2, a_3 \in \mathbb{R}$ are weighting parameters, and $u_1, u_2 \in \mathbb{R}$ are realizations of an uniformly distributed random variable $U \sim U(0,1)$. If the updated position $\mathbf{p}(i+1)$ is outside $\mathcal{P}$, the particle is placed on the boundary of $\mathcal{P}$, and the velocity in the direction of the normal to the boundary is set to zero. When a stopping criterion is reached, the particle swarm optimizer returns the global best position $\mathbf{p}^{\text{opt}}$ discovered by any particle. We use a swarm of 20 particles and as a stopping criterion that the relative change of the best observed objective function value within the last 20 iterations is less than 10^{-6}. This criterion is satisfied after 22 iterations and the algorithm returns $\mathbf{p}^{\text{opt}} = (1.61, -2.05)$. Thus, the objective function g and with that the forward model $\mathcal{H}$ are evaluated 440 times in total by the optimization algorithm to obtain $\mathbf{p}^{\text{opt}}$.

To prove that $\mathbf{p}^{\text{opt}}$ is a solution to the approximated and relaxed inverse problem 3 according to the condition given in (4.56), we evaluate

$$\frac{1}{JR}\sum_{j,r}\frac{|B_{y,j}^{\text{obs}}(\mathbf{x}_r) - Q_{\text{B}}(\mathbf{A}_j[\nu_{\mathbf{p}^{\text{opt}}}])(\mathbf{x}_r)|}{|B_{y,j}^{\max}|} \tag{4.88}$$

on the observation training data $B_{y,j}^{\text{obs}}(\mathbf{x}_r)$ defined in equation (4.85). With $J = 8$ and $R = 10$,

$$\frac{1}{80}\sum_{j,r}\frac{|B_{y,j}^{\text{obs}}(\mathbf{x}_r) - Q_{\text{B}}(\mathbf{A}_j[\nu_{\mathbf{p}^{\text{opt}}}])(\mathbf{x}_r)|}{|B_{y,j}^{\max}|} = 1.16 \cdot 10^{-5} < 10^{-4} = \epsilon_{\text{tol,B}} \tag{4.89}$$

is obtained. Consequently, $\mathbf{p}^{\text{opt}} = (1.61, -2.05)$ is a solution to the approximated and relaxed inverse problem 3.

Tikhonov regularization If the finite-dimensional approximation of the search space from the set of functions $f_{\text{HB}} \in C^1(I, \mathbb{R})$ that satisfy the properties of Assumption 1 to the search space $\mathcal{P} \subset \mathbb{R}^2$ is not sufficient to regularize the inverse problem, the objective function g can be modified using the Tikhonov regularization [136]. Let X, Z be Hilbert spaces and $\mathcal{H} : X \to Z$ be a mapping between the two spaces. An inverse problem is defined by: given $y \in Y$ find $x \in X$ such that $\mathcal{H}(x) = y$. The generalized Tikhonov functional T_a of the inverse problem has the form

$$T_a(x; z) = d(\mathcal{H}(x), z) + aR(x) \tag{4.90}$$

where $d : Z \times Z \to \mathbb{R}$ is a data discrepancy function, e.g., a metric on Z, $a > 0$ is a regularization parameter, and $R : X \to \mathbb{R}$ is a regularization functional [136, Section 2.4]. Instead of minimizing the objective function g in the optimization problem (4.86), the generalized Tikhonov functional

$$g_{\text{reg}}(\mathbf{p}) \coloneqq g(\mathbf{p}) + a\,\|\mathbf{p} - \mathbb{E}[\mathbf{Y}]\|_{\mathbf{\Sigma}^{-1}}^2 \tag{4.91}$$

can be minimized. Thereby, $\mathbb{E}[\mathbf{Y}]$ is the expected value, and $\mathbf{\Sigma}$ is the covariance matrix of the random vector $\mathbf{Y}$ of the truncated KLE (4.40). Notice that by definition of the KLE and due to the assumption that the random variables are independent, it holds that $\mathbb{E}[\mathbf{Y}] = \mathbf{0}$ and $\mathbf{\Sigma} = \mathbb{I}$. This definition of the regularization functional R penalizes deviations of p_m from $\mathbb{E}[Y_m]$ the more, the smaller the variance of Y_m. Thus, expert knowledge of reasonable values of $\mathbf{p}$ according to the material measurements is incorporated. This regularization is related to determining the maximum a posteriori estimate defined in Section 3.3.1.

4.3.2 Stochastic model updating

In the stochastic setting, the parameters $\mathbf{p}$ and and the observations $\mathbf{q}^{\mathrm{obs}}$ are understood as realizations of random vectors $\mathbf{P}, \mathbf{Q}^{\mathrm{obs}}$ over a common sample space Ω. We assume that they are related via the forward model $\mathcal{H}$ (4.82) and the additive noise model (3.21)

$$\mathbf{Q}^{\mathrm{obs}} = \mathcal{H}(\mathbf{P}) + \mathbf{U}, \tag{4.92}$$

where $\mathbf{U} : \Omega \to \mathbb{R}^{JR}$ with $\mathbf{U} \sim \mathcal{N}(\mathbf{0}, \mathbf{\Sigma})$ and $\mathbf{\Sigma} = \sigma^2 \mathbb{I}$ with $\sigma \coloneqq 10^{-4}\,\mathrm{T}$ is a random vector that reflects the random measurement uncertainty of the measurement equipment.

In Chapter 3, the fundamentals of statistical inversion to determine the posterior probability density function $\pi_{\mathbf{P}|\mathbf{Q}^{\mathrm{obs}}}$ with Bayesian inference were introduced. Thereby, $\pi_{\mathbf{P}|\mathbf{Q}^{\mathrm{obs}}}$ describes the conditional probability density function of the random parameter vector $\mathbf{P}$ given the observation $\mathbf{Q}^{\mathrm{obs}} = \mathbf{q}^{\mathrm{obs}}$. Consequently, using stochastic model updating, we can not only estimate a deterministic parameter update $\mathbf{p}^{\mathrm{up}}$ but also quantify its uncertainty.
To apply Bayesian inference, a prior density function π_0 that reflects prior knowledge on the distribution of the random parameter vector $\mathbf{P}$ and a likelihood model $\pi_{\mathbf{Q}^{\mathrm{obs}}|\mathbf{P}}$ are required. Inserting the noise model into the probability density function $\pi_{\mathbf{U}}$ yields the likelihood model given in equation (3.27). The components p_m of the parameter vector $\mathbf{p} \in \mathbb{R}^M$ in the KLE-based $H(B)$-curve model $f^M_{\mathrm{HB}}(\mathbf{p}, \cdot)$, defined in equation (4.45), were defined as realizations of the random variables Y_m of the truncated KLE. Thus, we can use the knowledge of the stochastic properties of the random variables Y_m to build a prior model. According to the Karhunen-Loève Theorem [63, Theorem 4.6] the random variables Y_m have zero mean and are pairwise orthonormal (see equation (4.31)). Consequently, they have unit variance. Computing the KLE-based $H(B)$-curve model for the ARMCO® Pure Iron specimens yielded realizations Y_m^k for each random variable Y_m. By conducting the Kolmogorov-Smirnov test, introduced in Chapter 3, we verify that $Y_m \sim \mathcal{N}(0, 1)$. Since we assumed that the random variables are mutually independent, we can conclude that $\mathbf{Y} \sim \mathcal{N}(\mathbf{0}, \mathbb{I})$. As a result, the prior distribution of $\mathbf{P}$ is a normal distribution $\pi_0 \sim \mathcal{N}(\mathbf{m}_0, \mathbf{C}_0)$ with $\mathbf{m}_0 = \mathbf{0}$ and $\mathbf{C}_0 = \mathbb{I}$.

Since the $H(B)$-curve defined by the KLE-based $H(B)$-curve model is non-linear in B, the forward model $\mathcal{H}$ is non-linear. Thus, the posterior density function and the maximum a posteriori estimate are not easily determinable with the closed-form expressions in equations (3.30) and (3.35). Instead, we explore in this chapter, analogously to the non-linear case in Chapter 5, the posterior distribution by drawing samples using the Metropolis-Hastings algorithm with the preconditioned Crank-Nicolson proposal. Since the parameter space $\mathcal{P}$ is only two-dimensional, the movement of the Markov chain and the covariance ellipses of the prior and the posterior distribution can be visualized easily. Alternatively, due to the low dimensional parameter space, also numerical integration methods could be considered to compute the expected value and the covariance of the posterior distribution using equations (3.1) and (3.3) instead of sampling.
The Metropolis-Hastings algorithm is initialized with the expected value $\mathbf{m}_0 = \mathbf{0}$ of the prior distribution. The step size s tunes the proposal density of the Crank-Nicolson proposal distribution $\mathcal{N}(\sqrt{1 - s^2}\widetilde{\mathbf{p}}, s\mathbf{C}_0)$, where $\widetilde{\mathbf{p}}$ is the current value of the Markov chain and $\mathbf{C}_0$ is the covariance matrix of the prior distribution. The smaller the step size s, the higher the probability that the Euclidean distance between $\widetilde{\mathbf{p}}$ and the proposal for the next sample by the Metropolis-Hastings algorithm is small. For the choice of the step size $s = 1/4$, an acceptance rate of 8.75% is reached after 2000 samples. For $s = 1/8$, we obtain an acceptance rate of 21.66% after drawing 1000 samples. The 2D paths of the samples drawn by the two Markov chains are shown in Figure 4.14. The corresponding decays of the residual

$$E^{\mathrm{pCN}}(i) := \frac{1}{2} \left\| \mathcal{H}(\mathbf{p}_i) - \mathbf{q}^{\mathrm{obs}} \right\|^2_{\mathbf{\Sigma}^{-1}} \tag{4.93}$$

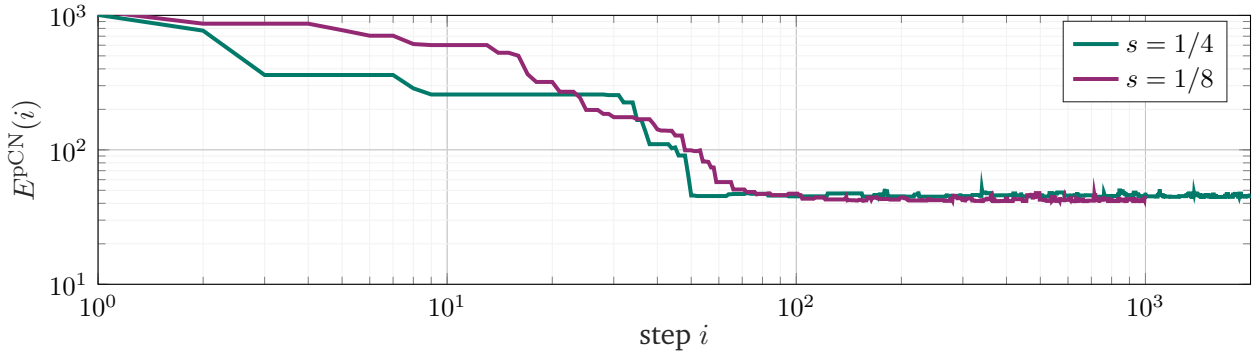

Figure 4.13: Residual $E^{\mathrm{pCN}}(i)$ (defined in equation (4.93)) between the observation $\mathbf{q}^{\mathrm{obs}}$ and the prediction $\mathcal{H}(\mathbf{p}_i)$ with the i-th sample of the Metropolis-Hastings algorithm with preconditioned Crank-Nicolson proposal for different step sizes s.

between the observation $\mathbf{q}^{\mathrm{obs}}$ and the prediction $\mathcal{H}(\mathbf{p}_i)$ with the i-th sample of the Markov chain are shown in Figure 4.13. This residual is the key quantity of the Metropolis-Hastings algorithm with preconditioned Crank-Nicolson proposal to determine with equation (3.45) the acceptance probability of the sample that is proposed by the Metropolis-Hastings algorithm.
After 50 steps for $s = 1/4$ and respectively 80 steps for $s = 1/8$, the residual E^{pCN} reaches a plateau. Therefore, we consider the first 50 (respectively 80) steps as burn-in and omit these samples in further data analysis. It can be observed that for $s = 1/8$ the the residual E^{pCN} and thus the values of the samples of the Markov chain change more often. Consequently, we observe for $s = 1/8$ a higher acceptance rate. However, the improvement of the residual E^{pCN} per step is smaller on average since the proposal is closer to the preceding sample in the Markov chain, leading to a longer burn-in phase for $s = 1/8$. Moreover, it can be observed that between the 100-th and the 1000-th step of the Markov chains the residual E^{pCN} for $s = 1/8$ is in almost every step slightly smaller than for $s = 1/4$, which is also a consequence of proposing close samples after already having found a sample with small residual.

Omitting the burn-in, we compute from the remaining samples the sample mean $\mathbf{m}_1$ and the sample covariance $\mathbf{C}_1$ with the equations (3.4) and (3.5) to estimate the posterior mean and the posterior covariance. For the sample mean, we obtain

$$\mathbf{m}_1 = \begin{cases} (1.44, -1.95) & s = 1/4, \ \text{1950 samples} \\ (1.48, -2.01) & s = 1/8, \ \text{920 samples.} \end{cases} \tag{4.94}$$

The covariance ellipses corresponding to $\mathbf{C}_1$ whose half-axes have the length of $1\sigma, 2\sigma$, and 3σ and point into the direction of the eigenvectors of $\mathbf{C}_1$ are shown in Figure 4.14 to visualize the posterior distributions. The observed sample variances for the Markov chain with step size $s = 1/4$ and 2000 steps are slightly smaller than for $s = 1/8$ and 1000 steps. It can be observed that the ground truth parameter $\mathbf{p}^{\mathrm{true}}$ lies within the 1σ-ellipse of both computed posterior distributions and the volumes of the posterior ellipses are significantly smaller than the volume of the prior ellipse, indicating smaller uncertainties.

For stochastic model updating, the posterior sample mean $\mathbf{m}_1$ is inserted into the forward model. We restrict the further analysis to sample mean $\mathbf{m}_1 = (1.44, -1.95)$ obtained with the step size $s = 1/4$ and after drawing 2000 samples. Analogously to the deterministic solution, we evaluate equation (4.88) on the observation training data $B^{\mathrm{obs}}_{y,j}(\mathbf{x}_r)$ (4.85) with $J = 8$ and $R = 10$ to proof that $\mathbf{m}_1$ is a solution to the approximated and relaxed inverse problem 3 according to the condition specified in (4.56). Indeed, it can be

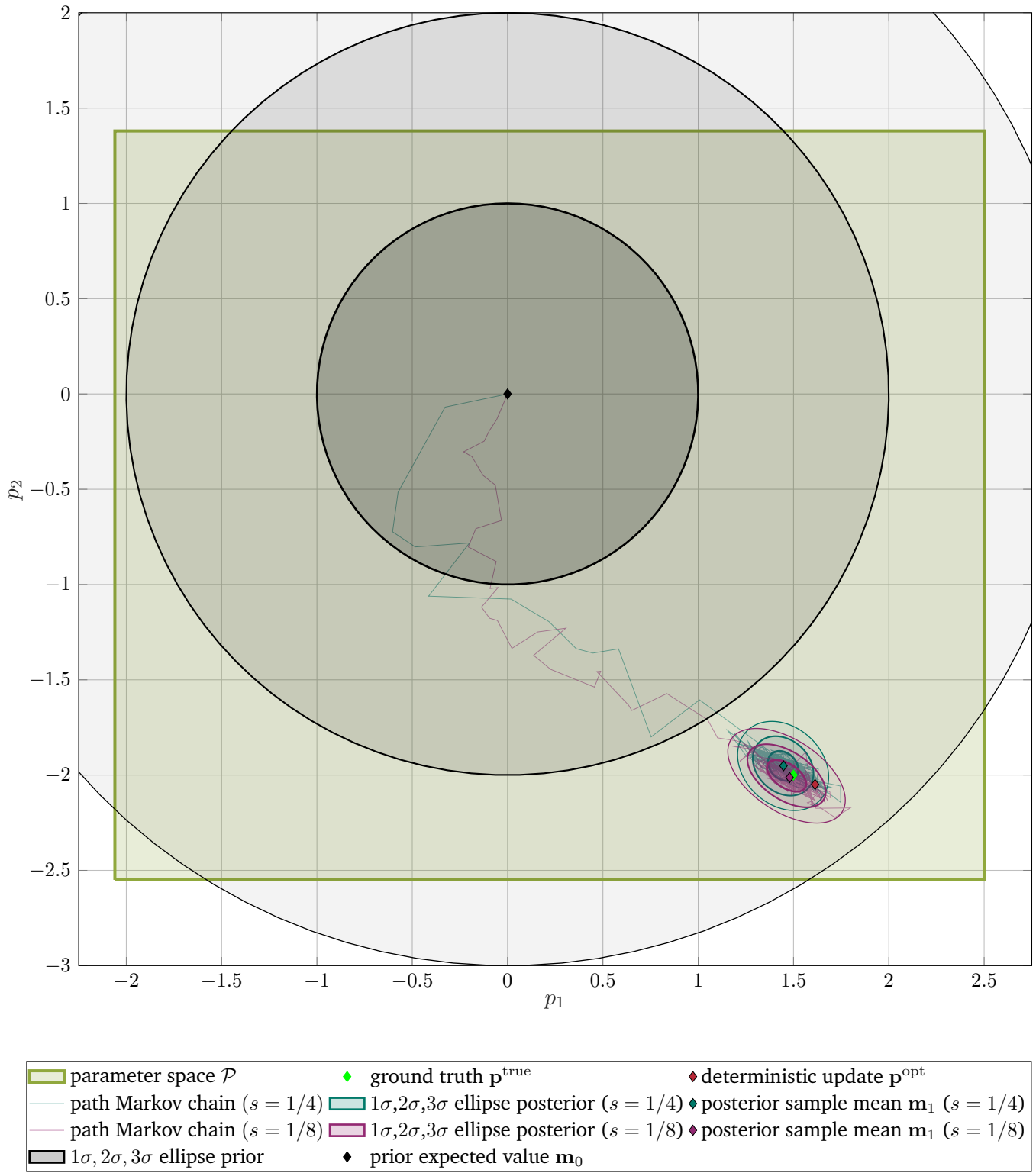

Figure 4.14: Comparison between the prior distribution and the sampled posterior distributions, the ground truth solution $\mathbf{p}^{\text{true}}$ and the deterministic model update $\mathbf{p}^{\text{opt}}$.

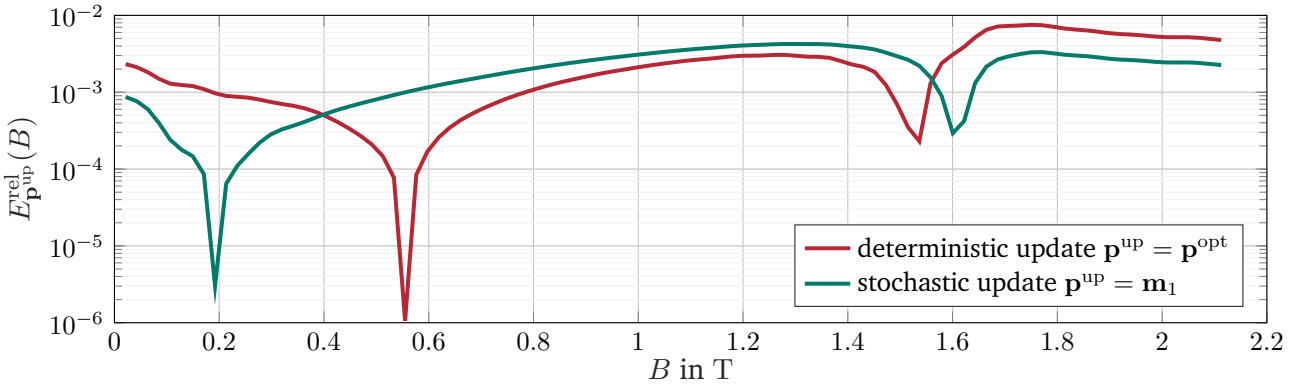

Figure 4.15: Relative error $E^{\mathrm{rel}}_{\mathbf{p}^{\mathrm{up}}}(B)$ (defined in equation (4.97)) between the updated $H(B)$-curve $f^2_{\mathrm{HB}}(\mathbf{p}^{\mathrm{up}}, B)$ and the ground truth $H(B)$-curve $f^2_{\mathrm{HB}}(\mathbf{p}^{\mathrm{true}}, B)$.

verified that

$$\frac{1}{80}\sum_{j,r}\frac{|B^{\mathrm{obs}}_{y,j}(\mathbf{x}_r) - Q_{\mathrm{B}}(\mathbf{A}_j[\nu_{\mathbf{m}_1}])(\mathbf{x}_r)|}{|B^{\mathrm{max}}_{y,j}|} = 8.99\cdot 10^{-6} < 10^{-4} = \epsilon_{\mathrm{tol,B}}. \tag{4.95}$$

4.3.3 Evaluation of the updated models

The $H(B)$-curve in the system model $\mathcal{M}(\mathbf{p}, \mathbf{s})$ of the iron-dominated accelerator magnet is updated by inserting the parameter vector

$$\mathbf{p}^{\mathrm{up}} := \begin{cases} \mathbf{p}^{\mathrm{opt}} & \text{deterministic model updating} \\ \mathbf{m}_1 & \text{stochastic model updating.} \end{cases} \tag{4.96}$$

To assess the quality of the updates we compare the resulting KLE-based $H(B)$-curve models and predictions of the quantity of interest Q_{B} with the system model $\mathcal{M}(\mathbf{p}^{\mathrm{up}}, \cdot)$.
The relative error

$$E^{\mathrm{rel}}_{\mathbf{p}^{\mathrm{up}}}(B) := \frac{|f^M_{\mathrm{HB}}(\mathbf{p}^{\mathrm{up}}, B) - f^M_{\mathrm{HB}}(\mathbf{p}^{\mathrm{true}}, B)|}{f_{\mathrm{HB}}(\mathbf{p}^{\mathrm{true}}, B)} \tag{4.97}$$

between the KLE-based $H(B)$-curve models for the ground truth parameter $\mathbf{p}^{\mathrm{true}}$ and the updated parameter $\mathbf{p}^{\mathrm{up}}$ is shown in Figure 4.15. The relative error does not exceed 1% for both, the deterministic and the stochastic model update.

The prediction of the field map quantities of interest Q_{B} of the (deterministically and stochastically) updated forward model $\mathcal{M}(\mathbf{p}^{\mathrm{up}}, \cdot)$ are compared at different positions $\mathbf{x}$ in the inner air gap and for $J = 6$ currents $I_j \in [20, 600]$ A. Contrary to the evaluations in equations (4.89) and (4.95), we are not interested in comparing the predictions to the training data defined in equation (4.85), but to ground truth observation data $Q_{\mathrm{B}}(\mathbf{A}_j[\nu_{\mathbf{p}^{\mathrm{true}}}])(\mathbf{x})$ for current excitations I_j and in positions $\mathbf{x} \in D$ that were not part of the training data set. Using equation (4.81), we evaluate the relative error

$$E^{\mathrm{rel}}_{\mathrm{B},j}(\mathbf{x}) := \frac{|Q_{\mathrm{B}}(\mathbf{A}_j[\nu_{\mathbf{p}^{\mathrm{up}}}])(\mathbf{x}) - Q_{\mathrm{B}}(\mathbf{A}_j[\nu_{\mathbf{p}^{\mathrm{true}}}])(\mathbf{x})|}{|B^{\mathrm{max}}_{y,j}|}, \tag{4.98}$$

where $|B^{\mathrm{max}}_{y,j}|$ is the absolute value of the maximal central magnetic flux density component B_y predicted by $\mathcal{M}(\mathbf{p}^{\mathrm{true}}, \cdot)$ that varies between $0.27\,\mathrm{T}$ for $I_1 = 102\,\mathrm{A}$ and $1.51\,\mathrm{T}$ for $I_J = 600\,\mathrm{A}$. A common threshold for

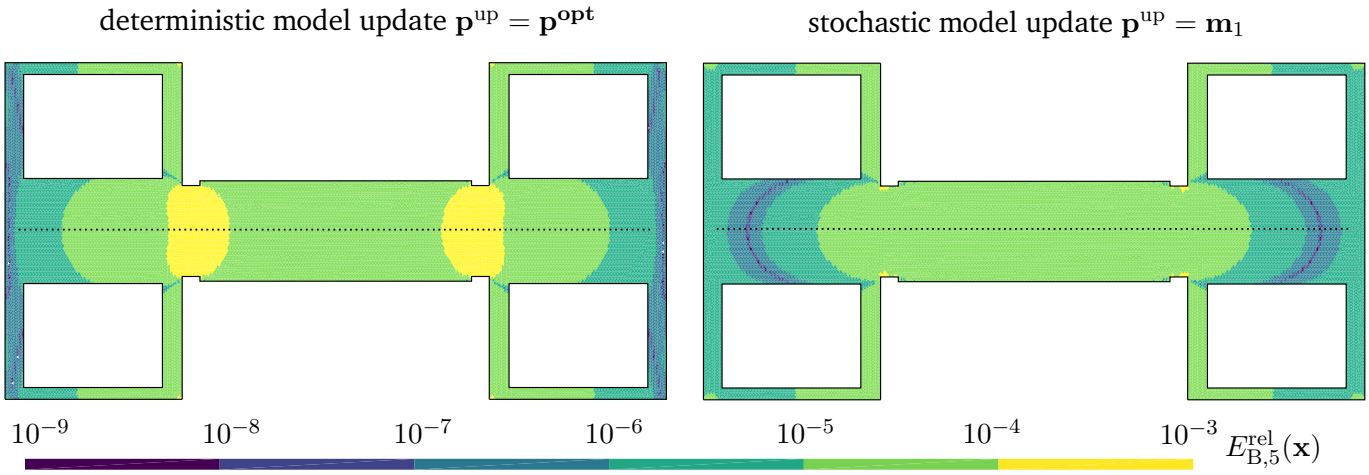

Figure 4.16: Relative error $E^{\mathrm{rel}}_{\mathrm{B},5}(\mathbf{x})$ (defined in equation (4.98)) of the prediction of the quantity of interest Q_{B} with the updated models compared to the ground truth prediction at $I_5 = 517\,\mathrm{A}$.

sufficient accuracy is that the relative error $E^{\mathrm{rel}}_{\mathrm{B},j}(\mathbf{x})$ should not exceed 1 unit in 10000.
The relative error $E^{\mathrm{rel}}_{\mathrm{B},5}(\mathbf{x})$ for the excitation current $I_5 = 517\,\mathrm{A}$ for all positions $\mathbf{x}$ in the inner air domain is shown in Figure 4.16. In all positions and for both model updates, the relative error $E^{\mathrm{rel}}_{\mathrm{B},5}(\mathbf{x})$ does not exceed 1 unit in 1000 and attains its maximum close to the shims. Besides the regions close to the shims, the accuracy requirement of a relative error $E^{\mathrm{rel}}_{\mathrm{B},j}(\mathbf{x})$ smaller than 1 unit in 10000 is met. In most positions, the relative error of the stochastic model update is smaller or equal to the relative error of the deterministic model update. The opposite holds only in a few positions close to the boundary. These observations can be explained by the following reasons:

1. For the excitation current $I_5 = 517\,\mathrm{A}$, the absolute value of the magnetic flux density is $1.55\,\mathrm{T}$ or more in the parts of the yoke close to the center of the air gap. In this domain, the relative error $E^{\mathrm{rel}}_{\mathbf{m}_1}(B)$ of the stochastically updated $H(B)$-curves is smaller than the relative error $E^{\mathrm{rel}}_{\mathbf{p}^{\mathrm{opt}}}(B)$ (see Figure 4.15). Consequently, the prediction with the stochastically updated model is slightly better.

2. Both solution parameter vectors $\mathbf{p}^{\mathrm{opt}}$ and $\mathbf{m}_1$ differ slightly more from the ground truth parameter vector $\mathbf{p}^{\mathrm{true}}$ in the first component than in the second component. Thus, the maximal relative error $E^{\mathrm{rel}}_{\mathrm{B},5}(\mathbf{x})$ is observed where the quantity of interest Q_{B} is the most sensitive to perturbations of the reluctivity in the direction of the parameter p_1 (see Figure 4.10 left).

Moreover, we evaluate $E^{\mathrm{rel}}_{\mathrm{B},j}(\mathbf{x})$ in positions $\mathbf{x}$ along the central axis of the air gap (dotted lines sketched in Figure 4.16) for $J = 5$ excitation currents $I_j \in [102, 600]\mathrm{A}$. A visualization of the resulting relative errors is given in Figure 4.17. For the excitation current levels $I_j = 102, 268, 434\,\mathrm{A}$ that interpolate the excitation currents for which data was included in observation training data (4.85), the relative error $E^{\mathrm{rel}}_{\mathrm{B},j}(\mathbf{x})$ is less than 1 unit in 10000. For the stochastic model update, this statement also holds in almost all positions $\mathbf{x}$ along the central line for the two higher excitation currents of $I_j = 517, 600\,\mathrm{A}$. The relative error $E^{\mathrm{rel}}_{\mathrm{B},j}(\mathbf{x})$ of the deterministic model update does not exceed 3 units in 10000 for all of the evaluated current excitations.

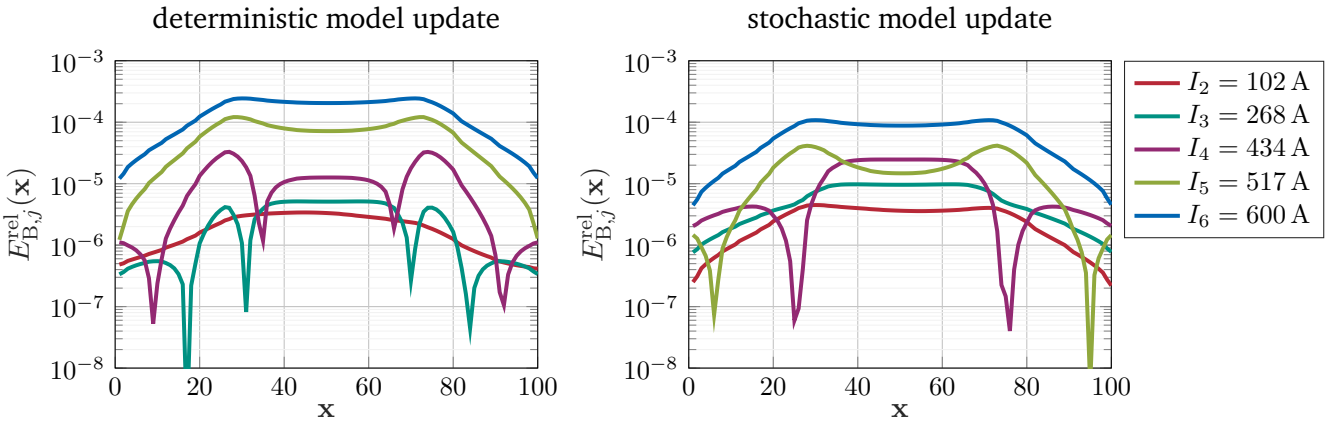

Figure 4.17: Relative error $E^{\mathrm{rel}}_{\mathrm{B},j}(\mathbf{x})$ (defined in equation (4.98)) of the prediction of the quantity of interest Q_{B} with the updated models compared to the ground truth prediction. The evaluation positions $\mathbf{x}$ are chosen along the dotted lines marked in Figure 4.16.

4.4 Summary

In this chapter, we updated the $H(B)$-curve of the component-centric system model (Section 1.2.2) of an iron-dominated magnet to improve its predictions of field-related quantities of interest. Thereby, we considered a test case inspired by the magnet system "PXMBHGGHWC-OR000113". An inverse problem as defined in Section 1.3.4 had to be solved to determine the update. For regularization, we used a low-rank approximation of the problem by considering only solutions in the span of a data-driven stochastic $H(B)$-curve model with only two parameters. This curve model was derived with the truncated KLE from measured (B, H)-data tables of yoke material specimens.
The parameters of the KLE-based $H(B)$-curve model were determined using deterministic model updating based on optimization, and stochastic model updating by applying Bayesian inference as introduced in Section 3.2. Specifically, Markov chain Monte Carlo sampling (Section 3.3.2) with the Metropolis-Hastings algorithm was applied because of the nonlinearity of the forward model. Due to the only two-dimensional parameter space, a visualization of the Markov chain was possible. The same method will also be applied in Chapter 5 to parameter spaces of higher dimensions.

5 Update of the magnetization of circular Halbach arrays

Multipole magnets that are composed of specifically circularly arranged permanent magnet (PM) blocks, are known as *Halbach arrays* [66]. The magnetization strengths and directions of the single blocks are crucial to obtain the specified multipole field. The magnet system of the FASER experiment [51] comprises three $0.57\,\mathrm{T}$ dipole magnets, each consisting of a series of circular Halbach arrays [3, Chapter 5]. They were designed, built, and measured at CERN. Magnetic flux density measurements of the built magnets revealed a variation of the higher-order multipole coefficients that differs from the prediction of these coefficients with the numerical design model. In this chapter, we combine a 3D FEM model of a FASER dipole with measurement data of the magnetization of the PM blocks, and measurements of the magnetic flux density and the multipole coefficients of the built magnet. The goal is a data-driven update of the magnetization of the PM blocks in the numerical design model to match the predictions with the measured observations. Parts of this chapter are already published in the author's paper [52].

Halbach arrays Karl Halbach derived the ideal magnetization of permanently magnetized material between two concentric circles such that a perfect multipole field inside the inner circle and zero magnetic flux density outside is achieved [66]. He proposed to approximate this ideal magnetization with geometrically identical trapezoidal blocks, each having a constant permanent magnetization [66, Section 4.2]. Therefore, permanent multipole magnets such as the dipole magnets of the FASER experiment [51], that follow this design, are known as circular Halbach arrays. More details on the magnetization of the individual blocks are given below.

In this chapter, we consider the first short FASER dipole "PXMDMCAHAC-CR000001". A picture of the magnet system and sketches of its PM blocks and their magnetization are shown in Figures 5.1 and 5.2. It is composed

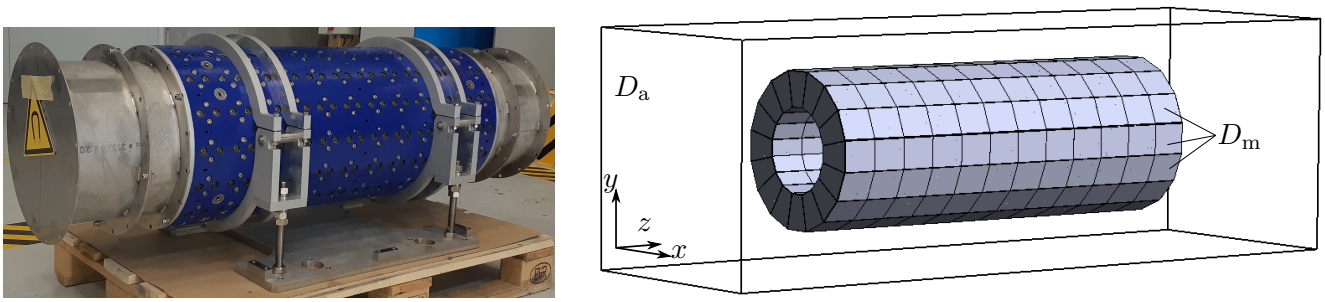

Figure 5.1: Left: First short FASER Halbach dipole "PXMDMCAHAC-CR000001" (Source: Melvin Liebsch). Right: Sketch of the corresponding three-dimensional computational domain D omitting the external construction steel ring. Figure adapted from [52].

of a series of 12 circular Halbach arrays, each composed of $K = 16$ trapezoidal PM Sm_2Co_{17} grade YXG32H blocks (see Figure 5.3). This design follows the best practice, suggested in [66, equation 25], of using at least 8 trapezoidal segments to build a circular Halbach array dipole.
The PM blocks of the $S = 12$ Halbach arrays are held in place by an aluminum guiding profile and aluminum pushing plates [3, Figure 32], which are neglected in the system model by considering that the permeability of aluminum is adequately described by the vacuum permeability μ_0. The PM blocks and their guiding structure are additionally surrounded by an external construction steel grade S355JR ring of $1.6\,\mathrm{cm}$ width with non-negligible permeability. However, the influence of this ring on the magnetic flux density in the center of the magnet system is low, since the ideal Halbach magnetization that is approximated by the PM blocks shields the magnetic flux density (see Figure 5.2).
The magnet system does not contain other sources than the PM blocks, i.e. $\mathbf{J} = 0$ and $D_{\mathbf{J}} = \emptyset$. The present electromagnetic fields can be described with sufficient accuracy by Maxwell's equations in the magnetostatic case and the constitutive equation (2.13). For the reluctivity ν, we assume

$$\nu(t) = \begin{cases} 1/\mu_0 & \text{in } D_{\mathrm{a}} \\ 1/(\mu_{\mathrm{r}}\mu_0) & \text{in } D_{\mathrm{m}} \\ f_{\mathrm{HB}}(t)/t & \text{in } D_{\mathrm{i}} \end{cases} \tag{5.1}$$

with relative permeability $\mu_r = 1.06$. This value is obtained by linear regression from the almost linear segment of the $B(H)$-curve of the PM Sm_2Co_{17} blocks. The actual $H(B)$-curve f_{HB} of the used construction steel grade S355JR ring was not available in the data sheets. Hence, we assumed the (B, H)-data table of construction steel grade S355 J2+N, which was measured with a split-coil permeameter [10], knowing that the choice of the curve only has a small influence on the magnetic flux density in the center of the magnet system. Nevertheless, we want to demonstrate by using a non-linear $H(B)$-curve that parts of the methods discussed in this chapter also apply to non-linear models.

We study the following two versions of a component-centric system model describing the first short FASER Halbach dipole:

1. **2D non-linear model.** A 2D cross-section of the computational domain $D = D_{\mathrm{a}} \cup D_{\mathrm{m}} \cup D_{\mathrm{i}}$ of one of the 12 circular Halbach arrays including the external construction steel ring is sketched in Figure 5.2. The subdomain $D_{\mathrm{m}} \coloneqq \mathrm{supp}(\mathbf{M})$ is the disjoint union of the PM blocks D^k with $1 \leq k \leq K = 16$.

2. **3D linear model.** Omitting the construction steel ring by setting $D_{\mathrm{i}} = \emptyset$ and considering the full series of 12 circular Halbach arrays yields the computational domain $D = D_{\mathrm{a}} \cup D_{\mathrm{m}}$ sketched in Figure 5.1. With $D^{k,s}$, we indicate the k-th PM block in the s-th Halbach array. Thus, the subdomain D_{m} containing the PM blocks is given by $D_{\mathrm{m}} = \bigcup_{k,s} D^{k,s}$.

In both cases, the boundary $\Gamma_{\mathrm{B}} = \partial D$ is chosen $8.5\,\mathrm{cm}$ from the magnet system such that, due to the shielding of the PM blocks, $\mathbf{B} \cdot \mathbf{n} = 0$ on Γ_{B} can be assumed (see Figure 5.2). The magnetic flux density generated by the magnet system can be simulated by solving the weak boundary value problem of magnetostatics in vector potential formulation: Given the magnetization $\mathbf{M}$ of the PM blocks, find $\mathbf{A} \in \mathcal{V}$ such that

$$\int_D \operatorname{curl} \mathbf{v} \cdot \nu(\|\operatorname{curl} \mathbf{A}\|) \operatorname{curl} \mathbf{A} \, \mathrm{d}V = \int_D \operatorname{curl} \mathbf{v} \cdot \mathbf{M} \, \mathrm{d}V \tag{5.2}$$

for all $\mathbf{v} \in \mathcal{V}$. The FEM software GetDP [60] is used to solve the problem. We provide the input files for the two models in [54]. The uniqueness of the solution to the 2D non-linear model is guaranteed by assuming that the $H(B)$-curve satisfies the conditions in Assumption 1. In the 3D linear model, we apply tree-cotree gauging to obtain a unique solution.

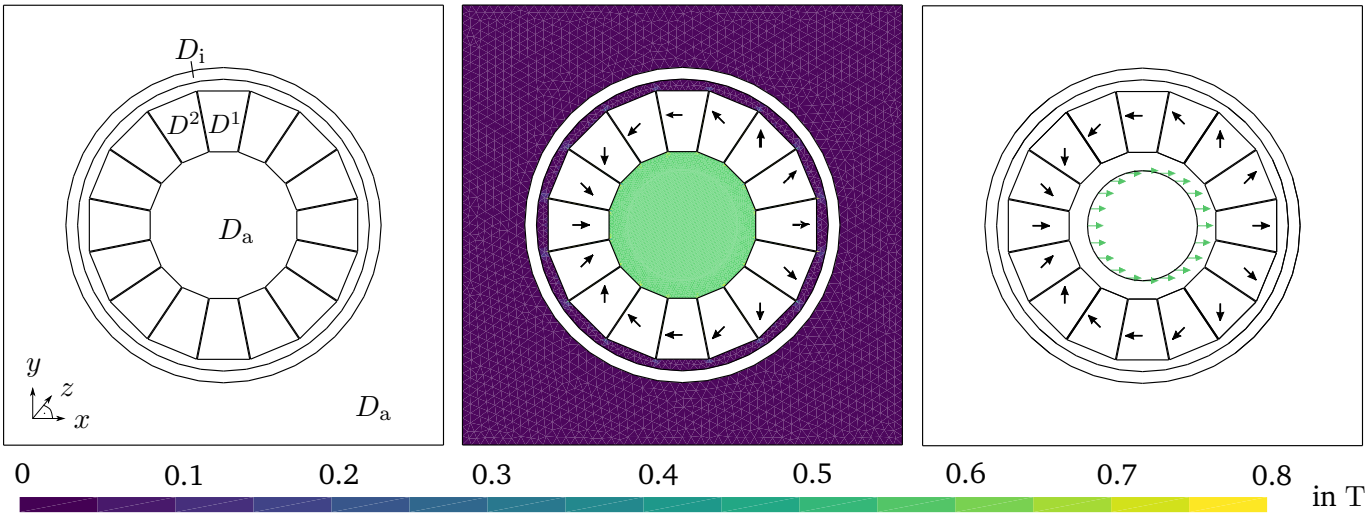

Figure 5.2: 2D cross-section of the first short FASER Halbach dipole. Left: Computational domain D. Center: Absolute value $|B_x|$ of the x-component of the magnetic flux density $\mathbf{B}$. Right: Magnetic flux density evaluated on a circle with radius $r_0 = 75\,\mathrm{mm}$. The nominal magnetization directions of the PM blocks D^k are sketched in black. Figure adapted from [52].

Quantities of interest Based on the magnetic vector potential $\mathbf{A}$, quantities of interest can be evaluated. Analogously to Chapter 4, quantities of interest that can be mathematically described with a linear functional $Q : \mathcal{V} \to \mathbb{R}^{N_2}$ of the form

$$Q(\mathbf{A}) \coloneqq \int_{D_\mathrm{obs}} q_1(\mathbf{A}) + q_2(\operatorname{curl} \mathbf{A})\,\mathrm{d}V \tag{5.3}$$

with linear functionals $q_1, q_2 : \mathcal{V} \to \mathbb{R}$ and an observation domain $D_\mathrm{obs} \subset D$ [117, Section 4.1] are studied. Again, we are interested in the *field map quantity of interest* Q_B, here defined by

$$Q_\mathrm{B}(\mathbf{A}) \coloneqq \mathbf{B}(\mathbf{x}) \tag{5.4}$$

for a position $\mathbf{x} \in D$ and the *multipole coefficient quantity of interest* $Q_{\mathrm{M},n}$ here defined by

$$Q_{\mathrm{M},n}(\mathbf{A})(z) \coloneqq (A_n(r_0)(z), B_n(r_0)(z))\,, \tag{5.5}$$

where $A_n(r_0)(z), B_n(r_0)(z)$ are the skew and normal multipole coefficients of order n defined in equation (2.80) on a centered circle with radius r_0 at the longitudinal position z of the magnet system.

Magnetization of the permanent magnet blocks Following [66], the ideal magnetization angle in the xy-plane of a circular Halbach $2L$-multipole composed of K segments changes by $360°(L+1)/K$ from one segment to the next. In the case of a $K = 16$ segmented dipole ($L = 1$), this leads to a change of the magnetization direction by $45°$ between neighboring segments. The nominal magnetization $\overline{\mathbf{M}}_{k,s}$ of the k-th segment $D^{k,s}$ in each of the $S = 12$ circular Halbach arrays of the first FASER dipole is given by

$$\overline{\mathbf{M}}_{k,s} \coloneqq \overline{m}_k \operatorname{vol}(D^{k,s})^{-1} \left(\cos(\overline{\alpha}_k), \sin(\overline{\alpha}_k), 0\right)^\top. \tag{5.6}$$

Thereby, $\overline{\alpha}_k \coloneqq 180° + 45°(k-1)$ are the nominal magnetization angles around the z-axis and $\overline{m}_k = 330\,\mathrm{A\,m^2}$ are the nominal magnetic moments for $1 \le k \le 16$ and $1 \le s \le 12$. The directions of the nominal magnetization

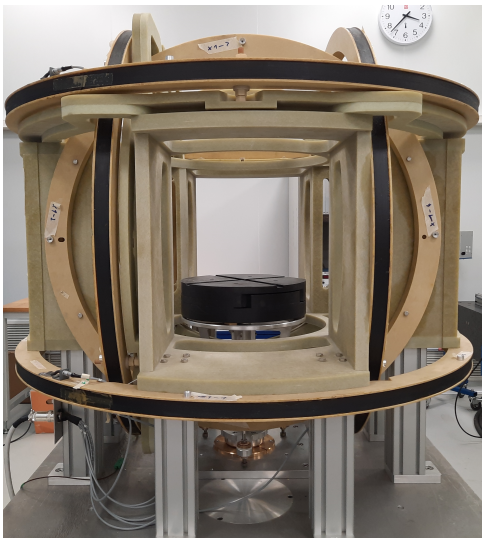

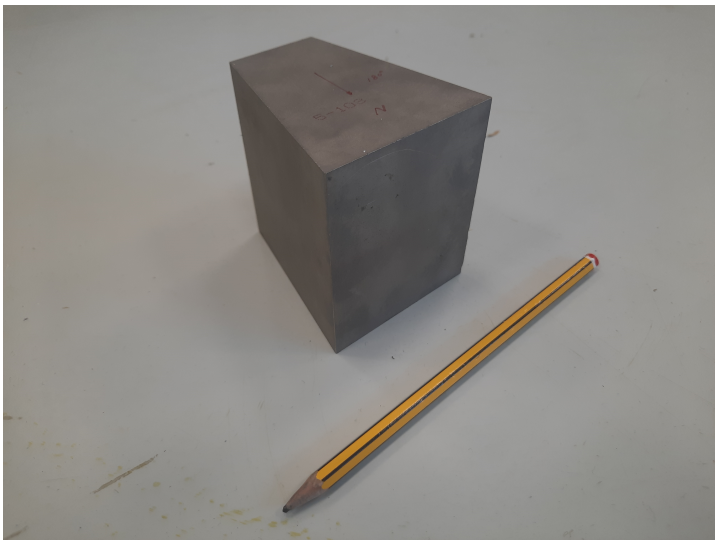

Figure 5.3: Left: Tri-axial Helmholtz coil system. Right: Trapezoidal permanently magnetized Sm_2Co_{17} blocks.

are sketched in Figure 5.2. Notice that the nominal magnetization angles around the x-axis and the y-axis are zero and that the nominal magnetization is independent of the array number s.

Due to manufacturing tolerances, the magnetizations $\mathbf{M}_{k,s}$ of the procured PM blocks can differ from the nominal magnetizations $\overline{\mathbf{M}}_{k,s}$. Their difference is denoted by the *magnetization deviation vector* $\Delta\mathbf{M}_{k,s} \in \mathbb{R}^3$, thus

$$\mathbf{M}_{k,s} = \overline{\mathbf{M}}_{k,s} + \Delta\mathbf{M}_{k,s}. \tag{5.7}$$

The magnetization $\mathbf{M}_{k,s}$ of each PM block was measured with a tri-axial Helmholtz coil system [115] (see Figure 5.3 (left)) before the assembly of the FASER dipoles. The measurement data is available in [45–47]. All measured magnetizations were within the specified tolerances [131]: The maximal measured deviation of the magnetic moment was less than 2% off the nominal value and the maximal measured deviation of the magnetization angle was less than $1.9°$. In this work, the measurement uncertainty of the Helmholtz coil system is neglected.

System model and forward model The system model (3.19) of a magnet system

$$\mathcal{M} : (\mathbf{p}, \mathbf{s}) \mapsto \mathbf{q} \tag{5.8}$$

maps a parameter $\mathbf{p}$ and an operation mode $\mathbf{s}$ to a prediction of a quantity of interest $\mathbf{q}$. Since the Halbach array's only magnetic sources are the PM blocks, there are no operation modes $\mathbf{s}$ to consider, and the system model $\mathcal{M}$ coincides by definition with the corresponding forward model $\mathcal{H} : \mathbf{p} \mapsto \mathbf{q}$.

To select suitable parameters $\mathbf{p}$ which are relevant to the first short FASER dipole, the case study [131, Figure 6] on the effects of possible deviations of the built magnet system from the numerical design model such as deviations of the nominal magnetization or misalignments of the PM blocks is considered. It was found that deviations of the magnetization have the largest impact on affecting the field quality by generating higher-order multipoles. Therefore, we consider in the following the magnetizations $\mathbf{M}_{k,s} \in \mathbb{R}^3$ of the $K \cdot S$

PM blocks of the magnet system as parameters of the system model. We define the magnetization parameter vector $\mathbf{p}$ by

$$\mathbf{p} \coloneqq \left(\mathbf{M}_{1,1}^{\top}, \ldots, \mathbf{M}_{16,1}^{\top}, \ldots, \mathbf{M}_{1,12}^{\top}, \ldots, \mathbf{M}_{16,12}^{\top}\right) \in \mathbb{R}^{16 \cdot 12 \cdot 3 = 576} \tag{5.9}$$

for the three-dimensional system model. In the two-dimensional case, the z-component of the magnetization can be neglected, leading to

$$\mathbf{p} \coloneqq \left(\mathbf{M}_{1}^{\top}, \ldots, \mathbf{M}_{16}^{\top}\right) \in \mathbb{R}^{16 \cdot 2 = 32}. \tag{5.10}$$

In the following, we denote with $\mathbf{M}^{\mathbf{p}}$ the magnetization that is defined by a parameter vector $\mathbf{p} \in \mathbb{R}^{576}$ or $\mathbf{p} \in \mathbb{R}^{32}$ with

$$\mathbf{M}_{k,s}^{\mathbf{p}} \coloneqq \left(p_{3K(s-1)+3(k-1)+1}, p_{3K(s-1)+3(k-1)+2}, p_{3K(s-1)+3(k-1)+3}\right)^{\top} \tag{5.11}$$

for $1 \leq k \leq 16$ and $1 \leq s \leq 12$ in the three-dimensional case and with

$$\mathbf{M}_{k}^{\mathbf{p}} \coloneqq \left(p_{2(k-1)+1}, p_{2(k-1)+2}\right)^{\top} \tag{5.12}$$

for $1 \leq k \leq 16$ in the two-dimensional case. Alternative approaches to describe and parameterize the magnetization of PM blocks which are affected by uncertainties are given, e.g., in [20, 102]. We choose the piecewise constant parametrization because the nominal values (5.6) are piecewise constant and with the Helmholtz coil system measurements, only piecewise constant magnetizations are observed.

Assuming that the $H(B)$-curve satisfies the conditions in Assumption 1 and applying tree-cotree gauging in the three-dimensional case, the mapping

$$\mathbf{p} \mapsto \mathbf{A}[\mathbf{M}^{\mathbf{p}}] \tag{5.13}$$

is well-defined, where $\mathbf{A}[\mathbf{M}^{\mathbf{p}}]$ is the solution to (5.2) with $\mathbf{M} = \mathbf{M}^{\mathbf{p}}$. Concatenating the mapping (5.13) with the quantity of interest Q defined in equation (5.3) yields the well-defined forward model

$$\mathcal{H} : \mathbf{p} \mapsto \mathbf{q} \coloneqq Q(\mathbf{A}[\mathbf{M}^{\mathbf{p}}]). \tag{5.14}$$

Notice that the forward model is only linear if the external construction steel ring with its non-linear $H(B)$-curve is omitted. We therefore distinguish in the following between the 2D non-linear forward model and the 3D linear forward model, where the external construction steel ring is omitted.

Mismatch of prediction and observation The predictions $\mathbf{q}$ of the forward model can be compared to measured observations $\mathbf{q}^{\mathrm{obs}}$ of the built magnet. Predictions with the forward model can be either based on the nominal magnetization parameter vector $\mathbf{p}_0$ or on the magnetization parameter vector $\mathbf{p}^{\mathrm{meas}}$ measured with the Helmholtz coil system. The prediction with $\mathbf{p}_0$ yields the nominal predictions using the numerical design model that neglects manufacturing errors. The prediction with $\mathbf{p}^{\mathrm{meas}}$ yields a first update of the system model according to the Helmholtz coil measurements.

In Figure 5.2 (center), the absolute value $|B_x|$ of the x-component of the magnetic flux density, predicted for $\mathbf{p}_0$ with the 2D non-linear forward model is shown in the air domain D_{a}. It can be seen that the nominal magnetization of the PM blocks produces a homogeneous horizontal field of around $0.578\,\mathrm{T}$ inside the circular Halbach array and shields the magnetic flux density from the exterior part of the air domain. Moreover, the magnetic flux density on the centered reference circle with radius $75\,\mathrm{mm}$ predicted for $\mathbf{p}_0$ with the 2D non-linear forward model is shown in Figure 5.2 (right). The corresponding absolute values of the skew multipole coefficients are shown in Figure 5.7 (left).

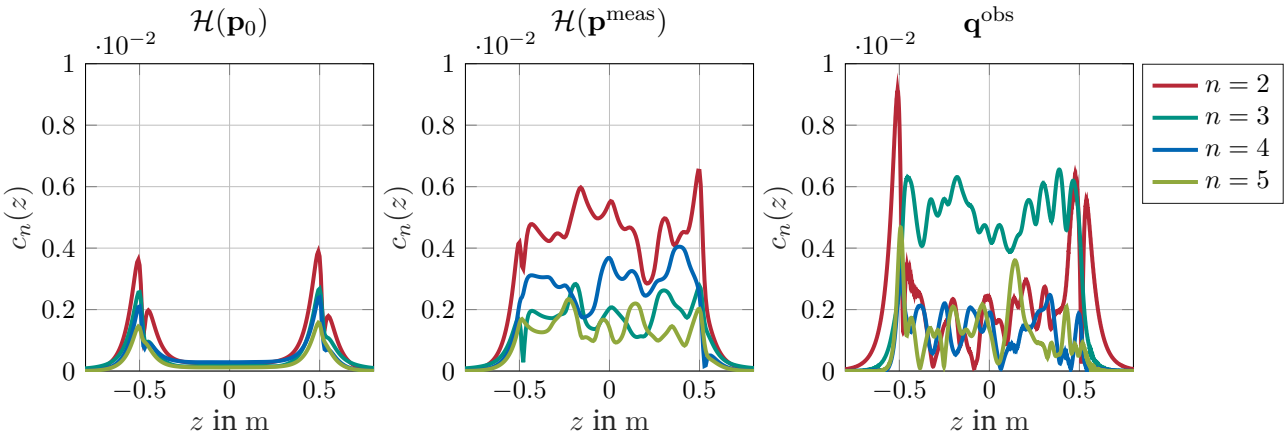

Figure 5.4: Comparison between the nominal prediction ($\mathcal{H}(\mathbf{p}_0)$), the prediction based on the Helmholtz coil measurements ($\mathcal{H}(\mathbf{p}^{\text{meas}})$), and the measured $\mathbf{q}^{\text{obs}}$ relative multipole coefficient $c_n(z)$ along the z-axis of the first FASER Halbach dipole. The predictions $\mathcal{H}(\mathbf{p}_0)$ and $\mathcal{H}(\mathbf{p}^{\text{meas}})$ are computed using a three-dimensional FEM model.

With the 3D linear forward model, we predict for $\mathbf{p}_0$ and $\mathbf{p}^{\text{meas}}$ the multipole coefficient quantity of interest $Q_{\text{M},n}$ on a circle with radius $r_0 = 75\,\text{mm}$ along the longitudinal z-axis of the magnet system. Based on $Q_{\text{M},n}$, the relative coefficients $c_n(z)$ defined by

$$c_n(z) \coloneqq \frac{\sqrt{(A_n(r_0)(z))^2 + (B_n(r_0)(z))^2}}{B_{\text{max}}}, \tag{5.15}$$

with $B_{\text{max}} = 0.578\,\text{T}$, are computed. Moreover, an observation $\mathbf{q}^{\text{obs}}$ of the relative coefficients $c_n(z)$ is derived from measurements of the magnetic flux density with a Hall probe mapper system on the same reference radius. The observation $\mathbf{q}^{\text{obs}}$ is plotted next to the nominal prediction $\mathcal{H}(\mathbf{p}_0)$ and the prediction $\mathcal{H}(\mathbf{p}^{\text{meas}})$ based on the Helmholtz coil measurements in Figure 5.4. The visualization of the observations $\mathbf{q}^{\text{obs}}$ can be also found in [49, Figure 13].The data sets are available in [48].
According to the nominal prediction $\mathcal{H}(\mathbf{p}_0)$, the relative coefficients $c_n(z)$ are almost constant for $z \in [-0.3, 0.3]\,\text{m}$ (the length of the magnet system in z-direction is $1\,\text{m}$). The observation $\mathbf{q}^{\text{obs}}$ differs from this prediction in the order of magnitude of 10^{-3} in the Euclidean norm. The observed relative coefficients $c_n(z)$ are not constant in the center of the magnet system, and the values of the coefficients are higher. Consequently, higher-order multipoles are present in the magnet system as built. However, the measured magnetic flux densities are still within the specifications [131]. In [49], the assumption is expressed that the segmented structure of the magnet system might cause the observed instability. According to [131], the mismatch between the prediction and the simulation might be caused by small misalignments of some PM blocks due to the forces during the magnet assembly. The prediction of the relative coefficients $c_n(z)$ based on the measured magnetization parameter vector $\mathbf{p}^{\text{meas}}$ are around a similar magnitude as the coefficients derived from the Hall probe measurements. Moreover, the predictions $\mathcal{H}(\mathbf{p}^{\text{meas}})$ also have an unstable pattern along the z-axis, however, the pattern differs from the pattern of the observations. To improve the prediction with the forward model and to gain insight into the magnetization deviations that might explain the observed relative coefficients $c_n(z)$, the magnetization parameter vector is updated in this chapter.

Forward and inverse problem Simulating predictions with the forward model and updating the magnetization parameter vector $\mathbf{p}$ is related to solving the following forward and inverse problems.

Problem 4. ***(Forward problem)*** *Given a magnetization parameter vector* $\mathbf{p}$*, find the magnetic vector potential* $\mathbf{A}[\mathbf{M}^{\mathbf{p}}] \in \mathcal{V}$ *that solves the weak formulation of the boundary value problem of magnetostatics in vector potential formulation* (5.2) *and evaluate the quantity of interest* $Q(\mathbf{A}[\mathbf{M}^{\mathbf{p}}])$.

Problem 5. ***(Inverse problem)*** *Given observations* $\mathbf{q}^{\mathrm{obs}}$ *of a quantity of interest* Q*. Find a real-valued vector* $\mathbf{p}$ *such that the solution* $\mathbf{A}[\mathbf{M}^{\mathbf{p}}] \in \mathcal{V}$ *of* (5.2) *satisfies* $Q(\mathbf{A}[\mathbf{M}^{\mathbf{p}}]) = \mathbf{q}^{\mathrm{obs}}$.

The observations $\mathbf{q}^{\mathrm{obs}}$ are typically affected by measurement uncertainty that can arise for example from vibrations of the Hall probe mapper, stage misalignment, wrong sensor calibrations, or random measurement uncertainty. For modern-day measurement equipment, a standard deviation $\sigma_{\mathbf{B}} = 10^{-4}$ of random measurement uncertainty for relative observations of the field map quantity of interest is Q_{B} can be assumed. For the relative dipole coefficient quantity of interest $Q_{\mathrm{M},1}$, a standard deviation of $\sigma_{\mathbf{M},1} = 10^{-4}$ and for relative higher-order multipole coefficients with $n > 1$, a standard deviation of $\sigma_{\mathbf{M},n} = 10^{-6}$ can be assumed. These values are typically estimated from repeated measurements.
However, a standard deviation of 10^{-6} can only be reached with rotating coil magnetometers. Computing multipole coefficients from magnetic flux density measurements with a Hall probe mapper system leads to higher uncertainties due to vibrations and misalignment (mapper system, magnet system, simulation) [90]. For the available data we therefore assume that

$$\sigma_{\mathbf{M},n}(z) = \begin{cases} 5 \cdot 10^{-5} & z \text{ in the homogeneous dipole region,} \\ 5 \cdot 10^{-3} & z \text{ in the fringe field region} \end{cases} \tag{5.16}$$

for $n > 1$. The value is chosen position-dependent because the effect of vibrations and misalignment is larger in the fringe field region. Similarly, due to vibrations and misalignment for the available measurements of the magnetic flux density, we assume the position-dependent standard deviation

$$\sigma_{\mathbf{B}}(z) = \begin{cases} 1 \cdot 10^{-4} & z \text{ in the homogeneous dipole region,} \\ 1 \cdot 10^{-3} & z \text{ in the fringe field region.} \end{cases} \tag{5.17}$$

Due to the affection of observations $\mathbf{q}^{\mathrm{obs}}$ by measurement uncertainty, a solution to the inverse problem 5 might not exist. Consequently, we relax the notion of a solution to the inverse problem similar to Chapter 4, by requesting that the predicted quantities of interest have a small distance to the observed quantities of interest for some error metric.

Problem 6. ***(Relaxed inverse problem)*** *Given observations* $\mathbf{q}^{\mathrm{obs}}$ *of a quantity of interest* Q *in* R *positions* $\mathbf{x}_r$ *and* z_r*, find a real-valued vector* $\mathbf{p}$ *such that the solution* $\mathbf{A}[\mathbf{M}^{\mathbf{p}}] \in \mathcal{V}$ *of* (5.2) *satisfies*

$$\frac{1}{R} \sum_r \left(\frac{|B_*^{\mathrm{obs}}(\mathbf{x}_r) - Q_{\mathrm{B}}(\mathbf{A}[\mathbf{M}^{\mathbf{p}}])_*(\mathbf{x}_r)|}{|B_{\max}|} \right) < \epsilon_{\mathrm{tol,B}} \tag{5.18}$$

for all components $* \in \{x, y, z\}$ *of the magnetic flux density, or respectively, depending on the quantity of interest,*

$$\frac{1}{2R} \sum_r \left(\frac{\left\| \left(A_n^{\mathrm{obs}}(r_0), B_n^{\mathrm{obs}}(r_0) \right)(z_r) - Q_{\mathrm{M},n}(\mathbf{A}[\mathbf{M}^{\mathbf{p}}])(r_0)(z_r) \right\|}{|B_{\max}|} \right) < \epsilon_{\mathrm{tol,M,n}} \tag{5.19}$$

for all $n \leq N$*. The tolerances are chosen by* $\epsilon_{\mathrm{tol,B}} = \epsilon_{\mathrm{tol,M},1} \coloneqq 10^{-4}$ *and* $\epsilon_{\mathrm{tol,M,n}} \coloneqq 5 \cdot 10^{-5}$ *for* $n > 1$.

Model updating In this chapter, we update the magnetization parameter vector $\mathbf{p}$ of system models of the first short FASER dipole by using the methods for statistical inversion introduced in Chapter 3. Due to the weighting of the prior and the likelihood model in the Bayesian approach, the updated parameter vector $\mathbf{p}^{\mathrm{up}}$ is not automatically a solution to the relaxed inverse problem 6 in the sense of the conditions (5.18) and (5.19). However, we verify these conditions for $\mathbf{p}^{\mathrm{up}}$ to prove that using this magnetization parameter vector provides a model update, at least on the regime of the training data, according to the definition of [145].
The Bayesian approach is particularly suitable for this application since measurement data concerning the magnetization of the PM blocks taken during the prototype phase and observations of the magnetic flux density and multipole coefficients measured for characterization are available but both are affected by uncertainties. Figure 5.5 shows an overview of the applied methods and sources of knowledge. The resulting updated system model $\mathcal{M}(\mathbf{p}^{\mathrm{up}})$ is a hybrid model [86] because measurement data and first principle-based knowledge of the underlying magnetostatic problem are combined to compute the updated magnetization parameter vector $\mathbf{p}^{\mathrm{up}}$.

State-of-the-art methods to update permanent magnetizations in subdomains of a computational domain D given observations of field-related quantities of interest that can be found in the literature include physics-informed neural networks [84], truncated singular value decomposition of a linear equation system [9, 35], optimization in combination with Tikhonov regularization [26], and Bayesian inference by computing the maximum a posteriori estimate for a linear problem [34]. Our method extends the latter approach by also considering non-linear system models. We address the ill-posedness of the underlying inverse problem by the finite-dimensional problem formulation based on the assumption that the magnetization is piecewise constant for each PM block, and by conducting a sensitivity analysis to improve the stability.

Structure of this chapter The remainder of this chapter is organized as follows: First, in Section 5.1 a sensitivity analysis similar to Section 4.2.2 based on Gâteaux derivatives is derived and conducted to identify observation positions where the quantities of interest $Q_{\mathbf{B}}$ and $Q_{\mathbf{M},n}$ are sensitive to changes of the magnetization parameter vector $\mathbf{p}$. It is verified that the observation positions chosen in the available data set [48] are suitable for detecting changes in $Q_{\mathbf{B}}$ and $Q_{\mathbf{M},n}$ that are caused by the mean magnetization deviation of the 13-th PM block of the Halbach array, according to the measurements with the Helmholtz coil system.
Subsequently, in Section 5.2, the methods of stochastic model updating introduced in Chapter 3 are applied. Using Bayesian inference, a posterior distribution of the magnetization parameter vector given an observation of a quantity of interest is derived. For the non-linear forward model, the posterior distribution is sampled with Markov chain Monte Carlo sampling using the Metropolis-Hastings algorithm with the preconditioned Crank-Nicolson proposal. For the linear forward model, the maximum a posteriori estimate is computed. First, it is verified on simulated observation data that both methods can retrieve a previously selected ground truth magnetization parameter vector with sufficient accuracy such that the sample mean of the Markov chain and the maximum a posteriori estimate solve the relaxed inverse problem 6 according to the criteria defined in the equations (5.18) and (5.19).
Afterwards, the linear system model of the first short FASER Halbach dipole is updated based on the measured observations [48] of the relative multipole coefficients $c_n(z)$. The update does not only reduce the mismatch between the measured and the predicted relative coefficients but also improves predictions of other quantities of interest that were not part of the training data.

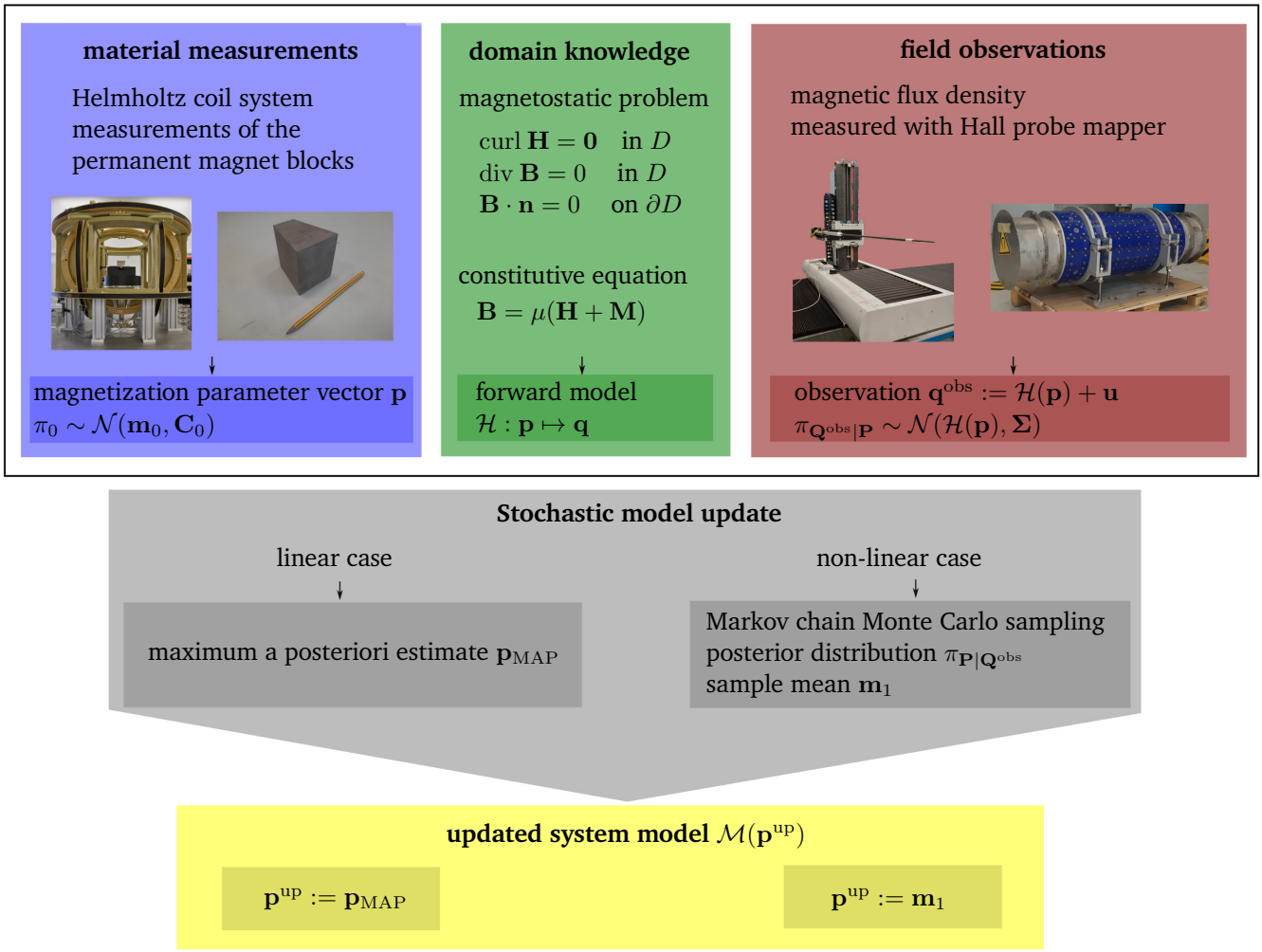

Figure 5.5: Overview of sources of knowledge and methods for data-driven updates of the magnetization of Halbach arrays. From the measurement of the magnetization of the PM blocks, a prior distribution of the magnetization parameter vector $\mathbf{p}$ is derived. This parameter vector is updated using statistical inference methods such as maximum a posteriori estimation and Markov chain Monte Carlo sampling. Thereby, the first principle-based magnetostatic problem is combined with observations $\mathbf{q}^{\text{obs}}$ of quantities of interest. Consequently, the resulting updated system model $\mathcal{M}(\mathbf{p}^{\text{up}})$ is a hybrid model. Notice that the material measurements and the measurements of the magnetic flux density are conducted during different phases of the magnet life cycle.

5.1 Sensitivity analysis

A sensitivity analysis is conducted to select suitable observation positions of the quantities of interest that are used as training data to compute the model update. Similar to the sensitivity analysis concerning perturbations of the source current density derived in [117, Proposition 4], we derive the weak formulation of a boundary value problem to determine the Gâteaux derivative of the magnetic vector potential in the direction of deviations from the nominal magnetization. Thereby, we follow the lines of the proof of [117, Proposition 2]. In Section 5.1, a similar method (see also [117, Proposition 2]) is used to study the sensitivity of solutions to the boundary value problem of magnetostatics in vector potential formulation to perturbations of the reluctivity in the iron domain.

Sensitivity of linear quantities of interest to deviations of the magnetization Recall that under the assumptions made in this chapter, the mapping $\mathbf{M} \mapsto \mathbf{A}[\mathbf{M}]$ is well-defined after gauging. Let $\overline{\mathbf{M}}$ be the nominal magnetization of the PM blocks and let $\Delta\mathbf{M}$ be a magnetization deviation. We define

$$\mathbf{M}_s \coloneqq \overline{\mathbf{M}} + s\Delta\mathbf{M} \tag{5.20}$$

for $s > 0$. Let $\mathbf{A} = \mathbf{A}[\overline{\mathbf{M}}], \mathbf{A}[\mathbf{M}_s] \in \mathcal{V}$ be the weak solutions that satisfy

$$\int_D \operatorname{curl}\mathbf{v} \cdot \nu(\|\operatorname{curl}\mathbf{A}\|) \operatorname{curl}\mathbf{A}\,\mathrm{d}V = \int_D \operatorname{curl}\mathbf{v} \cdot \overline{\mathbf{M}}\,\mathrm{d}V \tag{5.21}$$

$$\int_D \operatorname{curl}\mathbf{v} \cdot \nu(\|\operatorname{curl}\mathbf{A}[\mathbf{M}_s]\|) \operatorname{curl}\mathbf{A}[\mathbf{M}_s]\,\mathrm{d}V = \int_D \operatorname{curl}\mathbf{v} \cdot \mathbf{M}_s\,\mathrm{d}V \tag{5.22}$$

for all $\mathbf{v} \in \mathcal{V}$. The Gâteaux derivative of the mapping $\mathbf{M} \mapsto \mathbf{A}[\mathbf{M}]$ at $\overline{\mathbf{M}}$ in the direction of the deviation $\Delta\mathbf{M}$ is defined by

$$\mathbf{A}'[\Delta\mathbf{M}] \coloneqq \lim_{s \searrow 0} \frac{\mathbf{A}[\overline{\mathbf{M}} + s\Delta\mathbf{M}] - \mathbf{A}[\overline{\mathbf{M}}]}{s}. \tag{5.23}$$

Subtracting equation (5.21) from equation (5.22) yields

$$\begin{aligned}\int_D s\Delta\mathbf{M} \cdot \operatorname{curl}\mathbf{v}\,\mathrm{d}V = \;& \int_{D_\mathrm{i}} (\nu(\|\operatorname{curl}\mathbf{A}[\mathbf{M}_s]\|) \operatorname{curl}\mathbf{A}[\mathbf{M}_s] - \nu(\|\operatorname{curl}\mathbf{A}\|) \operatorname{curl}\mathbf{A}) \cdot \operatorname{curl}\mathbf{v}\,\mathrm{d}V \\ & + \int_{D_\mathrm{a}} 1/\mu_0 \operatorname{curl}(\mathbf{A}[\mathbf{M}_s] - \mathbf{A}) \cdot \operatorname{curl}\mathbf{v}\,\mathrm{d}V \\ & + \int_{D_\mathrm{m}} 1/(\mu_0\mu_\mathrm{r}) \operatorname{curl}(\mathbf{A}[\mathbf{M}_s] - \mathbf{A}) \cdot \operatorname{curl}\mathbf{v}\,\mathrm{d}V.\end{aligned} \tag{5.24}$$

Dividing by s and taking the limit $s \searrow 0$ we can conclude with [117, Lemma 3] that the Gâteaux derivative satisfies $\mathbf{A}' \in \mathcal{V}$ and

$$\begin{aligned}\int_D \Delta\mathbf{M} \cdot \operatorname{curl}\mathbf{v}\,\mathrm{d}V = \;& \int_{D_\mathrm{i}} \boldsymbol{\nu}_\mathrm{d}(\operatorname{curl}\mathbf{A}) \operatorname{curl}\mathbf{A}' \cdot \operatorname{curl}\mathbf{v}\,\mathrm{d}V \\ & + \int_{D_\mathrm{a}} 1/\mu_0 \operatorname{curl}\mathbf{A}' \cdot \operatorname{curl}\mathbf{v}\,\mathrm{d}V \\ & + \int_{D_\mathrm{m}} 1/(\mu_0\mu_\mathrm{r}) \operatorname{curl}\mathbf{A}' \cdot \operatorname{curl}\mathbf{v}\,\mathrm{d}V\end{aligned} \tag{5.25}$$

for all $\mathbf{v} \in \mathcal{V}$, where $\boldsymbol{\nu}_\mathrm{d}$ is the differential reluctivity tensor [117, definition 5] defined in equation (2.72). Consequently, the Gâteaux derivative $\mathbf{A}'[\Delta\mathbf{M}]$ in the direction of $\Delta\mathbf{M}$ at $\overline{\mathbf{M}}$ can be determined by solving equation (5.25) in GetDP [60].

Analogously to Chapter 4, the Gâteaux derivative $\mathbf{A}'[\Delta\mathbf{M}]$ of the magnetic vector potential can be inserted into linear quantities of interest Q to determine the Gâteaux derivative of the respective quantity of interest. In the following, we analyze the sensitivity of Q_B and $Q_{\mathrm{M},n}$ to deviations of the permanent magnetization of one PM block in a circular Halbach array by computing the Gâteaux derivative at the nominal magnetization into the direction of the deviation.

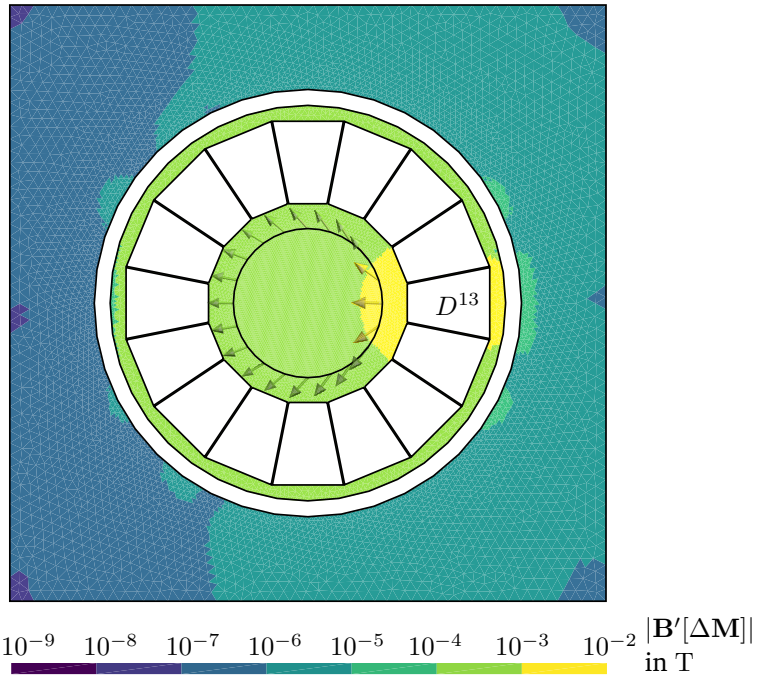

Figure 5.6: Gâteaux derivative $\mathbf{B}'[\Delta\mathbf{M}]$ of the magnetic flux density at the nominal magnetization in the direction of the sample mean magnetization deviation of the 13-th PM block defined in equation (5.26). On the air domain, the absolute value $|\mathbf{B}'[\Delta\mathbf{M}]|$ is visualized. On the circle with radius $75\,\mathrm{mm}$, $\mathbf{B}'[\Delta\mathbf{M}]$ is visualized.

Sensitivity analysis concerning deviations of the permanent magnetization in the FASER Halbach dipole
In this paragraph, the sensitivity of the linear quantities of interest Q_B and $Q_{\mathrm{M},n}$ to deviations of the permanent magnetization in the PM block D^{13} of the FASER Halbach dipole is studied with the 2D non-linear system model. Let $\overline{\mathbf{M}}$ be the nominal magnetization and let the deviation $\Delta\mathbf{M}$ be given by

$$\Delta\mathbf{M}_k = \begin{cases} \widehat{\Delta\mathbf{M}}_{13} \coloneqq \frac{1}{12}\sum_{s=1}^{12}\left(\mathbf{M}_{13,s} - \overline{\mathbf{M}}_{13,s}\right) = \left(7.00\cdot 10^4, -7.64\cdot 10^4\right)\,\mathrm{A\,m^{-1}} & k = 13 \\ \mathbf{0} & \text{else} \end{cases} \tag{5.26}$$

where $\widehat{\Delta\mathbf{M}}_{13}$ is the sample mean deviation of the measured magnetizations $\mathbf{M}_{13,s}$ from the nominal magnetization $\overline{\mathbf{M}}_{13,s}$ of the 13-th PM block (see equation (5.7)).

The Gâteaux derivative of the magnetic flux density in the direction of $\Delta\mathbf{M}$ at $\overline{\mathbf{M}}$ is determined by solving the weak problem (5.25) and computing $\mathbf{B}'[\Delta\mathbf{M}] = Q_\mathrm{B}(\mathbf{A}'[\Delta\mathbf{M}])$. A visualization of the absolute value $|\mathbf{B}'[\Delta\mathbf{M}]|$ of the Gâteaux derivative in the air domain D_a is given in Figure 5.6. Moreover, the Gâteaux derivative $\mathbf{B}'[\Delta\mathbf{M}]$ is shown on a centered circle with radius $75\,\mathrm{mm}$. The absolute values $|A_n'[\Delta\mathbf{M}]|$ of the Gâteaux derivative of the corresponding skew multipole coefficients are shown in Figure 5.7 next to the absolute values of the nominal skew multipole coefficients.
As expected, it can be seen that the absolute value $|\mathbf{B}'[\Delta\mathbf{M}]|$ of the Gâteaux derivative is maximal in the vicinity of the PM block D^{13} that is affected by the magnetization deviation. The maximal absolute value is of the order of magnitude of $10^{-3}\,\mathrm{T}$, leading to a change at least of the order of magnitude of 10^{-3} relative to the maximal magnetic flux density $B_\mathrm{max} = 0.578\,\mathrm{T}$, exceeding the assumed standard deviation of the random measurement uncertainty.

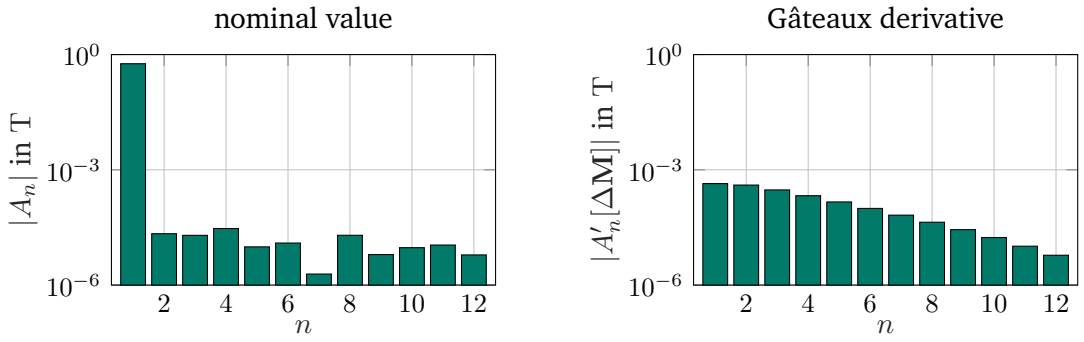

Figure 5.7: Left: Absolute values $|A_n|$ of the nominal skew multipole coefficients on the centered circle with radius $75\,\mathrm{mm}$. Right: Absolute values $|A'_n[\Delta\mathbf{M}]|$ of the Gâteaux derivative of the skew multipole coefficients in the direction of the sample mean magnetization deviation of the 13-th PM block (equation 5.26) and at the nominal magnetization on the centered circle with radius $75\,\mathrm{mm}$.

A similar reasoning can be used for observations of the multipole quantity of interest. According to the nominal prediction of the absolute values of the skew multipole coefficients $|A_n|$, the magnet system is an almost perfect skew dipole (see Figure 5.7). The corresponding Gâteaux derivatives $|A'_n[\Delta\mathbf{M}]|$, however, contain higher-order skew multipole coefficients, which for $2 \leq n \leq 8$ exceed the assumed standard deviation of the random measurement uncertainty.

We conclude that according to the results of the sensitivity analysis, the centered circle with radius $75\,\mathrm{mm}$ is a suitable choice to compare predictions and observations of the quantities of interest Q_B and $Q_{\mathrm{M},n}$. Hence, the data set available in [48], corresponding to a former measurement campaign [49] for magnet characterization, can be used as training data for model updating.

5.2 Stochastic model updating

The goal of this section is the derivation of stochastic model updates $\mathcal{M}(\mathbf{p}^\mathrm{up})$ of the system models of the first short FASER dipole, motivated by the observed mismatch between the numerical design model's predictions and the measured observations of the relative higher-order multipole coefficients $c_n(z)$ (Figure 5.4). To apply the methods of statistical inference introduced in Chapter 3, i.e., the Bayesian approach, the parameters $\mathbf{p}$ and the observations $\mathbf{q}^\mathrm{obs}$ are interpreted as random vectors $\mathbf{P} : \Omega \to \mathbb{R}^{N_1}$ and $\mathbf{Q}^\mathrm{obs} : \Omega \to \mathbb{R}^{N_2}$. The randomness reflects the uncertainty caused by the random occurrence of production errors of the PM blocks and the random measurement uncertainty affecting the observations.

A prior density function π_0 of the random parameter vector $\mathbf{P}$ can be estimated from the measurements of the magnetization of the PM blocks with the Helmholtz coil system. Having measurements of the magnetization of $S = 12$ PM blocks with the same nominal magnetization, we estimate the mean and the covariance matrix of $\mathbf{P}$ using the sample mean $\mathbf{m}_0$ and the sample covariance $\mathbf{C}_0$ defined in equations (3.4) and (3.5). Notice that due to the independence of the magnetization of the different PM blocks, the sample covariance matrix $\mathbf{C}_0$ is a block diagonal matrix. To be able to work with a normal distributed prior, it is moreover assumed that also within the blocks, the x, y, and z components are independent. It is verified by conducting the Kolmogorov-Smirnov test introduced in Chapter 3 that each random variable P_n with $1 \leq n \leq N_1$ is normal distributed. Consequently, it can be concluded from the independence and the normality of the random variables P_n that $\mathbf{P} \sim \mathcal{N}(\mathbf{m}_0, \mathbf{C}_0)$, where $\mathbf{C}_0$ is a diagonal matrix.

Besides the prior density function π_0, a likelihood model that describes the conditional probability density function $\pi_{\mathbf{Q}^{\text{obs}}|\mathbf{P}}$ is required for Bayesian inference. To set up a likelihood model, the uncertainty of the random observation vector $\mathbf{Q}^{\text{obs}}$ is estimated based on the standard deviations σ_{B} and $\sigma_{\text{M},n}$ of random measurement uncertainty defined in equations (5.16) and (5.17). With the additive noise model defined in equation (3.21), that omits errors and uncertainties of the forward model, the likelihood model $\pi_{\mathbf{Q}^{\text{obs}}|\mathbf{P}} \sim \mathcal{N}(\mathcal{H}(\mathbf{p}), \mathbf{\Sigma})$ with $\mathbf{\Sigma} = \sigma^2\mathbb{I}$ is obtained.

Observation training data Computing a stochastic model update requires training data of observed quantities of interest. Before applying the methods of statistical inference to measured data, the model is evaluated on simulated data based on a ground truth magnetization parameter vector $\mathbf{p}^{\text{true}}$, which is chosen as a realization of the random parameter vector $\mathbf{P} \sim \mathcal{N}(\mathbf{m}_0, \mathbf{C}_0)$. Using the additive noise model (3.21), the simulated observations

$$\mathbf{q}^{\text{obs}} = \mathcal{H}(\mathbf{p}^{\text{true}}) + \mathbf{u} \tag{5.27}$$

are generated, which take into account random measurement uncertainty. They can be interpreted as a realization of the random observation vector $\mathbf{Q}^{\text{obs}}$. The vector $\mathbf{u} \in \mathbb{R}^{N_2}$ is a realization of the random measurement uncertainty $\mathbf{U} \sim \mathcal{N}(\mathbf{0}, \mathbf{\Sigma})$ with $\mathbf{\Sigma} = \sigma^2\mathbb{I}$. Reasonable values for the standard deviation σ of the random measurement uncertainty are given in equations (5.16) and (5.17).

Measured observations of Q_{B} and $Q_{\text{M},n}$ on a centered circle with radius $75\,\text{mm}$ are available in the data sets [48] corresponding to the measurement report [49]. Even though these data sets were collected four years ago in the context of magnet characterization, we can verify by conducting the Gâteaux derivative-based sensitivity analysis conducted in Section 5.1 that the quantities of interest Q_{B} and $Q_{\text{M},n}$ are sufficiently sensitive to the expected variations of the magnetization parameter vector in the available observation positions. Hence, we use the same observation positions for the simulated training data.

To update the 2D non-linear system model, observations of the field map quantity of interest Q_{B} in $R = 60$ equally distributed positions $\{\mathbf{x}_1, \dots, \mathbf{x}_{60}\}$ on the centered circle with radius $75\,\text{mm}$ are used. In the 3D linear case, we use observations of the field map quantity of interest Q_{B} on a centered cylinder with radius $75\,\text{mm}$ in 60 radial times 156 longitudinal positions $\{\mathbf{x}_1, \dots, \mathbf{x}_R\}$ with $R = 60 \cdot 156 = 9360$, covering the full range of the magnet system including the fringe field. Moreover, observations of the multipole coefficient quantity of interest $Q_{\text{M},n}$ for $1 \leq n \leq 8$ on the same radius and in the same longitudinal positions $\{z_1, \dots, z_R\}$ are chosen. Consequently, the observation vector $\mathbf{q}^{\text{obs}}$ is given by

$$\mathbf{q}^{\text{obs}} := \begin{cases} \mathbf{q}_{\text{B}}^{\text{obs}} := \left(B_x^{\text{obs}}(\mathbf{x}_1), B_y^{\text{obs}}(\mathbf{x}_1), \dots, B_x^{\text{obs}}(\mathbf{x}_R), B_y^{\text{obs}}(\mathbf{x}_R)\right) + \mathbf{u} & \text{2D model, } Q_{\text{B}} \\ \mathbf{q}_{\text{B}}^{\text{obs}} := \left(B_x^{\text{obs}}(\mathbf{x}_1), B_y^{\text{obs}}(\mathbf{x}_1), B_z^{\text{obs}}(\mathbf{x}_1), \dots, B_x^{\text{obs}}(\mathbf{x}_R), B_y^{\text{obs}}(\mathbf{x}_R), B_z^{\text{obs}}(\mathbf{x}_R)\right) + \mathbf{u} & \text{3D model, } Q_{\text{B}} \\ \mathbf{q}_{\text{M}}^{\text{obs}} := \begin{array}{l} \left(A_1^{\text{obs}}(z_1), B_1^{\text{obs}}(z_1), \dots, A_8^{\text{obs}}(z_1), B_8^{\text{obs}}(z_1), \dots, \right. \\ \left. A_1^{\text{obs}}(z_R), B_1^{\text{obs}}(z_R), \dots, A_8^{\text{obs}}(z_R), B_8^{\text{obs}}(z_R)\right) + \mathbf{u} \end{array} & \text{3D model, } Q_{\text{M},n} \end{cases} \tag{5.28}$$

depending on the dimension of the system model and the observed quantity of interest.

In the following, we first validate the update of the 2D non-linear system model derived by Markov chain Monte Carlo sampling with the Metropolis-Hastings algorithm. Then, the updated 3D linear system model using the maximum a posteriori estimate is validated. Finally, we apply the latter updating scheme to the measured observations of the multipole coefficient quantity of interest $Q_{\text{M},n}$, whose corresponding relative coefficients $c_n(z)$ are shown in Figure 5.4 (right).

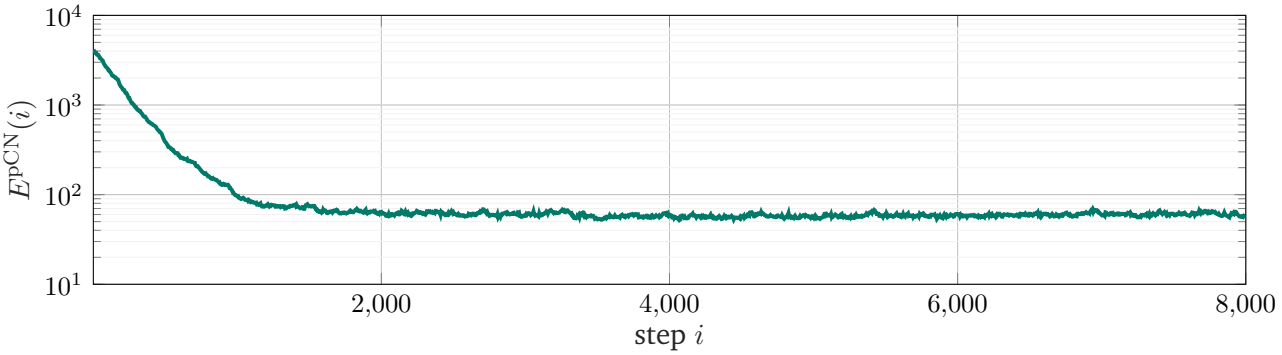

Figure 5.8: Values of the residual $E^{\mathrm{pCN}}(i)$ defined in equation (5.29) that is used in the Metropolis-Hastings algorithm with the preconditioned Crank-Nicolson proposal ($s = 1/100$) to compute the acceptance probability of the i-th proposal.

5.2.1 Validation in the 2D non-linear case

Due to the non-linearity of the forward model, we use the Metropolis-Hastings algorithm with the preconditioned Crank-Nicolson proposal to draw 8000 samples of the posterior distribution $\pi_{\mathbf{P}|\mathbf{Q}^{\mathrm{obs}}}$. The proposal density is given by $\mathcal{N}(\sqrt{1-s^2}\widetilde{\mathbf{p}}, s\mathbf{C}_0)$, where $\widetilde{\mathbf{p}}$ is the current value of the Markov chain and $\mathbf{C}_0$ is the covariance matrix of the prior distribution. The step size $s = 1/100$ is chosen significantly smaller than in the application in Chapter 4 because of the higher dimension $N_1 = 32$ of the parameter space. With this choice, an acceptance rate of 48.51% was reached. Due to the small step size, the Euclidean distances between the current states of the Markov chain and the proposals are small, leading to the necessity of drawing more samples than in Chapter 4. The values of the residual

$$E^{\mathrm{pCN}}(i) \coloneqq \frac{1}{2}\left\|\mathcal{H}(\mathbf{p}_i) - \mathbf{q}_{\mathrm{B}}^{\mathrm{obs}}\right\|_{\Sigma^{-1}}^2, \tag{5.29}$$

that is used in equation (3.44) to compute the acceptance probability, are shown in Figure 5.8. Thereby, $\mathcal{H}(\mathbf{p}_i)$ is the prediction of the quantity of interest based on the i-th state $\mathbf{p}_i$ of the Markov chain. Following the decay of the residual $E^{\mathrm{pCN}}(i)$, the first 2000 samples are considered as burn-in and are thus omitted in the computation of the sample mean $\mathbf{m_1}$ and the sample covariance $\mathbf{C}_1$ with the equations (3.4) and (3.5).

In Figure 5.9, the ground truth $\mathbf{p}^{\mathrm{true}}$, the expected value $\mathbf{m}_0$ of the prior distribution and the sample mean $\mathbf{m}_1$ of the posterior distribution is visualized. Moreover, the $1\sigma, 2\sigma$ and 3σ intervals around $\mathbf{m}_0$ and $\mathbf{m}_1$ according to the values on the diagonal of the covariance matrix $\mathbf{C}_0$ and the sample covariance matrix $\mathbf{C}_1$ are shown. The average absolute difference between the posterior sample mean $\mathbf{m}_1$ and the ground truth parameters $\mathbf{p}^{\mathrm{true}}$ is decreased by 43% compared to the average absolute difference between the prior expected value $\mathbf{m}_0$ and the ground truth parameters $\mathbf{p}^{\mathrm{true}}$. Moreover, the volumes of the 3σ intervals of the posterior distribution are decreased compared to the prior distribution. However, the ground truth parameters are not always in the range of the 3σ interval of the posterior. Nevertheless, it can be verified that the posterior sample mean $\mathbf{m}_1$ is a solution to the relaxed inverse problem 6 according to the condition defined in equation (5.18). Thus, updating the non-linear two-dimensional system model with the magnetization parameter vector $\mathbf{m}_1$ improves the predictions of the magnetic flux density at least on the regime of the training data.

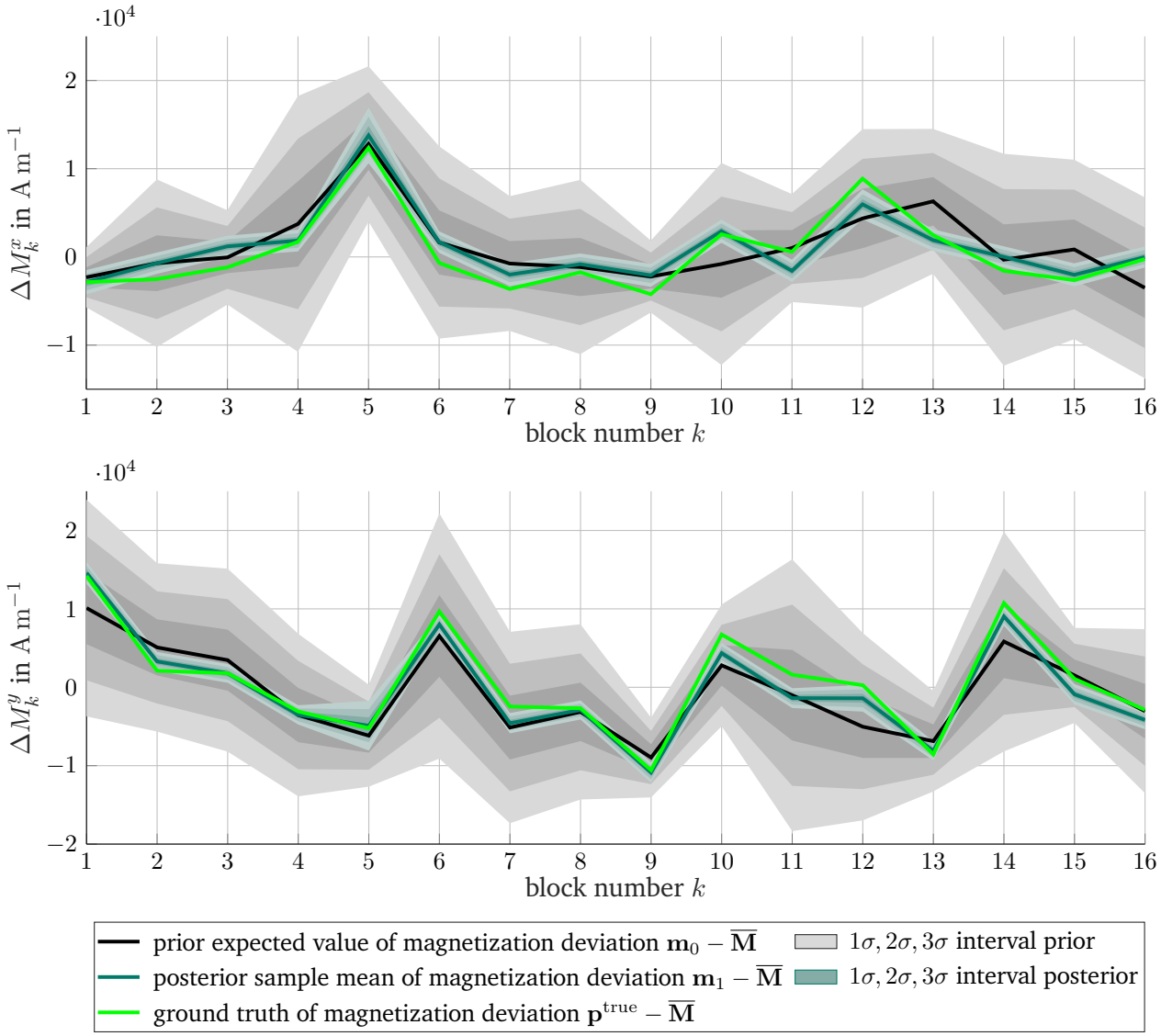

Figure 5.9: Comparison between the ground truth, the prior, and the posterior distribution for updating the 2D non-linear system model (top for x, bottom for y). The posterior distribution is determined based on observations $\mathbf{q}_{\text{B}}^{\text{obs}}$ of the field map quantity of interest. For all distributions, the discrete mean and the $1\sigma, 2\sigma, 3\sigma$ intervals are visualized with continuous curves to enhance readability.

5.2.2 Validation in the 3D linear case

The dimension N_1 of the parameter space of the three-dimensional system model is with $N_1 = 576$ significantly larger than for the two-dimensional system model with $N_1 = 32$. Consequently, a much smaller step size s and thus much more iterations of the Metropolis-Hastings algorithm with the Crank-Nicolson proposal would be required to obtain a sufficient acceptance rate. Moreover, the run time of the forward model, which is solved for every proposal of the Metropolis-Hastings algorithm, is much more time-consuming than in the two-dimensional case. For these two reasons (i) more iterations, and (ii) longer run-time per iteration, the computation of a stochastic model update using the Metropolis-Hastings algorithm with the Crank-Nicolson proposal is computationally prohibitive.
For this reason, the three-dimensional system model is simplified such that the forward model is linear. Due to the linearity and the assumption that the prior and the random measurement uncertainty are normal distributed, the maximum a posteriori estimate $\mathbf{p}_{\mathrm{MAP}}$ is given by the expected value of the posterior distribution (see equation (3.34)). Moreover, the posterior distribution $\pi_{\mathbf{P}|\mathbf{Q}^{\mathrm{obs}}} \sim \mathcal{N}(\mathbf{m}_1, \mathbf{C}_1)$ can be determined from the linear forward model $\mathcal{H}$, the covariance matrix of the random measurement uncertainty $\mathbf{\Sigma}$, the prior distribution $\pi_0 \sim \mathcal{N}(\mathbf{m}_0, \mathbf{C}_0)$ and observations $\mathbf{q}^{\mathrm{obs}}$ using the equations (3.28) and (3.29). In this section, we use the simulated observations $\mathbf{q}_{\mathrm{B}}^{\mathrm{obs}}$ of the magnetic flux density and the simulated observations $\mathbf{q}_{\mathrm{M}}^{\mathrm{obs}}$ of the multipole coefficients defined in equation (5.28). The resulting posterior distributions are denoted by

$$\begin{aligned} \pi^{\mathrm{B}}_{\mathbf{P}|\mathbf{Q}^{\mathrm{obs}}} &\sim \mathcal{N}(\mathbf{m}_1^{\mathrm{B}}, \mathbf{C}_1^{\mathrm{B}}) \\ \pi^{\mathrm{M}}_{\mathbf{P}|\mathbf{Q}^{\mathrm{obs}}} &\sim \mathcal{N}(\mathbf{m}_1^{\mathrm{M}}, \mathbf{C}_1^{\mathrm{M}}). \end{aligned} \tag{5.30}$$

In Figure 5.10, the ground truth $\mathbf{p}^{\mathrm{true}}$ is shown together with the expected value $\mathbf{m}_0$ of the prior distribution and the two expected values of the posterior distributions $\mathbf{m}_1^{\mathrm{B}}$ and $\mathbf{m}_1^{\mathrm{M}}$. Moreover the $1\sigma, 2\sigma$, and 3σ intervals according to the entries on the diagonal of $\mathbf{C}_0$, $\mathbf{C}_1^{\mathrm{B}}$ and $\mathbf{C}_1^{\mathrm{M}}$ are visualized, which can be used to estimate the uncertainty.
The average absolute difference between the maximum a posteriori estimate $\mathbf{m}_1^{\mathrm{B}}$ and the ground truth $\mathbf{p}^{\mathrm{true}}$ is 32% smaller than the average absolute difference between the prior mean $\mathbf{m}_0$ and ground truth. The same comparison yields an improvement of 28% for the maximum a posteriori estimate $\mathbf{m}_1^{\mathrm{M}}$. Moreover, the ground truth is only in very few positions outside the 3σ interval of both posterior distributions. The volumes of the $1\sigma, 2\sigma$, and 3σ intervals of the posterior distributions are smaller than for the prior distribution. It can be verified by checking the conditions (5.18) and (5.18) that both expected values $\mathbf{m}_1^{\mathrm{B}}$ and $\mathbf{m}_1^{\mathrm{M}}$ lead to a model update in the sense that the prediction of quantities of interest is improved at least in the regime of the training data.

Consequently, the computation of a stochastic model update of the three-dimensional linear system model using the maximum a posteriori estimator is validated for observations of Q_{B} and $Q_{\mathrm{M},n}$. In the following section, this method is applied to measured observations $\mathbf{q}_{\mathbf{M}}^{\mathrm{obs}}$ of $Q_{\mathrm{M},n}$.

5.2.3 Application to measured observations

In this section, the method of updating the magnetization parameter vector $\mathbf{p}$ of the three-dimensional linear system model of the first short FASER dipole by computing the maximum a posteriori estimate is applied to measurements of the magnetic flux density conducted with a Hall probe mapper system. More details on the measurement campaign are given in [49] and the measurement data is available in [48]. The observations $A_n^{\mathrm{obs}}(z_r), B_n^{\mathrm{obs}}(z_r)$ of the multipole coefficients are derived by approximating the integrals

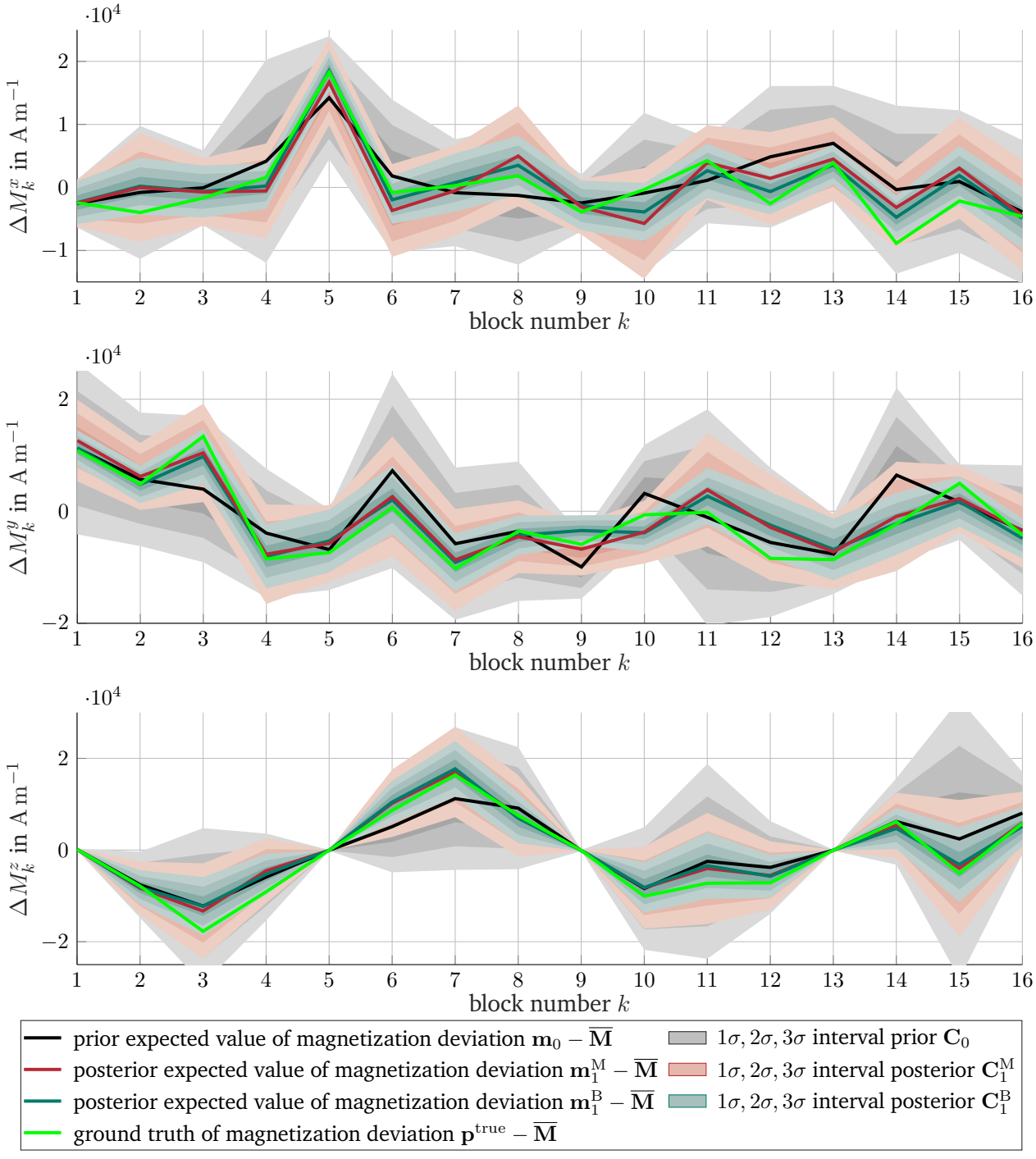

Figure 5.10: Comparison between the ground truth $\mathbf{p}^{\mathrm{true}}$, the prior, and the two posterior distributions for updating the 3D linear system model (top for x, center for y, bottom for z). One posterior distribution is determined based on observations $\mathbf{q}_{\mathrm{B}}^{\mathrm{obs}}$ of the field map quantity of interest, and the other based on observations $\mathbf{q}_{\mathrm{M}}^{\mathrm{obs}}$ of the multipole coefficient quantity of interest. For all distributions, the discrete expected values and the $1\sigma, 2\sigma, 3\sigma$ intervals are visualized with continuous curves to enhance readability.

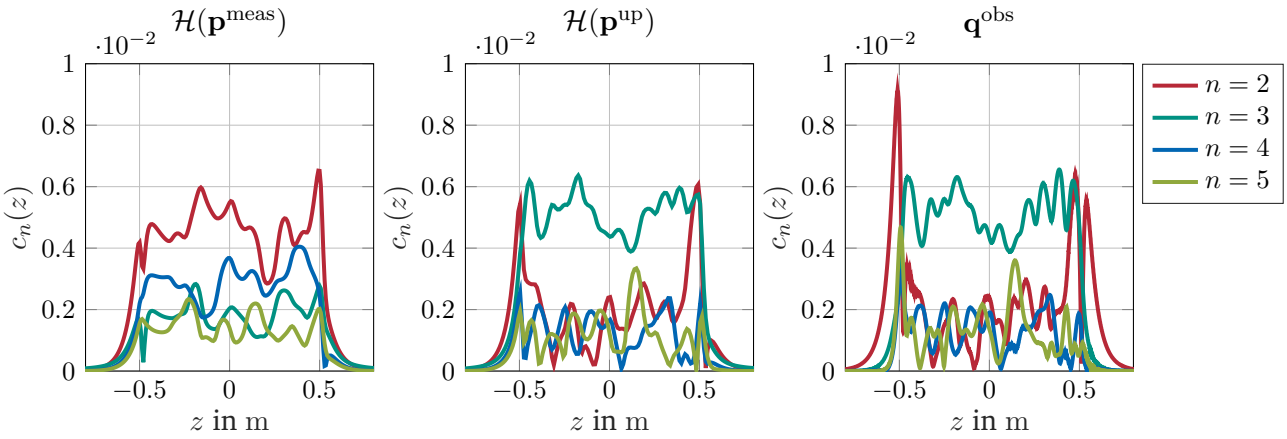

Figure 5.11: Comparison between the prediction $\mathcal{H}(\mathbf{p}^{\text{meas}})$ based on the Helmholtz coil measurements, the updated prediction $\mathcal{H}(\mathbf{p}^{\text{up}})$ based on the maximum a posteriori estimate and the measured observations $\mathbf{q}^{\text{obs}}$ of the relative multipole coefficients $c_n(z)$ defined in equation (5.15). The predictions $\mathcal{H}(\mathbf{p}^{\text{meas}})$ and $\mathcal{H}(\mathbf{p}^{\text{up}})$ are computed using a three-dimensional FEM model.

in equation (2.79) with a finite sum. This observation data was already used in equation (5.15) and in Figure 5.4 to compare system model predictions to measured observations. Due to a possible misalignment of the mapper system, the magnet system, and the simulation, the standard deviations defined in equation (5.16) are assumed.

The system model is updated by setting $\mathbf{p}^{\text{up}} = \mathbf{p}_{\text{MAP}} = \mathbf{m}_1^{\text{M}}$. We verify that the updated magnetization parameter vector is still within the 3σ neighborhood of the prior mean. Hence, unreasonable over-fitting is prevented. Analogously to Figure 5.4, the prediction of the relative coefficients $c_n(z)$ with the updated system model $\mathcal{H}(\mathbf{p}^{\text{up}})$ is compared in Figure 5.11 to the corresponding observations $\mathbf{q}^{\text{obs}}$ of $c_n(z)$ that can be determined from $\mathbf{q}_{\text{M}}^{\text{obs}}$ using equation (5.15). It can be seen that the magnitude and the pattern along the z-axis of the predicted relative coefficients $c_n(z)$ match well with the observations. However, this result is not surprising, since the coefficients $c_n(z)$ are via equation (5.15) closely related to the training data $\mathbf{q}_{\text{M}}^{\text{obs}}$, which was used to compute the update.
To assess the quality of predictions with the updated system model outside the regime of the training data, predictions and measurements of the field map quantity of interest Q_{B} are compared before and after the model update. Since the magnet system is a skew dipole, the comparison is restricted to the x-component of the magnetic flux density. We define the relative residual

$$E^{\text{rel}}(z, \mathbf{p}) := \frac{|B_x^{\text{obs}}(z) - Q_B(\mathbf{A}[\mathbf{M}^{\mathbf{p}}])_x|}{|B_{\max}|} \tag{5.31}$$

where $B_x^{\text{obs}}(z)$ are observations measured with a Hall probe and $Q_B(\mathbf{A}[\mathbf{M}^{\mathbf{p}}])_x$ are the corresponding predictions with the system model. In Figure 5.12, the relative residual $E^{\text{rel}}(z, \mathbf{p})$ is shown for the magnetization parameter vector $\mathbf{p}^{\text{meas}}$ measured with the Helmholtz coil system and for the updated parameter vector $\mathbf{p}^{\text{up}}$. Although the relative residual exceeds for both predictions and in most positions the common threshold of 1 unit in 10000, the relative residual for predictions with the updated parameter vector is in most positions of the homogeneous field region around one order of magnitude smaller than before the update.

There are several possible reasons why the relative residual between observations and updated predictions is not smaller. First, the measured observations $\mathbf{q}^{\text{obs}}$ are affected by uncertainty, and these uncertainties might not

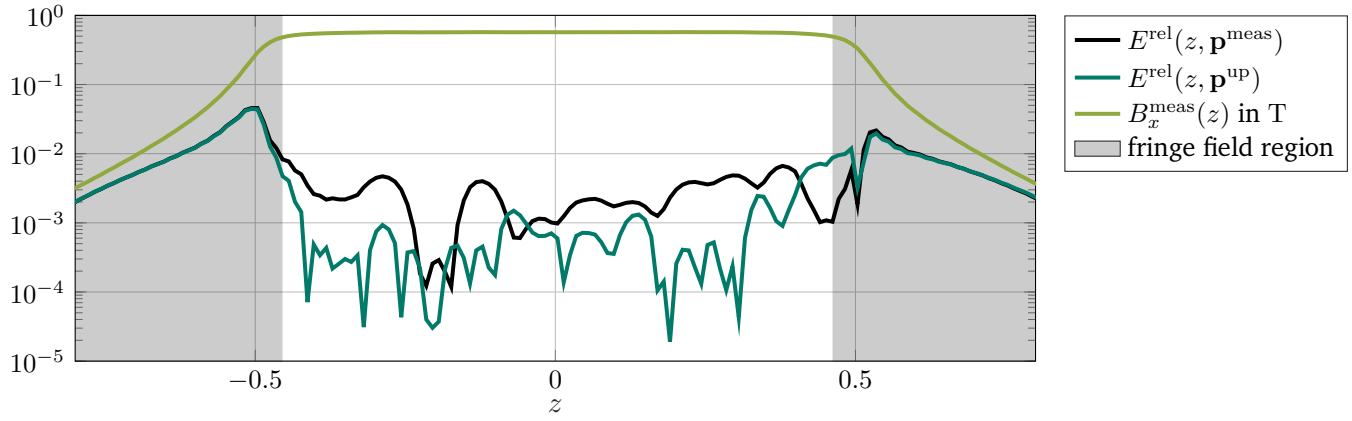

Figure 5.12: Relative residual $E^{\mathrm{rel}}(z, \mathbf{p})$ defined in equation (5.31) between predictions and measurements of the magnetic flux density before and after the model update. Figure adapted from [52].

be limited to the random measurement uncertainty considered in the noise model. Second, the forward model, which is an essential part of the additive noise model and for computing predictions is affected by aleatory and epistemic uncertainties such as the limited knowledge of other possibly relevant physical effects such as small demagnetizations of the PM blocks or uncertainty in their positioning.

5.3 Summary

In this chapter, the magnetization of PM blocks in component-centric system models (Section 1.2.2) of the first short FASER dipole was updated. To derive the stochastic model updates, we used the methods for statistical inference introduced in Chapter 3. Bayesian inference (Section 3.2) combined prior knowledge about the magnetization of the PM blocks that was measured with a tri-axial Helmholtz coil system before the assembly of the Halbach dipole with observations of field-related quantities of interest measured in a later phase of the life cycle of the magnet system.
Similarly to the updates of $B(H)$-curves in the previous chapter, we used Markov chain Monte Carlo sampling with the Metropolis-Hastings algorithm (Section 3.3.2) with the preconditioned Crank-Nicolson proposal to update a two-dimensional non-linear version of the system model that includes the outer construction steel ring of the FASER dipole. The permanent magnetizations of a three-dimensional linear system model of the FASER dipole that omits the steel ring were updated with the maximum a posteriori estimate introduced in Section 3.3.1. With this update, the prediction of the relative multipole coefficients $c_n(z)$ and the prediction of the magnetic flux density in the homogeneous field region were improved. In particular, adjustments of the magnetizations of the PM blocks within the 3σ neighborhood of the prior distribution were sufficient to explain the discrepancy between the predicted and measured relative multipole coefficients observed before the model update.

6 Determination of toroidal harmonic coefficients from the magnetic flux density

Operation-centric system models are typically used to store the information about the magnetic field gained during the characterization of a magnet system as built and are particularly relevant to predicting three-dimensional field maps for particle tracking [143]. In this chapter, a model based on the toroidal harmonic expansion (2.97) is studied for describing the magnetic flux density in curved magnet systems. The toroidal harmonic coefficients are the parameters of this system model. We aim to determine these coefficients from the magnetic flux density observable by standard methods of magnetic measurements. For this purpose, an integration-based and a fitting-based method are derived and evaluated on simulated magnetic flux density data.

System model We restrict the study to static fields at a given operation mode $\mathbf{s}_0$. Since operation-centric system models do not include a model of the magnet system, only quantities of interest in that operation mode can be predicted. Consequently, the system model coincides with the forward model

$$\mathcal{M}(\mathbf{p}, \mathbf{s}_0) = \mathcal{H}(\mathbf{p}). \tag{6.1}$$

The parameters $\mathbf{p}$ depend on the system model's definition. Most state-of-the-art operation-centric system models discussed in Section 1.3.1 are based on the scalar potential formulation of the magnetostatic boundary value problem, which yields under the assumption of linear permeability and the absence of sources, the Laplace equation with boundary conditions. The difference between the models is the choice of basis used to represent solutions to the Laplace equation. The approaches reach from classical expansions of the magnetic scalar potential [74, 119, 122] to an approach based on the double-layer potential and the BEM [92].
Criteria to choose a suitable representation of the magnetic scalar potential on a given domain D and for a given field are according to [135]:

1. The underlying coordinate system is such that symmetries of the magnet system coincide with an invariance along one of the coordinates, and the domain boundary coincides with an isosurface of one of the coordinates.

2. The contribution of the expansion terms to the described field decreases as the order increases. For example, the magnetic field generated by a perfect straight dipole magnet can be described by a single coefficient in the circular harmonic expansion (2.76). And, more generally, the field generated by most straight accelerator magnets can be described by only a few coefficients of the circular harmonic expansion.

3. The expansion's coefficients are directly observable by a measurement method, e.g., the circular harmonics can be directly observed with rotating coil magnetometers.

This chapter focuses on operation-centric system models for curved magnet systems, thus we assume that the computational domain is either a solid torus D or a toroidal wedge $\widetilde{D} \subset D$. According to the criteria above, the toroidal coordinate system defined in equation (2.82) is a suitable choice, since τ-isosurfaces are tori (see Section 2.4.2) and the rotational symmetry yields an invariance of the field regarding the toroidal angle φ. If a cylindrical computational domain in the free space of a curved magnet system is used instead of a toroidal domain, the circular harmonic expansion (2.76) might still be insufficient to describe the generated magnetic field because this expansion is based on the assumption (2.75) that the derivative with respect to the longitudinal component of the magnetic flux density vanishes. This limitation of the circular harmonic expansion is discussed in [135]. We illustrate this limitation with an example in Section 6.3.1.

As a result of these considerations, the system models on toroidal domains and toroidal wedges studied in this chapter are based on the toroidal harmonic expansion of the magnetic scalar potential

$$\begin{aligned}\phi_{\mathrm{m}}(\tau,\sigma,\varphi) = \mathcal{E}^{\mathrm{t}}\varphi + \sqrt{\kappa(\tau,\sigma)}\sum_{m,n=0}^{\infty} Q^{m}_{n-\frac{1}{2}}(\cosh(\tau)) \quad &\big(\mathcal{A}^{\mathrm{t}}_{n,m}\cos(n\sigma)\cos(m\varphi) + \mathcal{B}^{\mathrm{t}}_{n,m}\sin(n\sigma)\cos(m\varphi) \\ &+ \mathcal{C}^{\mathrm{t}}_{n,m}\cos(n\sigma)\sin(m\varphi) + \mathcal{D}^{\mathrm{t}}_{n,m}\sin(n\sigma)\sin(m\varphi)\big)\end{aligned} \tag{6.2}$$

or its normalized version (2.99) introduced in Section 2.4.2, where $Q^{m}_{n-1/2}$ are the associated Legendre functions of the second kind of half-integer degree (see Appendix 8.1), the coefficients $\mathcal{A}^{\mathrm{t}}_{n,m}, \mathcal{B}^{\mathrm{t}}_{n,m}, \mathcal{C}^{\mathrm{t}}_{n,m}, \mathcal{D}^{\mathrm{t}}_{n,m} \in \mathbb{R}$ are the toroidal harmonic coefficients, and $\mathcal{E}^{\mathrm{t}} \in \mathbb{R}$ is the linear coefficient. The symbol $\kappa(\tau,\sigma)$ defined in equation (2.95) is used to save on notation. The formulas for the toroidal harmonic expansion of the magnetic flux density are given in Appendix 8.2. For the special case that $\mathbf{B}$ is independent of φ, which is referred to as the rotationally symmetric case, the toroidal harmonic expansion of ϕ_{m} simplifies to equation (2.104).

We consider the following three use cases of operation-centric system models based on the toroidal harmonic expansion:

(i) Description of the magnetic flux density $\mathbf{B}$ in toroidal domains $D = U^2 \times S^1$, where U^2 is a disk with radius R and S^1 is a circle with radius ρ.

(ii) Description of the magnetic flux density $\mathbf{B}$ in a toroidal wedge $\widetilde{D} \subset D$ with toroidal angle $\varphi \in [0, l]$ and $l \leq 2\pi$.

(iii) Description of the average magnetic flux density $\int \mathbf{B}\,\mathrm{d}\varphi$ with respect to the coordinate φ.

For the first use case, the parameters $\mathbf{p}$ of the forward and the system model are given by the linear coefficient $\mathcal{E}^{\mathrm{t}}$ and the toroidal harmonic coefficients $\mathcal{A}^{\mathrm{t}}_{n,m}, \mathcal{B}^{\mathrm{t}}_{n,m}, \mathcal{C}^{\mathrm{t}}_{n,m}$ and $\mathcal{D}^{\mathrm{t}}_{n,m}$ (or respectively $\mathcal{A}^{\mathrm{t}}_{n}, \mathcal{B}^{\mathrm{t}}_{n}$ in the rotationally symmetric case). The forward model maps the parameters $\mathbf{p}$ to predictions of the magnetic flux density

$$\mathcal{H} : \mathbf{p} = (\mathcal{E}^{\mathrm{t}}, \mathcal{A}^{\mathrm{t}}_{n,m}, \mathcal{B}^{\mathrm{t}}_{n,m}, \mathcal{C}^{\mathrm{t}}_{n,m}, \mathcal{D}^{\mathrm{t}}_{n,m}) \mapsto \mathbf{B}(\tau,\sigma,\varphi) \tag{6.3}$$

using the formulas (8.12), (8.13), (8.14) and (8.15). The other two use cases are introduced in the following paragraphs in more detail.

Magnetic flux density on toroidal wedges For some curved accelerator magnets such as the curved dipole magnets of the ELENA decelerator [30] (see Figure 6.1 (left)), the computational domain of a toroidal wedge $\widetilde{D} \subset D$ is more suitable than the toroidal domain D because the aperture's air gap only covers a fraction of D. In rotationally symmetric machines such as the ITER tokamak [75] (see Figure 6.1 (right)), the nominal magnetic flux density is periodic on torus wedges of toroidal angle $\frac{\pi}{9}$ if all 18 toroidal field coils are powered with the same excitation current. Consequently, the description of the magnetic scalar potential and the

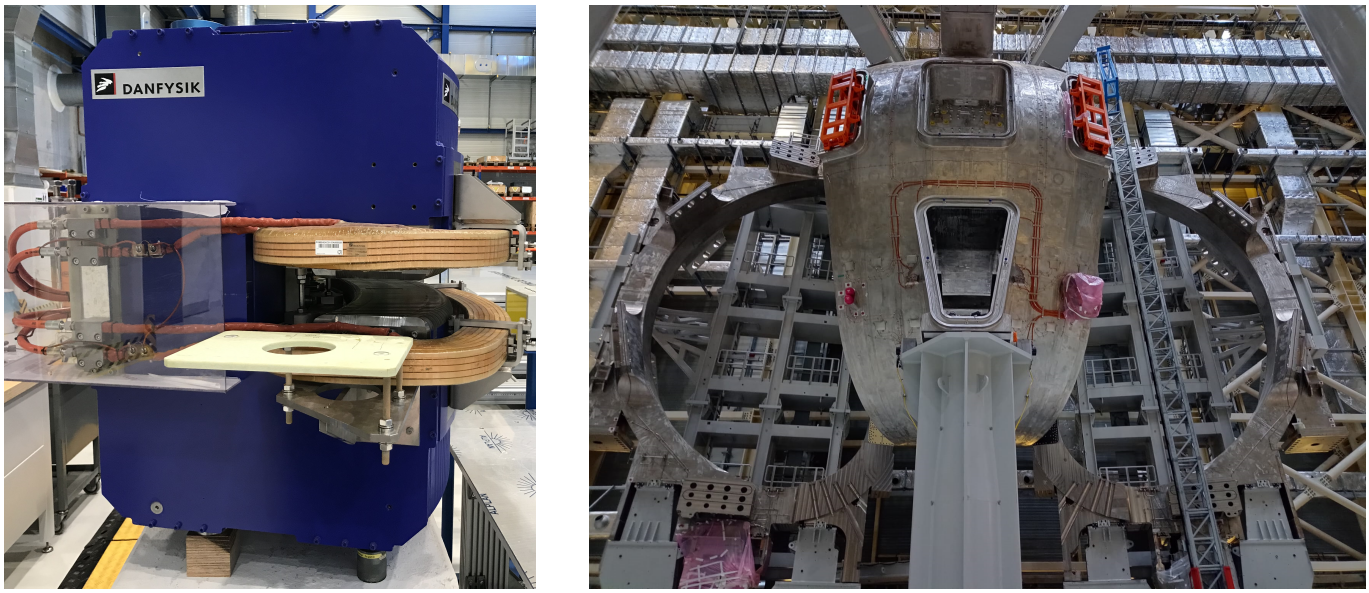

Figure 6.1: Left: Curved dipole magnet of the ELENA decelerator. Right: Part of the ITER tokamak (Source: Piotr Rogacki).

magnetic flux density on a toroidal wedge with $\varphi \in [0, \frac{\pi}{9}]$ is sufficient in this case. In this paragraph, the toroidal harmonic expansion on a toroidal wedge with $\varphi \in [0, l]$ is derived for $l \leq 2\pi$. Thereby, wedges with $\frac{2\pi}{l} \in \mathbb{N}$ are particularly suitable because equation (8.1) can be used to compute the associated Legendre functions of the second kind of half-integer degree and due to the periodicity, the number of toroidal harmonic coefficients concerning the order m can be reduced.

Let $\widetilde{D} \subset D$ be the toroidal wedge that covers the image of the toroidal coordinates for $\varphi \in [0, l]$. Assume that the magnetic flux density is periodic on $[0, l]$, i.e.

$$\mathbf{B}(\tau, \sigma, 0) = \mathbf{B}(\tau, \sigma, l) \tag{6.4}$$

for all $\tau \in (0, \infty)$ and all $\sigma \in [0, 2\pi]$. This condition is in particular satisfied in symmetric apertures, or if the bounds of the interval $[0, l]$ are chosen far from the magnet system, where it can be assumed that $\mathbf{B}(\tau, \sigma, 0) = \mathbf{B}(\tau, \sigma, l) = \mathbf{0}$. Exploiting the periodicity condition (6.4) yields with the same argumentation as in Section 2.4.2 the *toroidal harmonic expansion of* ϕ_m *on* $\widetilde{D}$

$$\begin{aligned}\phi_\mathrm{m}(\tau, \sigma, \varphi) = \mathcal{E}^\mathrm{t}\varphi + \sqrt{\kappa(\tau, \sigma)} \sum_{m,n=0}^{\infty} Q_{n-\frac{1}{2}}^{\frac{2\pi m}{l}}(\cosh(\tau)) \Bigg[&\mathcal{A}_{n,m}^\mathrm{t} \cos(n\sigma) \cos\left(\frac{2\pi m\varphi}{l}\right) + \mathcal{B}_{n,m}^\mathrm{t} \sin(n\sigma) \cos\left(\frac{2\pi m\varphi}{l}\right) \\ &+ \mathcal{C}_{n,m}^\mathrm{t} \cos(n\sigma) \sin\left(\frac{2\pi m\varphi}{l}\right) + \mathcal{D}_{n,m}^\mathrm{t} \sin(n\sigma) \sin\left(\frac{2\pi m\varphi}{l}\right)\Bigg].\end{aligned} \tag{6.5}$$

In comparison to the toroidal harmonic expansion of ϕ_m on D given in equation (6.2), the only difference is that the order m is replaced by the term $\frac{2\pi m}{l}$. The corresponding formulas for the magnetic flux density on $\widetilde{D}$ are given in Appendix 8.3. Again, the formulas only differ by replacing m with the term $\frac{2\pi m}{l}$. Consequently, toroidal harmonic coefficients on a toroidal wedge can be determined with the same methods as on the toroidal domain D.

The forward model to predict the magnetic flux density on the toroidal wedge is analogously defined to the mapping (6.3) by

$$\mathcal{H} : \mathbf{p} = (\mathcal{E}^{\mathrm{t}}, \mathcal{A}^{\mathrm{t}}_{n,m}, \mathcal{B}^{\mathrm{t}}_{n,m}, \mathcal{C}^{\mathrm{t}}_{n,m}, \mathcal{D}^{\mathrm{t}}_{n,m}) \mapsto \mathbf{B}(\tau, \sigma, \varphi), \tag{6.6}$$

where now the equations (8.33), (8.34) and (8.35) are used.

Average magnetic flux density In [119, Section 6.1.3], it is shown that if the magnetic scalar potential satisfies the Laplace equation in 3D Cartesian coordinates and if $[0, l]$ is a segment on the longitudinal y-axis of the magnet system, such that the respective component of the magnetic field satisfies $H_y(x, 0, z) = H_y(x, l, z)$ (e.g., due to symmetry or because the field equals zero), then the average magnetic scalar potential $\int_0^l \phi_{\mathrm{m}} \, \mathrm{d}y$ satisfies the Laplace equation in 2D Cartesian coordinates in the xz-plane. This result is useful because it justifies the application of the scaling laws of the multipole coefficients (2.81) also to integrated quantities as discussed in [119, Section 6.1.3]. In this paragraph, a similar result in toroidal coordinates is derived and discussed.

Given a toroidal wedge with $\varphi \in [0, l]$ and $l \leq 2\pi$ inside the air domain of a magnet system and assume that the φ-component of the magnetic field satisfies the symmetry condition $H_\varphi(\tau, \sigma, 0) = H_\varphi(\tau, \sigma, l)$. The latter condition is satisfied particularly if the interval bounds are chosen far from the aperture and for symmetric apertures.
If the magnetic scalar potential ϕ_{m} in the toroidal wedge satisfies the Laplace equation in toroidal coordinates (2.92), the average solution $\overline{\phi_{\mathrm{m}}}$ on $[0, l]$ defined by

$$\overline{\phi_{\mathrm{m}}}(\tau, \sigma) \coloneqq \int_0^l \phi_{\mathrm{m}}(\tau, \sigma, \varphi) \, \mathrm{d}\varphi. \tag{6.7}$$

satisfies the same simplified Laplace equation (2.100) as the magnetic scalar potential in the rotationally symmetric case (2.104). The following calculation justifies this claim:

$$\begin{aligned}
& \frac{\kappa(\tau,\sigma)^3}{a^3 \sinh(\tau)} \left[\frac{\partial}{\partial \tau} \left(\frac{a \sinh(\tau)}{\kappa(\tau,\sigma)} \frac{\partial \overline{\phi_{\mathrm{m}}}}{\partial \tau} \right) + \frac{\partial}{\partial \sigma} \left(\frac{a \sinh(\tau)}{\kappa(\tau,\sigma)} \frac{\partial \overline{\phi_{\mathrm{m}}}}{\partial \sigma} \right) \right] && (6.8) \\
= & \int_0^l \frac{\kappa(\tau,\sigma)^3}{a^3 \sinh(\tau)} \left[\frac{\partial}{\partial \tau} \left(\frac{a \sinh(\tau)}{\kappa(\tau,\sigma)} \frac{\partial \phi_{\mathrm{m}}}{\partial \tau} \right) + \frac{\partial}{\partial \sigma} \left(\frac{a \sinh(\tau)}{\kappa(\tau,\sigma)} \frac{\partial \phi_{\mathrm{m}}}{\partial \sigma} \right) \right] \mathrm{d}\varphi && (6.9) \\
= & -\int_0^l \frac{\kappa(\tau,\sigma)^3}{a^3 \sinh(\tau)} \left[\frac{\partial}{\partial \varphi} \left(\frac{a}{\kappa(\tau,\sigma) \sinh(\tau)} \frac{\partial \phi_{\mathrm{m}}}{\partial \varphi} \right) \right] \mathrm{d}\varphi && (6.10) \\
= & -\frac{\kappa(\tau,\sigma)^2}{a^2 \sinh^2(\tau)} \int_0^l \frac{\partial^2 \phi_{\mathrm{m}}}{\partial \varphi^2} \mathrm{d}\varphi && (6.11) \\
= & \frac{\kappa(\tau,\sigma)}{a \sinh(\tau)} \left[H_\varphi(\varphi) \right]_0^l . && (6.12)
\end{aligned}$$

Thereby, we used the Leibniz rule to interchange integration and differentiation in equation (6.9), the fact that the scaling factors h_τ, h_σ and h_φ are independent of φ in equation (6.9) and (6.11), and the definition of the magnetic scalar potential (2.35) according to that $H_\varphi = h_\varphi \partial \phi_{\mathrm{m}} / \partial \varphi$. The right-hand side of equation (6.12) equals zero if and only if the symmetry condition $H_\varphi(\tau, \sigma, 0) = H_\varphi(\tau, \sigma, l)$ is satisfied.
Consequently, the toroidal harmonic expansion of the magnetic scalar potential in the rotationally symmetric case (2.104) can also be used to describe the average magnetic scalar potential $\overline{\phi_{\mathrm{m}}}$. Formulas for the average magnetic flux density $\int_0^l \mathbf{B} \, \mathrm{d}\varphi$ are given in Appendix 8.3. They have the same structure as the rotationally symmetric magnetic flux density formulas. Hence, the toroidal harmonic coefficients of the average magnetic

flux density can be determined with the same methods as the coefficients in the rotationally symmetric case. The forward model, in this case, is defined by

$$\mathcal{H} : \mathbf{p} = (\mathcal{E}^{\mathrm{t}}, \mathcal{A}^{\mathrm{t}}_{n,0}, \mathcal{B}^{\mathrm{t}}_{n,0}) \mapsto \int_0^l \mathbf{B}(\tau, \sigma, \varphi)\, \mathrm{d}\varphi. \tag{6.13}$$

Notice that this result does not hold for the integrated transverse magnetic scalar potential defined by

$$\widetilde{\phi_{\mathrm{m}}}(\tau, \sigma) \coloneqq \int_0^l \phi_{\mathrm{m}}(\tau, \sigma, \varphi)\, \mathrm{d}\widetilde{\mathbf{r}} = \int_0^l \phi_{\mathrm{m}}(\tau, \sigma, \varphi) h_\varphi\, \mathrm{d}\varphi, \tag{6.14}$$

where $\mathrm{d}\widetilde{\mathbf{r}}$ is the line element describing the integration curve in toroidal coordinates that varies in φ. Due to the dependence of h_φ on both τ and σ the partial derivative with respect to τ and σ and the term h_φ can not be interchanged.

Inverse problem Determining the toroidal harmonic coefficients from observations of the magnetic flux density on a toroidal domain D can be formulated as the following inverse problem:

Problem 7. ***(Inverse problem)*** *Given observations* $\mathbf{B}^{\mathrm{obs}}$ *of the magnetic flux density in* D*, find the linear coefficient and the toroidal harmonic coefficients* $\mathbf{p} = (\mathcal{E}^{\mathrm{t}}, \mathcal{A}^{\mathrm{t}}_{n,m}, \mathcal{B}^{\mathrm{t}}_{n,m}, \mathcal{C}^{\mathrm{t}}_{n,m}, \mathcal{D}^{\mathrm{t}}_{n,m})$ *such that the equations* (8.12)*,* (8.13) *and* (8.14) *hold, i.e.* $\mathcal{H}(\mathbf{p}) = \mathbf{B}^{\mathrm{obs}}$.

Inverse problems can be defined equivalently for the other two use cases concerning the magnetic flux density on toroidal wedges and the average magnetic flux density. Notice that implementations of the forward model are limited to a finite number of parameters, thus we usually work with a finite-dimensional approximation of the inverse problem. In this case, and also if the observations $\mathbf{B}^{\mathrm{obs}}$ are affected by uncertainty, the condition $\mathcal{H}(\mathbf{p}) = \mathbf{B}^{\mathrm{obs}}$ has to be relaxed like in the preceding chapters to address that a solution to the inverse problem 7 might not exist.

Several approaches can be found in the literature to determine the toroidal harmonic coefficients from the magnetic flux density, the magnetic vector potential, or the magnetic scalar potential. Using the trigonometric functions' orthogonality, the toroidal harmonic expansion coefficients are determined by integration from the magnetic vector potential [36]. The same method is used in [150], where the magnetic scalar potential is integrated.
Another approach to determine a finite set of toroidal harmonic coefficients is fitting. In [58], toroidal harmonic coefficients are fitted to observations of the magnetic scalar potential, [19, 89, 133] suggest fitting the coefficients to observations of the magnetic flux density. Determining the toroidal harmonic coefficients based on observations of the magnetic flux density is advantageous because standard magnetic measurement methods can observe this quantity of interest. In contrast, the magnetic scalar and vector potential cannot be measured. In addition, many field simulation software allows calculating $\mathbf{B}$, while different potential formulations may be underlying. The approaches [19, 133] use knowledge of the observed field that leads to simplifications of the expansion, e.g., by assuming symmetries, whereas the recently published approach described in [89] is, like our approach, also suitable for general fields.
Similar to the approaches in the literature, we consider a determination method based on integration and an approach based on fitting. The derived integration method differs from the existing ones by integrating the magnetic flux density instead of a potential. The fitting method differs from existing methods by including gauging and considering optimal observation positions.

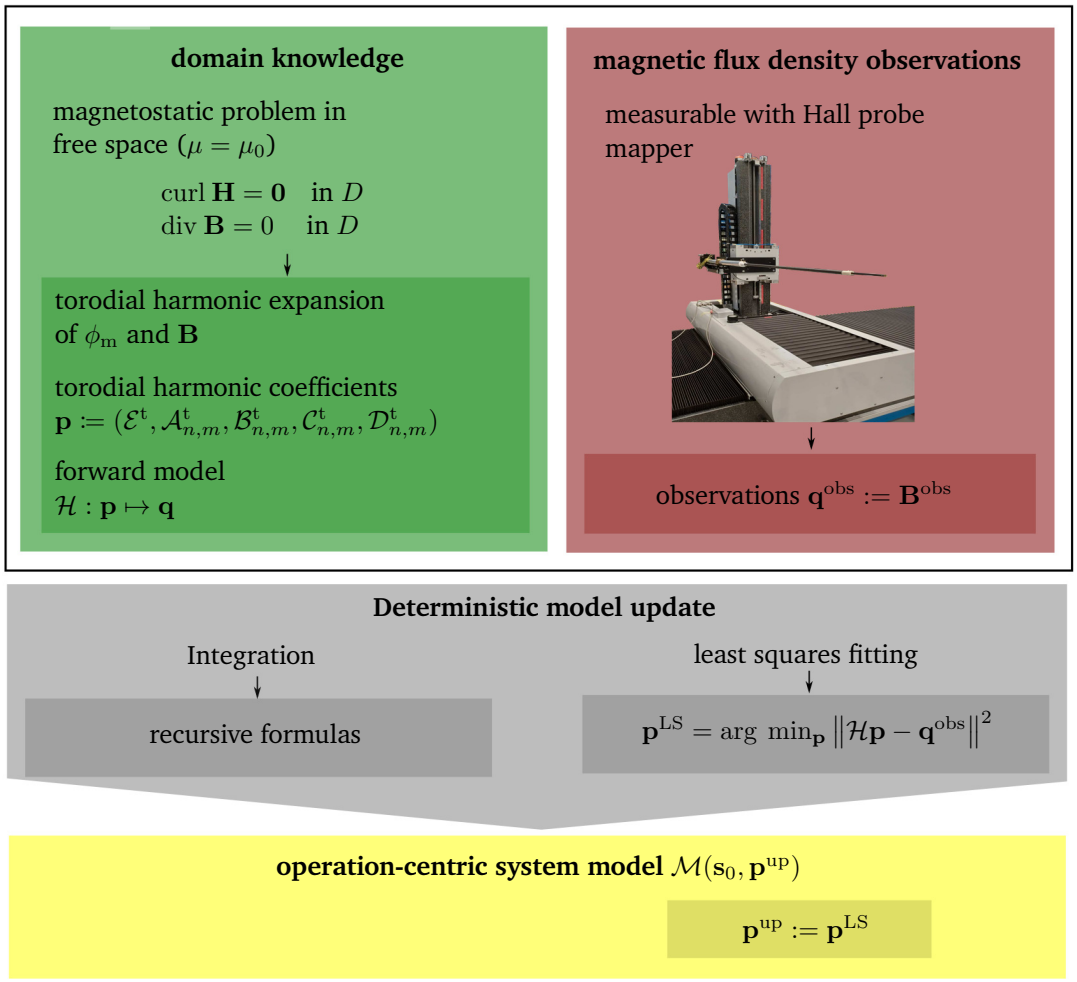

Figure 6.2: Overview of sources of knowledge and methods to build an operation-centric system model on a toroidal domain based on the toroidal harmonic expansion. From the magnetostatic problem in free space, the toroidal harmonic expansion of the magnetic scalar potential, and the magnetic flux density are derived using R-separation. The coefficients of this expansion are determined using integration and least squares fitting. The least squares fitting method is recommended since the recursive formulas obtained by integration are numerically unstable. The resulting system model can be used to predict the magnetic flux density in positions that were not included in the observations $\mathbf{q}^\mathrm{obs}$.

Structure of this chapter Figure 6.2 summarizes the methods and sources of knowledge combined in this chapter to determine the toroidal harmonic coefficients. The remainder of the chapter is organized as follows: First, in Section 6.1, some basic properties of the toroidal harmonic expansion are discussed, e.g., the linear occurrence of the toroidal harmonic coefficients and the linear dependence of the functions spanning the skew part of the magnetic flux density in the toroidal harmonic expansion. Due to the first property, the inverse problem 7 is linear. According to the second property, the magnetic flux density does not uniquely define the skew harmonic coefficients, hence gauging is required.
Subsequently, in Section 6.2, two methods are derived to determine the toroidal harmonic coefficients from magnetic flux density observations. The first method is based on the orthogonality of the trigonometric functions. Similar to the equations (2.78) and (2.79) for obtaining the circular harmonic coefficients, recursive formulas to determine the toroidal harmonics can be derived by integrating the magnetic flux density on τ-isolines. However, due to their recursive nature, these formulas are numerically unstable. More suitable for applications is the second method, which determines a finite number of toroidal harmonic coefficients by linear least squares fitting. Imposing a gauging condition on the skew harmonic coefficients, and optimizing the observation positions of the magnetic flux density improves the conditioning of the problem.
In the last section of this chapter, the least squares fitting method is applied for validation to simulated observations of the magnetic flux density generated by the coil arrangements of the ITER tokamak and of a curved CCT magnet. We show on rotationally symmetric data that the toroidal harmonic expansion is more suitable for describing the field inside the ITER tokamak than the circular harmonic expansion. Moreover, the operation-centric model based on the determined toroidal harmonic coefficients is assessed by evaluating the relative error between its predicted magnetic flux density and the ground truth magnetic flux density simulated with the software ROXIE [121]. For the ITER example, a few toroidal harmonic coefficients are sufficient to obtain a relative prediction error of the order of magnitude of 10^{-6}. Hence, the toroidal harmonic expansion is a suitable operation-centric system model in this case. In the curved CCT dipole example, more toroidal harmonic coefficients are required to predict the magnetic flux density in the center of the aperture with a relative error of the order of magnitude of 10^{-5}. Despite the large number of coefficients, the common threshold for sufficient accuracy of the relative prediction error of 1 unit in 10000 is exceeded in the fringe field region for the curved CCT example. An operation-centric system model that is not based on a periodicity assumption of the data, might be more suitable for this application.

6.1 Properties of the toroidal harmonic expansion

6.1.1 Linearity

The toroidal harmonic coefficients $\mathcal{A}^{\mathrm{t}}_{n,m}, \mathcal{B}^{\mathrm{t}}_{n,m}, \mathcal{C}^{\mathrm{t}}_{n,m}$ and $\mathcal{D}^{\mathrm{t}}_{n,m}$ appear as linear coefficients in both, the toroidal harmonic expansion of the magnetic scalar potential (2.99) and the toroidal harmonic expansions of the magnetic flux density components (8.12), (8.13) and (8.14). Consequently, the magnetic flux density can be computed from a given (finite) set of toroidal harmonic coefficients with a matrix-vector multiplication. The linearity is significant because it yields that the forward model $\mathcal{H}$ is linear. Conversely, the inverse problem 7 can be approximated and solved by resolving the corresponding finite linear equation system for the toroidal harmonic coefficients.
In this paragraph, the notation of this linear equation system is defined. The solution is discussed later in Section 6.2.2. In Appendix 8.2, the functions

$$\begin{array}{llll} f^{\mathcal{A}}_{n,m}, f^{\mathcal{B}}_{n,m}, f^{\mathcal{C}}_{n,m}, f^{\mathcal{D}}_{n,m}, & g^{\mathcal{A}}_{n,m}, g^{\mathcal{B}}_{n,m}, g^{\mathcal{C}}_{n,m}, g^{\mathcal{D}}_{n,m}, & h^{\mathcal{A}}_{n,m}, h^{\mathcal{B}}_{n,m}, h^{\mathcal{C}}_{n,m}, h^{\mathcal{D}}_{n,m} : & (\tau,\sigma,\varphi) \mapsto \mathbb{R} \\ f^{\mathcal{A}}_{n}, f^{\mathcal{B}}_{n}, & g^{\mathcal{A}}_{n}, g^{\mathcal{B}}_{n}, & h^{\mathcal{E}} : & (\tau,\sigma) \mapsto \mathbb{R} \end{array} \tag{6.15}$$

are defined such that the magnetic flux density components can be written as the linear combinations

$$B_\tau = \sum_{m,n=0}^{\infty} \left[\mathcal{A}^{\mathrm{t}}_{n,m} f^{\mathcal{A}}_{n,m} + \mathcal{B}^{\mathrm{t}}_{n,m} f^{\mathcal{B}}_{n,m} + \mathcal{C}^{\mathrm{t}}_{n,m} f^{\mathcal{C}}_{n,m} + \mathcal{D}^{\mathrm{t}}_{n,m} f^{\mathcal{D}}_{n,m}\right] \tag{6.16}$$

$$B_\sigma = \sum_{m,n=0}^{\infty} \left[\mathcal{A}^{\mathrm{t}}_{n,m} g^{\mathcal{A}}_{n,m} + \mathcal{B}^{\mathrm{t}}_{n,m} g^{\mathcal{B}}_{n,m} + \mathcal{C}^{\mathrm{t}}_{n,m} g^{\mathcal{C}}_{n,m} + \mathcal{D}^{\mathrm{t}}_{n,m} g^{\mathcal{D}}_{n,m}\right] \tag{6.17}$$

$$B_\varphi = \sum_{m,n=0}^{\infty} \left[\mathcal{A}^{\mathrm{t}}_{n,m} h^{\mathcal{A}}_{n,m} + \mathcal{B}^{\mathrm{t}}_{n,m} h^{\mathcal{B}}_{n,m} + \mathcal{C}^{\mathrm{t}}_{n,m} h^{\mathcal{C}}_{n,m} + \mathcal{D}^{\mathrm{t}}_{n,m} h^{\mathcal{D}}_{n,m}\right] + \mathcal{E}^{\mathrm{t}} h^{\mathcal{E}}. \tag{6.18}$$

If these series of toroidal harmonic expansions are truncated at $n = N$ and $m = M$, the equations (6.16), (6.17) and (6.18) can be collected in the linear equation system

$$\begin{pmatrix} B_\tau \\ B_\sigma \\ B_\varphi \end{pmatrix} = \begin{pmatrix} 0 & f^{\mathcal{A}} & f^{\mathcal{B}} & f^{\mathcal{C}} & f^{\mathcal{D}} \\ 0 & g^{\mathcal{A}} & g^{\mathcal{B}} & g^{\mathcal{C}} & g^{\mathcal{D}} \\ h^{\mathcal{E}} & h^{\mathcal{A}} & h^{\mathcal{B}} & h^{\mathcal{C}} & h^{\mathcal{D}} \end{pmatrix} \begin{pmatrix} \mathcal{E}^{\mathrm{t}} \\ \mathcal{A}^{\mathrm{t}} \\ \mathcal{B}^{\mathrm{t}} \\ \mathcal{C}^{\mathrm{t}} \\ \mathcal{D}^{\mathrm{t}} \end{pmatrix}. \tag{6.19}$$

Thereby, the vectors $\mathcal{A}^{\mathrm{t}}, \mathcal{B}^{\mathrm{t}}, \mathcal{C}^{\mathrm{t}}, \mathcal{D}^{\mathrm{t}}$ are defined by

$$\begin{aligned} \mathcal{A}^{\mathrm{t}} &\coloneqq \begin{pmatrix} \mathcal{A}^{\mathrm{t}}_{0,0} & \dots & \mathcal{A}^{\mathrm{t}}_{0,M} & \dots & \mathcal{A}^{\mathrm{t}}_{N,0} & \dots & \mathcal{A}^{\mathrm{t}}_{N,M} \end{pmatrix}^\top \\ \mathcal{B}^{\mathrm{t}} &\coloneqq \begin{pmatrix} \mathcal{B}^{\mathrm{t}}_{1,0} & \dots & \mathcal{B}^{\mathrm{t}}_{1,M} & \dots & \mathcal{B}^{\mathrm{t}}_{N,0} & \dots & \mathcal{B}^{\mathrm{t}}_{N,M} \end{pmatrix}^\top \\ \mathcal{C}^{\mathrm{t}} &\coloneqq \begin{pmatrix} \mathcal{C}^{\mathrm{t}}_{0,1} & \dots & \mathcal{C}^{\mathrm{t}}_{0,M} & \dots & \mathcal{C}^{\mathrm{t}}_{N,1} & \dots & \mathcal{C}^{\mathrm{t}}_{N,M} \end{pmatrix}^\top \\ \mathcal{D}^{\mathrm{t}} &\coloneqq \begin{pmatrix} \mathcal{D}^{\mathrm{t}}_{1,1} & \dots & \mathcal{D}^{\mathrm{t}}_{1,M} & \dots & \mathcal{D}^{\mathrm{t}}_{N,1} & \dots & \mathcal{D}^{\mathrm{t}}_{N,M} \end{pmatrix}^\top \end{aligned} \tag{6.20}$$

and the matrix entries are the corresponding vector-valued functions evaluated in (τ, σ, φ), summarizing the functions defined in (6.15), e.g.,

$$f^{\mathcal{A}} \coloneqq \begin{pmatrix} f^{\mathcal{A}}_{0,0} & \dots & f^{\mathcal{A}}_{0,M} & \dots & f^{\mathcal{A}}_{N,0} & \dots & f^{\mathcal{A}}_{N,M} \end{pmatrix}. \tag{6.21}$$

This notation omits the dependence of the functions on (τ, σ, φ) for readability. Notice that equation (6.19) is a finite-dimensional approximation of the forward model $\mathbf{q} = \mathcal{H}\mathbf{p}$ defined in equation (6.3).

In the rotationally symmetric case, the problem is simplified and the components of the magnetic flux density are given by

$$B_\tau = \sum_{n=0}^{\infty} \left[\mathcal{A}^{\mathrm{t}}_n f^{\mathcal{A}}_n + \mathcal{B}^{\mathrm{t}}_n f^{\mathcal{B}}_n\right] \tag{6.22}$$

$$B_\sigma = \sum_{n=0}^{\infty} \left[\mathcal{A}^{\mathrm{t}}_n g^{\mathcal{A}}_n + \mathcal{B}^{\mathrm{t}}_n g^{\mathcal{B}}_n\right] \tag{6.23}$$

$$B_\varphi = \mathcal{E}^{\mathrm{t}} h^{\mathcal{E}}, \tag{6.24}$$

with the spanning functions $f^{\mathcal{A}}_n, f^{\mathcal{B}}_n,\ g^{\mathcal{A}}_n, g^{\mathcal{B}}_n : (\tau, \sigma) \mapsto \mathbb{R}$ that satisfy

$$f^{\mathcal{A}}_n \coloneqq f^{\mathcal{A}}_{n,0}, \qquad f^{\mathcal{B}}_n \coloneqq f^{\mathcal{B}}_{n,0}, \qquad g^{\mathcal{A}}_n \coloneqq g^{\mathcal{A}}_{n,0}, \qquad g^{\mathcal{B}}_n \coloneqq g^{\mathcal{B}}_{n,0} \tag{6.25}$$

for all $n \in \mathbb{N}$. Analogously to the general case, we truncate the expansions in equation (6.22) and (6.23) at $n = N$ and collect the equations in the linear equation system

$$\begin{pmatrix} B_\tau \\ B_\sigma \\ B_\phi \end{pmatrix} = \begin{pmatrix} 0 & f^{\mathcal{A}} & f^{\mathcal{B}} \\ 0 & g^{\mathcal{A}} & g^{\mathcal{B}} \\ h^{\mathcal{E}} & 0 & 0 \end{pmatrix} \begin{pmatrix} \mathcal{E}^{\mathrm{t}} \\ \mathcal{A}^{\mathrm{t}} \\ \mathcal{B}^{\mathrm{t}} \end{pmatrix}. \tag{6.26}$$

In the following paragraph, we show that the functions $\{f_n^{\mathcal{A}}\}_{0\leq n}$ and the functions $\{g_n^{\mathcal{A}}\}_{0\leq n}$, which span the skew part of the magnetic flux density, are linearly dependent. Although the truncated sets $\{f_n^{\mathcal{A}}\}_{0\leq n\leq N}$ and $\{g_n^{\mathcal{A}}\}_{0\leq n\leq N}$ are linearly independent, it is observed that the matrix in equation (6.26) remains poorly conditioned. To improve the conditioning, a row that defines $\mathcal{A}_0^{\mathrm{t}}$ can be added to the matrix, taking advantage of the freedom of choice due to the linear dependence of the full set of functions. More details are discussed later in Section 6.2.2. The study of linear dependence is restricted to the rotationally symmetric case.

6.1.2 Linear dependence

In this paragraph, we show that there is a non-trivial choice of skew harmonic coefficients $\mathcal{A}_n^{\mathrm{t}}$ such that the corresponding magnetic scalar potential given by

$$\phi_{\mathrm{m}}(\tau,\sigma,\varphi) = \mathcal{E}^{\mathrm{t}}\varphi + \sqrt{\kappa(\tau,\sigma)}\sum_{n=0}^{\infty} Q^0_{n-\frac{1}{2}}(\cosh(\tau))\left(\mathcal{A}_n^{\mathrm{t}}\cos(n\sigma) + \mathcal{B}_n^{\mathrm{t}}\sin(n\sigma)\right) \tag{6.27}$$

is constant. Consequently, the corresponding magnetic flux density is zero, even though not all coefficients of the linear combination in the equations (6.22) and (6.23) are zero. Hence, the sets of functions $\{f_n^{\mathcal{A}}\}_{0\leq n}$ and $\{g_n^{\mathcal{A}}\}_{0\leq n}$ spanning the skew part of the magnetic flux density are linearly dependent and the forward mapping defined in equation (6.3) has a non-trivial kernel. A similar calculation to determine the expansion coefficients leading to a vector field with zero curl in a vector potential formulation in toroidal coordinates is conducted in [36].

Assume that the magnetic scalar potential ϕ_{m} in toroidal harmonic expansion equals a constant $c \in \mathbb{R}\setminus\{0\}$, yielding the equation

$$c = \mathcal{E}^{\mathrm{t}}\varphi + \sqrt{\kappa(\tau,\sigma)}\sum_{n=0}^{\infty} Q^0_{n-\frac{1}{2}}(\cosh(\tau))\left(\mathcal{A}_n^{\mathrm{t}}\cos(n\sigma) + \mathcal{B}_n^{\mathrm{t}}\sin(n\sigma)\right). \tag{6.28}$$

From this equation, the toroidal harmonic coefficients $\mathcal{A}_n^{\mathrm{t}}$ and $\mathcal{B}_n^{\mathrm{t}}$ can be obtained by multiplication with the term $\cos(l\sigma)/\sqrt{\kappa(\tau,\sigma)}$ (or respectively $\sin(l\sigma)/\sqrt{\kappa(\tau,\sigma)}$) and integration over σ on the interval $[-\pi,\pi]$. We begin with the determination of the skew toroidal harmonic coefficients by resolving

$$\int_{-\pi}^{\pi} c\frac{\cos(l\sigma)}{\sqrt{\kappa(\tau,\sigma)}}\,\mathrm{d}\sigma = \int_{-\pi}^{\pi} \frac{\cos(l\sigma)}{\sqrt{\kappa(\tau,\sigma)}}\left(\mathcal{E}^{\mathrm{t}}\varphi + \sqrt{\kappa(\tau,\sigma)}\sum_{n=0}^{\infty} Q^0_{n-\frac{1}{2}}(\cosh(\tau))\left(\mathcal{A}_n^{\mathrm{t}}\cos(n\sigma) + \mathcal{B}_n^{\mathrm{t}}\sin(n\sigma)\right)\right)\mathrm{d}\sigma \tag{6.29}$$

for $\mathcal{A}_n^{\mathrm{t}}$. This equation can be simplified by inserting the equation

$$\int_{-\pi}^{\pi} \frac{\cos(l\sigma)}{\sqrt{\kappa(\tau,\sigma)}}\,\mathrm{d}\sigma = 2\sqrt{2}Q^0_{l-\frac{1}{2}}(\cosh(\tau)), \tag{6.30}$$

which is given in [36, Section 5], into equation (6.29), yielding

$$\begin{aligned} 2\sqrt{2}Q^0_{l-\frac{1}{2}}(\cosh(\tau))c = \;& 2\sqrt{2}Q^0_{l-\frac{1}{2}}(\cosh(\tau))\mathcal{E}^{\mathrm{t}}\varphi \\ & + \textstyle\sum_{n=0}^{\infty} Q^0_{n-\frac{1}{2}}(\cosh(\tau)) \int_{-\pi}^{\pi} \quad \frac{\mathcal{A}^{\mathrm{t}}_n}{2}\left(\cos((n-l)\sigma)+\cos((n+l)\sigma)\right) \\ & \qquad + \frac{\mathcal{B}^{\mathrm{t}}_n}{2}\left(\sin((n-l)\sigma)+\sin((n+l)\sigma)\right)\,\mathrm{d}\sigma \\ = \;& 2\sqrt{2}Q^0_{l-\frac{1}{2}}(\cosh(\tau))\mathcal{E}^{\mathrm{t}}\varphi + \mathcal{A}^{\mathrm{t}}_l \quad \delta_l \pi Q^0_{l-\frac{1}{2}}(\cosh(\tau)), \end{aligned} \tag{6.31}$$

where $\delta_l \coloneqq 2$ for $l = 0$ and $\delta_l \coloneqq 1$ for $l > 0$. Thereby, we used the addition formulas [2, equation 4.3.16, 4.3.17] and the equations $\int_0^{2\pi} \sin(m\sigma)\,\mathrm{d}\sigma = 0$ for all $m \in \mathbb{N}_0$ and $\int_0^{2\pi} \cos(m\sigma)\,\mathrm{d}\sigma = 0$ for all integers $m > 0$. Since the left-hand side of equation (6.31) is independent of φ, the linear coefficient $\mathcal{E}^{\mathrm{t}}$ has to equal zero. Resolving equation (6.31) for $\mathcal{A}^{\mathrm{t}}_l$ yields

$$\mathcal{A}^{\mathrm{t}}_l = \frac{2\sqrt{2}c}{\delta_l \pi} \neq 0. \tag{6.32}$$

To obtain the normal toroidal harmonic coefficients $\mathcal{B}^{\mathrm{t}}_n$, the term $\cos(l\sigma)$ in equation (6.29) is replaced with $\sin(l\sigma)$ and the equation

$$\int_{-\pi}^{\pi} \frac{\sin(l\sigma)}{\sqrt{\kappa(\tau,\sigma)}}\,\mathrm{d}\sigma = 0 \tag{6.33}$$

is inserted, yielding the equation

$$\begin{aligned} 0 = \;& \textstyle\sum_{n=0}^{\infty} Q^0_{n-\frac{1}{2}}(\cosh(\tau)) \int_{-\pi}^{\pi} \frac{\mathcal{A}^{\mathrm{t}}_n}{2}\left(\sin((n-l)\sigma)+\sin((n+l)\sigma)\right) + \frac{\mathcal{B}^{\mathrm{t}}_n}{2}\left(\cos((n-l)\sigma)-\cos((n+l)\sigma)\right)\,\mathrm{d}\sigma \\ = \;& \mathcal{B}^{\mathrm{t}}_l \delta_l \pi Q^0_{l-\frac{1}{2}}(\cosh(\tau)), \end{aligned} \tag{6.34}$$

where $\delta_l \coloneqq 0$ for $l = 0$ and $\delta_l \coloneqq 1$ for $l > 0$. Hence, $\mathcal{B}^{\mathrm{t}}_n = 0$ for all $n \geq 0$.
In conclusion, there is a non-trivial choice of skew toroidal harmonic coefficients $\mathcal{A}^{\mathrm{t}}_n$, trivial normal toroidal harmonic coefficients $\mathcal{B}^{\mathrm{t}}_n$ and trivial linear coefficient $\mathcal{E}^{\mathrm{t}}$, such that the magnetic scalar potential ϕ_{m} is constant. Inserting these coefficients into the equations (6.22) and (6.23) yields that the functions $\{f^{\mathcal{A}}_n\}_{0\leq n}$ and the functions $\{g^{\mathcal{A}}_n\}_{0\leq n}$ are linearly dependent. Equation (6.25) yields that $\{f^{\mathcal{A}}_n\}_{0\leq n} \subset \{f^{\mathcal{A}}_{n,m}\}_{0\leq n,m}$ and $\{g^{\mathcal{A}}_n\}_{0\leq n} \subset \{g^{\mathcal{A}}_{n,m}\}_{0\leq n,m}$, thus also in the general case, the functions spanning the skew part of the magnetic flux density are linearly dependent.

The consequence of the observed linear dependence is that the skew toroidal harmonic coefficients are not uniquely determinable from the magnetic flux density. Hence, the inverse problem 7 is ill-posed.
To address the ill-posedness, an additional condition defining a relation between one or more skew toroidal harmonic coefficients can be imposed, e.g., $\mathcal{A}^{\mathrm{t}}_0 = 0$ or $\mathcal{A}^{\mathrm{t}}_0 = \mathcal{A}^{\mathrm{t}}_1$. Due to the linear dependence of the functions spanning the skew part of the magnetic flux density, the choice of the imposed condition does not affect the value of the magnetic flux density. Thus, all sets of resulting coefficients based on different imposed conditions are solutions to the inverse problem 7. However, the choice of the imposed condition affects the value of the magnetic scalar potential, e.g., the magnetic scalar potential in the focal ring is given by

$$\lim_{\tau\to\infty} \phi_{\mathrm{m}}(\tau,\sigma,\phi) = \mathcal{E}^{\mathrm{t}}\phi + \frac{\pi}{\sqrt{2}}\mathcal{A}^{\mathrm{t}}_0. \tag{6.35}$$

Consequently, the choice of the imposed condition can be understood as a gauging condition such as setting $\phi_{\mathrm{m}}(\mathbf{x}_0) = \phi_0$ at an arbitrary point $\mathbf{x}_0 \in D$ and with an arbitrary constant $\phi_0 \in \mathbb{R}$ as discussed in Section 2.2.2. We will also see later in Section 6.2.1 that the derived formulas to compute the skew harmonic coefficients from the magnetic flux density by integration are recursive and require a value for $\mathcal{A}^{\mathrm{t}}_0$ to determine the further coefficients $\mathcal{A}^{\mathrm{t}}_n$ with $n > 0$. In this method, gauging can conveniently be applied by imposing a value for $\mathcal{A}^{\mathrm{t}}_0$.

6.2 Methods to determine the toroidal harmonics

Two different methods are derived in this section to solve the inverse problem 7. The first method is based on integrating the magnetic flux density, leading to recursive formulas, the second method resolves the linear system of equations (6.19) with the least squares method and yields an approximation of a finite set of toroidal harmonic coefficients.

6.2.1 Integration of the magnetic flux density

Using the orthogonality of the trigonometric functions, the circular harmonic coefficients $\mathcal{A}_n^{\mathrm{c}}, \mathcal{B}_n^{\mathrm{c}}$ can be determined by integrating the radial component B_r of the magnetic flux density (see equations (2.78) and (2.79)). In this section, similar formulas are derived for the toroidal harmonic coefficients $\mathcal{A}_n^{\mathrm{t}}, \mathcal{B}_n^{\mathrm{t}}$ and the linear coefficient $\mathcal{E}^{\mathrm{t}}$. We restrict the study to the rotationally symmetric case ($\partial \mathbf{B}/\partial\varphi = 0$).

As in the circular harmonic case, the formulas are based on integrating the magnetic flux density components $B_\tau, B_\sigma, B_\varphi$. For this purpose, the following integrals are introduced

$$I_k^\tau(\tau) \coloneqq \int_0^{2\pi} \frac{1}{\sqrt{\kappa(\tau,\sigma)}} B_\tau(\tau,\sigma)\cos(k\sigma)\,\mathrm{d}\sigma, \tag{6.36}$$

$$I_k^\sigma(\tau) \coloneqq \int_0^{2\pi} \frac{1}{\sqrt{\kappa(\tau,\sigma)}} B_\sigma(\tau,\sigma)\cos(k\sigma)\,\mathrm{d}\sigma, \tag{6.37}$$

$$I^\varphi(\tau) \coloneqq \int_0^{2\pi} B_\varphi(\tau,\sigma)\,\mathrm{d}\sigma, \tag{6.38}$$

where $k \geq 0$ is an integer. The choice of the integrands is driven by the idea of exploiting the orthogonality of the trigonometric functions as much as possible. In the following paragraphs, it is shown that the skew toroidal harmonic coefficients $\mathcal{A}_n^{\mathrm{t}}$ can be determined from the term $I_k^\tau(\tau)$, the normal coefficients $\mathcal{B}_n^{\mathrm{t}}$ can be determined from $I_k^\sigma(\tau)$, and the linear coefficient can be determined from $I^\varphi(\tau)$.

Determination of the normal toroidal harmonic coefficients Inserting the toroidal harmonic expansion of B_σ given in equation (8.15) into equation (6.37) yields

$$\begin{aligned}
I_k^\sigma(\tau) = & \int_0^{2\pi} \tfrac{B_\sigma(\tau,\sigma)}{\sqrt{\kappa(\tau,\sigma)}}\cos(k\sigma)\,\mathrm{d}\sigma \\
= & \int_0^{2\pi} -\tfrac{\mu_0}{a}\textstyle\sum_{n=0}^{\infty} \widetilde{Q}^0_{n-\frac{1}{2}}(\tau)\mathcal{B}_n^{\mathrm{t}} \left[\frac{1}{2}\sin(\sigma)\sin(n\sigma) + n\cosh(\tau)\cos(n\sigma) - n\cos(\sigma)\cos(n\sigma)\right]\cos(k\sigma)\mathrm{d}\sigma \\
= & \int_0^{2\pi} -\tfrac{\mu_0}{a}\textstyle\sum_{n=0}^{\infty} \widetilde{Q}^0_{n-\frac{1}{2}}(\tau)\mathcal{B}_n^{\mathrm{t}} \left[\frac{1-2n}{8}\cos((n-k-1)\sigma) + \frac{1-2n}{8}\cos((n+k-1)\sigma)\right. \\
& \qquad -\frac{1+2n}{8}\cos((n-k+1)\sigma) - \frac{1+2n}{8}\cos((n+k+1)\sigma) \\
& \qquad \left. + \frac{n\cosh(\tau)}{2}\cos((n-k)\sigma) + \frac{n\cosh(\tau)}{2}\cos((n+k)\sigma)\right]\mathrm{d}\sigma.
\end{aligned}$$

Thereby, we used the addition formulas [2, equation 4.3.16, 4.3.17] and fact that $\int_0^{2\pi}\sin(m\sigma)\,\mathrm{d}\sigma = 0$ for all $m \in \mathbb{N}_0$. Moreover, also the integral $\int_0^{2\pi}\cos(m\sigma)\,\mathrm{d}\sigma$ equals zero for integers $m > 0$. Consequently, inserting

$k = 0, 1$ into the last equation yields

$$I_0^\sigma(\tau) = -\frac{4\pi\mu_0}{a}\left(\frac{1-2}{8}\widetilde{Q}^0_{1-\frac{1}{2}}(\tau)\mathcal{B}^{\mathrm{t}}_1\right), \tag{6.39}$$

$$I_1^\sigma(\tau) = -\frac{2\pi\mu_0}{a}\left(\frac{1-4}{8}\widetilde{Q}^0_{2-\frac{1}{2}}(\tau)\mathcal{B}^{\mathrm{t}}_2 + \frac{\cosh(\tau)}{2}\widetilde{Q}^0_{1-\frac{1}{2}}(\tau)\mathcal{B}^{\mathrm{t}}_1\right). \tag{6.40}$$

Otherwise, for $k \geq 2$, the right-hand side simplifies to

$$I_k^\sigma(\tau) = -\frac{2\pi\mu_0}{a}\left(\frac{1-2(k+1)}{8}\widetilde{Q}^0_{k+1-\frac{1}{2}}(\tau)\mathcal{B}^{\mathrm{t}}_{k+1} - \frac{1+2(k-1)}{8}\widetilde{Q}^0_{k-1-\frac{1}{2}}(\tau)\mathcal{B}^{\mathrm{t}}_{k-1} + \frac{k\cosh(\tau)}{2}\widetilde{Q}^0_{k-\frac{1}{2}}(\tau)\mathcal{B}^{\mathrm{t}}_k\right). \tag{6.41}$$

Resolving the equations (6.39), (6.40), and (6.41) for the normal toroidal harmonic coefficients, and knowing that $\mathcal{B}^{\mathrm{t}}_0 = 0$ (by definition) yields the recursive equation system

$$\mathcal{B}^{\mathrm{t}}_n = \begin{cases} 0 & n = 0 \\ \frac{a2I_0^\sigma(\tau)}{\pi\mu_0\widetilde{Q}^0_{1-\frac{1}{2}}(\tau)} & n = 1 \\ \frac{4}{3\widetilde{Q}^0_{2-\frac{1}{2}}(\tau)}\left(\cosh(\tau)\widetilde{Q}^0_{1-\frac{1}{2}}(\tau)\mathcal{B}^{\mathrm{t}}_1 + \frac{aI_1^\sigma(\tau)}{\pi\mu_0}\right) & n = 2 \\ \frac{4}{(2n-1)\widetilde{Q}^0_{n-\frac{1}{2}}(\tau)}\left((n-1)\cosh(\tau)\widetilde{Q}^0_{n-1-\frac{1}{2}}(\tau)\mathcal{B}^{\mathrm{t}}_{n-1} - \frac{2n-3}{4}\widetilde{Q}^0_{n-2-\frac{1}{2}}(\tau)\mathcal{B}^{\mathrm{t}}_{n-2} + \frac{aI_{n-1}^\sigma(\tau)}{\pi\mu_0}\right) & n \geq 3 \end{cases} \tag{6.42}$$

Determination of the skew toroidal harmonic coefficients With similar reasoning, the skew toroidal harmonic coefficients can be determined from the integral $I_k^\tau(\tau)$ defined in equation (6.36). Inserting the toroidal harmonic expansion of B_τ yields

$$\begin{aligned} I_k^\tau(\tau) = \int_0^{2\pi}\sum_{n=0}^{\infty} -\frac{\mu_0\mathcal{A}^{\mathrm{t}}_n}{aQ^0_{n-\frac{1}{2}}(\cosh(\tau_0))}\Bigg[&\left(\frac{\sinh(\tau)Q^0_{n-\frac{1}{2}}(\cosh(\tau))}{4} + \frac{\cosh(\tau)\frac{\mathrm{d}}{\mathrm{d}\tau}Q^0_{n-\frac{1}{2}}(\cosh(\tau))}{2}\right) \\ &(\cos((n-k)\sigma) + \cos((n+k)\sigma)) \\ &- \frac{\frac{\mathrm{d}}{\mathrm{d}\tau}Q^0_{n-\frac{1}{2}}(\cosh(\tau))}{4}(\cos((n-k-1)\sigma) + \cos((n-k+1)\sigma)) \\ &- \frac{\frac{\mathrm{d}}{\mathrm{d}\tau}Q^0_{n-\frac{1}{2}}(\cosh(\tau))}{4}(\cos((n+k-1)\sigma) + \cos((n+k+1)\sigma))\Bigg]\,\mathrm{d}\sigma. \end{aligned}$$

Depending on the integer k, this equation can be further simplified to

$$I_0^\tau(\tau) = -\frac{\mu_0}{a}\left(2\pi\mathcal{A}^{\mathrm{t}}_0\frac{S^0_{-\frac{1}{2}}(\cosh(\tau))}{Q^0_{-\frac{1}{2}}(\cosh(\tau_0))} - \mathcal{A}^{\mathrm{t}}_1\pi\frac{\frac{\mathrm{d}}{\mathrm{d}\tau}Q^0_{1-\frac{1}{2}}(\cosh(\tau))}{Q^0_{1-\frac{1}{2}}(\cosh(\tau_0))}\right)$$

$$I_1^\tau(\tau) = -\frac{\mu_0}{a}\left(-\pi\mathcal{A}^{\mathrm{t}}_0\frac{\frac{\mathrm{d}}{\mathrm{d}\tau}Q^0_{-\frac{1}{2}}(\cosh(\tau))}{Q^0_{-\frac{1}{2}}(\cosh(\tau_0))} + \pi\mathcal{A}^{\mathrm{t}}_1\frac{S^0_{1-\frac{1}{2}}(\cosh(\tau))}{Q^0_{1-\frac{1}{2}}(\cosh(\tau_0))} - \pi\mathcal{A}^{\mathrm{t}}_2\frac{\frac{\mathrm{d}}{\mathrm{d}\tau}Q^0_{2-\frac{1}{2}}(\cosh(\tau))}{Q^0_{2-\frac{1}{2}}(\cosh(\tau_0))}\right) \tag{6.43}$$

$$I_k^\tau(\tau) = -\frac{\mu_0}{a}\left(-\pi\mathcal{A}^{\mathrm{t}}_{k-1}\frac{\frac{\mathrm{d}}{\mathrm{d}\tau}Q^0_{k-1-\frac{1}{2}}(\cosh(\tau))}{2Q^0_{k-1-\frac{1}{2}}(\cosh(\tau_0))} + \pi\mathcal{A}^{\mathrm{t}}_k\frac{S^0_{k-\frac{1}{2}}(\cosh(\tau))}{Q^0_{k-\frac{1}{2}}(\cosh(\tau_0))} + \pi\mathcal{A}^{\mathrm{t}}_{k+1}\frac{\frac{\mathrm{d}}{\mathrm{d}\tau}Q^0_{k+1-\frac{1}{2}}(\cosh(\tau))}{2Q^0_{k+1-\frac{1}{2}}(\cosh(\tau_0))}\right),$$

where the last equation holds only for $k \geq 2$. Thereby, the abbreviation $S^0_{n-\frac{1}{2}}(\cosh(\tau))$ was used to save on notation, which we define by

$$S^0_{n-\frac{1}{2}}(\cosh(\tau)) \coloneqq \frac{1}{2}\sinh(\tau)Q^0_{n-\frac{1}{2}}(\cosh(\tau)) + \cosh(\tau)\frac{\mathrm{d}}{\mathrm{d}\tau}Q^0_{n-\frac{1}{2}}(\cosh(\tau)). \tag{6.44}$$

Resolving for the skew toroidal harmonic coefficients yields the recursive equation system

$$\mathcal{A}^{\mathrm{t}}_n = \begin{cases} \frac{Q^0_{1-\frac{1}{2}}(\cosh(\tau_0))}{\frac{\mathrm{d}}{\mathrm{d}\tau}Q^0_{1-\frac{1}{2}}(\cosh(\tau))}\left(\frac{2S^0_{-\frac{1}{2}}(\cosh(\tau))}{Q^0_{-\frac{1}{2}}(\cosh(\tau_0))}\mathcal{A}^{\mathrm{t}}_0 + \frac{aI^\tau_0(\tau)}{\pi\mu_0}\right) & n = 1 \\ \frac{2Q^0_{2-\frac{1}{2}}(\cosh(\tau_0))}{\frac{\mathrm{d}}{\mathrm{d}\tau}Q^0_{2-\frac{1}{2}}(\cosh(\tau))}\left(-\frac{\frac{\mathrm{d}}{\mathrm{d}\tau}Q^0_{-\frac{1}{2}}(\cosh(\tau))}{Q^0_{-\frac{1}{2}}(\cosh(\tau_0))}\mathcal{A}^{\mathrm{t}}_0 + \frac{S^0_{1-\frac{1}{2}}(\cosh(\tau))}{Q^0_{1-\frac{1}{2}}(\cosh(\tau_0))}\mathcal{A}^{\mathrm{t}}_1 + \frac{aI^\tau_1(\tau)}{\pi\mu_0}\right) & n = 2 \\ \frac{2Q^0_{n-\frac{1}{2}}(\cosh(\tau_0))}{\frac{\mathrm{d}}{\mathrm{d}\tau}Q^0_{n-\frac{1}{2}}(\cosh(\tau))}\left(-\frac{\frac{\mathrm{d}}{\mathrm{d}\tau}Q^0_{n-2-\frac{1}{2}}(\cosh(\tau))}{2Q^0_{n-2-\frac{1}{2}}(\cosh(\tau_0))}\mathcal{A}^{\mathrm{t}}_{n-2} + \frac{S^0_{n-1-\frac{1}{2}}(\cosh(\tau))}{Q^0_{n-1-\frac{1}{2}}(\cosh(\tau_0))}\mathcal{A}^{\mathrm{t}}_{n-1} + \frac{aI^\tau_{n-1}(\tau)}{\pi\mu_0}\right) & n \geq 3. \end{cases} \tag{6.45}$$

Notice that unlike for the normal toroidal harmonic coefficients, the recursive formulas for the skew toroidal harmonic coefficients require $\mathcal{A}^{\mathrm{t}}_0$. This is due to the linear dependence of the functions spanning the skew part of the magnetic flux density shown in Section 6.1. Consequently, any value can be chosen for $\mathcal{A}^{\mathrm{t}}_0$ to determine a valid solution. Selecting this value means gauging the solution.

Determination of the linear coefficient The linear coefficient $\mathcal{E}^{\mathrm{t}}$ can be directly determined from the φ-component of the magnetic flux density in a single observation position by

$$\mathcal{E}^{\mathrm{t}} = -\frac{a\sinh(\tau)}{\mu_0\kappa(\tau,\sigma)}B_\varphi(\tau,\sigma). \tag{6.46}$$

However, if observations of B_φ on a τ-isocircle are available, also the integral $I^\varphi(\tau)$ defined in equation (6.38) can be used to compute the average solution

$$\mathcal{E}^{\mathrm{t}} = -\frac{a\tanh(\tau)}{2\pi\mu_0}I^\varphi(\tau). \tag{6.47}$$

Limitations Although the recursive formulas (6.42) and (6.45) provide an expression for every toroidal harmonic coefficient, the formulas are unsuitable for determining the toroidal harmonic coefficients from a finite set of magnetic flux density observations $\mathbf{B}^{\mathrm{obs}}$, i.e. for solving the inverse problem 7. Their limited applicability to real-world examples is caused by the recursion and the fact that the formulas are based on the evaluation of the integrals $I^\tau_k(\tau)$ and $I^\sigma_k(\tau)$ defined in equation (6.36) and (6.37). Any error or uncertainty that is related to these terms is propagated to the toroidal harmonic coefficients. These errors and uncertainties are caused, e.g., by uncertainties of the magnetic flux density observations and approximation errors of the integral evaluation, which we compute from a finite set of observations using the trapezoidal rule [107]. Due to the recursion, the coefficients $\mathcal{A}^{\mathrm{t}}_n$ and $\mathcal{B}^{\mathrm{t}}_n$ are not only affected by the errors and uncertainties in the evaluation of the integrals $I^\tau_k(\tau)$ and respectively $I^\sigma_k(\tau)$ with $k = n-1$ but all integrals with $k \leq n-1$. Consequently, the determination of toroidal harmonic coefficients with this method is unstable (see also the example in Section 6.3.1). Instead, we typically solve the inverse problem 7 with the least squares fitting method described in the next paragraph.
Following equation (6.25) it holds that $\mathcal{A}^{\mathrm{t}}_{n,0} = \mathcal{A}^{\mathrm{t}}_n$ and $\mathcal{B}^{\mathrm{t}}_{n,0} = \mathcal{B}^{\mathrm{t}}_n$ for all $n \in \mathbb{N}$. Consequently, integration-based formulas for the toroidal harmonic expansion in the general case would also be affected by the same problem of recursive error propagation.

6.2.2 Linear least squares fitting

In Section 6.1, the finite linear equation system (6.19) was introduced, which relates the toroidal harmonic coefficients to the components of the magnetic flux density with a matrix-vector multiplication. To work with a finite equation system, the toroidal harmonic expansion of the magnetic flux density is truncated at $n = N$ and $m = M$. This truncation yields a finite-dimensional approximation of the forward model $\mathcal{H}\mathbf{p}$ defined in equation (6.3).
Given at least as many observations of the magnetic flux density as unknown toroidal harmonics, the equation system (6.19) can be resolved to determine values for the toroidal harmonic coefficients. Because a finite expansion is only an approximation and since observations $\mathbf{B}^{\mathrm{obs}}$ of the magnetic flux density are affected by uncertainty, typically observations in more positions than unknown coefficients are used, and the coefficients are determined by linear least squares fitting.

Truncation of the toroidal harmonic expansion The fitting of the toroidal harmonic coefficients requires a finite number of coefficients. In general, no prior knowledge is available about which of the functions

$$f_{n,m}^{\mathcal{A}}, f_{n,m}^{\mathcal{B}}, f_{n,m}^{\mathcal{C}}, f_{n,m}^{\mathcal{D}}, \quad g_{n,m}^{\mathcal{A}}, g_{n,m}^{\mathcal{B}}, g_{n,m}^{\mathcal{C}}, g_{n,m}^{\mathcal{D}}, \quad h_{n,m}^{\mathcal{A}}, h_{n,m}^{\mathcal{B}}, h_{n,m}^{\mathcal{C}}, h_{n,m}^{\mathcal{D}}, h^{\mathcal{E}} \ : \ (\tau, \sigma, \varphi) \mapsto \mathbb{R}, \tag{6.48}$$

spanning the toroidal harmonic expansion of the magnetic flux density are the most relevant to describe a given observation of the magnetic flux density. For example, knowledge of symmetry can be used to omit several degrees n or orders m. Otherwise, the number of coefficients is limited by truncating the toroidal harmonic expansion at some $N, M \in \mathbb{N}$ and considering only the functions listed in equation (6.48) with $n \leq N$ and $m \leq M$. We will see that this choice is suitable for the applications demonstrated in Section 6.3.

Given a set of R observations of the magnetic flux density $\mathbf{B}^{\mathrm{obs}}$ at the positions $\{(\tau_r, \sigma_r, \varphi_r)\}_{1 \leq r \leq R}$ in a toroidal domain D. We define the observation vector $\mathbf{q}^{\mathrm{obs}}$ by

$$\mathbf{q}^{\mathrm{obs}} \coloneqq \left(\mathbf{B}^{\mathrm{obs}}(\tau_1, \sigma_1, \varphi_1)^\top, \ldots, \mathbf{B}^{\mathrm{obs}}(\tau_R, \sigma_R, \varphi_R)^\top \right)^\top. \tag{6.49}$$

Solving the finite-dimensional equation system (6.19) in R positions simultaneously yields by abuse of notation with the matrix

$$\mathcal{H} \coloneqq \begin{pmatrix} 0 & f^{\mathcal{A}}(\tau_1, \sigma_1, \varphi_1) & f^{\mathcal{B}}(\tau_1, \sigma_1, \varphi_1) & f^{\mathcal{C}}(\tau_1, \sigma_1, \varphi_1) & f^{\mathcal{D}}(\tau_1, \sigma_1, \varphi_1) \\ 0 & g^{\mathcal{A}}(\tau_1, \sigma_1, \varphi_1) & g^{\mathcal{B}}(\tau_1, \sigma_1, \varphi_1) & g^{\mathcal{C}}(\tau_1, \sigma_1, \varphi_1) & g^{\mathcal{D}}(\tau_1, \sigma_1, \varphi_1) \\ h^{\mathcal{E}}(\tau_1, \sigma_1, \varphi_1) & h^{\mathcal{A}}(\tau_1, \sigma_1, \varphi_1) & h^{\mathcal{B}}(\tau_1, \sigma_1, \varphi_1) & h^{\mathcal{C}}(\tau_1, \sigma_1, \varphi_1) & h^{\mathcal{D}}(\tau_1, \sigma_1, \varphi_1) \\ \vdots & \vdots & \vdots & \vdots & \vdots \\ 0 & f^{\mathcal{A}}(\tau_R, \sigma_R, \varphi_R) & f^{\mathcal{B}}(\tau_R, \sigma_R, \varphi_R) & f^{\mathcal{C}}(\tau_R, \sigma_R, \varphi_R) & f^{\mathcal{D}}(\tau_R, \sigma_R, \varphi_R) \\ 0 & g^{\mathcal{A}}(\tau_R, \sigma_R, \varphi_R) & g^{\mathcal{B}}(\tau_R, \sigma_R, \varphi_R) & g^{\mathcal{C}}(\tau_R, \sigma_R, \varphi_R) & g^{\mathcal{D}}(\tau_R, \sigma_R, \varphi_R) \\ h^{\mathcal{E}}(\tau_R, \sigma_R, \varphi_R) & h^{\mathcal{A}}(\tau_R, \sigma_R, \varphi_R) & h^{\mathcal{B}}(\tau_R, \sigma_R, \varphi_R) & h^{\mathcal{C}}(\tau_R, \sigma_R, \varphi_R) & h^{\mathcal{D}}(\tau_R, \sigma_R, \varphi_R) \end{pmatrix} \tag{6.50}$$

and the parameter vector

$$\mathbf{p} \coloneqq \begin{pmatrix} \mathcal{E}^{\mathrm{t}} & \mathcal{A}^{\mathrm{t}} & \mathcal{B}^{\mathrm{t}} & \mathcal{C}^{\mathrm{t}} & \mathcal{D}^{\mathrm{t}} \end{pmatrix}^\top, \tag{6.51}$$

as defined in equation (6.20), the finite-dimensional linear system of equations

$$\mathbf{q}^{\mathrm{obs}} = \mathcal{H}\mathbf{p}. \tag{6.52}$$

Linear least squares solution We can assume that the number of rows of the matrix $\mathcal{H}$ defined in equation (6.50) exceeds its number of columns since at least as many equations as unknowns are required to solve the inverse problem: Find $\mathbf{p}$ such that $\mathbf{q}^{\mathrm{obs}} = \mathcal{H}\mathbf{p}$. Since measured magnetic flux density observations are affected by measurement uncertainty and due to the truncation of the expansion, a solution $\mathbf{p}$ to the latter equation might not exist. Thus, we seek an approximate solution that minimizes the residual vector defined by

$$\mathbf{r} \coloneqq \mathbf{q}^{\mathrm{obs}} - \mathcal{H}\mathbf{p} \tag{6.53}$$

concerning the squared Euclidean norm. Notice that if errors and uncertainties of the forward model $\mathcal{H}$ are neglected and if we assume that the uncertainties affecting $\mathbf{q}^{\mathrm{obs}}$ can be described with the additive noise model defined in Section 3.1 and a perturbation vector $\mathbf{u}$, which is a realization of the random vector $\mathbf{U} \sim \mathcal{N}(\mathbf{0}, \sigma^2\mathbb{I})$ describing the random measurement uncertainty, then the least squares solution $\mathbf{p}^{\mathrm{LS}}$ coincides with the maximum likelihood estimate given in equation (3.33) [12, Section 1.2].
It can be shown that the linear least squares solution $\mathbf{p}^{\mathrm{LS}}$ is the unique solution to the linear equation system

$$\mathcal{H}^\top\mathcal{H}\mathbf{p} = \mathcal{H}^\top\mathbf{q}^{\mathrm{obs}}, \tag{6.54}$$

if $\mathcal{H}$ has full rank [59, p.268]. The latter assumption holds because the truncated sets $\{f^{\mathcal{A}}_{n,m}\}_{0\leq n,m\leq N,M}$ and $\{g^{\mathcal{A}}_{n,m}\}_{0\leq n,m\leq N,M}$ spanning the skew part of the truncated toroidal harmonic expansion of the magnetic flux density are linearly independent. To compute the least squares solution, we solve equation (6.52) with QR decomposition [59, Section 6.5.1].

Improvement of the conditioning by gauging The conditioning of a problem measures its sensitivity to small changes in the data [59, p.24]. The conditioning of the linear systems of equations (6.54) can be quantified with the condition number [59, Theorem 3.5]. Concerning the Euclidean norm, the condition number of $\mathcal{H}^\top\mathcal{H}$ is given by

$$\kappa_2(\mathcal{H}^\top\mathcal{H}) \coloneqq \left\|\mathcal{H}^\top\mathcal{H}\right\|_2 \left\|(\mathcal{H}^\top\mathcal{H})^{-1}\right\|_2 = \frac{\sigma_{\max}(\mathcal{H}^\top\mathcal{H})}{\sigma_{\min}(\mathcal{H}^\top\mathcal{H})} = \kappa_2(\mathcal{H})^2 \tag{6.55}$$

where $\sigma_{\max}(\mathcal{H}^\top\mathcal{H})$ and $\sigma_{\min}(\mathcal{H}^\top\mathcal{H})$ are the maximal and the minimal singular values of $\mathcal{H}^\top\mathcal{H}$. The smaller the condition number, the smaller the relative Euclidean difference between the least squares solutions for observations $\mathbf{q}^{\mathrm{obs}}$ affected by different perturbations [59, Theorem 3.5]. Discussing the condition number $\kappa_2(\mathcal{H})$ is equivalent to discussing the condition number $\kappa_2(\mathcal{H}^\top\mathcal{H})$ due to equation (6.55).
Even though the matrix $\mathcal{H}$ defined in equation (6.50) has full rank, it is often poorly conditioned. Including the gauging condition $\phi_{\mathrm{m}}(\tau_0, 0, 0) = 0$, where $\cosh(\tau_0) = \rho/R$, by appending the row

$$\begin{pmatrix} 0 & \sqrt{\kappa(\tau_0,0)}\widetilde{Q}^0_{0-\frac{1}{2}}(\tau_0) & \dots & \sqrt{\kappa(\tau_0,0)}\widetilde{Q}^M_{0-\frac{1}{2}}(\tau_0) & \dots & \sqrt{\kappa(\tau_0,0)}\widetilde{Q}^0_{N-\frac{1}{2}}(\tau_0) & \dots & \sqrt{\kappa(\tau_0,0)}\widetilde{Q}^M_{N-\frac{1}{2}}(\tau_0) & \mathbf{0} \end{pmatrix} \tag{6.56}$$

to the matrix $\mathcal{H}$ and appending the value 0 to the observation vector $\mathbf{q}^{\mathrm{obs}}$ improves the condition number $\kappa_2(\mathcal{H})$ in both test cases studied in the following section (see Table 6.2 and Table 6.3). Notice that by abuse of notation, we use the same symbol $\mathcal{H}$ for the matrix with the additional row.

Adjusting the experimental design is a possibility to further improve the condition number of the linear least squares problem. The following paragraph discusses optimal observation positions $(\tau, \sigma, \varphi) \in D$ regarding the condition number. The study is restricted to the rotationally symmetric case.

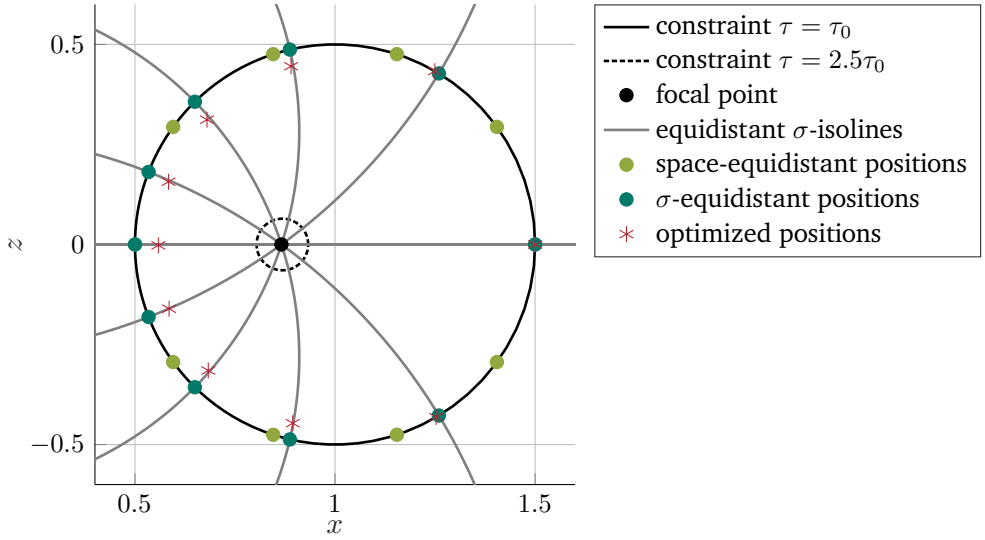

Figure 6.3: Observation positions of the magnetic flux density to determine the toroidal harmonic coefficients by least squares fitting.

Improvement of the conditioning by experimental design The coefficients of the matrix $\mathcal{H}$ defined in equation (6.50) depend on the positions $\{(\tau_r, \sigma_r, \varphi_r)\}_{1 \le r \le R}$ in which the magnetic flux density is observed. In the rotationally symmetric case, the toroidal angle φ can be omitted and the positions $\{(\tau_r, \sigma_r)\}_{1 \le r \le R}$ can be summarized with the two vectors $\boldsymbol{\tau} := (\tau_1, \ldots, \tau_R)$ and $\boldsymbol{\sigma} := (\sigma_1, \ldots, \sigma_R)$. We use the notation $\mathcal{H}(\boldsymbol{\tau}, \boldsymbol{\sigma})$ to indicate the dependence of $\mathcal{H}$ on $\boldsymbol{\tau}$ and $\boldsymbol{\sigma}$.
Particularly, if the observations $\mathbf{q}^{\text{obs}}$ of the magnetic flux density are determined by magnetic measurements instead of simulations, a measurement setup having only a few measurement positions and an optimal conditioning of the problem is favorable. For improving the condition number of the matrix $\mathcal{H}(\boldsymbol{\tau}, \boldsymbol{\sigma})$, the following optimization problem is formulated [7]

$$\begin{aligned} \min_{\boldsymbol{\tau}, \boldsymbol{\sigma} \in \mathbb{R}^R} \quad & \kappa_2(\mathcal{H}(\boldsymbol{\tau}, \boldsymbol{\sigma})) & & \\ \text{s.t.} \quad & \tau_0 < \tau_r < 2.5\tau_0 & & \forall\, 1 \le r \le R \\ & 0 \le \sigma_r \le 2\pi & & \forall\, 1 \le r \le R. \end{aligned} \tag{6.57}$$

We use the particle swarm algorithm [81], that is available in MATLAB® [95, 130], to solve the optimization problem. The algorithm is introduced in more detail in Section 4.3.1. To reduce the number of required iterations, the search space is bounded towards the focal ring by the $2.5\tau_0$-isosurface, omitting a small toroidal domain (see Figure 6.3).
The optimized experimental setup is computed for a toroidal domain D with toroidal radius $\rho = 1\,\text{m}$ and poloidal radius $R = 0.5\,\text{m}$ (eccentricity 2). It is supposed that the truncation threshold of the toroidal harmonic expansion is $N = 9$ and that observations in $R = 10$ positions are considered to determine the toroidal harmonic coefficients with the least squares solution. The optimal positions are visualized in Figure 6.3. Noticeably, the optimal positions are not equally distributed in space but almost equally distributed according to the poloidal angle σ. Indeed, changing the observation positions on the boundary of D from a space-equidistant distribution to a σ-equidistant distribution improves the condition number by one order of magnitude. The values for the condition number $\kappa_2(\mathcal{H})$ for the different experimental setups shown in Figure 6.3 are summarized in Table 6.1.

Table 6.1: Condition number of the linear least squares problem to determine the toroidal harmonic coefficients for the three different distributions of observation positions shown in Figure 6.3.

	space-equidistant positions	σ-equidistant positions	optimized positions
$\kappa_2(\mathcal{H})$	$1.33 \cdot 10^7$	$3.33 \cdot 10^6$	$1.45 \cdot 10^6$

6.3 Application and validation

In this section, the two algorithms to determine the toroidal harmonic coefficients by integration and least squares fitting are applied to magnetic flux density observations obtained from ROXIE [121] simulations. In practice, measurement uncertainties are also affecting these observations. In the following, these uncertainties are neglected and we apply the methods derived in Section 6.2 directly to the ROXIE output data. Thus, also the considerations regarding optimal experimental design discussed in the preceding section are omitted.
We focus on the validation of the algorithms rather than claiming that a generalized field description based on the toroidal harmonic expansion is the most suitable operation-centric system model for the considered use cases, which are:

1. **ITER tokamak** The magnetic flux density generated by the superconducting coil arrangement (Figure 6.4) of the ITER tokamak before plasma injection.
2. **Curved CCT dipole** The magnetic flux density generated by a curved CCT dipole (Figure 6.11) with a bending angle of about 45 degrees.

In both cases, training data of magnetic flux density data to determine the toroidal harmonic coefficients is taken on a reference torus, i.e. a τ-isosurface in the toroidal coordinate system enclosing a toroidal domain D. In the ITER example, the eccentricity of D is $\rho/R = 3.1$, in the curved CCT example, the eccentricity is 6. The determined coefficients are subsequently validated by comparing the predicted magnetic flux density to ground truth magnetic flux density observations simulated with the same ROXIE model as the training data but evaluated at different positions inside the toroidal domain D.

6.3.1 ITER tokamak

The International Thermonuclear Experimental Reactor (ITER) [75] is a test reactor for nuclear fusion which is currently built in the south of France. The reactor's design is based on the tokamak principle [11]. A magnet system consisting of six central solenoidal coils surrounded by 18 toroidal field coils, six poloidal coils, and 18 corrector coils is used to confine, shape, and stabilize the plasma, and to ramp up and create a position equilibrium of the plasma current. Figure 6.4 shows the coil arrangement of the magnet system omitting the correction coils. Inside the free space surrounded by the coil arrangement a toroidal domain D with toroidal radius $\rho = 7\,\mathrm{m}$ and the poloidal radius $R = 2.3\,\mathrm{m}$ can be placed. We choose the focal ring of the toroidal coordinate system such that ∂D is a τ-isosurface.
In tokamak devices, not only the coils but also the plasma itself has a non-negligible contribution to the magnetic field inside the aperture. However, the domain inside the aperture is in the presence of the plasma not source-free, hence, the magnetic scalar potential does not satisfy the Laplace equation. Consequently, we consider the magnetic field generated by the coil system at the moment before the plasma injection to obtain a

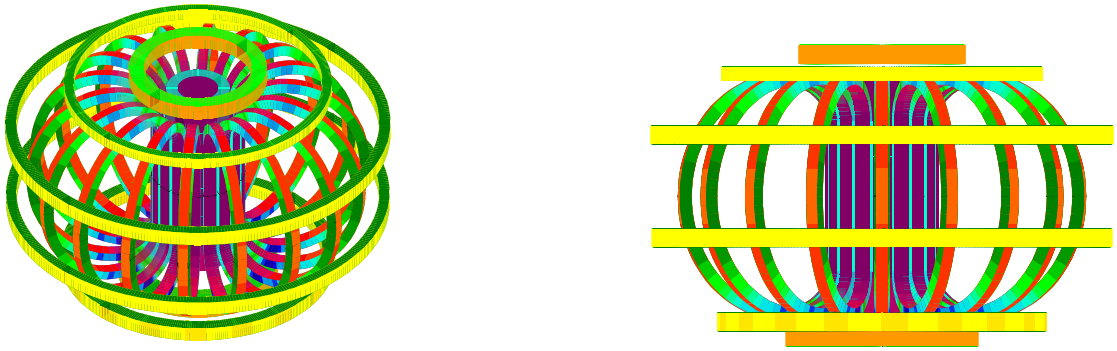

Figure 6.4: Superconducting coil arrangement of the ITER tokamak from two perspectives. The arrangement consists of 6 solenoidal coils that are stacked in the center. The central solenoid is surrounded by 18 identical toroidal field coils and six poloidal field coils. The correction coils are not included in this model. The toroidal domain D, that is placed inside the coil arrangement, has the toroidal radius $\rho = 7\,\mathrm{m}$ and the poloidal radius $R = 2.3\,\mathrm{m}$. This figure is generated with ROXIE [121].

valid test case for the formulation studied in this work. In this test case, a constant current of $68\,\mathrm{kA}$ is applied to each toroidal field coil. The considered constant powering of the poloidal field coils is 25.4, -6.4, 1.0, 1.0, 2.6, and 32.9 kA from top to bottom. The solenoidal coils in the center of the aperture are constantly powered with 36.96, 35.08, 36.20, 36.20, 33.92, and 28.82 kA from top to bottom. To test not only the determination of the toroidal harmonics in the general case but also in the rotationally symmetric case, we also consider a powering scheme without current in the toroidal field coils. Figure 6.5 shows the absolute value of the magnetic flux density on ∂D in the general case and the rotationally symmetric case simulated in ROXIE.
As discussed in the introduction of this chapter, for symmetry reasons it is sufficient to build the system model only on a toroidal wedge $\widetilde{D} \subset D$ with toroidal angle $\varphi \in [0, \pi/9]$. To apply the methods of determining the toroidal harmonic coefficients, magnetic flux density observations on a grid of 432 positions with respect to the poloidal angle σ and 100 positions with respect to the toroidal angle φ are chosen on $\partial\widetilde{D}$. For verification, the magnetic flux density observations on the boundary of a concentric toroidal wedge $\widetilde{D}_{\mathrm{test}}$ with poloidal radius $1\,\mathrm{m}$ are considered. Due to the concentric position of the toroidal wedge $\widetilde{D}_{\mathrm{test}}$, its boundary $\partial\widetilde{D}_{\mathrm{test}}$ is not a τ-isosurface.

In the following, we evaluate the determination of the toroidal harmonics in the rotationally symmetric case with the integration and the fitting method described in Section 6.2. We find that the toroidal harmonic coefficients determined with the integration method diverge. Nevertheless, the fitting method can be validated. Moreover, we show that for the considered example due to the low eccentricity of $\rho/R = 3.1$ an operation-centric model based on circular harmonic coefficients is not suitable. Subsequently, the determination of the toroidal harmonic coefficients by fitting is evaluated on the general ground truth data shown in Figure 6.5 (left).

Limitation of the circular harmonic expansion The magnetic flux density generated by the solenoidal and the poloidal field coils does not satisfy the requirement that $\partial B_y/\partial y = 0$ in equation (2.75) which is necessary to describe the corresponding magnetic scalar potential with the circular harmonic expansion given in equation (2.76). As discussed in [150], for magnet systems with high eccentricity ρ/R, the circular harmonic expansion is nevertheless often used as an operation-centric system model because the determination of the coefficients, which are directly measurable with rotating coil magnetometers, is much easier than the determination of the toroidal harmonic coefficients. One reason for which this acknowledged error still yields a

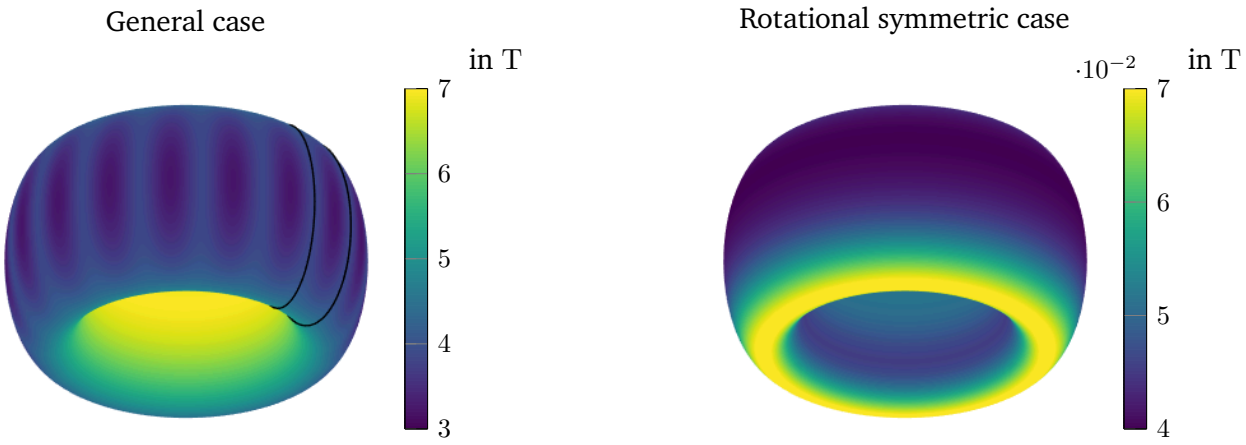

Figure 6.5: Absolute value of the magnetic flux density generated by the coil arrangement of the ITER tokamak shown in Figure 6.4 for the powering scheme before the plasma injection. The absolute value is visualized on the boundary of a toroidal domain D with toroidal radius $\rho = 7\,\mathrm{m}$ and the poloidal radius $R = 2.3\,\mathrm{m}$ placed inside free space surrounded by the coil arrangement. The magnetic flux density observations in these positions are used to determine the toroidal harmonic coefficients. Left: Magnetic field which is generated if all coils are powered. The black lines mark one toroidal wedge of length $l = \pi/9$. Right: Rotationally symmetric field, generated when the toroidal field coils are turned off.

system model feasible for operation is that the toroidal harmonic multipole fields converge to the corresponding circular harmonic multipole fields as observed by [25, Figure 4].
We use the present example of the rotationally symmetric magnetic flux density data on the toroidal domain with eccentricity 3.1 to demonstrate the limitations of the circular harmonic expansion for toroidal domains with low eccentricity.

Given $R = 432$ equally in space distributed observations $\mathbf{B}^{\mathrm{obs}}$ of the magnetic flux density in the rotationally symmetric case on $\partial\widetilde{D}$, we determine the toroidal harmonic coefficients $\mathbf{p}^{\mathrm{t}} = (\mathcal{E}^{\mathrm{t}}, \mathcal{A}_n^{\mathrm{t}}, \mathcal{B}_n^{\mathrm{t}})$ using the least squares fitting approach described in Section 6.2.2 with the truncation threshold $N = 20$. The same number of circular harmonic coefficients $\mathbf{p}^{\mathrm{c}} = (\mathcal{A}_n^{\mathrm{c}}, \mathcal{B}_n^{\mathrm{c}})$ is determined by approximating the equations (2.78) and (2.79) with the trapezoidal rule [107]. The determined harmonic coefficients are the parameters of the forward models $\mathcal{H}^{\mathrm{t}}$ and $\mathcal{H}^{\mathrm{c}}$ based on toroidal and the circular harmonic expansions of the magnetic flux density. We use the superscripts in the notation to distinguish the two models that are used here.
With each system model, the magnetic flux density on $\partial\widetilde{D}_{\mathrm{test}}$ is predicted and compared to the ground truth magnetic flux density $\mathbf{B}^{\mathrm{true}}$ obtained from the ROXIE simulation for validation. Let $\mathbf{B}^{\mathrm{t,pred}} = \mathcal{H}^{\mathrm{t}}(\mathbf{p}^{\mathrm{t}})$ and $\mathbf{B}^{\mathrm{c,pred}} = \mathcal{H}^{\mathrm{c}}(\mathbf{p}^{\mathrm{c}})$ be the two predictions. For the components $* \in \{\tau, \sigma\}$ and each model $\mathrm{x} \in \{\mathrm{t}, \mathrm{c}\}$, the relative error

$$E_*^{\mathrm{x}}(\tau,\sigma) \coloneqq \frac{\left\| B_*^{\mathrm{x,pred}}(\tau,\sigma) - B_*^{\mathrm{x,true}}(\tau,\sigma) \right\|}{B_{\max}} \tag{6.58}$$

is shown in Figure 6.6, where $B_{\max} = 0.07\,\mathrm{T}$ is the maximal magnetic flux density for the considered operation mode in the rotationally symmetric case. It can be seen that the relative errors of the predictions based on the toroidal harmonic coefficients $\mathbf{p}^{\mathrm{t}}$ are multiple orders of magnitudes smaller than the relative errors of the predictions based on the circular harmonic coefficients $\mathbf{p}^{\mathrm{c}}$. Hence, the circular harmonic expansion is infeasible to build an operation-centric system model for this example field.

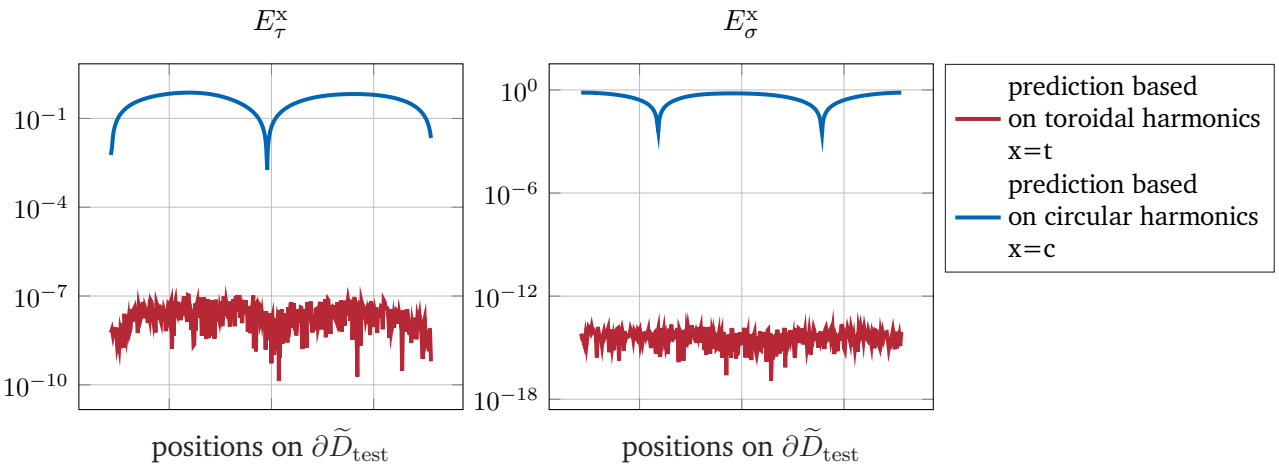

Figure 6.6: Relative error E^{x}_{*} defined in (6.58) between the predicted magnetic flux density and the ground truth magnetic flux density simulated with the ROXIE model evaluated on $\partial\widetilde{D}_{\mathrm{test}}$ for the rotationally symmetric magnetic flux density data of the ITER example. The two predictions in comparison are based on the circular harmonic expansion and the toroidal harmonic expansion. The toroidal harmonics are determined by fitting and shown in Figure 6.7.

Limitation of the integration method The last paragraph showed that the fitting method is suitable for determining the toroidal harmonic coefficients in the rotationally symmetric case. Figure 6.7 shows the absolute values of the toroidal harmonic coefficients $\mathcal{A}^{\mathrm{t}}_{n}, \mathcal{B}^{\mathrm{t}}_{n}$ scaled with $1/Q^{0}_{n-1/2}(\rho/R)$ obtained by fitting and by integration. In both cases, the gauging $\mathcal{A}^{\mathrm{t}}_{0} = 0$ is applied. While the absolute values of the toroidal harmonic coefficients determined by fitting decrease as $n \to \infty$, the coefficients determined by the integration method diverge. As discussed in Section 6.2.1, this method is thus unfeasible for determining the toroidal harmonics.

Validation of the fitting method in the general case After validating in the preceding paragraphs that the fitting method is suitable for building a system model based on the toroidal harmonic expansion to describe and predict the magnetic flux density generated by the solenoidal and the poloidal field coils of the ITER tokamak, the fitting approach is evaluated in this paragraph for the general case.
For the truncation thresholds $N = 15$ and $M = 4$, the absolute values of the determined toroidal harmonic coefficients are visualized in Figure 6.8. As in the rotationally symmetric case, a decreasing trend for $|\mathcal{A}^{\mathrm{t}}_{n,m}|, |\mathcal{B}^{\mathrm{t}}_{n,m}|$ and $|\mathcal{C}^{\mathrm{t}}_{n,m}|$ as the order m and the degree n increase can be observed, indicating that the expansion is suitable to describe the observed field according to the criteria of [135]. The toroidal harmonic coefficients $|\mathcal{D}^{\mathrm{t}}_{n,m}|$ are small independently of the order and the degree. Notice that the plotted values are normalized with $1/Q^{m}_{n-1/2}(\cosh(\tau_0))$, where $\cosh(\tau_0) = \rho/R$ and that the gauging condition $\phi_{\mathrm{m}}(\tau_0, 0, 0) = 0$ was imposed. A comparison of the numerically estimated condition numbers $\kappa_2(\mathcal{H})$ with and without gauging are given in Table 6.2.

For validation, the determined parameters $\mathbf{p}^{\mathrm{LS}} = (\mathcal{E}^{\mathrm{t}}, \mathcal{A}^{\mathrm{t}}_{n,m}, \mathcal{B}^{\mathrm{t}}_{n,m}, \mathcal{C}^{\mathrm{t}}_{n,m}\mathcal{D}^{\mathrm{t}}_{n,m})$ shown in Figure 6.8 are inserted into the forward model $\mathcal{H}$ and used to predict the magnetic flux density $\mathbf{B}^{\mathrm{pred}} = \mathcal{H}(\mathbf{p}^{\mathrm{LS}})$ on the toroidal wedge $\widetilde{D}_{\mathrm{test}}$ on which simulated ground truth data $\mathbf{B}^{\mathrm{true}}$ of the magnetic flux density is available. For each

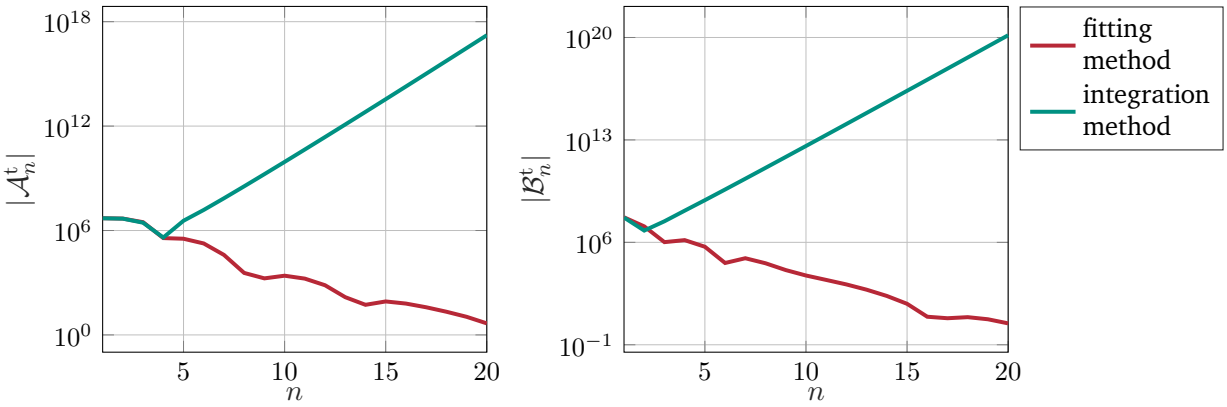

Figure 6.7: Comparison of the absolute values of the toroidal harmonic coefficients determined by the integration method described in Section 6.2.1 and the fitting method described in Section 6.2.2 for the rotationally symmetric magnetic flux density data of the ITER example.

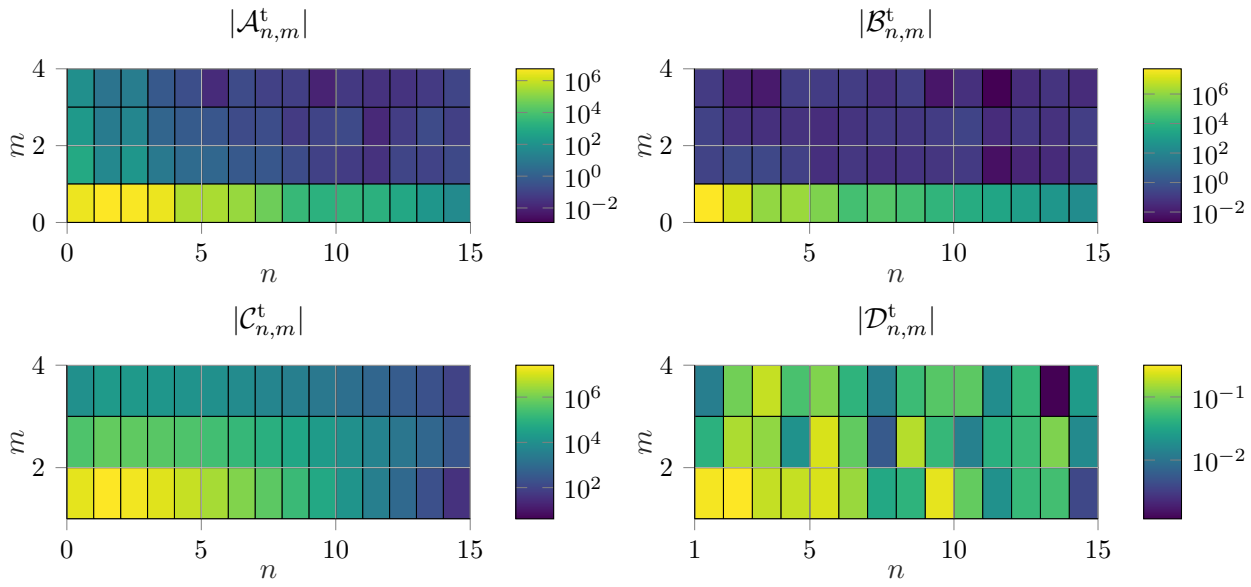

Figure 6.8: Absolute values of the fitted toroidal harmonic coefficients for the coil arrangement of the ITER tokamak. Notice that the coefficients are scaled with $1/Q^m_{n-1/2}(\cosh(\tau_0))$, where $\cosh(\tau_0) = \rho/R$ and the gauging condition $\phi_{\mathrm{m}}(\tau_0, 0, 0) = 0$ is imposed.

Table 6.2: Condition number of the linear least squares problem to determine the toroidal harmonic coefficients ($N = 15$, $M = 4$) for the coil arrangement of the ITER tokamak before and after gauging with the condition $\phi_{\mathrm{m}}(\tau_0, 0, 0) = 0$.

	with gauging	without gauging
$\kappa_2(\mathcal{H})$	$4.43 \cdot 10^8$	$1.51 \cdot 10^{17}$

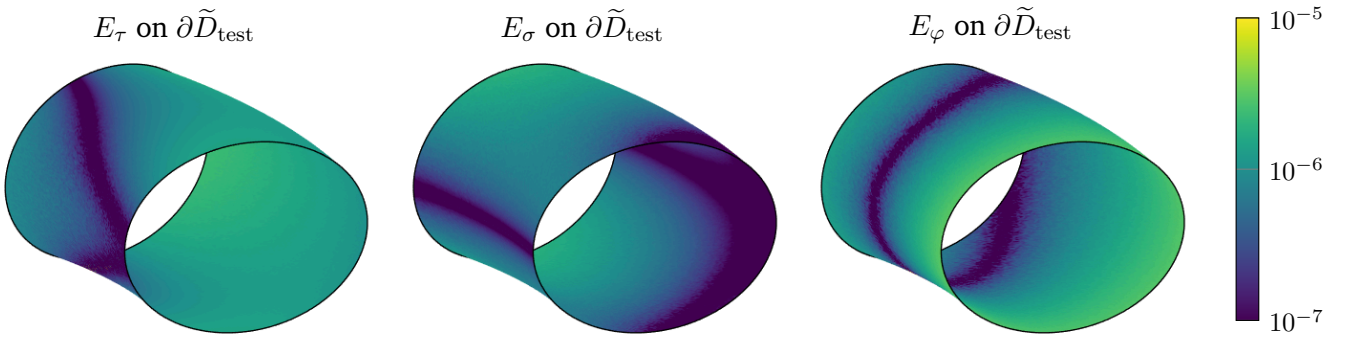

Figure 6.9: Relative error E_* defined in equation (6.59) between the predicted magnetic flux density based on the toroidal harmonic coefficients ($N = 15$, $M = 4$) shown in Figure 6.8 and the ground truth magnetic flux density simulated with the ROXIE model. The relative error is evaluated on the boundary of the toroidal wedge $\widetilde{D}_{\text{test}}$, which is chosen concentric to the toroidal wedge $\widetilde{D}$ shown in Figure 6.5 (left) on which the magnetic flux density observations to determine the toroidal harmonic coefficients are given.

component $* \in \{\tau, \sigma, \varphi\}$ we define the relative error

$$E_*(\tau,\sigma,\varphi) := \frac{\left\| B_*^{\text{pred}}(\tau,\sigma,\varphi) - B_*^{\text{true}}(\tau,\sigma,\varphi) \right\|}{B_{\max}} \tag{6.59}$$

between the predicted magnetic flux density and the ground truth magnetic flux density simulated with the ROXIE model, where $B_{\max} = 6.98\,\text{T}$ is the maximal magnetic flux density for the considered operation mode. The relative errors E_* evaluated on $\partial\widetilde{D}_{\text{test}}$ are shown in Figure 6.9. In all positions and for all components, the relative errors are of the order of magnitude of 10^{-6} and hence below the threshold of 1 unit in 10000 that is typically considered sufficient for the simulation of accelerator magnets.
To study the influence of the choice of the truncation thresholds N and M, the average relative error

$$\overline{E_*} := \frac{1}{100 \cdot 432} \sum_{i=1}^{100} \sum_{j=1}^{432} E_*(\tau_{i,j}, \sigma_j, \varphi_i) \tag{6.60}$$

on the data grid on $\partial\widetilde{D}_{\text{test}}$ is shown for different values of N and M in Figure 6.10. It can be seen that the thresholds $M \geq 1$ and $N \geq 5$ should be selected to predict the magnetic flux density on $\partial\widetilde{D}_{\text{test}}$ in average better than 1 unit in 10000. Considering further functions with orders higher than $M = 2$ or increasing the number of considered degrees to more than $N = 10$ does not further improve the prediction. Consequently, in this case, only a few toroidal harmonic coefficients are sufficient to describe the observed field. According to [135], this fact indicates that the toroidal harmonic expansion is a suitable field description in this case.
One reason for the observation that the average relative error is not further improved, despite the increment of the truncation thresholds N and M, is that the data $\mathbf{B}^{\text{obs}}$ violates the periodicity assumption (6.4) up to the order of magnitude of 10^{-5} T.

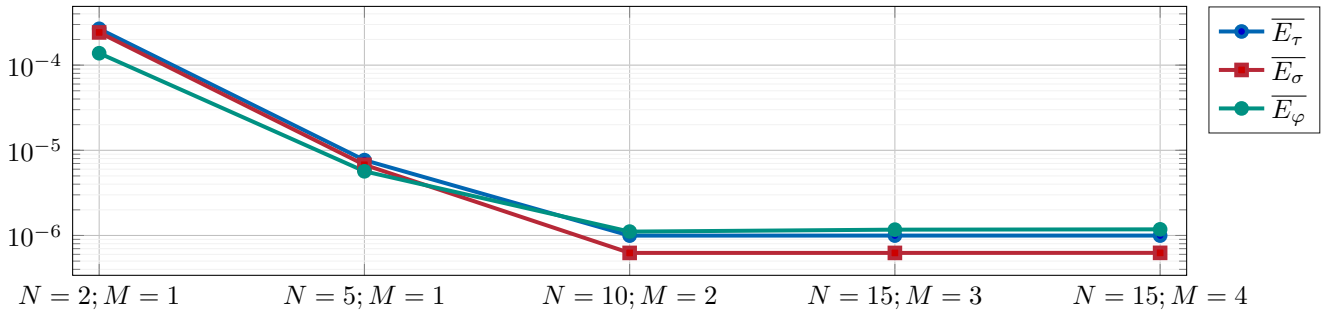

Figure 6.10: Average relative error defined in equation (6.60) on $\partial\widetilde{D}_{\text{test}}$ between the predicted magnetic flux density based on the determined toroidal harmonic coefficients for different truncation thresholds N and M and the ground truth magnetic flux density simulated with the ROXIE model for the ITER example.

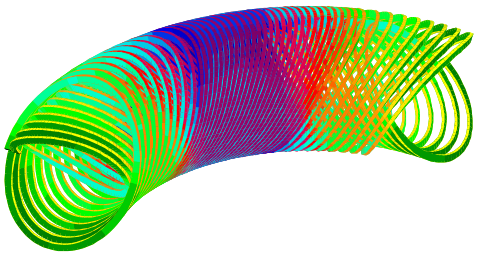

Figure 6.11: Curved CCT dipole with a bending angle of around 45 degrees. The cable characteristics, pitch lengths, and slot sizes are chosen equivalently to the curved CCT demonstrator described in [69]. This figure is generated with ROXIE [121].

6.3.2 Curved CCT dipole

The concept of canted cosine theta (CCT) magnets was first proposed by [97]. They consist of two nested solenoids both tilted with the angle θ but in opposite directions. Hence, the solenoidal field components cancel out, while the dipolar field components of the two coils are added, yielding a uniform dipole field in the air gap. The objective of the Fusillo study at CERN is the development of a strongly curved CCT magnet which is bent over 90 degrees [69]. Curved CCT magnet systems find use, e.g., for field corrections and are particularly suitable for compact particle accelerators [82] and compact ion therapy gantry systems [149].

We consider a curved CCT magnet system similar to the prototype magnet developed in the Fusillo project [69] in this section. The curved CCT magnet shown in Figure 6.11 has a bend angle of around 45 degrees, the toroidal radius $\rho = 600\,\text{mm}$. The poloidal radii of the solenoids are $\rho = 125\,\text{mm}$ and $\rho = 147.9\,\text{mm}$. Hence, the source-free computational domain in the center of the magnet system has the shape of a toroidal wedge. The cable characteristics, pitch lengths, and slot sizes are chosen identically to the prototype magnet developed in the Fusillo project. The groves in the winding mandrel are $17.10 \times 5.88\,\text{mm}$, housing 70 wires of $0.985\,\text{mm}$ in diameter.
To apply and validate the algorithm for determining the toroidal harmonics, the curved CCT magnet is simulated using ROXIE [121]. Thereby a static excitation current of $287.5\,\text{A}$ per wire is applied, leading to a maximal field of $1.46\,\text{T}$.

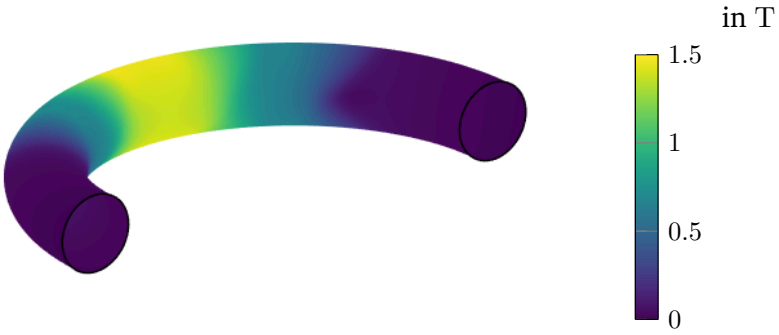

Figure 6.12: Absolute value of the magnetic flux density generated by the curved CCT magnet system shown in Figure 6.11 for the excitation current of $287.5\,\mathrm{A}$ per wire. The absolute value is visualized on the boundary of the toroidal wedge $\widetilde{D}$, which has a toroidal angle of 180 degrees, the toroidal radius $\rho = 600\,\mathrm{mm}$ and the poloidal radius $R = 100\,\mathrm{mm}$. The magnetic flux density observations in these positions are used to determine the toroidal harmonic coefficients.

To determine the toroidal harmonic coefficients using the least squares fitting approach described in Section 6.2.2, observations of the magnetic flux density on a grid covering the boundary of a toroidal wedge $\widetilde{D}$ with toroidal angle $\varphi \in [0, \pi]$, a toroidal radius $\rho = 600\,\mathrm{mm}$ and a poloidal radius $R = 100\,\mathrm{mm}$ is chosen. Thus, the toroidal wedge is concentric to the solenoids. The step size of the grid is 432 observations with respect to the poloidal angle and 180 observations regarding the toroidal angle. The focal ring of the toroidal coordinate system is set such that the boundary of the toroidal wedge $\widetilde{D}$ is a τ-isosurface.
The longitudinal center of the magnet system regarding the toroidal angle φ is aligned with the center of the toroidal wedge $\widetilde{D}$. Since the toroidal wedge covers the angle of 180 degrees, while the magnet system is only bent around 45 degrees, the toroidal wedge and hence the magnetic flux density observations cover the central field and the fringe field. The condition that $\mathbf{B}(\tau, \sigma, 0) = \mathbf{B}(\tau, \sigma, \pi)$, which is specified in equation (6.4) as a requirement to apply the toroidal harmonic expansion to the magnetic flux density on torus wedges, is violated by $6.97 \cdot 10^{-3}\,\mathrm{T}$ at most for all components of the magnetic flux density. The absolute values of the magnetic flux density observations on $\partial\widetilde{D}$ are shown in Figure 6.12.

The toroidal harmonic coefficients are determined by least squares fitting as described in Section 6.2.2. For the truncation thresholds $N = 10$ and $M = 50$, we obtain the coefficients whose absolute values are visualized in Figure 6.13. Notice that to obtain these values, we used the normalization of the toroidal harmonic expansion with $1/Q^m_{n-1/2}(\cosh(\tau_0))$, where $\cosh(\tau_0) = \rho/R$, and applied gauging by imposing the condition $\phi_\mathrm{m}(\tau_0, 0, 0) = 0$. Table 6.3 emphasizes the influence of the gauging on the numerically estimated condition number $\kappa_2(\mathcal{H})$. For the toroidal harmonics, a decreasing trend of the absolute values as the degree n and the order m increase can be observed. According to the conditions discussed in the introduction of this chapter and in [135], the decrease indicates the suitability of the toroidal harmonic expansion to describe the field.

To validate the determined parameter values $\mathbf{p}^\mathrm{LS}$ of the toroidal harmonic coefficients $\mathcal{A}^\mathrm{t}_{n,m}, \mathcal{B}^\mathrm{t}_{n,m}, \mathcal{C}^\mathrm{t}_{n,m}$ and $\mathcal{D}^\mathrm{t}_{n,m}$ and the linear coefficient $\mathcal{E}^\mathrm{t}$ and to justify the chosen thresholds N and M, the magnetic flux density is predicted on the boundary of a toroidal wedge $\widetilde{D}_\mathrm{test}$, which is chosen concentric to the wedge $\widetilde{D}$, with a poloidal radius of $80\,\mathrm{mm}$. Notice that this surface is not an isosurface of the toroidal harmonic coordinate system. Let $\mathbf{B}^\mathrm{pred} = \mathcal{H}(\mathbf{p}^\mathrm{LS})$ be the magnetic flux density predicted by the forward model. As for the ITER example, we evaluate for each component $* \in \{\tau, \sigma, \varphi\}$ the relative error E_* defined in equation (6.59) between the predicted magnetic flux density and the ground truth magnetic flux density $\mathbf{B}^\mathrm{true}$ simulated with the ROXIE

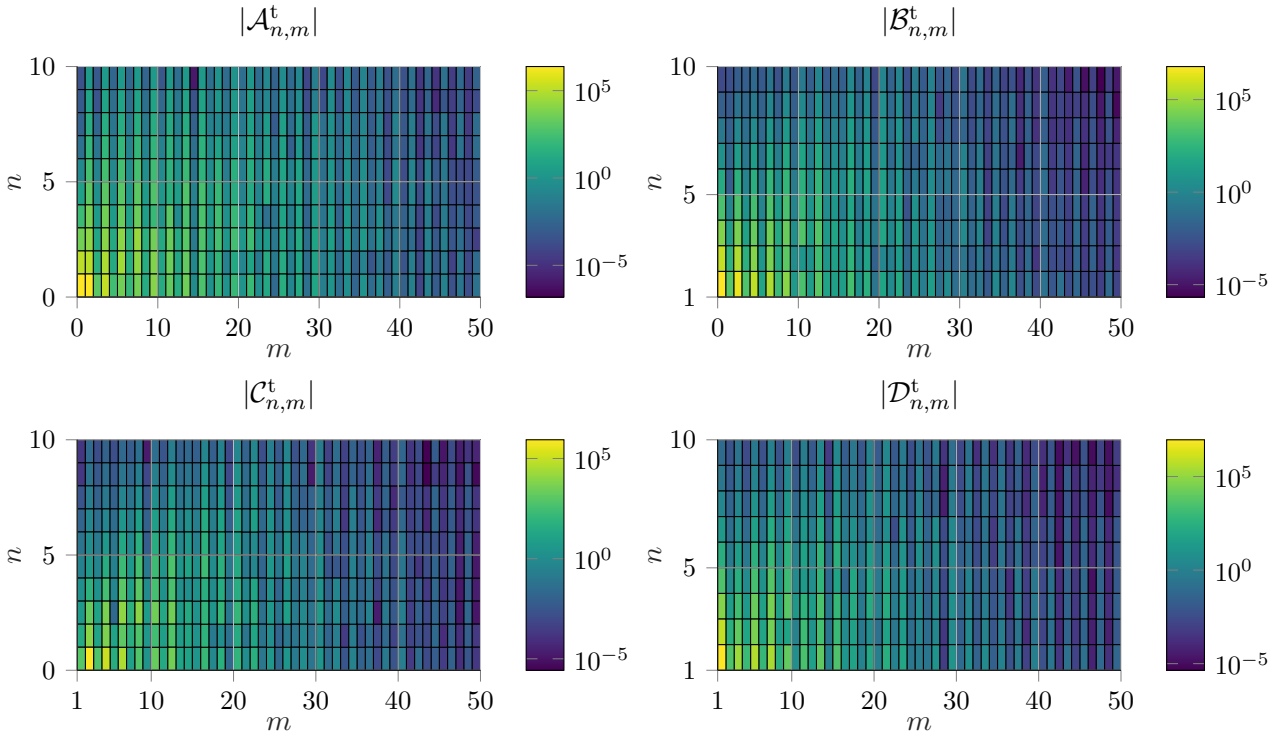

Figure 6.13: Absolute values of the fitted toroidal harmonic coefficients for the curved CCT magnet system. Notice that the coefficients are scaled with $1/Q^m_{n-1/2}(\cosh(\tau_0))$, where $\cosh(\tau_0) = \rho/R$ and the gauging condition $\phi_{\mathrm{m}}(\tau_0, 0, 0) = 0$ is imposed.

Table 6.3: Condition number of the linear least squares problem to determine the toroidal harmonic coefficients ($N = 10$, $M = 50$) for the curved CCT dipole before and after gauging with the condition $\phi_{\mathrm{m}}(\tau_0, 0, 0) = 0$.

	with gauging	without gauging
$\kappa_2(\mathcal{H})$	$7.72 \cdot 10^7$	$4.26 \cdot 10^{16}$

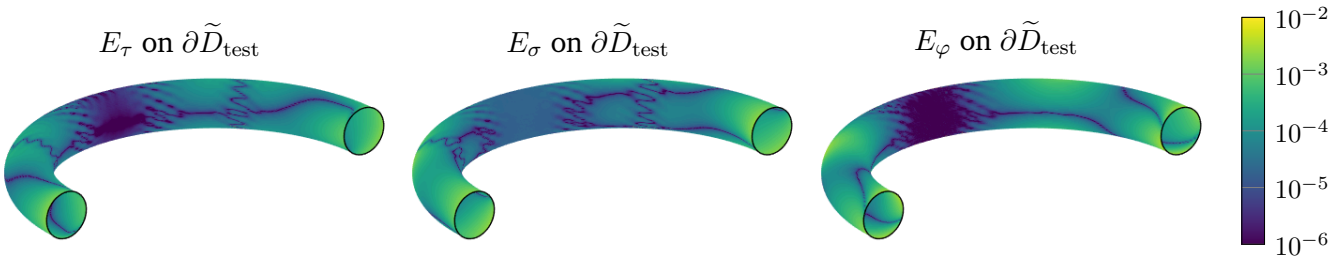

Figure 6.14: Relative error E_* defined in equation (6.59) between the predicted magnetic flux density based on the toroidal harmonic coefficients ($N = 10$, $M = 50$) shown in Figure 6.13 and the ground truth magnetic flux density simulated with the ROXIE model. The relative error is evaluated on the boundary of the toroidal wedge $\widetilde{D}_{\text{test}}$, which is chosen concentric to the toroidal wedge $\widetilde{D}$ shown in Figure 6.12 on which the magnetic flux density observations to determine the toroidal harmonic coefficients are given.

model. Here, the maximal magnetic flux density for the considered operation mode is $B_{\max} = 1.46\,\text{T}$. Figure 6.14 shows $E_*(\tau, \sigma, \varphi)$ evaluated on the boundary of the toroidal wedge $\widetilde{D}_{\text{test}}$. In the central field region the relative errors E_τ and E_φ are of the order of magnitude of 10^{-6}, the relative error E_σ is with the magnitude of 10^{-5} slightly bigger but still below the threshold of 1 unit in 10000. However, in the fringe field regions, the relative error between prediction and ground truth exceeds this limit, in particular towards the ends of the toroidal wedge at $\varphi = 0$ and $\varphi = \pi$. Possible reasons for this mismatch might be that the considered orders and degrees of the toroidal harmonic coefficients are insufficient to describe the field with the truncated toroidal harmonic expansion in this region and that the condition (6.4) is violated by the observations.

To illustrate that the predictions of the magnetic flux density with the generalized field description of the curved CCT magnet system based on toroidal harmonic coefficients improve the more toroidal harmonic coefficients are considered, the average

$$\overline{E_*} := \frac{1}{180 \cdot 432} \sum_{i=1}^{180} \sum_{j=1}^{432} E_*(\tau_{i,j}, \sigma_j, \varphi_i) \tag{6.61}$$

of the relative errors E_* on the chosen observation grid on $\partial\widetilde{D}_{\text{test}}$ is shown in Figure 6.15 for different truncation thresholds N and M. It can be seen that to a certain extent, a possibility to further improve the predictive capacities of the system model is increasing the truncation thresholds N and M. However, this strategy contradicts the idea of a compact field description with only a few harmonic coefficients. Moreover, the errors at the ends of the toroidal wedge $\widetilde{D}_{\text{test}}$ will not decrease by considering more coefficients, since the periodic ansatz does not match the data. Therefore, another method without periodicity assumption, e.g., the BEM-based generalized field description described in [92], might be more suitable to build a system model of the generated field in this case.

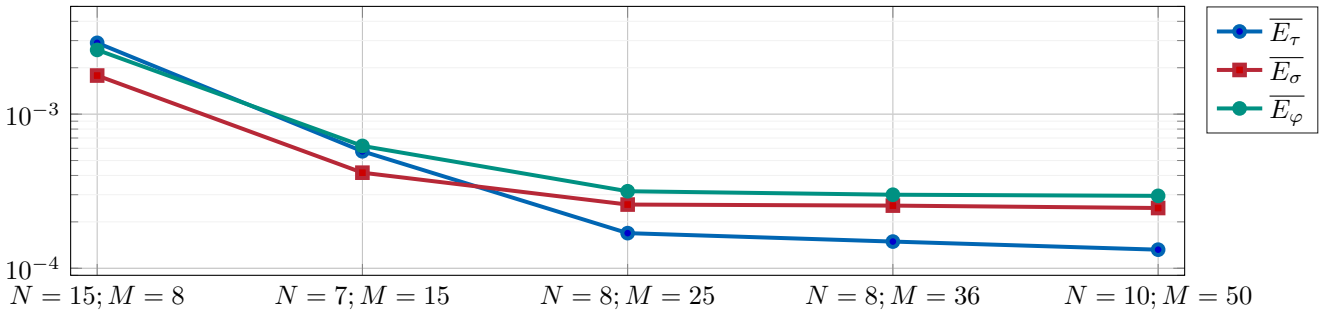

Figure 6.15: Average relative error defined in equation (6.61) on $\partial\widetilde{D}_{\text{test}}$ between the predicted magnetic flux density based on the determined toroidal harmonic coefficients for different truncation thresholds N and M and the ground truth magnetic flux density simulated with the ROXIE model for the curved CCT example.

6.4 Summary

In this chapter, we derived and evaluated two methods to determine the coefficients of the toroidal harmonic expansion, introduced in Section 2.4.2, from observations of the magnetic flux density. The determination of these coefficients is an ill-posed inverse problem as defined in Section 1.3.4. We showed that one cause of the ill-posedness is the non-uniqueness of the solution because the functions spanning the skew part of the magnetic flux density in the toroidal harmonic expansion are linearly dependent. Consequently, the forward model has a non-trivial kernel and the skew coefficients can not be uniquely determined from the magnetic flux density. As discussed in Section 2.2.2, a gauging condition is required to uniquely determine a solution to the boundary value problem of magnetostatics in scalar potential formulation under Neumann boundary conditions.

The fitting-based method to determine the toroidal harmonic coefficients was used to build and update operation-centric system models (Section 1.2.2), describing the magnetic fields generated by the coil arrangements of the ITER tokamak and a curved CCT dipole. Particularly in the ITER example, the magnetic flux density was describable with only a few toroidal harmonic coefficients. However, for the curved CCT example, alternative operation-centric system models based on other expansions, not requiring a periodicity assumption of the data might be more suitable.

7 Conclusion and prospects for future research

Conclusion In this thesis, three system models of accelerator magnets were derived and updated for predicting quantities of interest for operation and magnet introspection. This task was challenging for multiple reasons, e.g., the uncertainties affecting measurable quantities related to the magnet system, the limited knowledge of the governing physical processes, and the necessity to identify and reasonably adapt model parameters.
To face these challenges, we used hybrid modeling, i.e. combining first principle-based with data-driven methods. This strategy linked different sources of knowledge about a magnetic system, including data from different measurement campaigns, and established useful connections between the models and data sets operated in the TE-MSC-TM section at CERN. The field-related quantities predicted with the resulting hybrid models were reliable, even in areas outside the range of the training data, because the models were both based on physical laws and adapted to measured observations.

Concerning the simulation of iron-dominated magnet systems, a method to update the non-linear $H(B)$-curve of the yoke using a data-driven $H(B)$-curve model based on split-coil permeameter measurements of yoke material specimens and the KLE was derived in Chapter 4. The KLE provided a low-rank approximation of the corresponding inverse problem requiring only two parameters to be determined. Despite the few parameters, the data-driven $H(B)$-curve model was more suitable for describing the measured data than common closed-form expressions based on physical laws. Even though the KLE-based $H(B)$-curve model is material-specific, we observed similar modes of the KLE for different materials. Moreover, it was shown that a sensitivity analysis based on the Gâteaux derivative in the direction of the KLE modes can be used to assess the inverse problem's stability and to identify suitable observation positions of comparable quantities of interest for model updating. A deterministic approach based on particle swarm optimization and a stochastic approach based on Markov chain Monte Carlo sampling were compared for model updating. Both updated models met at operation modes that interpolate the operation modes used in the training data, the common accuracy requirement of a relative prediction error of less than 1 unit in 10000. Also for higher excitation currents that extrapolate the currents of the training data, the relative error never exceeded 3 units in 10000 in all analyzed positions. Suppose that an application requires only a deterministic update of the parameter values without uncertainty quantification. In that case, the optimization-based approach is already sufficient and requires fewer evaluations of the forward model and less theoretical background on Bayesian inference and Markov chains than the stochastic approach.

In Chapter 5, the observed mismatch between predictions of the numerical design model of the first short FASER Halbach dipole and measured higher-order multipole coefficients was explained by adjusting the magnetization of the PM blocks in the range of their manufacturing variations. To update the three-dimensional model of the magnet system with its high dimensional parameter space, stochastic model updating based on Markov chain Monte Carlo sampling was unfeasible due to the large number of required model evaluations and the increased computation time per evaluation of the 3D FEM model. Omitting the outer construction-steel ring was a reasonable acknowledged error to obtain a linear system model that can be stochastically updated with the maximum a posteriori estimate, whose computation required fewer evaluations of the time-consuming FEM model. Similar to the previous chapter, a sensitivity analysis based on Gâteaux derivatives helped to

identify suitable measurement positions to observe the data used for model updating. It turned out that the data collected during a measurement campaign four years ago, before the installation of the magnet system, was suitable.

A method based on integrating the magnetic flux density and a method based on least squares fitting to determine the coefficients of the toroidal harmonic expansion from magnetic flux density observations were derived in Chapter 6. While the integration method was unsuitable for application due to recursive error propagation, the fitting-based method was verified on the example of the magnetic field generated by the coil arrangements of the ITER tokamak and by a curved CCT dipole. In the ITER example, very few toroidal harmonic coefficients were sufficient to describe the magnetic field, whereas in the curved CCT example more coefficients were required and the field prediction was less accurate.
As for any other scalar potential formulation, a gauging condition was required to uniquely determine the magnetic scalar potential under Neumann boundary conditions. We showed that a non-trivial linear combination of skew harmonic coefficients yields a constant scalar potential, and thus, the functions spanning the skew part of the magnetic flux density are linearly dependent.

Prospects for future research In this work, we assumed for each system model that only one aspect e.g. the material curve requires an update to improve the model's predictions. In future works, updating multiple aspects of a system model could be considered, e.g., for an iron-dominated magnet the material curve of the yoke and the yoke geometry. The sensitivity analysis regarding different parameter sets derived in [117] could be used to quantify the relevance of a parameter to predict a specific quantity of interest. Particularly interesting in this context would be the investigation if a quantity of interest can be sensitive to one parameter set and at the same time insensitive to another parameter set in an observation position and an operation mode. This investigation could be conducted by computing Gâteaux derivatives in the direction of parameter variations with the methods described in [117]. If such positions and operation modes can be identified, different aspects of the model could be updated independently.

Deriving a low-rank approximation of an inverse problem based on the KLE and measured observations is neither limited to $B(H)$-curves nor to parameters that are real-valued functions. Instead, the KLE can be applied to any aspect of a magnet system affected by uncertainty that can be described with a random field. While in this thesis hysteresis is omitted, further research could include updating hysteresis curves using similar methods. A description of hysteresis models using the KLE can already be found in [77]. Further possibilities to enhance the component-centric system model derived in Chapter 4, are besides the inclusion of hysteresis, the inclusion of eddy currents or temperature effects.
Moreover, the investigations on updating $B(H)$-curves in this thesis were limited to simulated magnetic flux density observations. If an iron-dominated magnet system with both (B, H)-data of the yoke material and measured observation data of a quantity of interest becomes available, the verification of the proposed method on these data sets would complete this study.

We did not apply model order reduction methods or surrogate models to accelerate the computation time for evaluating the forward model in this work. Our approach has the advantage that no additional recognized errors are introduced to the forward model. However, some methods such as the Markov chain Monte Carlo sampling became infeasible due to the computation time. For this application, the investigation of a surrogate model could be interesting. Moreover, alternative methods to explore the posterior distribution such as approximate inference could be studied in this case.

Our study of methods to determine the toroidal harmonic coefficients showed that their determination is much more challenging than the determination of the circular harmonic coefficients, which are directly observable by rotating coil magnetometers. In [25], the observation is described that the multipole fields of the toroidal harmonic expansion converge to those of the circular harmonic expansion for toroidal domains with high eccentricity. If this observation would be supported with a calculation estimating the difference between both fields in dependence on the eccentricity, the importance of the acknowledged error, when considering the circular harmonic expansion for simplicity, could be quantified.
Furthermore, we only considered measurements of the magnetic flux density taken with a Hall probe mapper system to determine the toroidal harmonic coefficients. Another common approach to measuring integrated fields in curved magnet systems is by curved fluxmeters. Analogously to the least squares fitting method based on the magnetic flux density, a least squares fitting approach based on the fluxmeter measurements could be derived.

To compute the update of the first short FASER dipole's magnetizations, Helmholtz coil measurement data of the magnetizations was combined with measurement data of the magnetic flux density conducted with a Hall probe mapper system four years ago. The assumed standard deviations of the random and systematic measurement uncertainty in the fringe field regions are relatively large in this data set. In the meantime, the vibrations and the sensor orientation of the Hall probe mapper system are better understood, leading to smaller measurement uncertainties of recently taken measurements with the same system. Consequently, the weighting of the different data sets according to their uncertainty with the Bayesian approach would be different if more recent data was available. In this context, the computation of subsequent updates of a magnet system during its life cycle using Bayesian inference could be investigated. In each iteration, the previous update could be used as a prior model and the most recent measurement data could be used to determine the update. Furthermore, a modeler could adapt the weighting of different data sets by including his expert knowledge of outdated measurement methods. This approach could be particularly interesting in the refurbishing process of a magnet system.

8 Appendix

8.1 Associated Legendre functions of half-integer degree

The associated Legendre functions of the second kind of half-integer degree $Q^m_{n-\frac{1}{2}} : \mathbb{R} \to \mathbb{R}$ are given for $x > 1$ and integers $n, m \geq 0$ by [2, equation 8.1.3]

$$Q^m_{n-\frac{1}{2}}(x) = \frac{(-1)^m\sqrt{\pi}}{2^{n+\frac{1}{2}}}\frac{\Gamma(n+m+\frac{1}{2})}{\Gamma(n+1)}\frac{1}{x^{n+m+\frac{1}{2}}}(x^2-1)^{\frac{m}{2}}\, F\left(\frac{1}{2}\left(n+m+\frac{3}{2}\right), \frac{1}{2}\left(n+m+\frac{1}{2}\right); n+1; x^{-2}\right), \tag{8.1}$$

where Γ is the Gamma function and F denotes the hypergeometric function that is for real parameters $a, b, c \in \mathbb{R}$ and a real argument $0 < z < 1$ given by [2, equation 15.1.1]

$$F(a,b;c;z) = \frac{\Gamma(c)}{\Gamma(a)\Gamma(b)}\sum_{k=0}^{\infty}\frac{\Gamma(a+k)\Gamma(b+k)}{\Gamma(c+k)}\frac{z^k}{k!} = \sum_{k=0}^{\infty} S(k) \tag{8.2}$$

with the function S defined by

$$S(k) := \begin{cases} 1 & k = 0, \\ \frac{(a+k-1)(b+k-1)}{(c+k-1)}\frac{z}{k}S(k-1) & k > 0. \end{cases} \tag{8.3}$$

Notice that we evaluate the associated Legendre functions (8.1) for arguments $x = \cosh(\tau) = \rho/R > 1$ due to the definition of the major radius ρ and the minor radius R. To evaluate $Q^m_{-\frac{3}{2}}(x)$ we use the recursive formula [64, equation 8.732]

$$2nx\, Q^m_{n-\frac{1}{2}}(x) = (n-m+1/2)\, Q^m_{n+\frac{1}{2}}(x) + (n+m-1/2)\, Q^m_{n-\frac{3}{2}}(x) \tag{8.4}$$

which yields for $n = 0$ the identity

$$Q^m_{-\frac{3}{2}}(x) = Q^m_{\frac{1}{2}}(x). \tag{8.5}$$

Discussions on the evaluation and implementation of the associated Legendre functions of the second kind of half-integer degree can be found, e.g., in [124, 133, 134]. We implement them using the series given in equation 8.2 truncated at $k = K$. An estimation of the truncation error is given in [133]. We choose $K = 50$.

Inserting $x = \cosh(\tau)$ into equation (8.1) yields

$$\begin{aligned} Q^m_{n-\frac{1}{2}}(\cosh(\tau)) = \; & \frac{(-1)^m\sqrt{\pi}}{2^{n+\frac{1}{2}}}\frac{\Gamma\left(n+m+\frac{1}{2}\right)}{\Gamma(n+1)}\frac{\tanh^m(\tau)}{\cosh^{n+\frac{1}{2}}(\tau)} \\ & F\left(\tfrac{1}{2}\left(n+m+\tfrac{3}{2}\right), \tfrac{1}{2}\left(n+m+\tfrac{1}{2}\right); n+1; \cosh^{-2}(\tau)\right). \end{aligned} \tag{8.6}$$

Notice that it can be verified with Mathematica [142] that the term

$$\sqrt{\cosh(\tau)-\cos(\sigma)}Q^m_{n-1/2}(\cosh(\tau)) \tag{8.7}$$

is finite for $\tau \to \infty$ for all $\sigma \in [0, 2\pi]$ and $n, m \geq 0$. However, the term

$$\sqrt{\cosh(\tau)-\cos(\sigma)}P^m_{n-1/2}(\cosh(\tau)) \tag{8.8}$$

diverges for $\tau \to \infty$ for all $\sigma \in [0, 2\pi]$ and $n, m \geq 0$, where the concatenation of the associated Legendre functions of the first kind of half-integer degree $P^m_{n-1/2}$ with $\cosh(\tau)$ is given by [133, equation A.1]

$$\begin{aligned} P^m_{n-\frac{1}{2}}(\cosh(\tau)) = \; & \frac{\Gamma\left(n+m+\frac{1}{2}\right)}{2^m\, m!\, \Gamma\left(n-m+\frac{1}{2}\right)} \tanh^m(\tau)\cosh^{n-\frac{1}{2}}(\tau) \\ & F\left(\tfrac{1}{2}\left(m-n+\tfrac{1}{2}\right), \tfrac{1}{2}\left(m-n+\tfrac{3}{2}\right); m+1; \tanh^2(\tau)\right). \end{aligned} \tag{8.9}$$

For this reason, solutions to the Laplace equation involving $\sqrt{\cosh(\tau)-\cos(\sigma)}P^m_{n-1/2}(\cosh(\tau))$ can be omitted if the computational domain includes the focal ring of the toroidal coordinate system [19, 25].

The derivative of $Q^m_{n-\frac{1}{2}}(x)$ with respect to x is given by [64, equation 8.732]

$$(x^2-1)\frac{\mathrm{d}Q^m_{n-1/2}(x)}{\mathrm{d}x} = \left(n-\frac{1}{2}\right)x\, Q^m_{n-\frac{1}{2}}(x) - \left(n+m-\frac{1}{2}\right)Q^m_{n-\frac{3}{2}}(x). \tag{8.10}$$

Applying the chain rule yields

$$\frac{\mathrm{d}Q^m_{n-\frac{1}{2}}(\cosh(\tau))}{\mathrm{d}\tau} = \frac{\left(n-\frac{1}{2}\right)}{\tanh(\tau)}Q^m_{n-\frac{1}{2}}(\cosh(\tau)) - \frac{\left(n+m-\frac{1}{2}\right)}{\sinh(\tau)}Q^m_{n-\frac{3}{2}}(\cosh(\tau)). \tag{8.11}$$

8.2 Magnetic flux density in toroidal coordinates

Computing $\mathbf{B} = -\mu_0 \operatorname{grad}\phi_\mathrm{m}$ for the normalized toroidal harmonic expansion (2.99) of the magnetic scalar potential ϕ_m yields the magnetic flux density in toroidal coordinates.

General case

$$\begin{aligned} B_\tau = \sum_{m,n=0}^{\infty} \; & \mathcal{A}^\mathrm{t}_{n,m}\left(-\frac{\mu_0\cos(n\sigma)\cos(m\varphi)\kappa(\tau,\sigma)}{aQ^m_{n-\frac{1}{2}}(\cosh(\tau_0))}\left[\frac{\sinh(\tau)}{2\sqrt{\kappa(\tau,\sigma)}}Q^m_{n-\frac{1}{2}}(\cosh(\tau)) + \sqrt{\kappa(\tau,\sigma)}\frac{\mathrm{d}}{\mathrm{d}\tau}Q^m_{n-\frac{1}{2}}(\cosh(\tau))\right]\right) \\ & + \mathcal{B}^\mathrm{t}_{n,m}\left(-\frac{\mu_0\sin(n\sigma)\cos(m\varphi)\kappa(\tau,\sigma)}{aQ^m_{n-\frac{1}{2}}(\cosh(\tau_0))}\left[\frac{\sinh(\tau)}{2\sqrt{\kappa(\tau,\sigma)}}Q^m_{n-\frac{1}{2}}(\cosh(\tau)) + \sqrt{\kappa(\tau,\sigma)}\frac{\mathrm{d}}{\mathrm{d}\tau}Q^m_{n-\frac{1}{2}}(\cosh(\tau))\right]\right) \\ & + \mathcal{C}^\mathrm{t}_{n,m}\left(-\frac{\mu_0\cos(n\sigma)\sin(m\varphi)\kappa(\tau,\sigma)}{aQ^m_{n-\frac{1}{2}}(\cosh(\tau_0))}\left[\frac{\sinh(\tau)}{2\sqrt{\kappa(\tau,\sigma)}}Q^m_{n-\frac{1}{2}}(\cosh(\tau)) + \sqrt{\kappa(\tau,\sigma)}\frac{\mathrm{d}}{\mathrm{d}\tau}Q^m_{n-\frac{1}{2}}(\cosh(\tau))\right]\right) \\ & + \mathcal{D}^\mathrm{t}_{n,m}\left(-\frac{\mu_0\sin(n\sigma)\sin(m\varphi)\kappa(\tau,\sigma)}{aQ^m_{n-\frac{1}{2}}(\cosh(\tau_0))}\left[\frac{\sinh(\tau)}{2\sqrt{\kappa(\tau,\sigma)}}Q^m_{n-\frac{1}{2}}(\cosh(\tau)) + \sqrt{\kappa(\tau,\sigma)}\frac{\mathrm{d}}{\mathrm{d}\tau}Q^m_{n-\frac{1}{2}}(\cosh(\tau))\right]\right) \end{aligned} \tag{8.12}$$

$$
\begin{aligned}
B_\sigma = \sum_{m,n=0}^{\infty} \quad & \mathcal{A}^{\mathrm{t}}_{n,m}\left(-\frac{\mu_0 Q^m_{n-\frac{1}{2}}(\cosh(\tau))\cos(m\varphi)\kappa(\tau,\sigma)}{aQ^m_{n-\frac{1}{2}}(\cosh(\tau_0))}\left[\frac{\sin(\sigma)}{2\sqrt{\kappa(\tau,\sigma)}}\cos(n\sigma)-\sqrt{\kappa(\tau,\sigma)}n\sin(n\sigma)\right]\right)\\
&+\mathcal{B}^{\mathrm{t}}_{n,m}\left(-\frac{\mu_0 Q^m_{n-\frac{1}{2}}(\cosh(\tau))\cos(m\varphi)\kappa(\tau,\sigma)}{aQ^m_{n-\frac{1}{2}}(\cosh(\tau_0))}\left[\frac{\sin(\sigma)}{2\sqrt{\kappa(\tau,\sigma)}}\sin(n\sigma)+\sqrt{\kappa(\tau,\sigma)}n\cos(n\sigma)\right]\right)\\
&+\mathcal{C}^{\mathrm{t}}_{n,m}\left(-\frac{\mu_0 Q^m_{n-\frac{1}{2}}(\cosh(\tau))\sin(m\varphi)\kappa(\tau,\sigma)}{aQ^m_{n-\frac{1}{2}}(\cosh(\tau_0))}\left[\frac{\sin(\sigma)}{2\sqrt{\kappa(\tau,\sigma)}}\cos(n\sigma)-\sqrt{\kappa(\tau,\sigma)}n\sin(n\sigma)\right]\right)\\
&+\mathcal{D}^{\mathrm{t}}_{n,m}\left(-\frac{\mu_0 Q^m_{n-\frac{1}{2}}(\cosh(\tau))\sin(m\varphi)\kappa(\tau,\sigma)}{aQ^m_{n-\frac{1}{2}}(\cosh(\tau_0))}\left[\frac{\sin(\sigma)}{2\sqrt{\kappa(\tau,\sigma)}}\sin(n\sigma)+\sqrt{\kappa(\tau,\sigma)}n\cos(n\sigma)\right]\right)
\end{aligned}
\tag{8.13}
$$

$$
\begin{aligned}
B_\varphi = \quad & \mathcal{E}^{\mathrm{t}}\tfrac{-\mu_0\kappa(\tau,\sigma)}{a\sinh(\tau)}\\
&+\sum_{m,n=0}^{\infty} \quad \mathcal{A}^{\mathrm{t}}_{n,m}\left(\frac{\mu_0\kappa(\tau,\sigma)^{3/2}}{aQ^m_{n-\frac{1}{2}}(\cosh(\tau_0))\sinh(\tau)}Q^m_{n-\frac{1}{2}}(\cosh(\tau))m\sin(m\varphi)\cos(n\sigma)\right)\\
&+\mathcal{B}^{\mathrm{t}}_{n,m}\left(\frac{\mu_0\kappa(\tau,\sigma)^{3/2}}{aQ^m_{n-\frac{1}{2}}(\cosh(\tau_0))\sinh(\tau)}Q^m_{n-\frac{1}{2}}(\cosh(\tau))m\sin(m\varphi)\sin(n\sigma)\right)\\
&+\mathcal{C}^{\mathrm{t}}_{n,m}\left(\frac{-\mu_0\kappa(\tau,\sigma)^{3/2}}{aQ^m_{n-\frac{1}{2}}(\cosh(\tau_0))\sinh(\tau)}Q^m_{n-\frac{1}{2}}(\cosh(\tau))m\cos(m\varphi)\cos(n\sigma)\right)\\
&+\mathcal{D}^{\mathrm{t}}_{n,m}\left(\frac{-\mu_0\kappa(\tau,\sigma)^{3/2}}{aQ^m_{n-\frac{1}{2}}(\cosh(\tau_0))\sinh(\tau)}Q^m_{n-\frac{1}{2}}(\cosh(\tau))m\cos(m\varphi)\sin(n\sigma)\right)
\end{aligned}
\tag{8.14}
$$

Rotationally symmetric case

$$
\begin{aligned}
B_\tau &= \sum_{n=0}^{\infty} \quad \mathcal{A}^{\mathrm{t}}_{n}\left(-\frac{\mu_0\cos(n\sigma)\kappa(\tau,\sigma)}{aQ^0_{n-\frac{1}{2}}(\cosh(\tau_0))}\left[\frac{\sinh(\tau)}{2\sqrt{\kappa(\tau,\sigma)}}Q^0_{n-\frac{1}{2}}(\cosh(\tau))+\sqrt{\kappa(\tau,\sigma)}\tfrac{\mathrm{d}}{\mathrm{d}\tau}Q^0_{n-\frac{1}{2}}(\cosh(\tau))\right]\right)\\
&\quad +\mathcal{B}^{\mathrm{t}}_{n}\left(-\frac{\mu_0\sin(n\sigma)\kappa(\tau,\sigma)}{aQ^0_{n-\frac{1}{2}}(\cosh(\tau_0))}\left[\frac{\sinh(\tau)}{2\sqrt{\kappa(\tau,\sigma)}}Q^0_{n-\frac{1}{2}}(\cosh(\tau))+\sqrt{\kappa(\tau,\sigma)}\tfrac{\mathrm{d}}{\mathrm{d}\tau}Q^0_{n-\frac{1}{2}}(\cosh(\tau))\right]\right)\\
B_\sigma &= \sum_{n=0}^{\infty} \quad \mathcal{A}^{\mathrm{t}}_{n}\left(-\frac{\mu_0 Q^0_{n-\frac{1}{2}}(\cosh(\tau))\kappa(\tau,\sigma)}{aQ^0_{n-\frac{1}{2}}(\cosh(\tau_0))}\left[\frac{\sin(\sigma)}{2\sqrt{\kappa(\tau,\sigma)}}\cos(n\sigma)-\sqrt{\kappa(\tau,\sigma)}n\sin(n\sigma)\right]\right)\\
&\quad +\mathcal{B}^{\mathrm{t}}_{n}\left(-\frac{\mu_0 Q^0_{n-\frac{1}{2}}(\cosh(\tau))\kappa(\tau,\sigma)}{aQ^0_{n-\frac{1}{2}}(\cosh(\tau_0))}\left[\frac{\sin(\sigma)}{2\sqrt{\kappa(\tau,\sigma)}}\sin(n\sigma)+\sqrt{\kappa(\tau,\sigma)}n\cos(n\sigma)\right]\right)\\
B_\varphi &= -\mathcal{E}^{\mathrm{t}}\ \tfrac{\mu_0\kappa(\tau,\sigma)}{a\sinh(\tau)}
\end{aligned}
\tag{8.15}
$$

To save on notation, we introduce the functions

$$f^{\mathcal{A}}_{n,m}, f^{\mathcal{B}}_{n,m}, f^{\mathcal{C}}_{n,m}, f^{\mathcal{D}}_{n,m}, \quad g^{\mathcal{A}}_{n,m}, g^{\mathcal{B}}_{n,m}, g^{\mathcal{C}}_{n,m}, g^{\mathcal{D}}_{n,m}, \quad h^{\mathcal{A}}_{n,m}, h^{\mathcal{B}}_{n,m}, h^{\mathcal{C}}_{n,m}, h^{\mathcal{D}}_{n,m}, h^{\mathcal{E}} \ : \ (\tau,\sigma,\varphi) \mapsto \mathbb{R} \tag{8.16}$$

which are defined by

$$f^{\mathcal{A}}_{n,m}(\tau,\sigma,\varphi) := -\frac{\mu_0 \cos(n\sigma)\cos(m\varphi)\kappa(\tau,\sigma)}{aQ^m_{n-\frac{1}{2}}(\cosh(\tau_0))}\left[\frac{\sinh(\tau)}{2\sqrt{\kappa(\tau,\sigma)}}Q^m_{n-\frac{1}{2}}(\cosh(\tau)) + \sqrt{\kappa(\tau,\sigma)}\frac{\mathrm{d}}{\mathrm{d}\tau}Q^m_{n-\frac{1}{2}}(\cosh(\tau))\right] \tag{8.17}$$

$$f^{\mathcal{B}}_{n,m}(\tau,\sigma,\varphi) := -\frac{\mu_0 \sin(n\sigma)\cos(m\varphi)\kappa(\tau,\sigma)}{aQ^m_{n-\frac{1}{2}}(\cosh(\tau_0))}\left[\frac{\sinh(\tau)}{2\sqrt{\kappa(\tau,\sigma)}}Q^m_{n-\frac{1}{2}}(\cosh(\tau)) + \sqrt{\kappa(\tau,\sigma)}\frac{\mathrm{d}}{\mathrm{d}\tau}Q^m_{n-\frac{1}{2}}(\cosh(\tau))\right] \tag{8.18}$$

$$f^{\mathcal{C}}_{n,m}(\tau,\sigma,\varphi) := -\frac{\mu_0 \cos(n\sigma)\sin(m\varphi)\kappa(\tau,\sigma)}{aQ^m_{n-\frac{1}{2}}(\cosh(\tau_0))}\left[\frac{\sinh(\tau)}{2\sqrt{\kappa(\tau,\sigma)}}Q^m_{n-\frac{1}{2}}(\cosh(\tau)) + \sqrt{\kappa(\tau,\sigma)}\frac{\mathrm{d}}{\mathrm{d}\tau}Q^m_{n-\frac{1}{2}}(\cosh(\tau))\right] \tag{8.19}$$

$$f^{\mathcal{D}}_{n,m}(\tau,\sigma,\varphi) := -\frac{\mu_0 \sin(n\sigma)\sin(m\varphi)\kappa(\tau,\sigma)}{aQ^m_{n-\frac{1}{2}}(\cosh(\tau_0))}\left[\frac{\sinh(\tau)}{2\sqrt{\kappa(\tau,\sigma)}}Q^m_{n-\frac{1}{2}}(\cosh(\tau)) + \sqrt{\kappa(\tau,\sigma)}\frac{\mathrm{d}}{\mathrm{d}\tau}Q^m_{n-\frac{1}{2}}(\cosh(\tau))\right] \tag{8.20}$$

$$g^{\mathcal{A}}_{n,m}(\tau,\sigma,\varphi) := -\frac{\mu_0 Q^m_{n-\frac{1}{2}}(\cosh(\tau))\cos(m\varphi)\kappa(\tau,\sigma)}{aQ^m_{n-\frac{1}{2}}(\cosh(\tau_0))}\left[\frac{\sin(\sigma)}{2\sqrt{\kappa(\tau,\sigma)}}\cos(n\sigma) - \sqrt{\kappa(\tau,\sigma)}n\sin(n\sigma)\right] \tag{8.21}$$

$$g^{\mathcal{B}}_{n,m}(\tau,\sigma,\varphi) := -\frac{\mu_0 Q^m_{n-\frac{1}{2}}(\cosh(\tau))\cos(m\varphi)\kappa(\tau,\sigma)}{aQ^m_{n-\frac{1}{2}}(\cosh(\tau_0))}\left[\frac{\sin(\sigma)}{2\sqrt{\kappa(\tau,\sigma)}}\sin(n\sigma) + \sqrt{\kappa(\tau,\sigma)}n\cos(n\sigma)\right] \tag{8.22}$$

$$g^{\mathcal{C}}_{n,m}(\tau,\sigma,\varphi) := -\frac{\mu_0 Q^m_{n-\frac{1}{2}}(\cosh(\tau))\sin(m\varphi)\kappa(\tau,\sigma)}{aQ^m_{n-\frac{1}{2}}(\cosh(\tau_0))}\left[\frac{\sin(\sigma)}{2\sqrt{\kappa(\tau,\sigma)}}\cos(n\sigma) - \sqrt{\kappa(\tau,\sigma)}n\sin(n\sigma)\right] \tag{8.23}$$

$$g^{\mathcal{D}}_{n,m}(\tau,\sigma,\varphi) := -\frac{\mu_0 Q^m_{n-\frac{1}{2}}(\cosh(\tau))\sin(m\varphi)\kappa(\tau,\sigma)}{aQ^m_{n-\frac{1}{2}}(\cosh(\tau_0))}\left[\frac{\sin(\sigma)}{2\sqrt{\kappa(\tau,\sigma)}}\sin(n\sigma) + \sqrt{\kappa(\tau,\sigma)}n\cos(n\sigma)\right] \tag{8.24}$$

$$h^{\mathcal{A}}_{n,m}(\tau,\sigma,\varphi) := \frac{\mu_0\kappa(\tau,\sigma)^{3/2}}{aQ^m_{n-\frac{1}{2}}(\cosh(\tau_0))\sinh(\tau)}Q^m_{n-\frac{1}{2}}(\cosh(\tau))m\sin(m\varphi)\cos(n\sigma) \tag{8.25}$$

$$h^{\mathcal{B}}_{n,m}(\tau,\sigma,\varphi) := \frac{\mu_0\kappa(\tau,\sigma)^{3/2}}{aQ^m_{n-\frac{1}{2}}(\cosh(\tau_0))\sinh(\tau)}Q^m_{n-\frac{1}{2}}(\cosh(\tau))m\sin(m\varphi)\sin(n\sigma) \tag{8.26}$$

$$h^{\mathcal{C}}_{n,m}(\tau,\sigma,\varphi) := \frac{\mu_0\kappa(\tau,\sigma)^{3/2}}{aQ^m_{n-\frac{1}{2}}(\cosh(\tau_0))\sinh(\tau)}Q^m_{n-\frac{1}{2}}(\cosh(\tau))m\cos(m\varphi)\cos(n\sigma) \tag{8.27}$$

$$h^{\mathcal{D}}_{n,m}(\tau,\sigma,\varphi) := \frac{\mu_0\kappa(\tau,\sigma)^{3/2}}{aQ^m_{n-\frac{1}{2}}(\cosh(\tau_0))\sinh(\tau)}Q^m_{n-\frac{1}{2}}(\cosh(\tau))m\cos(m\varphi)\sin(n\sigma) \tag{8.28}$$

$$h^{\mathcal{E}}(\tau,\sigma) := \frac{-\mu_0\kappa(\tau,\sigma)}{a\sinh(\tau)}. \tag{8.29}$$

Inserting these functions into the equations (8.12), (8.13) and (8.14) yields

$$\begin{aligned} B_\tau(\tau,\sigma,\varphi) = &\sum_{m,n=0}^{\infty}\left[\mathcal{A}^{\mathrm{t}}_{n,m}f^{\mathcal{A}}_{n,m}(\tau,\sigma,\varphi)+\mathcal{B}^{\mathrm{t}}_{n,m}f^{\mathcal{B}}_{n,m}(\tau,\sigma,\varphi)+\mathcal{C}^{\mathrm{t}}_{n,m}f^{\mathcal{C}}_{n,m}(\tau,\sigma,\varphi)+\mathcal{D}^{\mathrm{t}}_{n,m}f^{\mathcal{D}}_{n,m}(\tau,\sigma,\varphi)\right]\\ B_\sigma(\tau,\sigma,\varphi) = &\sum_{m,n=0}^{\infty}\left[\mathcal{A}^{\mathrm{t}}_{n,m}g^{\mathcal{A}}_{n,m}(\tau,\sigma,\varphi)+\mathcal{B}^{\mathrm{t}}_{n,m}g^{\mathcal{B}}_{n,m}(\tau,\sigma,\varphi)+\mathcal{C}^{\mathrm{t}}_{n,m}g^{\mathcal{C}}_{n,m}(\tau,\sigma,\varphi)+\mathcal{D}^{\mathrm{t}}_{n,m}g^{\mathcal{D}}_{n,m}(\tau,\sigma,\varphi)\right]\\ B_\varphi(\tau,\sigma,\varphi) = &\sum_{m,n=0}^{\infty}\left[\mathcal{A}^{\mathrm{t}}_{n,m}h^{\mathcal{A}}_{n,m}(\tau,\sigma,\varphi)+\mathcal{B}^{\mathrm{t}}_{n,m}h^{\mathcal{B}}_{n,m}(\tau,\sigma,\varphi)+\mathcal{C}^{\mathrm{t}}_{n,m}h^{\mathcal{C}}_{n,m}(\tau,\sigma,\varphi)+\mathcal{D}^{\mathrm{t}}_{n,m}h^{\mathcal{D}}_{n,m}(\tau,\sigma,\varphi)\right]\\ &+\mathcal{E}^{\mathrm{t}}h^{\mathcal{E}}(\tau,\sigma) \end{aligned} \tag{8.30}$$

Analogously in the rotationally symmetric case, the magnetic flux density components can be rewritten

$$\begin{aligned} B_\tau(\tau,\sigma) = &\sum_{n=0}^{\infty}\left[\mathcal{A}^{\mathrm{t}}_{n}f^{\mathcal{A}}_{n}(\tau,\sigma)+\mathcal{B}^{\mathrm{t}}_{n}f^{\mathcal{B}}_{n}(\tau,\sigma)\right]\\ B_\sigma(\tau,\sigma) = &\sum_{n=0}^{\infty}\left[\mathcal{A}^{\mathrm{t}}_{n}g^{\mathcal{A}}_{n}(\tau,\sigma)+\mathcal{B}^{\mathrm{t}}_{n}g^{\mathcal{B}}_{n}(\tau,\sigma)\right]\\ B_\varphi(\tau,\sigma) = &\mathcal{E}^{\mathrm{t}}h^{\mathcal{E}}(\tau,\sigma), \end{aligned} \tag{8.31}$$

where the functions $f^{\mathcal{A}}_n, f^{\mathcal{B}}_n,\ g^{\mathcal{A}}_n, g^{\mathcal{B}}_n:\ (\tau,\sigma)\mapsto\mathbb{R}$ are given by

$$f^{\mathcal{A}}_n \coloneqq f^{\mathcal{A}}_{n,0}, \qquad f^{\mathcal{B}}_n \coloneqq f^{\mathcal{B}}_{n,0}, \qquad g^{\mathcal{A}}_n \coloneqq g^{\mathcal{A}}_{n,0}, \qquad g^{\mathcal{B}}_n \coloneqq g^{\mathcal{B}}_{n,0}. \tag{8.32}$$

In Figure 8.1, the absolute values of the functions $f^{\mathcal{A}}_{n,m}, g^{\mathcal{B}}_{n,m}$ and $h^{\mathcal{C}}_{n,m}$ at the point $(1.2\tau_0,0,0)$ in the interior of D are plotted as functions of n and m. Thereby, the parameter τ_0 is chosen such that $\cosh(\tau_0)=\rho/R=\epsilon$, where ϵ is the eccentricity of the toroidal domain. We compare a toroidal domain D_1 with eccentricity $\epsilon=2$ and a domain D_2 with eccentricity $\epsilon=10$. It can be observed that the functions converge to zero for $n\to\infty$ and $m\to\infty$. The convergence concerning m is much slower for the functions on the toroidal domain D_2 with higher eccentricity. Consequently, the natural scaling, neglecting the toroidal harmonic coefficients, of the functions spanning the toroidal harmonic expansion of the magnetic flux density is such that functions with a low order and a low degree are weighted more, and this observation holds in particular in domains with low eccentricity.

8.3 Magnetic flux density on toroidal wedges

The toroidal harmonic expansion of magnetic flux density on a toroidal wedge $\widetilde{D}\subset D$ that covers the domain $\varphi\in[0,l]$ can be derived from the toroidal harmonic expansion of ϕ_{m} on $\widetilde{D}$ given in equation (6.5) using the equation $\mathbf{B}=-\mu_0\operatorname{grad}\phi_{\mathrm{m}}$, which yields

$$\begin{aligned} B_\tau = \sum_{m,n=0}^{\infty} \quad &\mathcal{A}^{\mathrm{t}}_{n,m}\left(-\frac{\mu_0\cos(n\sigma)\cos\left(\frac{2\pi m}{l}\varphi\right)\kappa(\tau,\sigma)}{a}\left[\frac{\sinh(\tau)}{2\sqrt{\kappa(\tau,\sigma)}}Q^{\frac{2\pi m}{l}}_{n-\frac12}(\cosh(\tau))+\sqrt{\kappa(\tau,\sigma)}\tfrac{\mathrm{d}}{\mathrm{d}\tau}Q^{\frac{2\pi m}{l}}_{n-\frac12}(\cosh(\tau))\right]\right)\\ &+\mathcal{B}^{\mathrm{t}}_{n,m}\left(-\frac{\mu_0\sin(n\sigma)\cos\left(\frac{2\pi m}{l}\varphi\right)\kappa(\tau,\sigma)}{a}\left[\frac{\sinh(\tau)}{2\sqrt{\kappa(\tau,\sigma)}}Q^{\frac{2\pi m}{l}}_{n-\frac12}(\cosh(\tau))+\sqrt{\kappa(\tau,\sigma)}\tfrac{\mathrm{d}}{\mathrm{d}\tau}Q^{\frac{2\pi m}{l}}_{n-\frac12}(\cosh(\tau))\right]\right)\\ &+\mathcal{C}^{\mathrm{t}}_{n,m}\left(-\frac{\mu_0\cos(n\sigma)\sin\left(\frac{2\pi m}{l}\varphi\right)\kappa(\tau,\sigma)}{a}\left[\frac{\sinh(\tau)}{2\sqrt{\kappa(\tau,\sigma)}}Q^{\frac{2\pi m}{l}}_{n-\frac12}(\cosh(\tau))+\sqrt{\kappa(\tau,\sigma)}\tfrac{\mathrm{d}}{\mathrm{d}\tau}Q^{\frac{2\pi m}{l}}_{n-\frac12}(\cosh(\tau))\right]\right)\\ &+\mathcal{D}^{\mathrm{t}}_{n,m}\left(-\frac{\mu_0\sin(n\sigma)\sin\left(\frac{2\pi m}{l}\varphi\right)\kappa(\tau,\sigma)}{a}\left[\frac{\sinh(\tau)}{2\sqrt{\kappa(\tau,\sigma)}}Q^{\frac{2\pi m}{l}}_{n-\frac12}(\cosh(\tau))+\sqrt{\kappa(\tau,\sigma)}\tfrac{\mathrm{d}}{\mathrm{d}\tau}Q^{\frac{2\pi m}{l}}_{n-\frac12}(\cosh(\tau))\right]\right) \end{aligned} \tag{8.33}$$

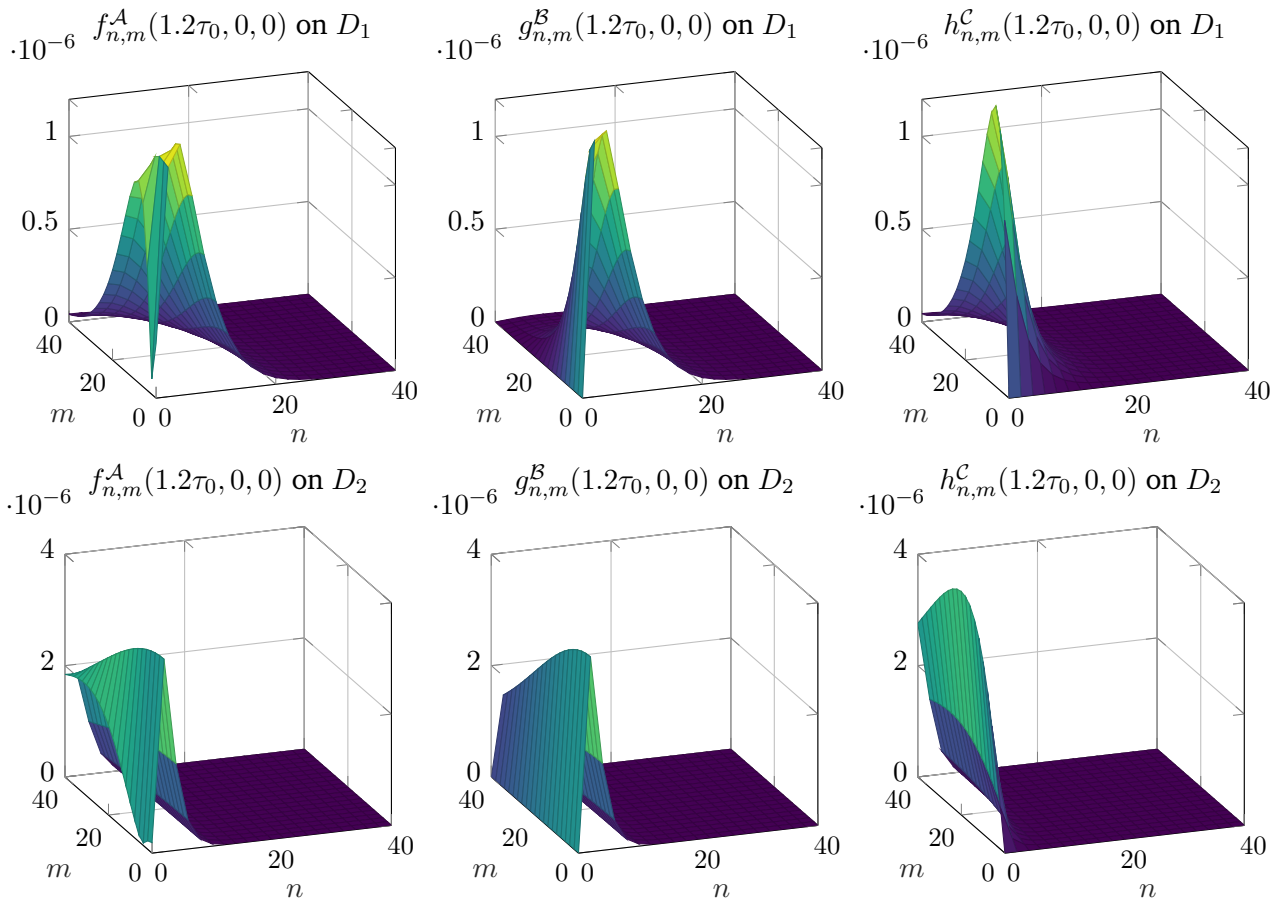

Figure 8.1: Absolute values of the functions $f^{\mathcal{A}}_{n,m}, g^{\mathcal{B}}_{n,m}$ and $h^{\mathcal{C}}_{n,m}$ which are part of the toroidal harmonic expansion of the magnetic flux density evaluated at the point $(1.2\tau_0, 0, 0)$ and plotted as functions of the degree n and the order m. Top row: Toroidal domain D_1 with eccentricity $\epsilon = 2$. Bottom row: Toroidal domain D_2 with eccentricity $\epsilon = 10$.

$$
\begin{aligned}
B_\sigma = \sum_{m,n=0}^{\infty} \quad & \mathcal{A}^{\mathrm{t}}_{n,m} \left(-\frac{\mu_0 Q^{\frac{2\pi m}{l}}_{n-\frac{1}{2}}(\cosh(\tau))\cos\left(\frac{2\pi m}{l}\varphi\right)\kappa(\tau,\sigma)}{a} \left[\frac{\sin(\sigma)}{2\sqrt{\kappa(\tau,\sigma)}}\cos(n\sigma) - \sqrt{\kappa(\tau,\sigma)}n\sin(n\sigma) \right] \right) \\
& + \mathcal{B}^{\mathrm{t}}_{n,m} \left(-\frac{\mu_0 Q^{\frac{2\pi m}{l}}_{n-\frac{1}{2}}(\cosh(\tau))\cos\left(\frac{2\pi m}{l}\varphi\right)\kappa(\tau,\sigma)}{a} \left[\frac{\sin(\sigma)}{2\sqrt{\kappa(\tau,\sigma)}}\sin(n\sigma) + \sqrt{\kappa(\tau,\sigma)}n\cos(n\sigma) \right] \right) \\
& + \mathcal{C}^{\mathrm{t}}_{n,m} \left(-\frac{\mu_0 Q^{\frac{2\pi m}{l}}_{n-\frac{1}{2}}(\cosh(\tau))\sin\left(\frac{2\pi m}{l}\varphi\right)\kappa(\tau,\sigma)}{a} \left[\frac{\sin(\sigma)}{2\sqrt{\kappa(\tau,\sigma)}}\cos(n\sigma) - \sqrt{\kappa(\tau,\sigma)}n\sin(n\sigma) \right] \right) \\
& + \mathcal{D}^{\mathrm{t}}_{n,m} \left(-\frac{\mu_0 Q^{\frac{2\pi m}{l}}_{n-\frac{1}{2}}(\cosh(\tau))\sin\left(\frac{2\pi m}{l}\varphi\right)\kappa(\tau,\sigma)}{a} \left[\frac{\sin(\sigma)}{2\sqrt{\kappa(\tau,\sigma)}}\sin(n\sigma) + \sqrt{\kappa(\tau,\sigma)}n\cos(n\sigma) \right] \right)
\end{aligned}
\tag{8.34}
$$

$$
\begin{aligned}
B_\varphi = \quad & \mathcal{E}^{\mathrm{t}} \tfrac{-\mu_0\kappa(\tau,\sigma)}{a\sinh(\tau)} \\
& + \sum_{m,n=0}^{\infty} \quad \mathcal{A}^{\mathrm{t}}_{n,m} \left(\tfrac{\mu_0\kappa(\tau,\sigma)^{3/2}}{a\sinh(\tau)} Q^{\frac{2\pi m}{l}}_{n-\frac{1}{2}}(\cosh(\tau)) \tfrac{2\pi m}{l} \sin\left(\tfrac{2\pi m}{l}\varphi\right)\cos(n\sigma) \right) \\
& \quad + \mathcal{B}^{\mathrm{t}}_{n,m} \left(\tfrac{\mu_0\kappa(\tau,\sigma)^{3/2}}{a\sinh(\tau)} Q^{\frac{2\pi m}{l}}_{n-\frac{1}{2}}(\cosh(\tau)) \tfrac{2\pi m}{l} \sin\left(\tfrac{2\pi m}{l}\varphi\right)\sin(n\sigma) \right) \\
& \quad + \mathcal{C}^{\mathrm{t}}_{n,m} \left(\tfrac{-\mu_0\kappa(\tau,\sigma)^{3/2}}{a\sinh(\tau)} Q^{\frac{2\pi m}{l}}_{n-\frac{1}{2}}(\cosh(\tau)) \tfrac{2\pi m}{l} \cos\left(\tfrac{2\pi m}{l}\varphi\right)\cos(n\sigma) \right) \\
& \quad + \mathcal{D}^{\mathrm{t}}_{n,m} \left(\tfrac{-\mu_0\kappa(\tau,\sigma)^{3/2}}{a\sinh(\tau)} Q^{\frac{2\pi m}{l}}_{n-\frac{1}{2}}(\cosh(\tau)) \tfrac{2\pi m}{l} \cos\left(\tfrac{2\pi m}{l}\varphi\right)\sin(n\sigma) \right).
\end{aligned}
\tag{8.35}
$$

Averaging these components for $\varphi \in [0, l]$ yields the following formulas

$$
\begin{aligned}
\int_0^l B_\tau \,\mathrm{d}\varphi \quad = \quad \sum_{n=0}^{\infty} \quad & \mathcal{A}^{\mathrm{t}}_{n,0} \left(-\tfrac{\mu_0 l\cos(n\sigma)\kappa(\tau,\sigma)}{a} \left[\tfrac{\sinh(\tau)}{2\sqrt{\kappa(\tau,\sigma)}} Q^0_{n-\frac{1}{2}}(\cosh(\tau)) + \sqrt{\kappa(\tau,\sigma)}\tfrac{\mathrm{d}}{\mathrm{d}\tau} Q^0_{n-\frac{1}{2}}(\cosh(\tau)) \right] \right) \\
& + \mathcal{B}^{\mathrm{t}}_{n,0} \left(-\tfrac{\mu_0 l\sin(n\sigma)\kappa(\tau,\sigma)}{a} \left[\tfrac{\sinh(\tau)}{2\sqrt{\kappa(\tau,\sigma)}} Q^0_{n-\frac{1}{2}}(\cosh(\tau)) + \sqrt{\kappa(\tau,\sigma)}\tfrac{\mathrm{d}}{\mathrm{d}\tau} Q^0_{n-\frac{1}{2}}(\cosh(\tau)) \right] \right) \\
\int_0^l B_\sigma \,\mathrm{d}\varphi \quad = \quad \sum_{n=0}^{\infty} \quad & \mathcal{A}^{\mathrm{t}}_{n,0} \left(-\tfrac{\mu_0 l Q^0_{n-\frac{1}{2}}(\cosh(\tau))\kappa(\tau,\sigma)}{a} \left[\tfrac{\sin(\sigma)}{2\sqrt{\kappa(\tau,\sigma)}}\cos(n\sigma) - \sqrt{\kappa(\tau,\sigma)}n\sin(n\sigma) \right] \right) \\
& + \mathcal{B}^{\mathrm{t}}_{n,0} \left(-\tfrac{\mu_0 l Q^0_{n-\frac{1}{2}}(\cosh(\tau))\kappa(\tau,\sigma)}{a} \left[\tfrac{\sin(\sigma)}{2\sqrt{\kappa(\tau,\sigma)}}\sin(n\sigma) + \sqrt{\kappa(\tau,\sigma)}n\cos(n\sigma) \right] \right) \\
\int_0^l B_\varphi \,\mathrm{d}\varphi \quad = \quad & -\mathcal{E}^{\mathrm{t}} \quad \tfrac{\mu_0 l\kappa(\tau,\sigma)}{a\sinh(\tau)}.
\end{aligned}
\tag{8.36}
$$

Thereby, we use that $\int_0^l \sin\left(\frac{2\pi m}{l}\varphi\right) \,\mathrm{d}\varphi = 0$ for all $m \geq 0$ and $\int_0^l \cos\left(\frac{2\pi m}{l}\varphi\right) \,\mathrm{d}\varphi = l$ iff $m = 0$, and the fact that $\mathcal{C}^{\mathrm{t}}_{n,0}, \mathcal{D}^{\mathrm{t}}_{n,0} = 0$ for all $n \geq 0$.

The structure of these equations equals the structure of the magnetic flux density components in the rotationally symmetric case (8.15). Indeed, the average magnetic scalar potential $\int_0^l \phi_{\mathrm{m}} \mathrm{d}\varphi$ and the magnetic scalar potential in the rotationally symmetric case satisfy the same differential equation (2.100), as shown in the introduction of Chapter 6.

List of acronyms

ARMCO American Rolling Milling Company

BEM boundary element method

CCT canted cosine theta

CERN European Organization for Nuclear Research

FASER Forward Search Experiment

FEM finite element method

GUM Guide to the Expression of Uncertainty in Measurement

HL-LHC High Luminosity Large Hadron Collider

ITER International Thermonuclear Experimental Reactor

KLE Karhunen-Loève expansion

LHC Large Hadron Collider

PM permanent magnet

R&D Research and Development

ROXIE Routine for the Optimization of magnet X - sections, Inverse field calculation and coil End design

SESAME Synchrotron-Light for Experimental Science and Applications in the Middle East

Bibliography

[1] A. A.-E. Abdallh, P. Sergeant, and L. Dupré, *A non-destructive methodology for estimating the magnetic material properties of an asynchronous motor*, *IEEE Transactions on Magnetics*, vol. 48, no. 4, pp. 1621–1624, 2012. DOI: 10.1109/TMAG.2011.2173171.

[2] M. Abramowitz and I. A. Stegun, *Handbook of mathematical functions with formulas, graphs, and mathematical tables*. Nat. Bureau of Standards, 1964, vol. 55.

[3] H. Abreu *et al.*, *The FASER detector*, *arXiv preprint arXiv:2207.11427*, 2022.

[4] R. J. Adler and J. E. Taylor, *Random fields and geometry*. Springer Science & Business Media, 2009. DOI: 10.1007/978-0-387-48116-6.

[5] AK Steel, *ARMCO product description*, https://www.aksteel.eu/products/armco-pure-iron/, Accessed: 02.08.2002.

[6] R. Albanese and G. Rubinacci, *Integral formulation for 3d eddy-current computation using edge elements*, *IEE Proceedings A (Physical Science, Measurement and Instrumentation, Management and Education, Reviews)*, vol. 135, no. 7, pp. 457–462, 1988. DOI: 10.1049/ip-a-1.1988.0072.

[7] A. Alshareef, *Investigation of matrix properties for the determination of toroidal harmonics*, Bachelor thesis, TU Darmstadt, 2023.

[8] M. Amodeo, P. Arpaia, M. Buzio, V. Di Capua, and F. Donnarumma, *Hysteresis modeling in iron-dominated magnets based on a multi-layered narx neural network approach*, *International Journal of Neural Systems*, vol. 31, no. 09, p. 2 150 033, 2021. DOI: 10.1142/S0129065721500337.

[9] L. Arbenz, O. Chadebec, C. Espanet, Y. Rtimi, and G. Cauffet, *Characterization of permanent magnet magnetization*, *IEEE Transactions on Magnetics*, vol. 53, no. 11, pp. 1–4, 2017. DOI: 10.1109/TMAG.2017.2692391.

[10] P. Arpaia, M. Buzio, L. Fiscarelli, G. Montenero, and L. Walckiers, *High-performance permeability measurements: A case study at CERN*, in *2010 IEEE Instrumentation & Measurement Technology Conference Proceedings*, IEEE, 2010, pp. 58–61. DOI: 10.1109/IMTC.2010.5488003.

[11] L. Artsimovich, *Tokamak devices*, *Nuclear Fusion*, vol. 12, no. 2, p. 215, 1972. DOI: 10.1088/0029-5515/12/2/012.

[12] J. M. Bardsley, *Computational Uncertainty Quantification for Inverse Problems: An Introduction to Singular Integrals*. SIAM, 2018, ISBN: 9781611975376.

[13] S. Bartels, *Numerical approximation of partial differential equations*. Springer, 2016, vol. 64. DOI: 10.1007/978-3-319-32354-1.

[14] C. Beattie, *Galerkin eigenvector approximations*, *Mathematics of computation*, vol. 69, no. 232, pp. 1409–1434, 2000.

[15] G. Bedrosian, *A new method for coupling finite element field solutions with external circuits and kinematics*, *IEEE Transactions on Magnetics*, vol. 29, no. 2, pp. 1664–1668, 1993. DOI: 10.1109/20.250726.

[16] BIPM *et al.*, *Evaluation of measurement data — Supplement 1 to the "Guide to the expression of uncertainty in measurement" — Propagation of distributions using a Monte Carlo method*, Joint Committee for Guides in Metrology, JCGM 101:2008, 2008.

[17] O. Biro, *Edge element formulations of eddy current problems*, *Computer methods in applied mechanics and engineering*, vol. 169, no. 3-4, pp. 391–405, 1999. DOI: 10.1016/S0045-7825(98)00165-0.

[18] C. M. Bishop, *Pattern recognition and machine learning*. Springer, 2006, ISBN: 978-0-387-31073-2.

[19] G. T. Bodwin, H. S. Chung, and J. Repond, *Implementation of maxwell's equations in the reconstruction of the magnetic field in the g- 2 storage ring*, *Journal of Instrumentation*, vol. 14, no. 07, 2019. DOI: 10.1088/1748-0221/14/07/P07002.

[20] Z. Bontinck, *Simulation and robust optimization for electric devices with uncertainties*, Ph.D. dissertation, TU Darmstadt, 2018.

[21] A. Bossavit, *Computational electromagnetism: variational formulations, complementarity, edge elements*. Academic Press, 1998. DOI: 10.1016/B978-0-12-118710-1.X5000-4.

[22] L. Bottura, E. Felcini, G. De Rijk, and B. Dutoit, *GaToroid: A novel toroidal gantry for hadron therapy*, *Nuclear Instruments and Methods in Physics Research Section A: Accelerators, Spectrometers, Detectors and Associated Equipment*, vol. 983, p. 164 588, 2020. DOI: 10.1016/j.nima.2020.164588.

[23] D. Braess, *Finite Elemente: Theorie, schnelle Löser und Anwendungen in der Elastizitätstheorie*. Springer-Verlag, 2007. DOI: 10.1007/978-3-540-72450-6.

[24] J. Brauer, *Simple equations for the magnetization and reluctivity curves of steel*, *IEEE Transactions on Magnetics*, vol. 11, no. 1, pp. 81–81, 1975. DOI: 10.1109/TMAG.1975.1058555.

[25] L. Brouwer, S. Caspi, D. Robin, and W. Wan, *3D toroidal field multipoles for curved accelerator magnets*, in *Proceedings of PAC2013, Pasadena, CA (United States)*, 2021.

[26] F. Bruckner *et al.*, *Solving large-scale inverse magnetostatic problems using the adjoint method*, *Scientific reports*, vol. 7, no. 1, p. 40 816, 2017. DOI: 10.1038/srep40816.

[27] O. S. Brüning and S. D. Fartoukh, *Field quality specification for the LHC main dipole magnets*, Tech. Rep., 2001.

[28] D. Calvetti and E. Somersalo, *Bayesian Scientific Computing*. Springer Nature, 2023, vol. 215. DOI: 10.1007/978-3-031-23824-6.

[29] D. Calvetti and E. Somersalo, *Inverse problems: From regularization to bayesian inference*, *Wiley Interdisciplinary Reviews: Computational Statistics*, vol. 10, no. 3, e1427, 2018. DOI: 10.1002/wics.1427.

[30] CERN, *ELENA project*, https://espace.cern.ch/elena-project/SitePages/Home.aspx, Accessed: 05.05.2024.

[31] CERN, *Magnetic measurements*, https://te-msc-mm.web.cern.ch/mission, Accessed: 13.09.2023.

[32] CERN, *Our mission*, https://home.cern/about/who-we-are/our-mission, Accessed: 12.09.2023.

[33] M. Cessenat, *Mathematical methods in electromagnetism: linear theory and applications*. World Scientific, 1996.

[34] G. Chavin-Collin *et al.*, *A priori Bayesian Information for Inverse Resolution of Integral Formulation applied to Thin Regions Magnetization Identification*, https://hal.science/hal-03051630, 2020.

[35] G. Chavin-Collin *et al.*, *An Inverse Integral Formulation for Steel Shell Magnetization Identification*, https://hal.science/hal-02278819, 2019.

[36] R. K. Cooper, V. Neil, and J. Beal, *A method for the design of air-core magnets in toroidal geometry*, *Part. Accel.*, vol. 2, pp. 325–334, 1971.

[37] S. L. Cotter, G. O. Roberts, A. M. Stuart, and D. White, *MCMC methods for functions: Modifying old algorithms to make them faster*, *Statistical Science*, vol. 28, no. 3, pp. 424–446, 2013. DOI: 10.1214/13-STS421.

[38] B. Cranganu-Cretu, G. Preda, O. Mihalache, Z. Chen, and K. Miya, *BH curve reconstruction from MFL signals based on genetic algorithms*, *International Journal of Applied Electromagnetics and Mechanics*, vol. 15, no. 1-4, pp. 283–289, 2002. DOI: 10.3233/JAE-2002-466.

[39] E. Creusé, P. Dular, and S. Nicaise, *About the gauge conditions arising in finite element magnetostatic problems*, *Computers & Mathematics with Applications*, vol. 77, no. 6, pp. 1563–1582, 2019. DOI: 10.1016/j.camwa.2018.06.030.

[40] W. D. D'Haeseleer, W. N. Hitchon, J. D. Callen, and J. L. Shohet, *Flux coordinates and magnetic field structure: a guide to a fundamental tool of plasma theory*. Springer Science & Business Media, 2012.

[41] K. R. Das and A. Imon, *A brief review of tests for normality*, *American Journal of Theoretical and Applied Statistics*, vol. 5, no. 1, pp. 5–12, 2016. DOI: 10.11648/j.ajtas.20160501.12.

[42] Dassault Systèmes, *Opera simulation software*, https://www.3ds.com/de/produkte-und-services/simulia/produkte/opera/, Accessed: 16.10.2023.

[43] P. Deuflhard, *Newton methods for nonlinear problems: affine invariance and adaptive algorithms*. Springer Science & Business Media, 2011, vol. 35. DOI: 10.1007/978-3-642-23899-4.

[44] Y. Dodge, *The concise encyclopedia of statistics*. Springer Science & Business Media, 2008. DOI: 10.1007/978-0-387-32833-1.

[45] O. Dunkel, *Result file of magnetic measurements of PM blocks for FASER project (1st batch)*, https://edms.cern.ch/document/2445634/1, Accessed: 12.06.2024.

[46] O. Dunkel, *Result file of magnetic measurements of PM blocks for FASER project (2nd batch)*, https://edms.cern.ch/document/2445649/1, Accessed: 12.06.2024.

[47] O. Dunkel, *Result file of magnetic measurements of PM blocks for FASER project (3rd batch)*, https://edms.cern.ch/document/2445652/1, Accessed: 12.06.2024.

[48] O. Dunkel, M. Liebsch, and M. Pentella, *Magnetic measurements of the 1st short FASER permanent dipole magnet (PXMDMCAHAC-CR000001)*, https://edms.cern.ch/document/2401280/1, Accessed: 11.06.2024.

[49] O. Dunkel, M. Pentella, and M. Liebsch, *Magnetic measurement results of the 1st short (1 m) FASER permanent dipole magnet (out of 2 short and 1 long)*, Tech. Rep., 2020.

[50] H. W. Engl, M. Hanke, and A. Neubauer, *Regularization of inverse problems*. Springer Science & Business Media, 1996, vol. 375, ISBN: 978-0-7923-6140-4.

[51] FASER collaboration, *Faser*, https://faser.web.cern.ch/, Accessed: 21.03.2024.

[52] L. Fleig, M. Liebsch, S. Russenschuck, and S. Schöps, *Combination of measurement data and domain knowledge for simulation of Halbach arrays with Bayesian inference*, *IEEE Transactions on Magnetics*, 2023. DOI: 10.1109/TMAG.2023.3301976.

[53] L. Fleig, M. Liebsch, S. Russenschuck, and S. Schöps, *Identification of B(H) curves using the Karhunen Loève expansion*, *IEEE Access*, pp. 1–1, 2024. DOI: 10.1109/ACCESS.2024.3393348.

[54] L. Fleig, M. Liebsch, E. Schnaubelt, S. Russenschuck, and S. Schöps, *Simulation of Halbach arrays in GetDP*, https://doi.org/10.5281/zenodo.8187209.

[55] A. Formisano, *Regularization of inverse magnetostatic problems: Possibilities and pitfalls*, *COMPEL-The international journal for computation and mathematics in electrical and electronic engineering*, vol. 24, no. 3, pp. 740–752, 2005. DOI: 10.1108/03321640510598102.

[56] P. Frauenfelder, C. Schwab, and R. A. Todor, *Finite elements for elliptic problems with stochastic coefficients*, *Computer methods in applied mechanics and engineering*, vol. 194, no. 2-5, pp. 205–228, 2005. DOI: 10.1016/j.cma.2004.04.008.

[57] F. N. Fritsch and R. E. Carlson, *Monotone piecewise cubic interpolation*, *SIAM Journal on Numerical Analysis*, vol. 17, no. 2, pp. 238–246, 1980. DOI: 10.1137/0717021.

[58] L. Gambini, M. Breschi, E. Felcini, A. Cristofolini, and L. Bottura, *An algorithm for toroidal field harmonics computation in arbitrary magnetic configurations*, *IEEE Transactions on Applied Superconductivity*, vol. 30, no. 4, pp. 1–5, 2020. DOI: 10.1109/TASC.2020.2970907.

[59] W. Gander, M. J. Gander, and F. Kwok, *Scientific computing-An introduction using Maple and MATLAB*. Springer Science & Business, 2014, vol. 11. DOI: 10.1007/978-3-319-04325-8.

[60] C. Geuzaine, *GetDP: A general finite-element solver for the de Rham complex*, *PAMM*, vol. 7, no. 1, pp. 1 010 603–1 010 604, 2007. DOI: 10.1002/pamm.200700750.

[61] C. Geuzaine and J.-F. Remacle, *Gmsh: A 3-D finite element mesh generator with built-in pre- and post-processing facilities*, *International Journal for Numerical Methods in Engineering*, vol. 79, 2009. DOI: 10.1002/nme.2579.

[62] O. Ghattas and K. Willcox, *Learning physics-based models from data: Perspectives from inverse problems and model reduction*, *Acta Numerica*, vol. 30, pp. 445–554, 2021. DOI: 10.1017/S0962492921000064.

[63] G. Giambartolomei, *The Karhunen-Loeve theorem*, diploma thesis, Universita di Bologna, 2015.

[64] I. S. Gradshteyn and I. M. Ryzhik, *Table of integrals, series, and products*. Academic press, 2007.

[65] D. J. Griffiths, *Introduction to electrodynamics*. Prentice Hall, 1999.

[66] K. Halbach, *Design of permanent multipole magnets with oriented rare earth cobalt material*, *Nuclear instruments and methods*, vol. 169, no. 1, pp. 1–10, 1980. DOI: 10.1016/0029-554X(80)90094-4.

[67] J. Harlim, *Data-Driven Computational Methods: Parameter and Operator Estimations*. Cambridge University Press, 2018. DOI: 10.1017/9781108562461.

[68] T. Hastie, R. Tibshirani, J. H. Friedman, and J. H. Friedman, *The elements of statistical learning: data mining, inference, and prediction*. Springer, 2009, vol. 2. DOI: 10.1007/978-0-387-84858-7.

[69] A. Haziot *et al.*, *Curved-canted-cosine-theta (CCCT) dipole prototype development at CERN*, *IEEE Transactions on Applied Superconductivity*, vol. 34, no. 5, pp. 1–8, 2024. DOI: 10.1109/TASC.2024.3353149.

[70] B. Heise, *Analysis of a fully discrete finite element method for a nonlinear magnetic field problem*, *SIAM Journal on Numerical Analysis*, vol. 31, no. 3, pp. 745–759, 1994. DOI: 10.1137/0731040.

[71] K. Henrichsen, *Permeameter*, Tech. Rep., 1965.

[72] T. Hülsmann, A. Bartel, S. Schöps, and H. De Gersem, *Extended brauer model for ferromagnetic materials: Analysis and computation*, *COMPEL: The International Journal for Computation and Mathematics in Electrical and Electronic Engineering*, vol. 33, no. 4, pp. 1251–1263, 2014. DOI: 10.1108/COMPEL-11-2012-0359.

[73] D. Ioan, G. Ciuprina, W. H. Schilders, P. Benner, *et al.*, *Complexity reduction of electromagnetic systems*, *Model order reduction, applications*, pp. 145–200, 2021. DOI: 10.1515/9783110499001-005.

[74] I. G. Ion *et al.*, *Local field reconstruction from rotating coil measurements in particle accelerator magnets*, *Nuclear Instruments and Methods in Physics Research Section A: Accelerators, Spectrometers, Detectors and Associated Equipment*, vol. 1011, p. 165 580, 2021. DOI: 10.1016/j.nima.2021.165580.

[75] ITER, *Fusion energy*, https://www.iter.org/, Accessed: 05.05.2024.

[76] J. D. Jackson, *Classical electrodynamics*. Wiley & Sons, 1998.

[77] R. Jankoski, *Stochastic modeling of magnetic properties by using random fields*, Ph.D. dissertation, TU Darmstadt, 2018.

[78] J. Kaipio and E. Somersalo, *Statistical and computational inverse problems*. Springer Science & Business Media, 2006, vol. 160. DOI: 10.1007/b138659.

[79] B. Kaltenbacher, M. Kaltenbacher, and S. Reitzinger, *Identification of nonlinear B–H curves based on magnetic field computations and multigrid methods for ill-posed problems*, *European Journal of Applied Mathematics*, vol. 14, no. 1, pp. 15–38, 2003. DOI: 10.1017/S0956792502005089.

[80] J. B. Keller, *Inverse problems*, *Amer. Math. Monthly*, vol. 83, pp. 107–118, 1976. DOI: 10.2307/2976988.

[81] J. Kennedy and R. Eberhart, *Particle swarm optimization*, in *Proceedings of ICNN'95-international conference on neural networks*, IEEE, vol. 4, 1995, pp. 1942–1948. DOI: 10.1109/ICNN.1995.488968.

[82] G. Kirby *et al.*, *Superconducting curved canted–cosine–theta (CCT) for the HIE-ISOLDE recoil separator ring at CERN*, *IEEE Transactions on Applied Superconductivity*, vol. 32, no. 6, pp. 1–5, 2022. DOI: 10.1109/TASC.2022.3158332.

[83] A. Kirsch, *An introduction to the mathematical theory of inverse problems*. Springer, 2011, vol. 120. DOI: 10.1007/978-1-4419-8474-6.

[84] A. Kovacs *et al.*, *Magnetostatics and micromagnetics with physics informed neural networks*, *Journal of Magnetism and Magnetic Materials*, vol. 548, p. 168 951, 2022. DOI: 10.1016/j.jmmm.2021.168951.

[85] M. A. Krasnosel'skii, G. M. Vainikko, P. P. Zabreyko, Y. B. Ruticki, and V. Y. Stet'senko, *Approximate solution of operator equations*. Springer Dordrecht, 2012. DOI: 10.1007/978-94-010-2715-1.

[86] S. Kurz *et al.*, *Hybrid modeling: Towards the next level of scientific computing in engineering*, *Journal of Mathematics in Industry*, vol. 12, no. 1, pp. 1–12, 2022. DOI: 10.1186/s13362-022-00123-0.

[87] C. Lanczos, *Linear differential operators*. Van Nostrand, 1961. DOI: 10.1137/1.9781611971187.

[88] O. Le Maître and O. M. Knio, *Spectral methods for uncertainty quantification: with applications to computational fluid dynamics*. Springer Science & Business Media, 2010. DOI: 10.1007/978-90-481-3520-2.

[89] J. Li, K. Wang, K. Wang, X. Yan, and K. Zhu, *Evaluation of field quality for curved magnets*, *IEEE Transactions on Applied Superconductivity*, 2024.

[90] M. Liebsch, *Inference of boundary data from magnetic measurements of accelerator magnets*, Ph.D. dissertation, TU Darmstadt, 2022.

[91] M. Liebsch, S. Russenschuck, and J. Kaeske, *An induction-coil magnetometer for mid-plane measurements in spectrometer magnets*, *Sensors and Actuators A: Physical*, vol. 355, p. 114 334, 2023. DOI: 10.1016/j.sna.2023.114334.

[92] M. Liebsch, S. Russenschuck, and S. Kurz, *BEM-based magnetic field reconstruction by ensemble Kálmán filtering*, *Computational Methods in Applied Mathematics*, vol. 23, no. 2, pp. 405–424, 2023. DOI: 10.1515/cmam-2022-0121.

[93] Little Beast Engineering, *The Rat GUI*, https://rat-gui.ch/, Accessed: 09.11.2023.

[94] M. Loève, *Elementary probability theory*. Springer, 1977. DOI: 10.1007/978-1-4684-9464-8.

[95] MathWorks, *Particle swarm optimization*, https://ch.mathworks.com/help/gads/particleswarm.html, Accessed: 05.04.2024.

[96] G. Mendes and Â. Ferreira, *Extending the multiphysics modelling of electric machines in a digital twin concept*, in *2021 11th IEEE International Conference on Intelligent Data Acquisition and Advanced Computing Systems: Technology and Applications (IDAACS)*, IEEE, vol. 2, 2021, pp. 689–693. DOI: 10.1109/IDAACS53288.2021.9660964.

[97] D. Meyer and R. Flasck, *A new configuration for a dipole magnet for use in high energy physics applications*, *Nuclear Instruments and Methods*, vol. 80, no. 2, pp. 339–341, 1970. DOI: 10.1016/0029-554X(70)90784-6.

[98] A. A. Mohammadi, A.-C. Pop, and J. Gyselinck, *An approach for the BH curve identification of magnetic core of synchronous reluctance machines*, *IEEE Transactions on Magnetics*, vol. 57, no. 1, pp. 1–8, 2020. DOI: 10.1109/TMAG.2020.3031465.

[99] P. Monk, *Finite element methods for Maxwell's equations*. Oxford University Press, 2003.

[100] P. Moon and D. E. Spencer, *Field theory handbook: including coordinate systems, differential equations and their solutions*. Springer, 1988.

[101] W. L. Oberkampf, S. M. DeLand, B. M. Rutherford, K. V. Diegert, and K. F. Alvin, *Error and uncertainty in modeling and simulation*, *Reliability Engineering & System Safety*, vol. 75, no. 3, pp. 333–357, 2002. DOI: 10.1016/S0951-8320(01)00120-X.

[102] P. Offermann and K. Hameyer, *Stochastic models for the evaluation of magnetisation faults*, *COMPEL: The International Journal for Computation and Mathematics in Electrical and Electronic Engineering*, vol. 33, no. 1/2, pp. 245–253, 2013. DOI: 10.1108/COMPEL-10-2012-0210.

[103] C. Pechstein, *Multigrid-newton-methods for nonlinear magnetostatic problems*, diploma thesis, Johannes Kepler Universität Linz, 2004.

[104] C. Pechstein and B. Jüttler, *Monotonicity-preserving interproximation of B–H-curves*, *Journal of Computational and Applied Mathematics*, vol. 196, no. 1, pp. 45–57, 2006. DOI: 10.1016/j.cam.2005.08.021.

[105] J.-P. Penot, *Calculus without derivatives*. Springer, 2013, vol. 266. DOI: 10.1007/978-1-4614-4538-8.

[106] M. Pentella, *Characterization of magnetic materials at extreme ranges of field, temperature, and permeability*, Ph.D. dissertation, Politecnico di Torino, 2022.

[107] R. Plato, *Numerische Mathematik kompakt: Grundlagenwissen für Studium und Praxis*. Vieweg, 2006. DOI: 10.1007/978-3-8348-9059-7.

[108] V. Pricop, *Hysteresis effects in the core of particle accelerator magnets*, Ph.D. dissertation, Universitatea Transilvania din Brașov, 2016.

[109] R. Rai and C. K. Sahu, *Driven by data or derived through physics? A review of hybrid physics guided machine learning techniques with cyber-physical system (CPS) focus*, *IEEE Access*, vol. 8, pp. 71 050–71 073, 2020. DOI: 10.1109/ACCESS.2020.2987324.

[110] R. Ramarotafika, A. Benabou, and S. Clenet, *Stochastic modeling of soft magnetic properties of electrical steels: Application to stators of electrical machines*, *IEEE Transactions on Magnetics*, vol. 48, no. 10, pp. 2573–2584, 2012. DOI: 10.1109/TMAG.2012.2201734.

[111] R. Rannacher, *Numerik 2: Numerik partieller Differentialgleichungen* (Lecture Notes). Heidelberg University Publishing, 2017. DOI: 10.17885/heiup.281.370.

[112] F. Rapetti, A. Alonso Rodriguez, and E. De Los Santos, *On the tree gauge in magnetostatics*, *J*, vol. 5, no. 1, pp. 52–63, 2022. DOI: 10.3390/j5010004.

[113] A. Rasheed, O. San, and T. Kvamsdal, *Digital twin: Values, challenges and enablers from a modeling perspective*, *IEEE Access*, vol. 8, pp. 21 980–22 012, 2020. DOI: 10.1109/ACCESS.2020.2970143.

[114] S. Reitzinger, B. Kaltenbacher, and M. Kaltenbacher, *A note on the approximation of B-H curves for nonlinear magnetic field computations*, *Johannes Kepler Universität, Linz*, 2003.

[115] V. Remondino, O. Dunkel, and D. Giloteaux, *Design, calibration and qualification of the CERN Helmholtz coils system*, Tech. Rep., 2017.

[116] F. Rohlf and R. Sokal, *Statistical Tables* (Collection Of Tables To Accompany Biometry). W. H. Freeman, 1995, ISBN: 9780716724124.

[117] U. Römer, *Numerical approximation of the magnetoquasistatic model with uncertainties and its application to magnet design*, Ph.D. dissertation, TU Darmstadt, 2015.

[118] U. Römer, S. Schöps, and T. Weiland, *Stochastic modeling and regularity of the nonlinear elliptic curl–curl equation*, *SIAM/ASA Journal on Uncertainty Quantification*, vol. 4, no. 1, pp. 952–979, 2016. DOI: 10.1137/15M1026535.

[119] S. Russenschuck, *Field computation for accelerator magnets: analytical and numerical methods for electromagnetic design and optimization*. John Wiley & Sons, 2011. DOI: 10.1002/9783527635467.

[120] S. Russenschuck, *Field simulation for accelerator magnets*. John Wiley & Sons, 2024.

[121] S. Russenschuck, *ROXIE: Routine for the optimization of magnet x-sections, inverse field computation and coil end design*, in *1st International ROXIE Users Meeting and Workshop, Geneva, Switzerland*, 1998. DOI: 10.5170/CERN-1999-001.

[122] S. Russenschuck, G. Caiafa, L. Fiscarelli, M. Liebsch, C. Petrone, and P. Rogacki, *Challenges in extracting pseudo-multipoles from magnetic measurements*, *International Journal of Modern Physics A*, vol. 34, no. 36, p. 1 942 022, 2019. DOI: 10.1142/S0217751X19420223.

[123] C. Schwab and R. A. Todor, *Karhunen–Loève approximation of random fields by generalized fast multipole methods*, *Journal of Computational Physics*, vol. 217, no. 1, pp. 100–122, 2006. DOI: 10.1016/j.jcp.2006.01.048.

[124] J. Segura and A. Gil, *Evaluation of toroidal harmonics*, *Computer Physics Communications*, vol. 124, no. 1, pp. 104–122, 2000. DOI: 10.1016/S0010-4655(99)00428-2.

[125] SESAME, *Magnets and IDs*, https://www.sesame.org.jo/accelerators/technology/magnets-and-ids, Accessed: 23.02.2024.

[126] S. Sorti, C. Petrone, S. Russenschuck, and F. Braghin, *Data-driven modeling of nonlinear materials in normal-conducting magnets*, *Physical Review Accelerators and Beams*, vol. 25, no. 5, p. 052 401, 2022. DOI: 10.1103/PhysRevAccelBeams.25.052401.

[127] S. Sorti, C. Petrone, S. Russenschuck, and F. Braghin, *Data-driven simulation of transient fields in air–coil magnets for accelerators*, *Nuclear Instruments and Methods in Physics Research Section A: Accelerators, Spectrometers, Detectors and Associated Equipment*, vol. 1011, p. 165 571, 2021, ISSN: 0168-9002. DOI: 10.1016/j.nima.2021.165571.

[128] H. Stachowiak, *Allgemeine Modelltheorie*. Wien: Springer, 1973.

[129] Z. Tang, *Estimateurs d'erreur a posteriori résiduels en éléments finis pour la résolution de problemes d'électromagnétisme en formulations potentielles*, Ph.D. dissertation, Lille 1, 2012.

[130] The MathWorks Inc., *Matlab version: R2020b*, https://www.mathworks.com, Natick, Massachusetts, United States, 2020.

[131] P. Thonet, O. Dunkel, M. Liebsch, M. Pentella, and C. Petrone, *Design, manufacture and measurement of three permanent magnet dipoles for FASER experiment*, *IEEE Transactions on Applied Superconductivity*, vol. 32, no. 6, pp. 1–5, 2022. DOI: 10.1109/TASC.2022.3191284.

[132] M. von Tresckow, H. De Gersem, and D. Loukrezis, *Error approximation and bias correction in dynamic problems using a recurrent neural network/finite element hybrid model*, *arXiv preprint arXiv:2307.02349*, 2023.

[133] B. P. Van Milligen and A. L. Fraguas, *Expansion of vacuum magnetic fields in toroidal harmonics*, *Computer physics communications*, vol. 81, no. 1-2, pp. 74–90, 1994. DOI: 10.1016/0010-4655(94)90112-0.

[134] D. Veres, T. Vaszary, E. Benedetto, and D. Barna, *A new algorithm for optimizing the field quality of curved cct magnets*, *IEEE Transactions on Applied Superconductivity*, vol. 32, no. 5, pp. 1–14, 2022. DOI: 10.1109/TASC.2022.3162389.

[135] D. Veres, T. Vaszary, and D. Barna, *Optimization of the winding of a curved canted-cosine-theta magnet for heavy ion therapy*, Tech. Rep., 2021.

[136] C. R. Vogel, *Computational methods for inverse problems*. SIAM, 2002. DOI: 10.1137/1.9780898717570.

[137] H.-P. Wan and W.-X. Ren, *Stochastic model updating utilizing Bayesian approach and Gaussian process model*, *Mechanical Systems and Signal Processing*, vol. 70, pp. 245–268, 2016. DOI: 10.1016/j.ymssp.2015.08.011.

[138] L. Wang, *Karhunen-Loève expansions and their applications*, Ph.D. dissertation, The London School of Economics and Political Science, 2008.

[139] J. Webb, *Edge elements and what they can do for you*, *IEEE Transactions on magnetics*, vol. 29, no. 2, pp. 1460–1465, 1993. DOI: 10.1109/20.250678.

[140] J. Willard, X. Jia, S. Xu, M. Steinbach, and V. Kumar, *Integrating physics-based modeling with machine learning: A survey*, *arXiv preprint arXiv:2003.04919*, vol. 1, no. 1, pp. 1–34, 2020.

[141] Z. Włodarski, *Analytical description of magnetization curves*, *Physica B: Condensed Matter*, vol. 373, no. 2, pp. 323–327, 2006. DOI: 10.1016/j.physb.2005.12.242.

[142] Wolfram Research, Inc., *Mathematica, Version 13.0*, https://www.wolfram.com/mathematica, Accessed: 14.04.2024.

[143] A. Wolski, *Beam Dynamics in High Energy Particle Accelerators*. Imperial College Press, 2014. DOI: 10.1142/p899.

[144] L. Wright and S. Davidson, *How to tell the difference between a model and a digital twin*, *Advanced Modeling and Simulation in Engineering Sciences*, vol. 7, no. 1, pp. 1–13, 2020. DOI: 10.1186/s40323-020-00147-4.

[145] Y. Xiong, W. Chen, K.-L. Tsui, and D. W. Apley, *A better understanding of model updating strategies in validating engineering models*, *Computer Methods in Applied Mechanics and Engineering*, vol. 198, no. 15, pp. 1327–1337, 2009, ISSN: 0045-7825. DOI: 10.1016/j.cma.2008.11.023.

[146] D. Xiu, *Numerical methods for stochastic computations: a spectral method approach*. Princeton university press, 2010. DOI: 10.1515/9781400835348.

[147] I. Yousept, *Optimal control of quasilinear H(curl)-elliptic partial differential equations in magnetostatic field problems*, *SIAM Journal on Control and Optimization*, vol. 51, no. 5, pp. 3624–3651, 2013. DOI: 10.1137/120904299.

[148] E. Zeidler, *Nonlinear functional analysis and its applications: II/B: Nonlinear monotone operators*. Springer Science & Business Media, 2013. DOI: 10.1007/978-1-4612-0981-2.

[149] X. Zhang *et al.*, *Design and test of a curved canted–cosine–theta superconducting dipole magnet for next generation ion therapy*, *IEEE Transactions on Applied Superconductivity*, vol. 33, no. 6, pp. 1–7, 2023. DOI: 10.1109/TASC.2023.3272576.

[150] B. W. Zotter, *Potential and wave equations in toroidal coordinates*, Tech. Rep., 1977.

Acknowledgments

I would like to thank everyone who supported me and my work on this thesis.

First of all, Dr.-Ing. Stephan Russenschuck and Prof. Dr. Sebastian Schöps, you are a great team of supervisors. Thank you so much for your ideas for this project and for your commitment to supervising me. The constant exchange with you, your professional expertise, and your encouragement and patience to let me pursue mathematical details are invaluable and have made this work possible in the first place.

Melvin Liebsch, you and your first hand experience in being a PhD student paved me the way to work on my project. You accompanied this project from day one and like no other: We had uncountable discussions about any imaginable detail and you always gave me valuable feedback. Thanks for being my third supervisor.

With their professional and technical expertise in modeling, materials, magnet systems, measurements, and mathematical concepts Ulrich Römer, Herbert Egger, Stefan Kurz, Stefano Sgobba, Pierre Thonet, Pierre Bauer, Erik Schnaubelt, Mariano Pentella, Matthias Bonora, and Jens Kaeske supported my research. Thanks a lot for always having an open ear for discussions, answering all my questions, and showing me new perspectives. Thanks to Olaf Dunkel, Mariano Pentella, and Melvin Liebsch who conducted the measurements and provided with me their post-processed measurement data. Without you, this thesis would have been purely theoretical. I extend my gratitude to Alaa Alshareef for her contribution to this work through her thesis.
Special thanks also go to Thomas Rimbot, who worked with me on the toroidal harmonic coefficients. You always believed in my formulas and went with me through all the integrals and addition theorems.

I would also like to take this opportunity to thank my two former supervisors Andreas Herty and Klaus Hoschke, who accompanied and supported me in my personal and professional development and formed me as a scientist.

Not forgetting my colleagues and friends at CERN and the Technical University of Darmstadt, who have made the last three years an unforgettable experience, in the office and especially outside the office. I would also like to thank my friends at home and my mother for always being there for me, believing in me, and supporting me in living my dreams.

This work has been supported by the Gentner Programme of the German Federal Ministry of Education and Research and the Graduate School of Computational Engineering at the Technical University of Darmstadt.
Grammarly and DeepL have been used to improve writing quality and ensure grammar and spelling.